UNIVERSITY OF CALIFORNIA

Los Angeles

Stochastic Modeling and Control of Film Porosity, Surface Roughness and Thickness in Thin Film Growth

A dissertation submitted in partial satisfaction of the requirements for the degree Doctor of Philosophy in Chemical Engineering

by

Gangshi Hu

2010

The dissertation of Gangshi Hu is approved.

Tsu-Chin Tsao

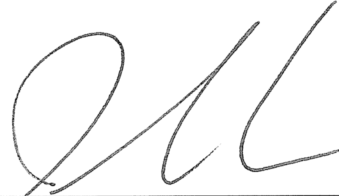

James F. Davis

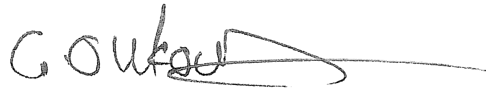

Gerassimos Orkoulas, Committee Co-Chair

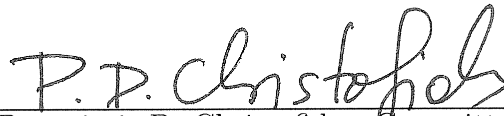

Panagiotis D. Christofides, Committee Co-Chair

University of California, Los Angeles

2010

Contents

1 Introduction **1**

1.1 Background on modeling and control of thin film microstructure . . . 1

1.2 Dissertation objectives and structure 9

2 Output Feedback Covariance Control of Surface Roughness **14**

2.1 Introduction 14

2.2 Preliminaries 16

2.2.1 Stochastic PDEs with distributed control 16

2.2.2 Model reduction 20

2.2.3 State feedback control 22

2.3 Output feedback control 23

2.3.1 Measured output with sensor noise 23

2.3.2 Dynamic output feedback control 26

2.3.3 Analysis of closed-loop infinite-dimensional system 31

2.4 Simulation results 41
2.4.1 Linearized stochastic KSE 42
2.4.2 Linear dynamic output feedback control of linearized stochastic KSE 46
2.4.3 Dynamic output feedback control of nonlinear stochastic KSE 51
2.5 Conclusions 58

3 Parameter Estimation for a Stochastic PDE Model of a Sputtering Process 60

3.1 Introduction 60
3.2 Preliminaries 62
3.2.1 Process description 62
3.2.2 KMC model of the sputtering process 65
3.2.3 Stochastic PDE model of the sputtering process 69
3.2.4 Model reduction 74
3.3 Parameter estimation of the nonlinear stochastic PDE model 75
3.3.1 System of deterministic ODEs for state covariance 76
3.3.2 Parameter estimation 77
3.4 Feedback control of surface roughness 83
3.4.1 Distributed control problem formulation 84

3.4.2 State feedback control 87

3.4.3 Output feedback control 88

3.5 Numerical simulations 93

3.5.1 Model parameter estimation 94

3.5.2 Closed-loop simulation under state feedback control 97

3.5.3 Closed-Loop simulation under output feedback control 102

3.6 Conclusions 105

4 Model Predictive Control of Surface Roughness 108

4.1 Introduction 108

4.2 Nonlinear model predictive controller design 110

4.2.1 Preliminaries 110

4.2.2 Model reduction 112

4.2.3 Model predictive controller design 115

4.2.4 Analysis of the closed-loop infinite-dimensional system 123

4.3 Simulation results 131

4.3.1 Model predictive control of the stochastic Kuramoto-Sivashinsky equation 132

4.3.2 Model predictive control of an ion-sputtering process 140

4.4 Conclusions 152

5 Modeling and Control of Film Porosity **154**

5.1 Introduction 154

5.2 Thin film deposition process description and modeling 155

5.2.1 On-lattice kinetic Monte Carlo model of film growth 156

5.2.2 Adsorption process 158

5.2.3 Migration process 161

5.2.4 Simulation algorithm 162

5.3 Open-loop simulations 165

5.3.1 Definition of film site occupancy ratio 165

5.3.2 Film site occupancy ratio evolution profile 167

5.3.3 Partial film site occupancy ratio 170

5.4 Construction of ODE models for complete and partial film site occupancy ratio 177

5.4.1 Deterministic dynamic model of complete film site occupancy ratio 177

5.4.2 Stochastic dynamic model of partial film site occupancy ratio 178

5.4.3 Parameter estimation and dependence 181

5.5 Model predictive control design 189

5.5.1 Regulation of complete film site occupancy ratio 190

5.5.2 Fluctuation regulation of partial film site occupancy ratio . . . 192

5.5.3 Closed-loop simulations 194

5.6 Conclusions 200

6 Simultaneous Regulation of Surface Roughness and Porosity 203

6.1 Introduction 203

6.2 Thin film deposition process 204

6.2.1 Description and modeling 204

6.2.2 Definitions of surface morphology and film porosity 207

6.3 Dynamic models construction and parameter estimation 210

6.3.1 Edward-Wilkinson-type equation of surface height 210

6.3.2 Deterministic dynamic model of film site occupancy ratio . . . 216

6.3.3 Parameter estimation 217

6.4 Model predictive control 221

6.4.1 MPC formulation for regulation of roughness and porosity . . 222

6.4.2 MPC formulation based on reduced-order model 224

6.5 Simulation results 226

6.6 Conclusions 234

7 Simultaneous Regulation of Film Surface Roughness, Porosity, and Thickness Using Deposition Rate 236

7.1 Introduction 236

7.2 Preliminaries 237
7.2.1 On-lattice kinetic Monte Carlo model of film growth 237
7.2.2 Definitions of thin film microstructure 241
7.3 Dynamic model construction and parameter estimation 243
7.3.1 Edwards-Wilkinson-type equation of surface height using deposition rate as manipulated input 243
7.3.2 Dynamic model of film site occupancy ratio 248
7.3.3 Parameter estimation 252
7.4 Model predictive controller design 253
7.4.1 Reduced-order model for surface roughness 255
7.4.2 MPC formulation 257
7.5 Simulation results 261
7.5.1 Regulation of surface roughness with/without constrained film thickness 262
7.5.2 Regulation of film porosity by manipulating deposition rate . . 265
7.5.3 Simultaneous regulation of surface roughness and film porosity with constrained film thickness 265
7.6 Conclusions 269
8 Conclusions **271**

Bibliography **273**

List of Figures

2.1 The closed-loop surface covariance under linear dynamic output feedback control using 11 measurement sensors. The horizontal dashed lines represent the range in which the surface covariance $\mathrm{Cov}_{\mathrm{h}}$ is expected to be based on the theoretical estimates of Theorem 2.1. . . . 48

2.2 Comparison of the surface covariance under linear dynamic output feedback controllers with 7, 11 and 15 measurement sensors. 50

2.3 The closed-loop profile of the surface covariance under linear dynamic output feedback control with 6 measurement sensors. 50

2.4 The closed-loop surface covariance profile of the nonlinear stochastic KSE under linear dynamic output feedback control with 11 measurement sensors. The horizontal dashed lines represent the range in which the surface covariance $\mathrm{Cov}_{\mathrm{h}}$ is expected to be based on the theoretical estimates of Theorem 2.1. 53

2.5 Comparison of the closed-loop surface covariance profiles of the nonlinear stochastic KSE under linear and nonlinear state feedback control. The horizontal dashed lines represent the range in which the surface covariance $\mathrm{Cov_h}$ is expected to be based on the theoretical estimates of Theorem 1 in [62]. 56

2.6 The surface covariance of nonlinear KSE under nonlinear dynamic output feedback controllers with different numbers of measurement sensors. 58

3.1 Schematic of the rule to determine P_{e}. P_{e} is defined as $\frac{1}{7}$ times the number of occupied sites in a box of size 3×3 centered at the particle on the top of site i; $P_{\mathrm{e}} = 1$ in the left figure and $P_{\mathrm{e}} = \frac{4}{7}$ in the right figure, where the particle marked by $\bullet$ is on the top of site i. 64

3.2 Profiles of the state covariance $\langle \alpha_n^2(t) \rangle$ for $n = 1$, 3, 5, 7, and 9. . . . 95

3.3 Profiles of the expected value for $\alpha_n f_{n\alpha}(t)$ for $n = 1$, 3, 5, 7, and 9. . 96

3.4 The covariance matrix for the first 20 states: a diagonally dominant matrix. 97

3.5 Comparison of the open-loop profile of the expected surface roughness of the sputtering process from the kMC simulator and that from the solution of the stochastic KSE using the estimated parameters. 98

3.6 Closed-loop surface roughness profiles in the sputtering process under state feedback controllers of different order, m: initial surface roughness is 0.5. 101
3.7 Profiles of the expected open-loop surface roughness of the sputtering process. 101
3.8 Closed-loop surface roughness profiles in the sputtering process under state feedback controllers of different order m: initial surface roughness is 0 (flat initial surface). 103
3.9 A snapshot of the surface configuration at the end of the closed-loop simulation under the 40th order state feedback controller: initial surface roughness is 0.5. 103
3.10 Closed-loop surface roughness profiles in the sputtering process under output feedback controllers of different order, m: initial surface roughness is 0.5. 105
3.11 Closed-loop surface roughness profiles in the sputtering process under output feedback controllers of different order, m: initial surface roughness is 0 (flat initial surface). 106
3.12 A snapshot of the surface configuration at the end of the closed-loop simulation under the 40th order output feedback controller: initial surface roughness is 0.5. 106

4.1 Comparison of the open-loop expected surface roughness profile computed by averaging 100 independent simulation runs (solid line) and that from a single simulation run (dotted line) of the stochastic KSE of Eq. (4.49). 136

4.2 The closed-loop profile of the expected value of the surface roughness of the nonlinear KSE under predictive control (solid line) versus the reference trajectory. 139

4.3 Comparison of the expected closed-loop surface roughness of the nonlinear KSE under the proposed predictive controller (top figure) and under the nonlinear pole placement controller developed in [62] (bottom figure). Effect of model uncertainty. 141

4.4 Comparison of the open-loop profile of the expected surface roughness from the kMC simulator when $f = 0.5$ and βJ varies from 0.05 to 5. . 144

4.5 Comparison of the open-loop profile of the expected surface roughness from the kMC simulator when $\beta J = 2$ and f varies from 0.1 to 0.6. . 145

4.6 Comparison of open-loop profiles of the expected surface roughness from the kMC simulator when $\beta J = 2$ and f is 1) $f = 0.6$, 2) $f = 0.1$, and 3) time-varying. 146

4.7 Surface micro-configuration at the beginning of the closed-loop simulation run. The initial surface roughness is 0.5. 150

4.8 The closed-loop profile of the expected value of the surface roughness under predictive control. 151

4.9 Surface micro-configuration at the end of the closed-loop simulation run under predictive control. The final surface roughness is around 0.3. 152

5.1 Thin film growth process on a triangular lattice. 157

5.2 Schematic of the adsorption event with surface relaxation. In this event, particle A is the incident particle, particle B is the surface particle that is first hit by particle A, site C is the nearest vacant site to particle A among the sites that neighbor particle B, and site D is a stable site where particle A relaxes. 160

5.3 Illustration of the definition of film SOR of Eq. (5.4). 166

5.4 Mean value (solid lines) and variance (dashed line) of the complete film SOR versus time for a 1000 s open-loop deposition process with substrate temperature $T = 600$ K and deposition rate $W = 1$ layer/s. 168

5.5 Snapshots of the film microstructure at $t = 100$ s, 400 s, 700 s, and 1000 s of the open-loop deposition process with substrate temperature $T = 600$ K and deposition rate $W = 1$ layer/s. 169

5.6 Probability distribution functions (PDF) of film SOR at $t = 100$ s, 400 s, 700 s, and 1000 s of the open-loop deposition process. 171

5.7 Illustration of the definition of partial film SOR of Eq. (5.6). 172

5.8 Profiles of mean value (solid line) and variance (dashed line) of the partial film SOR in a 1000 s open-loop deposition process with substrate temperature $T = 600$ K and deposition rate $W = 1$ layer/s. 175

5.9 Probability distribution functions (PDF) of partial film SOR at $t = 100$ s, 400 s, 700 s, and 1000 s of the open-loop deposition process. 176

5.10 Histogram from 10000 simulation runs of the partial film SOR at the end ($t = 1000$ s) of the open-loop deposition process with substrate temperature $T = 600$ K and deposition rate $W = 1$ layer/s. 180

5.11 Profiles of the expected complete film SOR (solid line) and of the expected partial film SOR (dashed line) in a 1000 s open-loop deposition process and predictions from the deterministic ODE model (solid line with '+') and the stochastic ODE model (dashed line with '+') with estimated parameters; $T = 600$ K, $W = 1$ layer/s. 184

5.12 Variance of the partial film SOR with respect to time for a 1000 s open-loop deposition process (solid line) and the estimated steady-state level (dashed line); $T = 600$ K, $W = 1$ layer/s. 185

5.13 Dependence of steady-state values of film SOR, ρ^{ss}, on the lattice size for different temperatures. 186

5.14 Dependence of ρ^{ss} and $\rho_{\mathrm{p}}^{\mathrm{ss}}$ on the substrate temperature with deposition rate $W = 1$ layer/s. 188

5.15 Dependence of τ and τ_{p} on the substrate temperature with deposition rate $W = 1$ layer/s. 188

5.16 Dependence of $\mathrm{Var}_{\mathrm{p}}^{\mathrm{ss}}$ on the substrate temperature with deposition rate $W = 1$ layer/s. 189

5.17 Closed-loop profiles of the complete film SOR (solid line) and of the expected value of the complete film SOR (dotted line) under the controller of Eq. (5.23). The profile of the substrate temperature is also included (dash-dotted line). 196

5.18 Snapshots of the film microstructure at $t = 100$ s, 400 s, 700 s, and 1000 s of the closed-loop simulation under the feedback controller of Eq. (5.23) with $q_{\mathrm{sp},i} = 1$, $i = 1, \ldots, 5$. 198

5.19 Closed-loop profiles of the complete film SOR (solid line) and of the expected value of the complete film SOR (dotted line) under the controller of Eq. (5.24). The profile of the substrate temperature is also included (dash-dotted line). 199

5.20 Comparison of the variance of the partial film SOR for different weights: $q_{\mathrm{var},i} = 0$ (solid line) and $q_{\mathrm{var},i} = 10$ (dashed line). 200

5.21 Snapshots of the film microstructure at $t = 100$ s, 400 s, 700 s, and 1000 s of the closed-loop simulation under the feedback controller of Eq. (5.24) with $q_{\mathrm{sp},i} = 1$, $q_{\mathrm{var},i} = 10$, $i = 1, \ldots, 5$. 201

6.1 Thin film growth process on a triangular lattice with vertically incident particles from gas phase. 205

6.2 Schematic of the adsorption event with surface relaxation. In this event, particle A is the vertically incident particle, particle B is the surface particle that is first hit by particle A, site C is the nearest vacant site to particle A among the sites that neighbor particle B, and site D is a stable site where particle A relaxes. 206

6.3 Definition of surface height profile. A surface particle is a particle that is not blocked by particles from both of its neighboring columns in the vertical direction. 208

6.4 Histogram of surface height at $t = 400$ s for different sites ($x = 0a$, $25a$, $50a$, $75a$). 212

6.5 Histogram of surface height at $x = 50a$ for different time instants ($t = 100$ s, 200 s, 300 s, 400 s). 212

6.6 Dependence of $\ln(\nu)$ and σ^2 on the substrate temperature with deposition rate $W = 1$ layer/s. 220

6.7 Dependence of ρ^{ss} and τ on the substrate temperature with deposition rate $W = 1$ layer/s. 221

6.8 Profiles of the expected values of surface roughness square (solid line) and of the film SOR (dash-dotted line) under closed-loop operation with cost function including only penalty on surface roughness. 229

6.9 Profile of the instantaneous values of substrate temperature under closed-loop operation with cost function including only penalty on surface roughness. 229

6.10 Profiles of the expected values of surface roughness square (solid line) and of the film SOR (dash-dotted line) under closed-loop operation with cost function including only penalty on the film SOR. 230

6.11 Profile of the instantaneous value of substrate temperature under closed-loop operation with cost function including only penalty on the film SOR. 231

6.12 Profiles of the expected values of surface roughness square (solid line) and of the film SOR (dash-dotted line) at the end of the closed-loop simulations (t = 1000 s) with the following penalty weighting factors: $q_{\mathrm{r}^2,i}$ fixed at 1 for all i and for different values of q_{SOR}. 232

6.13 Snapshots of film microstructure at t = 1000 s of simulations under open-loop and closed-loop operations. Open-loop simulation is carried out at T = 500 K and W = 1 layer/s. Closed-loop simulations are carried out under three different control schemes: (I) roughness-only control; (II) SOR-only control; (III) simultaneous regulation of surface roughness and film SOR with $q_{\mathrm{r}^2,i} = 1$ and $q_{\mathrm{SOR}} = 10^4$. 233

7.1 Dependence of ν and σ^2 on the deposition rate with substrate temperature $T = 850$ K. 253

7.2 Dependence of r_{h} on the deposition rate with substrate temperature $T = 850$ K. 254

7.3 Dependence of ρ^{ss} and τ on the deposition rate with substrate temperature $T = 850$ K. 254

7.4 Profiles of the expected values of surface roughness square (solid line) and of the expected values of the film thickness (dash-dotted line) under closed-loop operation; roughness control problem with desired minimum of film thickness. 263

7.5 Profiles of the expected values of surface roughness square (solid line) and of the film thickness (dash-dotted line) under closed-loop operation; roughness control problem without desired minimum of film thickness. 264

7.6 Profiles of the expected values of deposition rate under closed-loop operation with (solid line) and without (dashed line) desired minimum of film thickness; roughness control problem. 264

7.7 Profiles of the expected values of film SOR (solid line) and of the deposition rate (dash-dotted line) under closed-loop operation; porosity-only control. 266

7.8 Profiles of the expected values of surface roughness square (solid line) and of the film thickness (dash-dotted line) under closed-loop operation; simultaneous regulation of film thickness, roughness and porosity. 267

7.9 Profiles of the expected values of film SOR (solid line) and of the deposition rate (dash-dotted line) under closed-loop operation; simultaneous regulation of film thickness, roughness and porosity. 267

7.10 Profiles of the instantaneous values of surface roughness square (solid line) and of the film thickness (dash-dotted line) under closed-loop operation; simultaneous regulation of film thickness, roughness and porosity. 268

7.11 Profiles of the instantaneous values of film SOR (solid line) and of the deposition rate (dash-dotted line) under closed-loop operation; simultaneous regulation of film thickness, roughness and porosity. 269

ACKNOWLEDGEMENTS

I would like to express my most gratitude to my co-advisor, Professor Panagiotis D. Christofides, for his guidance, encouragement, and support throughout my doctoral work. Being his student has been a great fortune for me in my doctoral research study and in my life as well.

I would like to equally thank my co-advisor, Professor Gerassimos Orkoulas, for his instruction and attention. His knowledge and achievements in the research area of microscopic simulations are admirable and helpful in my research study.

I would like to thank Professor James F. Davis and Professor Tsu-Chin Tsao for agreeing to serve on my doctoral committee.

Financial support from NSF, CBET-0652131, and from the UCLA Graduate Division through a 2008–2009 Doctoral Dissertation Year Fellowship, is gratefully acknowledged.

I am greatly indebted to my wife, Yiming Zhai, for her presence in this world with me as a ten-year-long classmate, a life-time friend, and, most importantly, an eternal soul mate. Her love and patience are essential to my research study as encouragement and relief. I am also proud of her for finally pursuing her Doctoral degree in Electrical Engineering.

Finally, I would like to thank my parents for their continuous support, encouragement, and love.

Chapter 2 is a version of: Hu, G., Y. Lou, and P. D. Christofides. Dynamic output

feedback covariance control of stochastic dissipative partial differential equations. *Chemical Engineering Science*, 63:4531–4542, 2008.

Chapter 3 is a version of: Hu, G., Y. Lou, and P. D. Christofides. Model parameter estimation and feedback control of surface roughness in a sputtering process. *Chemical Engineering Science*, 63:1810–1816, 2008.

Chapter 4 is a version of: Lou, Y., G. Hu, and P. D. Christofides. Model predictive control of nonlinear stochastic partial differential equations with application to a sputtering process. *AIChE Journal*, 54:2065–2081, 2008.

Chapter 5 is a version of: Hu, G., G. Orkoulas, and P. D. Christofides. Modeling and control of film porosity in thin film deposition. *Chemical Engineering Science*, 64:3668–3682, 2009.

Chapter 6 is a version of: Hu, G., G. Orkoulas, and P. D. Christofides. Stochastic modeling and simultaneous regulation of surface roughness and porosity in thin film deposition. *Industrial & Engineering Chemistry Research*, 48:6690–6700, 2009.

Chapter 7 is a version of: Hu, G., G. Orkoulas, and P. D. Christofides. Regulation of film thickness, surface roughness and porosity in thin film growth using deposition rate. *Chemical Engineering Science*, 64:3903–3913, 2009.

VITA

August 24, 1979	Born, Anshan, China
2002	Bachelor of Science, Chemical Engineering Tsinghua University Beijing, China
2002–2005	Software Developer Beijing Airda Electronic Equipment Company Beijing, China
2005	Master of Science, Chemical Engineering Tsinghua University Beijing, China
2006–2010	Graduate Student Researcher Department of Chemical and Biomolecular Engineering University of California, Los Angeles
2006–2010	Teaching Assistant/Associate/Fellow Department of Chemical and Biomolecular Engineering University of California, Los Angeles
2008	Best Presentation Session Award American Control Conference, Seattle, WA
2008–2009	Dissertation Year Fellowship University of California, Los Angeles
2010	Outstanding Ph.D. Student Award Department of Chemical and Biomolecular Engineering University of California, Los Angeles

PUBLICATIONS AND PRESENTATIONS

1. Christofides, P. D., Y. Lou, and G. Hu. Construction of nonlinear stochastic pdes for nonlinear feedback control of surface roughness: application to a sput-

tering process. *AIChE Annual Meeting*, paper 561d, San Francisco, California, 2006.

2. Christofides, P. D., Y. Lou, and G. Hu. Nonlinear feedback control of stochastic PDEs. *AIChE Annual Meeting*, paper 598d, San Francisco, California, 2006.

3. Hu, G., Y. Lou, and P. D. Christofides. Output feedback covariance control of nonlinear stochastic partial differential equations. *AIChE Annual Meeting*, paper 429c, Salt Lake City, Utah, 2007.

4. Hu, G., Y. Lou, and P. D. Christofides. Model parameter estimation and feedback control of surface roughness in a sputtering process. *Chemical Engineering Science*, 63:1810–1816, 2008.

5. Hu, G., Y. Lou, and P. D. Christofides. Dynamic output feedback covariance control of linear stochastic dissipative partial differential equations. *Proceedings of the American Control Conference*, 260–266, Seattle, Washington, 2008.

6. Hu, G., Y. Lou, and P. D. Christofides. Dynamic output feedback covariance control of stochastic dissipative partial differential equations. *Chemical Engineering Science*, 63:4531–4542, 2008.

7. Hu, G., X. Zhang, G. Orkoulas, and P. D. Christofides. Construction of stochastic differential equation models for porous thin film deposition processes. *AIChE Annual Meeting*, paper 546a, Philadelphia, Pennsylvania, 2008.

8. Hu, G., Y. Lou, G. Orkoulas, and P. D. Christofides. Model predictive control of thin film porosity using stochastic differential equations. *AIChE Annual Meeting*, paper 652c, Philadelphia, Pennsylvania, 2008.

9. Hu, G., G. Orkoulas, and P. D. Christofides. Modeling and control of film porosity in thin film deposition. *Chemical Engineering Science*, 64:3668–3682, 2009.

10. Hu, G., G. Orkoulas, and P. D. Christofides. Regulation of film thickness, surface roughness and porosity in thin film growth using deposition rate. *Chemical Engineering Science*, 64:3903–3913, 2009.

11. Hu, G., G. Orkoulas, and P. D. Christofides. Model predictive control of film porosity in thin film deposition. *Proceedings of the American Control Conference*, 4797–4804, St. Louis, Missouri, 2009.

12. Hu, G., G. Orkoulas, and P. D. Christofides. Stochastic modeling of film porosity in thin film deposition. *Proceedings of the American Control Conference*, 4771–4778, St. Louis, Missouri, 2009.

13. Hu, G., G. Orkoulas, and P. D. Christofides. Stochastic modeling and simultaneous regulation of surface roughness and porosity in thin film deposition. *Industrial & Engineering Chemistry Research*, 48:6690–6700, 2009.

14. Hu, G., G. Orkoulas, and P. D. Christofides. Simultaneous regulation of surface roughness and porosity in thin film growth. *Proceedings of IFAC International*

Symposium on Advanced Control of Chemical Processes, paper 169, 6 pages, Istanbul, Turkey, 2009.

15. Hu, G., J. Huang, G. Orkoulas, and P. D. Christofides. Investigation of film surface roughness and porosity dependence on lattice size in a porous thin film deposition process. *Physical Review E*, 80:041122, 2009.

16. Hu, G., G. Orkoulas, and P. D. Christofides. Simultaneous regulation of film thickness, surface roughness and porosity in a thin film growth. *AIChE Annual Meeting*, paper 573d, Nashville, Tennessee, 2009.

17. Hu, G., X. Zhang, G. Orkoulas, and P. D. Christofides. Simultaneous regulation of film thickness, surface roughness and porosity in a multiscale thin film growth process. *Proceedings of the 48th IEEE Conference on Decision and Control*, 2387–2394, Shanghai, China, 2009.

18. Huang, J., G. Hu, G. Orkoulas, and P. D. Christofides. Investigation of film surface roughness and porosity dependence on lattice size in a porous thin film deposition process. *AIChE Annual Meeting*, paper 222h, Nashville, Tennessee, 2009.

19. Huang, J., G. Hu, G. Orkoulas, and P. D. Christofides. Model predictive control of film surface root-mean-square roughness and slope: application to thin film solar cells. *Proceedings of the 21st International Symposium on Chemical Reaction Engineering*, Philadelphia, Pennsylvania, 2010.

20. Huang, J., G. Hu, G. Orkoulas, and P. D. Christofides. Lattice-size dependence and dynamics of surface mean slope in a thin film deposition process. *Proceedings of 8th IFAC Symposium on Dynamics and Control of Process Systems*, 6 pages, in press, Leuven, Belgium, 2010.

21. Huang, J., G. Hu, G. Orkoulas, and P. D. Christofides. Dynamics and lattice-size dependence of surface mean slope in thin-film deposition. *Industrial & Engineering Chemistry Research,* in press, 2010.

22. Lou, Y., G. Hu, P. D. Christofides and G. Orkoulas. Parameter identification for nonlinear stochastic pde model of a sputtering process. *Proceedings of 8th IFAC Symposium on Dynamics and Control of Process Systems-Volume 3*, 217–222, Cancún, Mexico, 2007.

23. Lou, Y., G. Hu, and P. D. Christofides. Nonlinear predictive control of thin film microstructure using a stochastic PDE model. *AIChE Annual Meeting*, paper 581c, Salt Lake City, Utah, 2007.

24. Lou, Y., G. Hu, and P. D. Christofides. Model predictive control of nonlinear stochastic partial differential equations. *AIChE Annual Meeting*, paper 437a, Salt Lake City, Utah, 2007.

25. Lou, Y., G. Hu, and P. D. Christofides. Model predictive control of nonlinear stochastic partial differential equations with application to a sputtering process. *AIChE Journal*, 54:2065–2081, 2008.

26. Lou, Y., G. Hu, and P. D. Christofides. Control configuration selection and nonlinear control of surface roughness in a sputtering process. *Proceedings of the 46th IEEE Conference on Decision and Control*, 231–238, New Orleans, Louisiana, 2007.

27. Lou, Y., G. Hu, and P. D. Christofides. Model predictive control of nonlinear stochastic partial differential equations with application to a sputtering process. *Proceedings of the American Control Conference*, 2476–2483, St. Louis, Missouri, 2009.

28. Zhang, X., G. Hu, G. Orkoulas, and P. D. Christofides. Multiscale modeling and control of a porous thin film deposition process. *AIChE Annual Meeting*, paper 140f, Nashville, Tennessee, 2009.

29. Zhang, X., G. Hu, G. Orkoulas, and P. D. Christofides. Controller and estimator design for regulation of film thickness, surface roughness and porosity in a multiscale thin film growth process. *Industrial & Engineering Chemistry Research,* in press, 2010.

30. Zhang, X., G. Hu, G. Orkoulas, and P. D. Christofides. Multivariable model predictive control of thin film surface roughness and slope for light trapping optimization. *Industrial & Engineering Chemistry Research,* in press, 2010.

31. Zhang, X., G. Hu, G. Orkoulas, and P. D. Christofides. Predictive control of surface mean slope and roughness in a thin film deposition process. *Chemical*

Engineering Science, accepted for publication, 2010.

ABSTRACT OF THE DISSERTATION

Stochastic Modeling and Control of Film Porosity, Surface Roughness and Thickness in Thin Film Growth

by

Gangshi Hu

Doctor of Philosophy in Chemical Engineering

University of California, Los Angeles, 2010

Professor Panagiotis D. Christofides, Co-Chair

Professor Gerassimos Orkoulas, Co-Chair

Currently, there is an increasing need to improve semiconductor manufacturing process operation and yield. This need has arisen due to the increased complexity and density of devices on the wafer, which is the result of increased wafer size and smaller device dimensions. Within this manufacturing environment, thin film microstructure, including thin film surface roughness and amount of internal film defects, has emerged as an important film quality variable, which strongly influences the electrical and mechanical properties of micro- electronic devices. On one hand, surface roughness of thin films controls the interfacial layer and properties between two successively deposited films. On the other hand, the amount of internal defects, usually expressed

as film porosity, plays an important role in determining the thin film microstructure. At this stage, previous research efforts have exclusively focused on control of thin film surface roughness and have not addressed the challenging issue of simultaneously regulating film surface roughness, porosity, and thickness while reducing run-to-run film variability.

This dissertation presents a unified and practical framework for modeling and control of film porosity, surface roughness, and thickness in thin film growth. Specifically, we will present novel definitions for describing film porosity, and stochastic modeling and parameter estimation techniques for constructing dynamic models for roughness, porosity, and film thickness. We will also present state/output feedback covariance control and model predictive control problem formulations and solutions which lead to a balanced trade-off in the closed-loop system between the three, possibly conflicting, control objectives of surface roughness, film thickness, and porosity regulation. The application of the proposed modeling and control methods to complex thin film deposition and sputtering processes will be discussed and simulation results will be shown to demonstrate the resulting closed-loop system performance and robustness.

Chapter 1

Introduction

1.1 Background on modeling and control of thin film microstructure

Currently, there is an increasing need to improve thin film semiconductor manufacturing process operation and yield due to its crucial role in a wide range of industries such as microelectronics, communications, optical electronics, and solar cells. Particularly in the industry of microelectronics, to fabricate thin film semiconductor devices with high and consistent performance, it is desirable that the operation of thin film preparation processes can be tightly controlled so that the increasingly stringent industrial requirements on the quality of such films can be satisfied. Within this manufacturing environment, thin film microstructure (in particular, thin film thickness, surface roughness, and amount of internal defects) has emerged as an important film

quality variable which strongly influences the electrical and mechanical properties of microelectronic devices [2, 54]. On one hand, surface roughness of thin films controls the interfacial layer and properties between two successively deposited films. On the other hand, the amount of internal defects, usually expressed as film porosity strongly influences film electrical properties since the vacancies in microscopic structure of a thin film provide free sites for undesired electrical static charge, high leakage current and longer latency, thereby lowering transistor operating speed. For example, low-k dielectric films of high porosity are being used in current interconnect technologies to meet resistive-capacitive delay goals and minimize cross-talk. However, increased porosity negatively affects the mechanical properties of dielectric films, increasing the risk of thermo-mechanical failures [48]. Furthermore, in the case of gate dielectrics, it is important to reduce thin film porosity as much as possible and eliminate the development of holes close to the interface.

Thus, real-time feedback control of thin film growth conditions, based on mathematical models, has become increasingly important in order to meet the stringent requirements on the quality of thin films and reduce thin film variability. In previous works, deposition uniformity and composition control has been accomplished on the basis of continuum-type distributed parameter models (see, for example, [3, 84, 19] for results on rapid thermal processing (RTP) and [5, 72] for results on plasma-enhanced chemical vapor deposition (PECVD)). However, precise control of thin film microstructure requires stochastic distributed models that predict how the film state

on the microscopic level is affected by changes in the controllable process parameters. In thin film growth processes, the film microstructure is directly shaped by microscopic processes, which are stochastic processes. Therefore, the stochastic nature of thin film growth processes must be fully considered in the modeling and control of the thin film microstructure of such processes. Furthermore, the development of modern surface roughness measurement techniques provides the opportunity to obtain surface roughness measurements in real-time using spectroscopic ellipsometry techniques [96], grazing-incidence small-angle X-ray scattering (GISAXS) [76] or by combination of on-line measurement techniques for measuring gas phase compositions with off-line measurement techniques for measuring surface roughness. An implementation of the latter approach can be found in [72], where it was used to measure carbon composition of thin films in plasma-enhanced chemical vapor deposition using combination of optical emission spectroscopy (OES) and X-ray photoelectron spectroscopy (XPS). Also, experimental methods have been developed to perform scanning tunneling microscopy (STM) measurements of the surface during epitaxial growth of semiconductor layers [89]. The desire to understand and control thin film microstructure has motivated extensive research on fundamental mathematical models describing the microscopic features, which include: 1) kinetic Monte Carlo (kMC) methods [35, 32, 79, 75], and 2) stochastic partial differential equations (PDEs) [31, 91, 26, 53].

KMC models were initially used to develop a methodology for feedback control of thin film surface roughness [57, 58, 21]. Specifically, in the context of surface

roughness control and optimization, a methodology for feedback control of surface roughness using kMC models was developed in [57, 58]. The methodology led to the design of (a) real-time roughness estimators by using multiple small lattice kMC simulators, adaptive filters and measurement error compensators, and (b) feedback controllers based on the real-time roughness estimators. The method was successfully applied to control surface roughness in a GaAs deposition process model [59]. Moreover, kMC methods were also used to study dynamics of complex deposition processes including multiple components with both short-range and long-range interactions and to perform predictive control design to control final surface roughness in [70]. However, the fact that kMC models are not available in closed-form makes it very difficult to use them for system-level analysis and the design and implementation of model-based feedback control systems. To achieve better closed-loop performance, it is desirable to design feedback controllers on the basis of deposition process models. An approach was reported in [81, 8] to identify linear deterministic models from outputs of kMC simulators and design controllers using linear control theory. This approach is effective in controlling macroscopic variables which are low statistical moments of the microscopic distributions (e.g., surface coverage, which is the zeroth moment of species distribution on a lattice). In this direction, other results also include the construction of linear/nonlinear deterministic models from input/output data using system identification techniques [27, 77, 93].

However, to control higher statistical moments of the microscopic distributions,

such as the surface roughness (the second moment of height distribution on a lattice) or even the microscopic configuration (such as the surface morphology), deterministic models may not be sufficient. This is because the effect of the stochastic nature of the microscopic processes becomes very significant in these cases and must be addressed in both the model construction and controller design. From a modeling point of view, closed-form process models, in the form of linear or nonlinear stochastic PDEs, can be derived based on the microscopic details and the corresponding master equation (e.g., [31, 86, 91, 26, 53]). Stochastic PDEs contain the surface morphology information of thin films, and thus, they may be used for the purpose of feedback controller design. For example, it has been experimentally verified that the Kardar-Parisi-Zhang (KPZ) equation [45] can describe the evolution of the surface morphology of gallium arsenide (GaAs) thin films which is consistent to the surface measured by atomic force microscopy (AFM) [11, 44]. The availability of stochastic PDE models for certain deposition and sputtering processes has motivated recent research on the development of a method for covariance feedback control of surface roughness based on linear stochastic PDE process models [61, 60]. This method involves reformulation of the linear stochastic PDE into a system of infinite linear stochastic ordinary differential equations (ODEs) by using modal decomposition, derivation of a finite-dimensional approximation that captures the dominant mode contribution to the surface roughness, and state feedback controller design based on the finite-dimensional approximation. Furthermore, based on the fact that kMC simulations

provide realizations of a stochastic process which are consistent with the master equation that describes the evolution of the probability distribution of the system being at a certain micro-configuration, a method to construct reduced-order approximations of the master equation was reported in [33]. Finally, novel, computationally-efficient optimization schemes for multiscale models were recently developed based on the concept of in-situ adaptive tabulation [85], based on the concept of coarse time-steppers [7, 13], and based on the concept of funneling [64, 65].

Furthermore, although stochastic PDE models are suitable for model-based controller design, the construction of stochastic PDE models for thin film growth and sputtering processes directly based on microscopic process rules is, in general, a very difficult task. This motivates the development of system identification methods for stochastic PDEs. Compared to deterministic systems, modeling and identification of dynamical systems described by stochastic ODEs/PDEs has received relatively limited attention and most of the results focus on stochastic ODE systems. Theoretical foundations on the analysis, parametric optimization, and optimal stochastic control for linear stochastic ODE systems can be found in the early work by Astrom [1]. More recently, likelihood-based methods for parameter estimation of stochastic ODE models have been developed [14, 50]. These methods determine the model parameters by solving an optimization problem to maximize a likelihood function or a posterior probability density function of a given sequence of measurements of a stochastic process. For many thin film growth or sputtering processes, kMC models are available,

which can be conveniently used to generate multiple independent observations of the same stochastic process. Consequently, statistical moments of the state such as the expected value (first order moment), covariance (second order moment), and even higher-order moments, can be obtained from the data set generated by kMC simulations. Since the dynamics of the state moments of a stochastic process may be described by deterministic differential equations, the issues of parameter estimation of stochastic models could be addressed by employing parameter estimation techniques for deterministic systems. Following this idea, a systematic identification approach was developed for linear stochastic PDEs [60] and a method for construction of linear stochastic PDE models for thin film growth using first principles-based microscopic simulations was developed and applied to construct linear stochastic PDE models for thin film deposition processes in two-dimensional lattices [71].

However, nonlinearities exist in many material preparation processes in which surface evolution can be modeled by stochastic PDEs. A typical example of such processes is the sputtering process whose surface evolution is described by the nonlinear stochastic Kuramoto-Sivashinsky equation (KSE). In a simplified setting, the sputtering process includes two types of surface micro-processes, erosion and diffusion. The nonlinearity of the sputtering process originates from the dependence of the rate of erosion on a nonlinear sputtering yield function [26]. Available methods for identification and construction of linear stochastic PDEs require the analytical solutions of state covariances [60, 71], which prevent their direct applications to non-

linear stochastic PDEs. This motivates research on the development of methods for parameter estimation of nonlinear stochastic PDE process models.

Model predictive control (MPC) is widely used in chemical process control due to its capability to handle input and state constraints, to tolerate model uncertainty and suppress external disturbances, and to force the closed-loop system to follow a target trajectory using optimal control action (see References [34, 4, 74, 78] for surveys of results and references in this area). In MPC, the control action is obtained by solving repeatedly, on-line, a finite horizon constrained open-loop optimal control problem. Recent efforts on predictive control of distributed parameter systems have focused on predictive control of deterministic parabolic PDEs including linear systems with distributed [30] and boundary [28] control and nonlinear systems with distributed control [29]. However, results on predictive control of stochastic distributed parameter systems, to the best of our knowledge, are not available.

In the context of modeling of thin film porosity, kMC models have been widely used to model the evolution of porous thin films in many deposition processes, such as the molecular beam epitaxial (MBE) growth of silicon films and copper thin film growth [56, 97]. Both monocrystalline and polycrystalline kMC models have been developed and simulated [55, 92]. The influence of the macroscopic parameters, i.e., the deposition rate and temperature, on the porous thin film microstructure has also been investigated using kMC simulators of deposition processes. With respect to porosity modeling for control, deterministic and stochastic ODE models of film porosity were

recently developed [40] to model the evolution of film porosity and its fluctuation and design MPC algorithms to control film porosity to a desired level and reduce run-to-run porosity variability. In MPC, the optimal manipulated input is obtained from the solution of an on-line optimization problem which minimizes a cost function that penalizes the errors from the set-points at designated finite horizons. MPC is widely used in the control of many chemical processes due to its capability to handle input and state constraints and its robustness against model uncertainty and external disturbances [69, 24]. At this stage, a careful look of the existing literature indicates that the simultaneous control of film surface roughness, thickness and porosity and reduction of fluctuations remains still an unresolved issue.

1.2 Dissertation objectives and structure

Motivated by the above considerations in Section 1.1, this dissertation focuses on the modeling and the control of film surface morphology and microstructural defects in thin film growth processes. Kinetic Monte Carlo models are developed to simulate the thin film growth processes on the basis of lattice structures. Surface height profile, surface roughness, film thickness, and film porosity are defined and computed from the kMC simulation data and are used to characterize the surface morphology and microstructure of the thin films. Stochastic and deterministic differential equation models are introduced to describe the evolution of the thin film surface morphology and internal microstructure and are used as the basis for the feedback control design.

The model parameters of the dynamic equation models can be estimated on the basis of the kMC simulation data using least-square methods. State and output feedback control algorithms and MPC algorithms are developed to regulate and stabilize the thin film surface roughness, film thickness, and film porosity at desired levels. Simultaneous control of these variables under a unified framework is addressed using MPC. The proposed control algorithms are successfully applied to the kMC models of the thin film growth processes under consideration through numerical simulations. This dissertation has the following structure:

Chapter 2 focuses on dynamic output feedback covariance control of stochastic PDEs subject to sensor noise. A linear dissipative stochastic KSE is considered in this chapter. A finite-dimensional approximation is initially obtained on the basis of the infinite stochastic ODE system that captures the dominant modal contribution to the surface covariance profile (e.g., surface roughness). A state feedback controller and a Kalman-Bucy filter are then designed on the basis of the finite-dimensional approximation. The dynamic output feedback covariance controller is subsequently obtained by combining the state feedback controller and the state estimator with a theoretical analysis performed to obtain the estimate of the closed-loop infinite-dimensional system. Applications of the linear and nonlinear dynamic output feedback controllers are presented to the both the linearized and the nonlinear stochastic KSEs are presented.

Chapter 3 focuses on model parameter estimation and model-based output feedback control of surface roughness in a sputtering process. Specifically, this sputtering

process involves two surface micro-processes (atom erosion and surface diffusion) and is simulated using a kMC simulation method and its surface height evolution can be adequately described by the stochastic KSE. First, the four parameters of the stochastic KSE are estimated for the best prediction of surface roughness profile in a least-square sense to the profile of the kMC simulation. This model parameter estimation process is performed by formulating the nonlinear stochastic KSE into a system of infinite nonlinear stochastic ODEs and constructing a finite-dimensional approximation that captures the dominant mode contribution to the state and the evolution of the state covariance. Subsequently, the finite-dimensional approximation and the estimated model parameters are used to design state and output feedback controllers and are applied to the kMC model of the sputtering process. Extensive closed-loop system simulations demonstrate that the controllers successfully reduce the expected surface roughness compared to the open-loop simulation results.

Chapter 4 focuses on the development of MPC algorithms for the control of surface roughness. Specifically, a method is developed for MPC of nonlinear stochastic PDEs to regulate the state variance (surface roughness) to a desired level. The MPC algorithm is formulated on the basis of the finite-dimensional approximation of the stochastic PDE that describes the evolution of the thin film surface profile. A linear closed-loop structure is introduced by applying the nonlinear state feedback controller developed in Chapter 3. In this way, the future state variance can be predicted in a computationally efficient way and is compared to a pre-calculated reference tra-

jectory. The optimization algorithm in the MPC formulation solves for the optimal pole placement which minimizes the deviation of the prediction from the reference trajectory. To demonstrate the method, the model predictive controller is applied to the stochastic KSE and to the kMC model of a sputtering process to regulate the surface roughness at a desired level.

In Chapters 5, 6, and 7, film porosity, an important thin film property that requires stringent monitoring and control together with the other thin film properties, is considered. The film porosity is first obtained from a thin film deposition process modeled on a triangular lattice, which allows vacancies and overhangs to develop. Appropriate definitions of film site occupancy ratio (SOR), i.e., fraction of film sites occupied by particles over total number of film sites, and its fluctuation are introduced to describe film porosity. In Chapter 5, deterministic and stochastic ODE models are derived to describe the time evolution of film SOR and its fluctuation. The coefficients of the ODE models are estimated on the basis of data obtained from the kMC simulator of the deposition process using least-square methods and their dependence on substrate temperature is determined. The developed dynamic models for the film SOR are used as the basis for the design of MPC algorithms to regulate the expected value of film SOR at a desired level and reduce run-to-run fluctuations by manipulating the substrate temperature. Simulation results demonstrate the applicability and effectiveness of the proposed film porosity modeling and control methods in the context of the deposition process under consideration.

Chapters 6 and 7 further extend the systematic methodology of stochastic modeling and MPC algorithm design to simultaneous regulation of film thickness, surface roughness, and film porosity, the latter of which is represented by film SOR introduced in Chapter 5. An Edward-Wilkinson (EW)-type equation and a deterministic ODE model are postulated to describe the dynamics and the time evolution of the surface height profile and of the film SOR. The coefficients of the dynamic equations of surface height and of film SOR are estimated on the basis of the deposition process data for a variety of operating conditions. In Chapter 6, the MPC algorithm simultaneously regulates the surface roughness and film porosity, and thus, the cost function includes penalty on the relative deviation of surface roughness square and film SOR from their respective set-point values. In Chapter 7, the deposition rate is used as the manipulated input for simultaneous regulation of film porosity, roughness, and thickness. Since the film thickness is essential in determining the electrical and mechanical properties of the thin films, a desired minimum value of the film thickness is included in the MPC formulation together with the desired surface roughness and film SOR. Simulation results demonstrate the applicability and effectiveness of the proposed modeling and control approach. It is also demonstrated in the closed-loop simulations that, when simultaneous control is carried out, a balanced trade-off is obtained in the closed-loop system between the three control objectives (porosity, surface roughness, and thickness) depending on the penalty weighting configuration in the MPC formulation.

Finally, Chapter 8 summarizes the contributions of this dissertation.

Chapter 2

Output Feedback Covariance Control of Surface Roughness

2.1 Introduction

The recent efforts on feedback control and optimization of thin film growth processes to achieve desired material micro-structure (see, for example, [18, 20, 21] and the references therein) have been motivated by the fact that the electrical and mechanical properties of thin films strongly depend on microstructural features such as interface width, island density and size distributions [2, 54], which significantly affect device performance. To fabricate thin film devices with high and consistent performance, it is desirable that the operation of thin film growth processes is tightly controlled.

However, so far, only state feedback covariance controllers have been developed

for stochastic partial differential equations (PDEs) and used for the control of the thin film growth process that can be described by the stochastic PDEs [70, 62]. In the design of a state feedback controller, it is assumed that the full state of the PDE can be measured in real-time at all positions and times. This assumption is not practical in many applications, where process output measurements are typically available from a finite (usually small) number of measurement sensors. Therefore, there is a strong motivation to develop dynamic output feedback covariance control methods for stochastic PDEs, which couple a state feedback control law to a dynamic state-observer that utilizes information from few measurement sensors. The observer-based covariance control structure for linear stochastic ODE systems was proposed in [37, 43], in which a Kalman filter is used as a state estimator and the estimated state is used by the feedback controller. However, the problem of output feedback covariance control for nonlinear systems and infinite-dimensional systems has not been studied.

In this chapter, a method is developed for dynamic output feedback covariance control of the state covariance of linear dissipative stochastic PDEs. Spatially distributed control actuation and sensor measurements with noise are considered when designing the dynamic output feedback controller. We initially formulate the stochastic PDE into a system of infinite stochastic ODEs by using modal decomposition and construct a finite-dimensional approximation to capture the dominant mode contribution to the surface covariance of the height profile. Subsequently, a state feedback controller and a Kalman-Bucy filter are designed on the basis of the finite-dimensional

approximation. The dynamic output feedback controller is obtained by combining the state feedback controller and the state estimator. Analysis of the closed-loop stability and the steady-state surface covariance under the dynamic output feedback controller are provided for the finite-dimensional approximation and the infinite-dimensional system. Applications of the linear dynamic output feedback controller to both the linearized and the nonlinear stochastic Kuramoto-Sivashinsky equation (KSE) are presented. We also present nonlinear state feedback controller and nonlinear output feedback controller designs and apply them to the nonlinear stochastic KSE [38].

2.2 Preliminaries

2.2.1 Stochastic PDEs with distributed control

We focus on linear dissipative stochastic PDEs with distributed control of the following form:

$$\frac{\partial h}{\partial t} = \mathcal{A}h + \sum_{i=1}^{p} b_i(x)u_i(t) + \xi(x,t) \tag{2.1}$$

subject to homogeneous boundary conditions and the initial condition $h(x,0) = h_0(x)$, where $x \in [-\pi, \pi]$ is the spatial coordinate, t is the time, $h(x,t)$ is the state of the PDE which corresponds to the height of the surface in a thin film growth process at position x and time t, $\mathcal{A}$ is a dissipative, self-adjoint spatial differential operator, $u_i(t)$ is the ith manipulated input, p is the number of manipulated inputs, and $b_i(x)$ is the ith actuator distribution function, which determines how the control action

computed by the ith control actuator, $u_i(t)$, is distributed (e.g., point or distributed actuation) in the spatial interval $[-\pi, \pi]$. $\xi(x,t)$ is a Gaussian white noise with the following expressions for its mean and covariance:

$$\begin{aligned} \langle \xi(x,t) \rangle &= 0, \\ \langle \xi(x,t)\xi(x',t') \rangle &= \sigma^2 \delta(x-x')\delta(t-t'), \end{aligned} \tag{2.2}$$

where σ is a real number, $\delta(\cdot)$ is the Dirac delta function, and $\langle \cdot \rangle$ denotes the expected value. Note that although $\langle \cdot \rangle$ is used to denote the expected value in literature (see, for example, [45, 91, 53, 66]), an alternative notation, $E(\cdot)$, is also commonly used (see, for example, [37, 12]). Throughout this work, we use $\langle \cdot \rangle$ to denote the expected value.

Gaussian white noise is chosen as the noise term in the stochastic PDE. The Gaussian white noise is a natural choice and works well in many process models. For example, stochastic PDEs with Gaussian white noise are reported in the modeling of surface height evolution of many microscopic processes, such as random deposition with surface relaxation, ballistic deposition and sputtering processes [31, 26, 53].

Our objective is to control the surface covariance of the process, $\mathrm{Cov_h}$, which is represented by the expected value of the standard deviation of the surface height from the desired height and is given as follows:

$$\mathrm{Cov_h}(t) = \left\langle \int_{-\pi}^{\pi} [h(x,t) - h_\mathrm{d}]^2 dx \right\rangle \tag{2.3}$$

where $h_{\mathrm{d}}(t)$ is the desired surface height.

To study the dynamics of Eq. (2.1), we initially consider the eigenvalue problem of the linear spatial differential operator of Eq. (2.1) subject to the operator homogenous boundary conditions, which takes the form:

$$\mathcal{A}\bar{\phi}_n(x) = \lambda_n \bar{\phi}_n(x), \quad n = 1, 2, \ldots, \tag{2.4}$$

where λ_n and $\bar{\phi}_n$ denote the nth eigenvalue and eigenfunction, respectively. To simplify our development and motivated by most practical applications, we consider stochastic PDEs for which $\mathcal{A}$ is a highly dissipative, self-adjoint operator (i.e., a second-order or fourth-order linear self-adjoint operator) and has eigenvalues which are real and satisfy $\lambda_1 \geq \lambda_2 \ldots$ and the sum $\sum_{i=1,\lambda_i \neq 0}^{\infty} \left| \frac{1}{\lambda_i} \right|$ converges to a finite positive number. Furthermore, the eigenfunctions $\{\bar{\phi}_1(x), \bar{\phi}_2(x), \ldots\}$ form a complete orthonormal set.

To present the method for feedback controller design, we initially formulate Eq. (2.1) into an infinite-dimensional stochastic ODE system using modal decomposition. To this end, we first expand the solution of Eq. (2.1) into an infinite series in terms of the eigenfunctions of the operator $\mathcal{A}$ as follows:

$$h(x,t) = \sum_{n=1}^{\infty} \alpha_n(t) \bar{\phi}_n(x) \tag{2.5}$$

where $\alpha_n(t)$ $(n = 1, 2, \ldots, \infty)$ are time-varying coefficients. Substituting the above

expansion for the solution, $h(x,t)$, into Eq. (2.1) and taking the inner product with $\bar{\phi}_n(x)$, the following system of infinite stochastic ODEs is obtained:

$$\frac{d\alpha_n}{dt} = \lambda_n \alpha_n + \sum_{i=1}^{p} b_i^n u_i(t) + \xi^n(t), n = 1, \ldots, \infty \tag{2.6}$$

where

$$b_i^n = \int_{-\pi}^{\pi} \bar{\phi}_n(x) b_i(x) dx \tag{2.7}$$

and

$$\xi^n(t) = \int_{-\pi}^{\pi} \xi(x,t) \bar{\phi}_n(x) dx \tag{2.8}$$

The covariance of $\xi_\alpha^n(t)$ can be computed by using the following result:

Result 1 *If (1) $f(x)$ is a deterministic function, (2) $\eta(x)$ is a random variable with $\langle \eta(x) \rangle = 0$ and covariance $\langle \eta(x)\eta(x') \rangle = \sigma^2 \delta(x - x')$, and (3) $\epsilon = \int_a^b f(x)\eta(x)dx$, then ϵ is a real random number with $\langle \epsilon \rangle = 0$ and covariance $\langle \epsilon^2 \rangle = \sigma^2 \int_a^b f^2(x)dx$ [1].*

Using Result 1, we obtain $\langle \xi^n(t)\xi^n(t') \rangle = \sigma^2 \delta(t - t')$.

In this chapter, the controlled variable is the surface covariance defined in Eq. (2.3). Without loss of generality, we pick $h_{\mathrm{d}}(t) = 0$. Therefore, $\mathrm{Cov}_{\mathrm{h}}(t)$ can be rewritten in terms of $\alpha_n(t)$ as follows [61]:

$$\begin{aligned} \mathrm{Cov}_{\mathrm{h}}(t) &= \left\langle \int_{-\pi}^{\pi} [h(x,t) - 0]^2 dx \right\rangle = \left\langle \int_{-\pi}^{\pi} [\sum_{n=1}^{\infty} \alpha_n(t) \bar{\phi}_n(x)]^2 dx \right\rangle \\ &= \left\langle \sum_{n=1}^{\infty} \alpha_n^2(t) \right\rangle = \sum_{n=1}^{\infty} \langle \alpha_n^2(t) \rangle. \end{aligned} \tag{2.9}$$

Eq. (2.9) provides a direct link between the surface covariance and the state covariance of the system of infinite stochastic ODEs of Eq. (2.6).

2.2.2 Model reduction

Owing to its infinite-dimensional nature, the system of Eq. (2.6) cannot be directly used as a basis for feedback controller design that can be implemented in practice (i.e., the practical implementation of such a controller will require the computation of infinite sums which cannot be done by a computer). Instead, we will use finite-dimensional approximations of the system of Eq. (2.6) for the purpose of model-based output feedback controller design. Specifically, we rewrite the system of Eq. (2.6) as follows:

$$\begin{aligned} \frac{dx_{\mathrm{s}}}{dt} &= \Lambda_{\mathrm{s}} x_{\mathrm{s}} + B_{\mathrm{s}} u + \xi_{\mathrm{s}}, \\ \frac{dx_{\mathrm{f}}}{dt} &= \Lambda_{\mathrm{f}} x_{\mathrm{f}} + B_{\mathrm{f}} u + \xi_{\mathrm{f}} \end{aligned} \tag{2.10}$$

where

$$\begin{aligned} x_{\mathrm{s}} &= [\alpha_1 \quad \dots \quad \alpha_m]^T, & x_{\mathrm{f}} &= [\alpha_{m+1} \quad \alpha_{m+2} \quad \dots]^T, \\ \Lambda_{\mathrm{s}} &= \mathrm{diag}\,[\lambda_1 \quad \dots \quad \lambda_m], & \Lambda_{\mathrm{f}} &= \mathrm{diag}\,[\lambda_{m+1} \quad \lambda_{m+2} \quad \dots], \\ \xi_{\mathrm{s}} &= [\xi^1 \quad \dots \quad \xi^m]^T, & \xi_{\mathrm{f}} &= [\xi^{m+1} \quad \xi^{m+2} \dots]^T, \end{aligned} \tag{2.11}$$

and

$$B_{\rm s} = \begin{bmatrix} b_1^1 & \dots & b_p^1 \\ \vdots & \ddots & \vdots \\ b_1^m & \dots & b_p^m \end{bmatrix}, \quad B_{\rm f} = \begin{bmatrix} b_1^{m+1} & \dots & b_p^{m+1} \\ b_1^{m+2} & \dots & b_p^{m+2} \\ \vdots & \vdots & \vdots \end{bmatrix}. \tag{2.12}$$

Note that the $x_{\rm s}$ subsystem is mth-order and the $x_{\rm f}$ subsystem is infinite-dimensional.

The expression of $\mathrm{Cov_h}$ in Eq. (2.9) can be rewritten in the following form:

$$\begin{aligned} \mathrm{Cov_h}(t) &= \sum_{n=1}^{m} \left\langle \alpha_n^2(t) \right\rangle + \sum_{n=m+1}^{\infty} \left\langle \alpha_n^2(t) \right\rangle \\ &= Tr[P_{\rm s}(t)] + Tr[P_{\rm f}(t)] \end{aligned} \tag{2.13}$$

where $P_{\rm s}$ and $P_{\rm f}$ are covariance matrices of the $x_{\rm s}$ and $x_{\rm f}$ which are defined as $P_{\rm s} = \langle x_{\rm s} x_{\rm s}^T \rangle$ and $P_{\rm f} = \langle x_{\rm f} x_{\rm f}^T \rangle$, respectively. $Tr[\cdot]$ denotes the trace of a matrix.

Neglecting the $x_{\rm f}$ subsystem, the following finite-dimensional approximation is obtained:

$$\frac{d\tilde{x}_{\rm s}}{dt} = \Lambda_{\rm s} \tilde{x}_{\rm s} + B_{\rm s} u + \xi_{\rm s} \tag{2.14}$$

and the surface covariance of the infinite-dimensional stochastic system, $\mathrm{Cov_h}$, can be approximated by $\widetilde{\mathrm{Cov}}_{\rm h}$, which is computed from the state of the finite-dimensional approximation of Eq. (2.14) as follows:

$$\widetilde{\mathrm{Cov}}_{\rm h}(t) = Tr[\tilde{P}_{\rm s}(t)] \tag{2.15}$$

where the tilde symbol denotes that the variable is associated with the finite-dimensional

system. See [23, 83, 19] for further results on model reduction of dissipative PDEs.

2.2.3 State feedback control

When the state of the finite-dimensional system of Eq. (2.14) is available, a linear state feedback controller can be designed to regulate the surface covariance. The closed-loop finite-dimensional system takes the following form:

$$\begin{aligned} \frac{d\tilde{x}_{\mathrm{s}}}{dt} &= \Lambda_{\mathrm{s}}\tilde{x}_{\mathrm{s}} + B_{\mathrm{s}}u + \xi_{\mathrm{s}}, \\ u &= G\tilde{x}_{\mathrm{s}}, \end{aligned} \tag{2.16}$$

where G is the gain matrix, which should be carefully designed so as to stabilize the closed-loop finite-dimensional system and obtain the desired closed-loop surface covariance. Note that the linear state feedback controller of Eq. (2.16) has been used to control the surface covariance in both thin film growth and ion-sputtering processes [61, 60].

Since the above state feedback control assumes a full knowledge of the states of the process at all positions and times, which may be a restrictive requirement for certain practical applications, we proceed to design output feedback controllers by combining the state feedback control law and a state observer.

2.3 Output feedback control

In this section, we design linear output feedback controllers by combining the state feedback control law of Eq. (2.16) and a dynamic state observer which estimates the state of the finite-dimensional system of Eq. (2.14) using the measured process output with sensor noise. First, a dynamic state observer is developed using a Kalman-Bucy filter approach, which yields an optimal estimate of the state of the finite-dimensional system by minimizing the mean square estimation error. The dynamic state observer is then coupled to the state feedback controller of Eq. (2.16) to construct a dynamic output feedback controller. For the special case where the number of measurement sensors is equal to the order of the finite-dimensional system, a static output feedback controller may be designed by following a static state estimation approach proposed in [10, 22].

2.3.1 Measured output with sensor noise

The state feedback controller of Eq. (2.16) requires the availability of the state $\tilde{x}_{\mathrm{s}}$, which implies that the value of the surface height profile, $h(x,t)$, is available at any location and time. However, from a practical point of view, measurements of the surface height profile are only available at a finite number of locations. Motivated by this, we design an output feedback controller that uses measurements of the surface height at distinct locations to enforce a desired closed-loop surface covariance. The sensor noise is modeled as a Gaussian white noise and is added to the surface height

measurements. Specifically, the measured process output is expressed as follows:

$$y(t) = \left[h(x_1,t) + \xi_y^1(t) \quad h(x_2,t) + \xi_y^2(t) \quad \ldots \quad h(x_q,t) + \xi_y^q(t) \right]^T \tag{2.17}$$

where x_i $(i = 1, 2, \ldots, q)$ denotes a location of a point measurement sensor and q is the number of measurement sensors. $\xi_y^1(t)$, $\xi_y^2(t)$, ..., $\xi_y^q(t)$ are independent Gaussian white noises with the following expressions for their means and covariances:

$$\begin{aligned} \langle \xi_y^i(t) \rangle &= 0, \qquad\qquad i = 1, 2, \ldots q, \\ \langle \xi_y^i(t) \xi_y^j(t') \rangle &= \varsigma^2 \delta_{ij} \delta(t - t'), \quad i = 1, 2, \ldots q, \quad j = 1, 2, \ldots q, \end{aligned} \tag{2.18}$$

where ς is a constant and δ_{ij} is the Kronecker delta function. Note that the sensor noises are independent of the system noises, ξ_{s} and ξ_{f}.

Using Eq. (2.5), the vector of measured outputs, $y(t)$, can be written in terms of x_{s} and x_{f} as follows:

$$\begin{aligned} y(t) &= \begin{bmatrix} \sum_{n=1}^{\infty} \alpha_n(t) \phi_n(x_1) + \xi_y^1(t) \\ \sum_{n=1}^{\infty} \alpha_n(t) \phi_n(x_2) + \xi_y^2(t) \\ \vdots \\ \sum_{n=1}^{\infty} \alpha_n(t) \phi_n(x_q) + \xi_y^q(t) \end{bmatrix} \\ &= C_{\mathrm{s}} x_{\mathrm{s}}(t) + C_{\mathrm{f}} x_{\mathrm{f}}(t) + \xi_y(t) \end{aligned} \tag{2.19}$$

where

$$C_{\mathrm{s}} = \begin{bmatrix} \phi_1(x_1) & \phi_2(x_1) & \dots & \phi_m(x_1) \\ \phi_1(x_2) & \phi_2(x_2) & \dots & \phi_m(x_2) \\ \vdots & \vdots & \ddots & \vdots \\ \phi_1(x_q) & \phi_2(x_q) & \dots & \phi_m(x_q) \end{bmatrix},$$

$$C_{\mathrm{f}} = \begin{bmatrix} \phi_{m+1}(x_1) & \phi_{m+2}(x_1) & \dots \\ \phi_{m+1}(x_2) & \phi_{m+2}(x_2) & \dots \\ \vdots & \vdots & \ddots \\ \phi_{m+1}(x_q) & \phi_{m+2}(x_q) & \dots \end{bmatrix}, \tag{2.20}$$

and

$$\xi_y(t) = \begin{bmatrix} \xi_y^1(t) & \xi_y^2(t) & \dots & \xi_y^q(t) \end{bmatrix}^T. \tag{2.21}$$

Consequently, the system of Eq. (2.10) with the measured process output vector can be written as follows:

$$\begin{aligned} \frac{dx_{\mathrm{s}}}{dt} &= \Lambda_{\mathrm{s}} x_{\mathrm{s}} + B_{\mathrm{s}} u + \xi_{\mathrm{s}}, \\ \frac{dx_{\mathrm{f}}}{dt} &= \Lambda_{\mathrm{f}} x_{\mathrm{f}} + B_{\mathrm{f}} u + \xi_{\mathrm{f}}, \\ y &= C_{\mathrm{s}} x_{\mathrm{s}} + C_{\mathrm{f}} x_{\mathrm{f}} + \xi_y. \end{aligned} \tag{2.22}$$

Neglecting the x_{f} subsystem, the following finite-dimensional stochastic ODE sys-

tem can be obtained:

$$\begin{aligned}\frac{d\tilde{x}_{\mathrm{s}}}{dt} &= \Lambda_{\mathrm{s}}\tilde{x}_{\mathrm{s}} + B_{\mathrm{s}}u + \xi_{\mathrm{s}}, \\ \tilde{y} &= C_{\mathrm{s}}\tilde{x}_{\mathrm{s}} + \xi_y,\end{aligned} \tag{2.23}$$

where the tilde symbols in $\tilde{x}_{\mathrm{s}}$ and $\tilde{y}$ denote the correspondence to a reduced-order system. The system of Eq. (2.23) is used as the basis for output feedback controller design.

2.3.2 Dynamic output feedback control

To design a dynamic output feedback controller, we first construct a dynamic state estimator using information from the measured output vector. Specifically, a Kalman-Bucy filter is designed for the optimal estimation of the state of the finite-dimensional system of Eq. (2.23) as follows [37]:

$$\frac{d\hat{x}_{\mathrm{s}}}{dt} = \Lambda_{\mathrm{s}}\hat{x}_{\mathrm{s}} + B_{\mathrm{s}}u + K(y - C_{\mathrm{s}}\hat{x}_{\mathrm{s}}), \quad \hat{x}_{\mathrm{s}}(0) = \hat{x}_{\mathrm{s}0} \tag{2.24}$$

where $\hat{x}_{\mathrm{s}}$ is the estimate of the state and K is a gain matrix, which is computed as follows [37]:

$$K = QC_{\mathrm{s}}^T V_y^{-1} \tag{2.25}$$

where V_y is the sensor noise intensity matrix and satisfies

$$\langle \xi_y(t)\xi_y(t')^T \rangle = V_y \delta(t - t') \tag{2.26}$$

and Q is the covariance matrix for the state estimation error and is defined as follows:

$$Q = \lim_{t \to \infty} \langle \tilde{e}(t) \tilde{e}(t)^T \rangle \tag{2.27}$$

where $\tilde{e}(t)$ is the estimation error

$$\tilde{e} = \tilde{x}_{\mathrm{s}} - \hat{x}_{\mathrm{s}}. \tag{2.28}$$

The covariance matrix for the state estimation error, Q, is the unique nonnegative-definite solution of the following algebraic Riccati equation [37]:

$$\Lambda_{\mathrm{s}} Q + Q \Lambda_{\mathrm{s}} - Q C_{\mathrm{s}}^T V_y^{-1} C_{\mathrm{s}} Q + V_{\mathrm{s}} = 0 \tag{2.29}$$

where V_{s} is the noise intensity matrix of the ξ_{s} and satisfies

$$\langle \xi_{\mathrm{s}}(t) \xi_{\mathrm{s}}(t')^T \rangle = V_{\mathrm{s}} \delta(t - t'). \tag{2.30}$$

The dynamic output feedback controller is designed by combining the state feedback controller of Eq. (2.16) and the state estimator of Eq. (2.24) and takes the following form:

$$\begin{aligned} \frac{d\hat{x}_{\mathrm{s}}}{dt} &= \Lambda_{\mathrm{s}} \hat{x}_{\mathrm{s}} + B_{\mathrm{s}} u + K(y - C_{\mathrm{s}} \hat{x}_{\mathrm{s}}), \quad \hat{x}_{\mathrm{s}}(0) = \hat{x}_{\mathrm{s}0}, \\ u &= G \hat{x}_{\mathrm{s}}. \end{aligned} \tag{2.31}$$

By applying the dynamic output feedback controller of Eq. (2.31) to the finite-dimensional system of Eq. (2.23), the following closed-loop finite dimensional system can be obtained as follows:

$$\begin{aligned} \frac{d\tilde{x}_{\mathrm{s}}}{dt} &= \Lambda_{\mathrm{s}}\tilde{x}_{\mathrm{s}} + B_{\mathrm{s}}u + \xi_{\mathrm{s}}, \\ \tilde{y} &= C_{\mathrm{s}}\tilde{x}_{\mathrm{s}} + \xi_y, \\ \frac{d\hat{x}_{\mathrm{s}}}{dt} &= \Lambda_{\mathrm{s}}\hat{x}_{\mathrm{s}} + B_{\mathrm{s}}u + K(\tilde{y} - C_{\mathrm{s}}\hat{x}_{\mathrm{s}}), \\ u &= G\hat{x}_{\mathrm{s}}. \end{aligned} \tag{2.32}$$

The closed-loop finite dimensional system of Eq. (2.32) can be written in terms of $\tilde{x}_{\mathrm{s}}$ and e using Eq. (2.28) as follows:

$$\begin{aligned} \frac{d\tilde{x}_{\mathrm{s}}}{dt} &= (\Lambda_{\mathrm{s}} + B_{\mathrm{s}}G)\tilde{x}_{\mathrm{s}} - B_{\mathrm{s}}G\tilde{e} + \xi_{\mathrm{s}}, \\ \frac{d\tilde{e}}{dt} &= (\Lambda_{\mathrm{s}} - KC_{\mathrm{s}})\tilde{e} + \xi_{\mathrm{s}} - K\xi_y. \end{aligned} \tag{2.33}$$

The stability of the closed-loop finite-dimensional system of Eq. (2.33) depends on the stability properties of the matrices $(\Lambda_{\mathrm{s}} + B_{\mathrm{s}}G)$ and $(\Lambda_{\mathrm{s}} - KC_{\mathrm{s}})$. Specifically, the stability of $(\Lambda_{\mathrm{s}} + B_{\mathrm{s}}G)$ depends on the appropriate design of the state feedback controller and the stability of $(\Lambda_{\mathrm{s}} - KC_{\mathrm{s}})$ depends on the appropriate design of the Kalman-Bucy filter. Owing to its cascaded structure, the system of Eq. (2.33) is asymptotically stable if both $(\Lambda_{\mathrm{s}} + B_{\mathrm{s}}G)$ and $(\Lambda_{\mathrm{s}} - KC_{\mathrm{s}})$ are stable matrices. A stable matrix is a matrix whose eigenvalues have all negative real parts. This results in the existence of a steady-state covariance matrix (e.g., a covariance matrix as

$t \rightarrow \infty$) of the closed-loop stochastic system [37]. To investigate the steady-state covariance matrix of the closed-loop system of Eq. (2.33), we rewrite Eq. (2.33) as follows:

$$\frac{d}{dt}\begin{bmatrix} \tilde{x}_s \\ \tilde{e} \end{bmatrix} = \begin{bmatrix} \Lambda_s + B_s G & -B_s G \\ \mathbf{0} & \Lambda_s - K C_s \end{bmatrix} \begin{bmatrix} \tilde{x}_s \\ \tilde{e} \end{bmatrix} + \begin{bmatrix} I_s & \mathbf{0} \\ I_s & -K \end{bmatrix} \begin{bmatrix} \xi_s \\ \xi_y \end{bmatrix} \tag{2.34}$$

where I_s is a mth-order elementary matrix and $\mathbf{0}$ denotes a zero matrix with an appropriate size.

The steady-state covariance matrix of the system of Eq. (2.34) is defined as follows:

$$\tilde{P} = \lim_{t\to\infty} \left\langle \begin{bmatrix} \tilde{x}_s(t) \\ \tilde{e}(t) \end{bmatrix} \begin{bmatrix} \tilde{x}_s(t)^T & \tilde{e}(t)^T \end{bmatrix} \right\rangle = \begin{bmatrix} \tilde{P}_s & \tilde{P}_{se} \\ \tilde{P}_{es} & \tilde{P}_e \end{bmatrix} \tag{2.35}$$

where $\tilde{P}_s$, $\tilde{P}_e$, $\tilde{P}_{se}$ and $\tilde{P}_{es}$ are covariance matrices of the following form:

$$\begin{aligned} \tilde{P}_s &= \lim_{t\to\infty} \langle \tilde{x}_s(t)\tilde{x}_s(t)^T \rangle, \\ \tilde{P}_e &= \lim_{t\to\infty} \langle \tilde{e}(t)\tilde{e}(t)^T \rangle, \\ \tilde{P}_{se} = \tilde{P}_{es}^T &= \lim_{t\to\infty} \langle \tilde{x}_s(t)\tilde{e}(t)^T \rangle, \end{aligned} \tag{2.36}$$

where $\tilde{P}$ is the unique positive-definite solution of the following Lyapunov equation

[37]:

$$
\begin{bmatrix} \Lambda_{\mathrm{s}} + B_{\mathrm{s}} G & -B_{\mathrm{s}} G \\ \mathbf{0} & \Lambda_{\mathrm{s}} - K C_{\mathrm{s}} \end{bmatrix} \tilde{P} + \tilde{P} \begin{bmatrix} \Lambda_{\mathrm{s}} + B_{\mathrm{s}} G & -B_{\mathrm{s}} G \\ \mathbf{0} & \Lambda_{\mathrm{s}} - K C_{\mathrm{s}} \end{bmatrix}^T
$$

$$
+ \begin{bmatrix} I_{\mathrm{s}} & \mathbf{0} \\ I_{\mathrm{s}} & -K \end{bmatrix} \begin{bmatrix} V_{\mathrm{s}} & \mathbf{0} \\ \mathbf{0} & V_y \end{bmatrix} \begin{bmatrix} I_{\mathrm{s}} & \mathbf{0} \\ I_{\mathrm{s}} & -K \end{bmatrix}^T = \mathbf{0}. \tag{2.37}
$$

When the solution of $\tilde{P}$ is available, the surface covariance of the finite-dimensional system, $\widetilde{\mathrm{Cov}}_{\mathrm{h}}$, can be obtained by using only $\tilde{P}_{\mathrm{s}}$.

Remark 2.1 *The surface covariance of the closed-loop finite-dimensional system,* $\widetilde{\mathrm{Cov}}_{\mathrm{h}}$ *under the linear output feedback controller of Eq. (2.31), can be solved from the Lyapunov equation of Eq. (2.37) with gain matrices G and K obtained from the separate designs of the state feedback control law of Eq. (2.16) and of the Kalman-Bucy filter of Eqs. (2.25) and (2.29). However, for a set-point regulation problem with a pre-specified desired surface covariance,* $\widetilde{\mathrm{Cov}}_{\mathrm{d}}$*, the above procedure is not directly applicable. Instead, an iterative procedure can be adopted to design the matrices G and K to approach a desired set-point in the closed-loop system. Specifically, the state feedback controller can be first designed so that the set-point value can be achieved when the full state of the finite-dimensional system is accessible by the controller (see Section 3.2 in [60] for more details on the state feedback gain design). This design will result in a control gain matrix, G_1 in the state feedback controller. Then, a*

Kalman filter can be designed separately to compute the Kalman filter gain matrix, K_1, by solving the Riccati equation. Subsequently, the surface covariance under the resulting output feedback controller (K_1, G_1), $\widetilde{\mathrm{Cov}}_{\mathrm{h,1}}$, can be obtained by solving the Lyapunov equation of Eq. (2.37). Due to the fact that less information of the surface state is used in the output feedback controller compared to the corresponding state feedback controller, estimation error always exists. Therefore, the closed-loop surface covariance, $\widetilde{\mathrm{Cov}}_{\mathrm{h,1}}$, will be different from the set-point value, $\widetilde{\mathrm{Cov}}_{\mathrm{d}}$. To enable the use of an iterative procedure to improve upon $\widetilde{\mathrm{Cov}}_{\mathrm{h,1}}$, a second set-point value for surface covariance, $\widetilde{\mathrm{Cov}}_{\mathrm{d,2}}$, is used to solve for another pair of gain matrices G_2 and K_2. A new $\widetilde{\mathrm{Cov}}_{\mathrm{h,2}}$ under the output feedback controller with gain matrices G_2 and K_2 is then obtained, which results in a different closed-loop surface covariance, $\widetilde{\mathrm{Cov}}_{\mathrm{h,2}}$. With the two sets of data as initial guesses, we can start an iterative procedure using, for example, Secant's method to solve for K_i, G_i that result in a closed-loop surface covariance, $\widetilde{\mathrm{Cov}}_{\mathrm{h,i}}$ sufficiently close to the desired surface covariance, $\widetilde{\mathrm{Cov}}_{\mathrm{d}}$. The iterative procedure terminates when the difference between the closed-loop finite-dimensional surface covariance under output feedback control is sufficiently close to the desired value $\widetilde{\mathrm{Cov}}_{\mathrm{d}}$.

2.3.3 Analysis of closed-loop infinite-dimensional system

We now proceed to characterize the accuracy with which the surface covariance in the closed-loop infinite-dimensional system is controlled by the finite-dimensional linear

dynamic output feedback controller. By applying the controller of Eq. (2.31) to the infinite-dimensional system of Eq. (2.10) and substituting the estimation error in Eq. (2.28), the infinite-dimensional closed-loop system takes the following form:

$$\begin{aligned} \frac{dx_{\rm s}}{dt} &= (\Lambda_{\rm s} + B_{\rm s}G)x_{\rm s} - B_{\rm s}Ge + \xi_{\rm s}, \\ \frac{de}{dt} &= (\Lambda_{\rm s} - KC_{\rm s})e - KC_{\rm f}x_{\rm f} + \xi_{\rm s} - K\xi_y, \\ \epsilon\frac{dx_{\rm f}}{dt} &= \Lambda_{{\rm f}\epsilon}x_{\rm f} + \epsilon(B_{\rm f}Gx_{\rm s} - B_{\rm f}Ge) + \epsilon\xi_{\rm f}, \end{aligned} \tag{2.38}$$

where e is the estimation error from the full-order system and is defined as $e = x_{\rm s} - \hat{x}_{\rm s}$, $\epsilon = \dfrac{|\lambda_1|}{|\lambda_{m+1}|}$, and $\Lambda_{{\rm f}\epsilon} = \epsilon\Lambda_{\rm f}$ is an infinite-dimensional stable matrix.

The infinite-dimensional system of Eq. (2.38) is then a singularly-perturbed system driven by white noise. We now proceed to characterize the accuracy with which the surface covariance is controlled in the closed-loop infinite-dimensional system. Theorem 2.1 provides a characterization of the surface covariance enforced by the dynamic output feedback controller in the closed-loop infinite dimensional system.

Theorem 2.1 *Consider the surface covariance of the finite-dimensional system of Eq. (2.33),* $\widetilde{\rm Cov}_{\rm h}$*,*

$$\tilde{P}_{\rm s} = \lim_{t\to\infty}\langle\tilde{x}_{\rm s}(t)\tilde{x}_{\rm s}(t)^T\rangle, \quad \widetilde{\rm Cov}_{\rm h} = Tr\{\tilde{P}_{\rm s}\}, \tag{2.39}$$

and the surface covariance of the infinite-dimensional system of Eq. (2.38), $\mathrm{Cov_h}$*,*

$$x = \begin{bmatrix} x_{\mathrm{s}} \\ x_{\mathrm{f}} \end{bmatrix}, \quad P = \lim_{t \to \infty} \langle x(t)x(t)^T \rangle, \quad \mathrm{Cov_h} = Tr\{P\}, \tag{2.40}$$

where $\langle \cdot \rangle$ *denotes the expected value. Then, there exists* $\epsilon^* > 0$ *such that if* $\epsilon \in (0, \epsilon^*]$*,* $\widetilde{\mathrm{Cov}}_{\mathrm{h}}$ *and* $\mathrm{Cov_h}$ *satisfy:*

$$\mathrm{Cov_h} \;=\; \widetilde{\mathrm{Cov}}_{\mathrm{h}} + O(\sqrt{\epsilon}). \tag{2.41}$$

Proof of Theorem 2.1. The proof of Theorem 2.1 includes several steps. First, we prove that the closed-loop infinite-dimensional system of Eq. (2.38) is exponentially stable for sufficiently small ϵ. Second, we prove that the contribution to the surface covariance from the x_{f} subsystem of Eq. (2.38) is $O(\epsilon)$, i.e.,

$$\mathrm{Cov_{hf}} \;=\; Tr\{P_{\mathrm{f}}\} = O(\epsilon) \tag{2.42}$$

where $\mathrm{Cov_{hf}}$ is the contribution to the surface covariance from the x_{f} subsystem of Eq. (2.38) and P_{f} is the covariance matrix defined as:

$$P_{\mathrm{f}} \;=\; \lim_{t \to \infty} \langle x_{\mathrm{f}}(t)x_{\mathrm{f}}(t)^T \rangle. \tag{2.43}$$

Then, we prove that the contribution to the surface covariance from the x_{s} subsystem

of Eq. (2.38) is as follows:

$$\text{Cov}_{\text{hs}} = Tr\{P_{\text{s}}\} = \widetilde{\text{Cov}_{\text{h}}} + O(\sqrt{\epsilon}) \tag{2.44}$$

where $\widetilde{\text{Cov}_{\text{h}}}$, defined in Eq. (2.15), is the surface covariance of the closed-loop finite-dimensional system of Eq. (2.33), and P_{s} is the covariance matrix of x_{s} in Eq. (2.38), which is defined as:

$$P_{\text{s}} = \lim_{t\to\infty} \langle x_{\text{s}}(t) x_{\text{s}}(t)^T \rangle. \tag{2.45}$$

Finally, the proof of Theorem 2.1 is completed by proving Eq. (2.41) based on the results in Eqs. (2.42) and (2.44).

Closed-loop infinite dimensional system stability. Referring to the closed-loop infinite-dimensional system of Eq. (2.38), we note that the fast subsystem (obtained by re-writing the system of Eq. (2.38) in the fast time scale $\tau = t/\epsilon$ and setting $\epsilon = 0$) takes the form:

$$\frac{d\bar{x}_{\text{f}}}{d\tau} = \Lambda_{\text{f}\epsilon} \bar{x}_{\text{f}}. \tag{2.46}$$

Due to the eigenspectrum of the linear operator of Eq. (2.1), all eigenvalues of $\Lambda_{\text{f}\epsilon}$ have negative real parts. Thus, the system of Eq. (2.46) is exponentially stable. Setting $\epsilon = 0$ in the system of Eq. (2.38), the closed-loop finite dimensional system is obtained:

$$\begin{aligned} \frac{d\tilde{x}_{\text{s}}}{dt} &= (\Lambda_{\text{s}} + B_{\text{s}} G)\tilde{x}_{\text{s}} - B_{\text{s}} G \tilde{e} + \xi_{\text{s}}, \\ \frac{d\tilde{e}}{dt} &= (\Lambda_{\text{s}} - K C_{\text{s}})\tilde{e} + \xi_{\text{s}} - K\xi_y, \end{aligned} \tag{2.47}$$

which is exponentially stable since the matrices $(\Lambda_s + B_s G)$ and $(\Lambda_s - KC_s)$ are stable matrices by design. Therefore, there exists (following similar arguments to Theorem A.1 in [49, p. 361]) a positive real number $\hat{\epsilon}$ such that $\forall \epsilon \in (0, \hat{\epsilon}]$ the zero solution of the closed-loop infinite-dimensional system of Eq. (2.38) is exponentially stable.

Proof of Eq. (2.42). We first note that the terms in the right-hand-side of the x_f subsystem of Eq. (2.38) constitute an $O(\epsilon)$ approximation to the term $\Lambda_{f\epsilon} x_f$. Consider also the following linear system:

$$\epsilon \frac{d\bar{x}_f}{dt} = \Lambda_{f\epsilon} \bar{x}_f + \epsilon \xi_f \tag{2.48}$$

which is exponentially stable. The exponential stability of the closed-loop infinite-dimensional system of Eq. (2.38) ensures that the zero solution of the x_f subsystem of Eq. (2.38) is exponentially stable, which guarantees that as $t \to \infty$, Cov_{hf} converges to a finite value. Now, we follow a similar approach to the one employed in the proof of Theorem A.1 in [49, p. 361] to compute the theoretical estimate of Cov_{hf}. Specifically, we have that there exists an $\hat{\epsilon}^* > 0$ such that if $\epsilon \in (0, \hat{\epsilon}^*]$, we have that:

$$x_f(t) = \bar{x}_f(t) + O(\sqrt{\epsilon}). \tag{2.49}$$

Therefore, we have the following estimate for $\langle \|x_f(t)\|_2^2 \rangle$:

$$\langle \|x_f(t)\|_2^2 \rangle = \langle \|\bar{x}_f(t) + O(\sqrt{\epsilon})\|_2^2 \rangle \leq 2\langle \|\bar{x}_f(t)\|_2^2 \rangle + O(\epsilon) \tag{2.50}$$

where $\langle\cdot\rangle$ denotes the expected value and $\|\cdot\|_2$ is the standard Euclidean norm. Note that $\langle\|x_{\rm f}(t)\|_2^2\rangle$ and $\langle\|\bar{x}_{\rm f}(t)\|_2^2\rangle$ are equal to the traces of the covariance matrices of $x_{\rm f}(t)$ and $\bar{x}_{\rm f}(t)$, i.e., $\langle x_{\rm f}(t)x_{\rm f}(t)^T\rangle = P_{\rm f}(t)$ and $\langle\bar{x}_{\rm f}(t)\bar{x}_{\rm f}(t)^T\rangle = \bar{P}_{\rm f}(t)$, respectively. Finally, as $t \to \infty$, $P_{\rm f}(t)$ and $\bar{P}_{\rm f}(t)$ converge to $P_{\rm f}$ and $\bar{P}_{\rm f}$, respectively (both $P_{\rm f}$ and $\bar{P}_{\rm f}$ are bounded quantities which follows from closed-loop stability). Because $\Lambda_{{\rm f}\epsilon}$ is a stable diagonal matrix, the trace of matrix $\bar{P}_{\rm f}$ can be computed as follows [60]:

$$Tr\{\bar{P}_{\rm f}\} = \frac{\epsilon}{2}\sum_{i=1}^{\infty}\left|\frac{1}{\lambda_{\epsilon i}}\right| \tag{2.51}$$

where $\lambda_{\epsilon i}$ ($i = 1, 2, \ldots, \infty$) are the eigenvalues of the matrix $\Lambda_{{\rm f}\epsilon}$ in Eq. (2.48). Due to the structure of the eigenspectrum of the linear operator of Eq. (2.4), $\sum_{i=1}^{\infty}\left|\frac{1}{\lambda_{\epsilon i}}\right|$ converges to a finite positive number, and thus, there exists a positive real number $k_{{\rm f}\epsilon}$ such that

$$Tr\{\bar{P}_{\rm f}\} < \frac{\epsilon}{2}k_{{\rm f}\epsilon}. \tag{2.52}$$

Therefore, it follows that

$$Tr\{\bar{P}_{\rm f}\} = \langle\|\bar{x}_{\rm f}(\infty)\|_2^2\rangle = O(\epsilon). \tag{2.53}$$

According to Eq. (2.50), it follows that the contribution to the surface covariance from the state $x_{\rm f}$ of the infinite-dimensional system of Eq. (2.38) is $O(\epsilon)$, i.e.,:

$$\text{Cov}_{\rm hf} = Tr\{P_{\rm f}\} = Tr\{\bar{P}_{\rm f}\} + O(\epsilon) = O(\epsilon) + O(\epsilon) = O(\epsilon). \tag{2.54}$$

This completes the proof of Eq. (2.42). $\square$

Proof of Eq. (2.44). We now focus on the x_{s} subsystem and the equation for the estimation error, e, in Eq. (2.38).

$$\frac{d}{dt}\begin{bmatrix} x_{\mathrm{s}} \\ e \end{bmatrix} = \begin{bmatrix} \Lambda_{\mathrm{s}} + B_{\mathrm{s}}G & -B_{\mathrm{s}}G \\ \mathbf{0} & \Lambda_{\mathrm{s}} - KC_{\mathrm{s}} \end{bmatrix}\begin{bmatrix} x_{\mathrm{s}} \\ e \end{bmatrix} + \begin{bmatrix} \mathbf{0} \\ -KC_{\mathrm{f}} \end{bmatrix} x_{\mathrm{f}} + \begin{bmatrix} I_{\mathrm{s}} & \mathbf{0} \\ I_{\mathrm{s}} & -K \end{bmatrix}\begin{bmatrix} \xi_{\mathrm{s}} \\ \xi_y \end{bmatrix}. \tag{2.55}$$

Let k_{1s} be a positive real number satisfying $k_{1s} > \|KC_{\mathrm{f}}\|_2$ and we have the following:

$$\|KC_{\mathrm{f}}x_{\mathrm{f}}\|_2 < \|KC_{\mathrm{f}}\|_2 \cdot \|x_{\mathrm{f}}\|_2 < k_{1s}\|x_{\mathrm{f}}\|_2. \tag{2.56}$$

From Eq. (2.49), we have the following estimate for $\|x_{\mathrm{f}}\|_2$ for $t \geq t_{\mathrm{b}}$ (where t_{b} is the time needed for $\|\bar{x}_{\mathrm{f}}(t)\|_2$ to approach zero and $t_{\mathrm{b}} \to 0$ as $\epsilon \to 0$):

$$\|x_{\mathrm{f}}(t)\|_2 = O(\sqrt{\epsilon}). \tag{2.57}$$

This implies that we have the following estimate for $KC_{\mathrm{f}}x_{\mathrm{f}}(t)$ for $t \geq t_{\mathrm{b}}$:

$$KC_{\mathrm{f}}x_{\mathrm{f}}(t) = O(\sqrt{\epsilon}). \tag{2.58}$$

Furthermore, the exponential stability of the closed-loop infinite-dimensional system of Eq. (2.38) ensures that the zero solution of the Eq. (2.55) is exponentially stable. Therefore, as $t \to \infty$, $\mathrm{Cov_{hs}}$ converges to a finite value. We now proceed to provide a theoretical estimate for $\mathrm{Cov_{hs}}$. We first consider the equations for the estimation errors in both Eqs. (2.33) and (2.38). The estimation error of the finite-dimensional system of Eq. (2.33), $\tilde{e}$, is described by the following equation:

$$\frac{d\tilde{e}}{dt} = (\Lambda_{\mathrm{s}} - KC_{\mathrm{s}})\tilde{e} + \xi_{\mathrm{s}} - K\xi_y. \tag{2.59}$$

The estimation error of the infinite-dimensional system of Eq. (2.38), e, is as follows:

$$\frac{de}{dt} = (\Lambda_{\mathrm{s}} - KC_{\mathrm{s}})e - KC_{\mathrm{f}}x_{\mathrm{f}} + \xi_{\mathrm{s}} - K\xi_y. \tag{2.60}$$

According to Eq. (2.58), the solution of Eq. (2.59) consists an $O(\sqrt{\epsilon})$ approximation of the solution of Eq. (2.60) [49, Theorem A.1, p. 361]. In particular, there exists an $\hat{\epsilon}^{**} > 0$ such that for all $\epsilon \in (0, \hat{\epsilon}^{**}]$, it holds that:

$$e(t) - \tilde{e}(t) = O(\sqrt{\epsilon}). \tag{2.61}$$

Based on Eq. (2.61), the right-hand-side of the $\tilde{x}_{\mathrm{s}}$ system of Eq. (2.33) constitutes an $O(\sqrt{\epsilon})$ approximation to the right-hand-side of the x_{s} subsystem of Eq. (2.38). Therefore, the solution for $\tilde{x}_{\mathrm{s}}$ of Eq. (2.33) consists an $O(\sqrt{\epsilon})$ approximation of the

solution for the x_s of Eq. (2.38) [49, Theorem A.1, p. 361]. In particular, there exists an $\hat{\epsilon}^{***} > 0$ such that for all $\epsilon \in (0, \hat{\epsilon}^{***}]$, it holds that:

$$x_\mathrm{s}(t) - \tilde{x}_\mathrm{s}(t) = O(\sqrt{\epsilon}) \tag{2.62}$$

and

$$\|x_\mathrm{s}(t)\|_2^2 - \|\tilde{x}_\mathrm{s}(t)\|_2^2 = (\|x_\mathrm{s}(t)\|_2 - \|\tilde{x}_\mathrm{s}(t)\|_2) \cdot (\|x_\mathrm{s}(t)\|_2 + \|\tilde{x}_\mathrm{s}(t)\|_2) = O(\sqrt{\epsilon}). \tag{2.63}$$

Because $\|x_\mathrm{s}(t)\|_2$ and $\|\tilde{x}_\mathrm{s}(t)\|_2$ are bounded for all $t > 0$, $\langle \|x_\mathrm{s}(t)\|_2^2 \rangle$ and $\langle \|\tilde{x}_\mathrm{s}(t)\|_2^2 \rangle$ are equal to the traces of the covariance matrices of $x_\mathrm{s}(t)$ and $\tilde{x}_\mathrm{s}(t)$, i.e., $\langle x_\mathrm{s}(t) x_\mathrm{s}(t)^T \rangle = P_\mathrm{s}(t)$ and $\langle \tilde{x}_\mathrm{s}(t) \tilde{x}_\mathrm{s}(t)^T \rangle = \tilde{P}_\mathrm{s}(t)$, respectively. Immediately, it follows that:

$$\mathrm{Cov}_\mathrm{hs} = Tr\{P_\mathrm{s}\} = Tr\{\tilde{P}_\mathrm{s}\} + O(\sqrt{\epsilon}) = \widetilde{\mathrm{Cov}}_\mathrm{h} + O(\sqrt{\epsilon}). \tag{2.64}$$

This completes the proof of Eq. (2.44). □

Proof of Eq. (2.41) in Theorem 2.1. The surface covariance from the closed-loop infinite-dimensional system of Eq. (2.38), Cov_h, includes contributions from both x_s and x_f subsystems of Eq. (2.38). Therefore, we have the following equation for Cov_h:

$$\mathrm{Cov}_\mathrm{h} = \mathrm{Cov}_\mathrm{hs} + \mathrm{Cov}_\mathrm{hf} \tag{2.65}$$

where Cov_hf and Cov_hs are defined in Eqs. (2.42) – (2.45). Using Eqs. (2.42) and

(2.44), we immediately have:

$$\text{Cov}_\text{h} = \widetilde{\text{Cov}}_\text{h} + O(\sqrt{\epsilon}) + O(\epsilon). \tag{2.66}$$

Since as $\epsilon \to 0$, it holds that:

$$\frac{O(\epsilon)}{O(\sqrt{\epsilon})} \to 0. \tag{2.67}$$

Therefore, the $O(\epsilon)$ term in Eq. (2.66) is very small relative to the term $O(\sqrt{\epsilon})$ and can be neglected. There exists an $\epsilon^* = \min(\hat{\epsilon}, \hat{\epsilon}^*, \hat{\epsilon}^{**}, \hat{\epsilon}^{***})$ such that if $\epsilon \in (0, \epsilon^*]$, then

$$\text{Cov}_\text{h} \quad = \quad \widetilde{\text{Cov}}_\text{h} + O(\sqrt{\epsilon}). \tag{2.68}$$

This completes the proof of Theorem 2.1. ■

Remark 2.2 *The minimum number of sensors required for the operation of the Kalman-Bucy filter is the number that satisfies the observability requirement of the system, which is typically a small number. If more measurement sensors are available, it may result in improved state estimation and closed-loop performance since more information of the surface profile is available for state estimation. However, a small number of measurement sensors is favorable in many applications when the cost and complexity of the overall control system is a concern. Further discussion regarding the selection of measurement sensors is provided in Section 2.4.*

Remark 2.3 *In the special case where the number of sensors is equal to the order of*

the x_{s} subsystem, i.e., $q = m$, a static output feedback controller can be designed, by following the state estimation method developed in [10, 22, 19], to estimate the state of the finite-dimensional system, $\tilde{x}_{\mathrm{s}}$, directly from the measured output, y, and the resulting static output feedback controller takes the form:

$$
\begin{aligned}
\hat{x}_{\mathrm{s}} &= C_{\mathrm{s}}^{-1} y, \\
u &= G \hat{x}_{\mathrm{s}}.
\end{aligned}
\tag{2.69}
$$

Note that the same state feedback control law of Eq. (2.16) is used in the static output feedback controller of Eq. (2.69).

2.4 Simulation results

In this section, we first present applications of the proposed linear output feedback covariance controller to the linearized stochastic KSE to demonstrate the effectiveness of the proposed output feedback covariance controllers. Then, both linear and nonlinear covariance control of the nonlinear stochastic KSE are considered. A nonlinear output feedback covariance controller is first developed by combining the linear state feedback control law and a nonlinear state observer and is applied to the nonlinear stochastic KSE. Finally, nonlinear state feedback controller and nonlinear output feedback controller designs are presented and applied to the nonlinear KSE.

2.4.1 Linearized stochastic KSE

The stochastic KSE is a fourth-order nonlinear stochastic PDE that describes the evolution of the height fluctuation for surfaces in a variety of material preparation processes including surface erosion by ion sputtering [26, 53], surface smoothing by energetic clusters [42] and ZrO_2 thin film growth by reactive ion beam sputtering [73]. The linearized stochastic KSE around the zero solution ($h(x,t) = 0$) takes the following form:

$$\begin{aligned} \frac{\partial h}{\partial t} &= -\frac{\partial^2 h}{\partial x^2} - \kappa \frac{\partial^4 h}{\partial x^4} + \sum_{i=1}^{p} b_i(x) u_i(t) + \xi(x,t), \\ y(t) &= \begin{bmatrix} h(x_1,t) + \xi_y^1(t) & h(x_2,t) + \xi_y^2(t) & \dots & h(x_q,t) + \xi_y^q(t) \end{bmatrix}^T, \end{aligned} \tag{2.70}$$

subject to periodic boundary conditions (PBCs):

$$\frac{\partial^j h}{\partial x^j}(-\pi,t) = \frac{\partial^j h}{\partial x^j}(\pi,t), \quad j = 0,1,2,3, \tag{2.71}$$

and the initial condition $h(x,0) = h_0(x)$, where $x \in [-\pi,\pi]$ is the spatial coordinate and $\kappa > 0$ is the instability parameter of the stochastic KSE.

The eigenvalue problem of the linear operator of Eq. (2.70) takes the form:

$$\begin{aligned} \mathcal{A}\bar{\phi}_n(x) &= -\frac{d^2\bar{\phi}_n(x)}{dx^2} - \kappa\frac{d^4\bar{\phi}_n(x)}{dx^4} = \lambda_n\bar{\phi}_n(x), \\ \frac{d^j\bar{\phi}_n}{dx^j}(-\pi) &= \frac{d^j\bar{\phi}_n}{dx^j}(\pi), \\ j = 0, 1, 2, 3, &\quad n = 1, 2, \ldots, \infty. \end{aligned} \tag{2.72}$$

A direct computation of the solution of the above eigenvalue problem yields $\lambda_0 = 0$ with $\psi_0 = 1/\sqrt{2\pi}$, and $\lambda_n = n^2 - \kappa n^4$ (λ_n is an eigenvalue of multiplicity two) with eigenfunctions $\phi_n = (1/\sqrt{\pi})\sin(nx)$ and $\psi_n = (1/\sqrt{\pi})\cos(nx)$ for $n = 1, \ldots, \infty$. Note that the $\bar{\phi}_n$ in the general eigenvalue problem formulation of Eq. (2.4) denotes either ϕ_n or ψ_n. From the expression of the eigenvalues, it follows that for a fixed value of $\kappa > 0$, the number of unstable eigenvalues of the operator $\mathcal{A}$ in Eq. (2.72) is finite and the distance between two consecutive eigenvalues (i.e., λ_n and λ_{n+1}) increases as n increases.

For $0 < \kappa < 1$, the operator of Eq. (2.4) possesses unstable eigenvalues. Thus, the zero solution of the open-loop system of Eq. (2.70) is unstable, which implies that the surface covariance increases with time due to the open-loop instability of the zero solution. An appropriately designed feedback controller is necessary to regulate the surface covariance to a desired value.

Using modal decomposition, the linearized stochastic KSE is formulated into an

infinite-dimensional stochastic ODE system as follows:

$$\begin{aligned}\frac{d\alpha_n}{dt} &= (n^2 - \kappa n^4)\alpha_n + \sum_{i=1}^{p} b_{i\alpha_n} u_i(t) + \xi_\alpha^n(t), \quad n = 1, \ldots, \infty, \\ \frac{d\beta_n}{dt} &= (n^2 - \kappa n^4)\beta_n + \sum_{i=1}^{p} b_{i\beta_n} u_i(t) + \xi_\beta^n(t), \quad n = 0, 1, \ldots, \infty.\end{aligned} \tag{2.73}$$

A finite-dimensional approximation of Eq. (2.73) can be then derived by neglecting the fast modes (i.e., modes of order $(m+1)$ and higher) and a system of the form of Eq. (2.14) is obtained for covariance controller design.

A linear state feedback controller is initially designed on the basis of the finite-dimensional approximation by following the method proposed in [60], which takes the following form:

$$u = B_{\mathrm{s}}^{-1} (\Lambda_{\mathrm{cs}} - \Lambda_{\mathrm{s}}) \tilde{x}_{\mathrm{s}} \tag{2.74}$$

where the matrix Λ_{cs} contains the desired poles of the closed-loop system; $\Lambda_{\mathrm{cs}} = \mathrm{diag}[\lambda_{\mathrm{c}\beta 0}\ \lambda_{\mathrm{c}\alpha 1}\ \ldots\ \lambda_{\mathrm{c}\alpha m}\ \lambda_{\mathrm{c}\beta 1}\ \ldots\ \lambda_{\mathrm{c}\beta m}]$. $\lambda_{\mathrm{c}\beta 0}$, $\lambda_{\mathrm{c}\alpha i}$ and $\lambda_{\mathrm{c}\beta i}$ $(i = 1, \ldots, m)$ are desired poles of the closed-loop finite-dimensional system, which satisfy $Re\{\lambda_{\mathrm{c}\alpha i}\} < 0$ for $i = 1, \ldots, m$ and $Re\{\lambda_{\mathrm{c}\beta i}\} < 0$ for $i = 0, 1, \ldots, m$. By applying the controller in Eq. (2.74), the dynamics of the closed-loop finite-dimensional system is fully described by the matrix Λ_{cs}.

To simplify the development, we assume that $p = 2m + 1$ (i.e., the number of control actuators is equal to the dimension of the finite dimensional system) and pick

the actuator distribution functions, $b_i(x)$, to have the following form:

$$b_i(x) = \begin{cases} \dfrac{1}{\sqrt{2\pi}}, & i = 1, \\ \dfrac{1}{\sqrt{\pi}} \sin[(i-1)x], & i = 2, \ldots, m+1, \\ \dfrac{1}{\sqrt{\pi}} \cos[(i-m-1)x], & i = m+2, \ldots, 2m+1. \end{cases} \tag{2.75}$$

Note that the actuator distribution functions are selected such that B_{s}^{-1} exists. The following parameters are used in the simulation:

$$\kappa = 0.1, \quad \sigma = 1, \quad \varsigma = 0.1, \quad m = 5. \tag{2.76}$$

We design the linear state feedback controller such that all the desired poles in Λ_{cs} are equal to -10. The surface covariance of the infinite-dimensional system under the state feedback controller is 0.55. The method to determine the values of the closed-loop poles to regulate the surface covariance to a set-point value can be found in [60] and is omitted here for brevity.

Eleven measurement sensors are used and are evenly placed on the spatial domain $[-\pi, \pi]$. A flat initial surface is assumed and zero initial state estimates are used for all simulations.

$$h_0(x) = 0, \quad x_{\mathrm{s}}(0) = \hat{x}_{\mathrm{s}}(0) = \mathbf{0}, \quad x_{\mathrm{f}}(0) = \mathbf{0}. \tag{2.77}$$

A 50th order stochastic ODE approximation of Eq. (2.70) is used to simulate the

process. The stochastic ODEs are solved using Euler-Maruyama approximation with time discretization size of $\Delta t = 10^{-4}$. The choices of the truncation order and time discretization size lead to the convergence of the solution. Since it is a stochastic process, the surface covariance profile is obtained by averaging the results of 1000 independent simulation runs using the same parameters to produce a smooth profile of surface covariance evolution.

Remark 2.4 *In this chapter, the sensors are uniformly placed in the whole spatial domain and the simulation results show that this is a good choice in the sense that the placement results in good closed-loop performance under output feedback control. In general, the optimal sensor placement should be determined so that the state estimation error is minimized. A systematic solution for the problem for optimal sensor placement for stochastic distributed parameter systems is currently lacking but is outside of the scope of the current work.*

2.4.2 Linear dynamic output feedback control of linearized stochastic KSE

In the closed-loop simulation under linear dynamic output feedback control, a Kalman-Bucy filter is designed to estimate the state of the finite-dimensional system. The gain matrix K is obtained from the solution of the algebraic Riccati equation of Eqs. (2.25) and (2.29). $\widetilde{\mathrm{Cov}}_{\mathrm{h}}$ is the surface covariance of the closed-loop finite-dimensional system under the finite-dimensional output feedback covariance controller and is the solution

of the Lyapunov equation of Eq. (2.37). According to Theorem 2.1, $\widetilde{\mathrm{Cov}}_{\mathrm{h}}$ is an $O(\sqrt{\epsilon})$ approximation of the closed-loop surface covariance of the infinite-dimensional system, $\mathrm{Cov}_{\mathrm{h}}$, i.e., the closed-loop surface covariance of the infinite-dimensional system is an $O(\sqrt{\epsilon})$ approximation of the desired value. To regulate the surface covariance to a desired value, the ϵ should be sufficiently small, which can be achieved by appropriately selecting the size of the finite-dimensional approximation used for covariance controller design. In this design, when $m = 5$, $\epsilon = 0.01$, which is a sufficiently small number compared to the desired closed-loop surface covariance.

Since we use 11 measurement sensors, $q = 2m+1$ and the observer gain matrix is a square matrix. The desired surface covariance is 1.1347. Based on this desired surface covariance, the gain matrices for both the state observer, K, and the state feedback control law, G, are determined via the iterative procedure of Remark 2.1. Note that because of the existence of the sensor noise, the surface covariance under the output feedback covariance controller is higher than the one under state feedback control where the same gain matrix, G is used and the full state of the surface is accessible. The closed-loop simulation result under the dynamic output feedback controller with 11 measurement sensors is shown in Figure 2.1. The controller successfully drives the surface covariance of the closed-loop infinite-dimensional system to a level which is within the range of the theoretical estimate of Theorem 2.1, i.e., $\sqrt{\epsilon} \simeq 0.1$ and $\mathrm{Cov}_{\mathrm{h}} = \widetilde{\mathrm{Cov}}_{\mathrm{h}} + O(0.1)$. The result shown in Figure 2.1 also confirms that the surface covariance contribution from the x_{f} subsystem is negligible and that the contribution

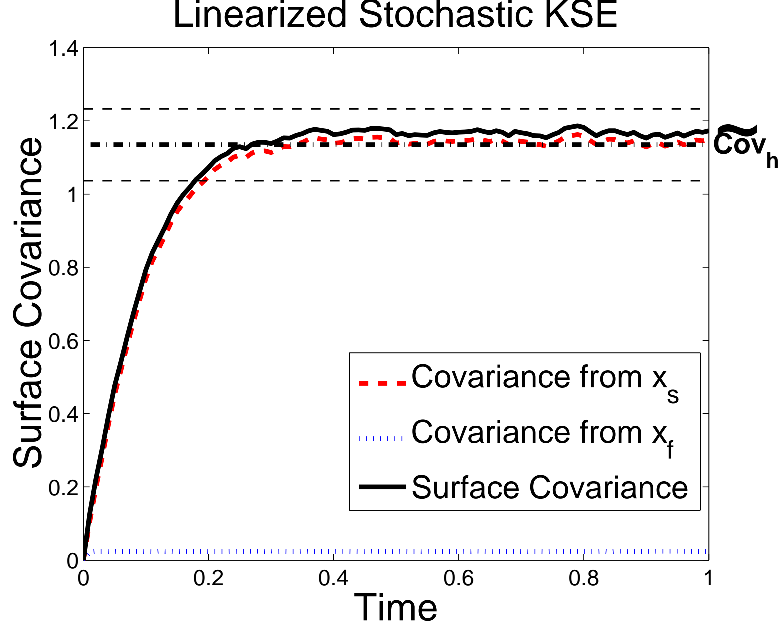

Figure 2.1: The closed-loop surface covariance under linear dynamic output feedback control using 11 measurement sensors. The horizontal dashed lines represent the range in which the surface covariance $\mathrm{Cov_h}$ is expected to be based on the theoretical estimates of Theorem 2.1.

from the x_{s} subsystem is dominant. Therefore, the design of the output feedback covariance controller based on the x_{s} subsystem can regulate the surface covariance of the infinite-dimensional closed-loop system to the desired level.

For dynamic output feedback control design, the number of the measurements is not needed to be equal to the dimension of the finite-dimensional system. A number of measurement sensors that is larger than the dimension of the finite-dimensional system results in a more accurate state estimation from the Kalman-Bucy filter. Therefore, the closed-loop surface covariance can be closer to the set-point value compared to the one in which the number of measurement sensors is equal to the dimension of the finite-dimensional system. On the other hand, when the number

of the measurement sensors is smaller than the dimension of the finite-dimensional system but is equal to or larger than the number of unstable modes of the system, it is still possible to design a stable Kalman-Bucy filter for state estimation. Figure 2.2 shows the comparison of closed-loop simulation results when different numbers of measurement sensors are used for state estimation. The feedback control law is the same for all simulations. Specifically, Figure 2.2 shows results from three closed-loop simulation runs with 7, 11 and 15 measurement sensors. It is clear that the control system which uses a larger number of measurement sensors is capable of controlling the surface covariance to a lower level. On the other hand, since the dimension of the finite-dimensional system is 11, it is possible to stabilize the surface covariance to a finite value when the number of measurement sensors is smaller than the dimension of the finite-dimensional system.

However, there is a minimum number of measurement sensors required by the dynamic output feedback controller to stabilize the system. In this study, a minimum of 7 measurement sensors are required. When the number of measurement sensors is fewer than the minimum number, 7, the output feedback controller cannot stabilize the closed-loop system. In Figure 2.3, we show the closed-loop simulation result under a linear dynamic output feedback controller using 6 measurement sensors. The surface covariance of the closed-loop system under such a controller is not stabilized to a finite value.

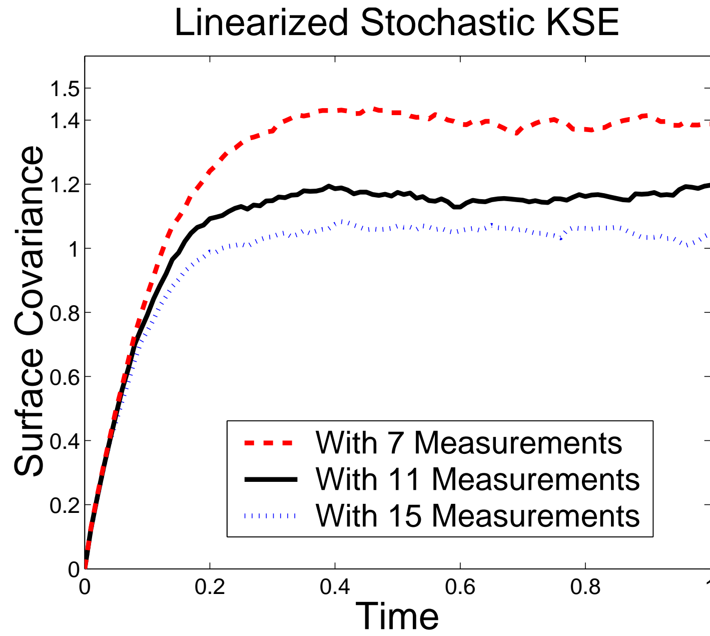

Figure 2.2: Comparison of the surface covariance under linear dynamic output feedback controllers with 7, 11 and 15 measurement sensors.

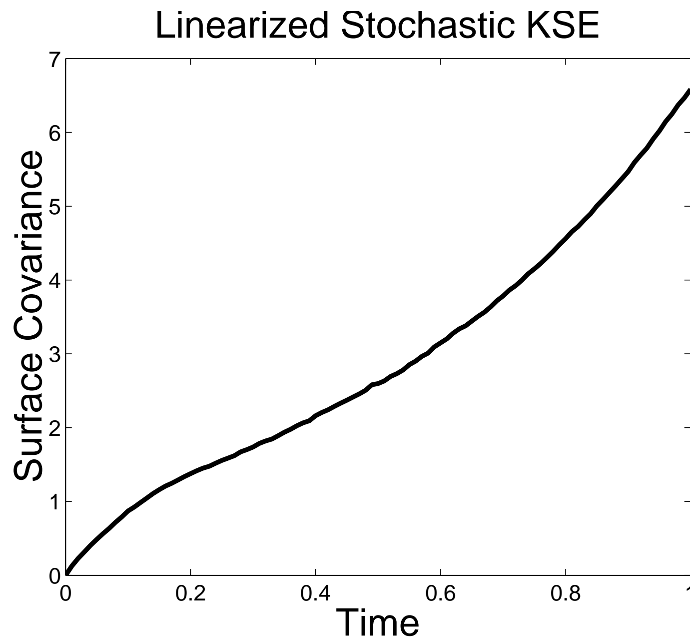

Figure 2.3: The closed-loop profile of the surface covariance under linear dynamic output feedback control with 6 measurement sensors.

2.4.3 Dynamic output feedback control of nonlinear stochastic KSE

In this subsection, the application of dynamic output feedback controllers to the nonlinear stochastic KSE is considered. We first formulate the nonlinear stochastic KSE into an infinite-dimensional nonlinear stochastic ODE system and a finite-dimensional approximation is derived as a basis for controller design. In addition to the linear output feedback controller, a nonlinear dynamic output feedback controller is also designed by combining a nonlinear state feedback controller developed in [62] and an appropriate nonlinear state estimator. Both linear and nonlinear dynamic output feedback controllers are applied to the nonlinear stochastic KSE and the closed-loop performance under both controllers is compared.

The nonlinear stochastic KSE with distributed control and measured output with sensor noise takes the following form:

$$
\begin{aligned}
\frac{\partial h}{\partial t} &= -\frac{\partial^2 h}{\partial x^2} - \kappa\frac{\partial^4 h}{\partial x^4} + \left(\frac{\partial h}{\partial x}\right)^2 + \sum_{i=1}^{p} b_i(x)u_i(t) + \xi(x,t), \\
y(t) &= \begin{bmatrix} h(x_1,t)+\xi_y^1(t) & h(x_2,t)+\xi_y^2(t) & \dots & h(x_q,t)+\xi_y^q(t) \end{bmatrix}^T,
\end{aligned}
\tag{2.78}
$$

subject to PBCs:

$$
\frac{\partial^j h}{\partial x^j}(-\pi,t) = \frac{\partial^j h}{\partial x^j}(\pi,t), \quad j = 0,1,2,3, \tag{2.79}
$$

and the initial condition:

$$
h(x,0) = h_0(x). \tag{2.80}
$$

The variables are defined in the same way as those in Eq. (2.70). Following a similar approach to the one presented in Section 2.4.1, the following system of infinite nonlinear stochastic ODEs with distributed control can be obtained:

$$
\begin{aligned}
\frac{d\alpha_n}{dt} &= (n^2 - \kappa n^4)\alpha_n + f_{n\alpha} + \sum_{i=1}^{p} b_{i\alpha_n} u_i(t) + \xi_\alpha^n(t), \quad n = 1, 2, \ldots, \infty, \\
\frac{d\beta_n}{dt} &= (n^2 - \kappa n^4)\beta_n + f_{n\beta} + \sum_{i=1}^{p} b_{i\beta_n} u_i(t) + \xi_\beta^n(t), \quad n = 0, 1, \ldots, \infty,
\end{aligned} \tag{2.81}
$$

where

$$
\begin{aligned}
f_{n\alpha} &= \int_{-\pi}^{\pi} \phi_n(x) \left(\sum_{j=1}^{\infty} \alpha_j(t) \frac{d\phi_j}{dx}(x) + \sum_{j=0}^{\infty} \beta_j(t) \frac{d\psi_j}{dx}(x) \right)^2 dx, \\
f_{n\beta} &= \int_{-\pi}^{\pi} \psi_n 1(x) \left(\sum_{j=1}^{\infty} \alpha_j(t) \frac{d\phi_j}{dx}(x) + \sum_{j=0}^{\infty} \beta_j(t) \frac{d\psi_j}{dx}(x) \right)^2 dx.
\end{aligned} \tag{2.82}
$$

The system of Eq. (2.81) can be rewritten in the following form with the measured output:

$$
\begin{aligned}
\frac{dx_s}{dt} &= \Lambda_s x_s + f_s(x_s, x_f) + B_s u + \xi_s, \\
\frac{dx_f}{dt} &= \Lambda_f x_f + f_f(x_s, x_f) + B_f u + \xi_f, \\
y &= C_s x_s + C_f x_f + \xi_y.
\end{aligned} \tag{2.83}
$$

Note that the dimension of the x_s subsystem is $2m + 1$ and the x_f subsystem is infinite-dimensional.

In the closed-loop simulation of the nonlinear stochastic KSE, we use the same actuator distribution functions, same value of the model parameter, κ, and same ini-

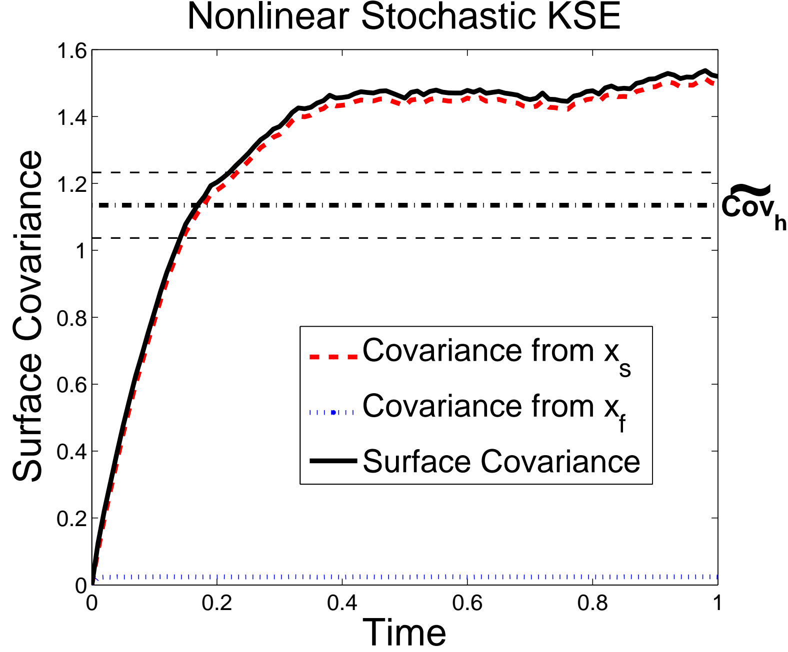

Figure 2.4: The closed-loop surface covariance profile of the nonlinear stochastic KSE under linear dynamic output feedback control with 11 measurement sensors. The horizontal dashed lines represent the range in which the surface covariance $\mathrm{Cov_h}$ is expected to be based on the theoretical estimates of Theorem 2.1.

tial conditions as those used in the closed-loop simulation of the linearized stochastic KSE. The linear dynamic output feedback controller developed in Section 2.4.2 is applied to the nonlinear stochastic KSE using 11 measurement sensors. A 50th order stochastic ODE approximation of Eq. (2.70) is used to simulate the nonlinear process.

The closed-loop simulation result of the nonlinear stochastic KSE under the linear dynamic output feedback controller is shown in Figure 2.4. The surface covariance is stabilized to a finite-value under the linear output feedback covariance controller, since the controller is designed to stabilize the linear part of the system of Eq. (2.22). Therefore, when we apply the linear controller to the nonlinear system, the closed-

loop system is locally stable. Although the nonlinear system is stabilized, there is a relatively big error between the closed-loop surface covariance and the set-point value, $\widetilde{\mathrm{Cov}}_{\mathrm{h}}$. As shown in Figure 2.4, this error is outside of the approximation error boundaries, $O(\sqrt{\epsilon})$, and thus it is not due to the use of a finite-dimensional approximation of the stochastic KSE for control design. This error is due to the nonlinearity of the system, which is not explicitly accounted for in the controller design. Therefore, a nonlinear controller is necessary to improve the closed-loop performance.

Nonlinear state feedback control design

In this subsection, the goal is to design a nonlinear output feedback controller which explicitly accounts for the nonlinearity of the stochastic KSE model of Eq. (2.78). Neglecting the x_{f} subsystem, the following $2m$-dimensional system is obtained:

$$\frac{d\tilde{x}_{\mathrm{s}}}{dt} = \Lambda_{\mathrm{s}}\tilde{x}_{\mathrm{s}} + f_{\mathrm{s}}(\tilde{x}_{\mathrm{s}}, 0) + B_{\mathrm{s}}u + \xi_{\mathrm{s}} \tag{2.84}$$

where the tilde symbol denotes that the state variable is associated with a finite-dimensional system.

Following the method proposed in [62], a nonlinear state feedback controller is first designed on the basis of the finite-dimensional approximation of Eq. (2.84) as follows:

$$u = B_{\mathrm{s}}^{-1}\left\{(\Lambda_{\mathrm{cs}} - \Lambda_{\mathrm{s}})\tilde{x}_{\mathrm{s}} - f_{\mathrm{s}}(\tilde{x}_{\mathrm{s}}, 0)\right\}. \tag{2.85}$$

Note that the nonlinear term, $f_{\mathrm{s}}(\tilde{x}_{\mathrm{s}}, 0)$, is explicitly accounted for in the nonlinear controller design. The choice of Λ_{cs} is similar to the choice in Eq. (2.74) and determines the dynamics of the closed-loop finite-dimensional system.

Under the nonlinear state feedback controller, the closed-loop finite-dimensional system is an approximate ($O(\sqrt{\epsilon})$ approximation) linear stochastic system (see the proof of Theorem 2.1 in [62]). The steady-state surface covariance of the closed-loop finite-dimensional system under the nonlinear state feedback controller can be obtained by following the method presented in Section 2.3.1. An analysis of the performance of the closed-loop nonlinear infinite-dimensional system enforced by the nonlinear state feedback controller of Eq. (2.85) can also been found in [62]. To show the effectiveness of the nonlinear state feedback controller, we apply both the linear state feedback controller of Eq. (2.74) and the nonlinear state feedback controller of Eq. (2.85) to the nonlinear stochastic KSE. The results are presented in Figure 2.5. Both the linear and nonlinear state feedback controllers stabilize the surface covariance to a finite value. However, the steady state surface covariance under the nonlinear controller is much closer to the set-point value compared to the one under the linear controller. The nonlinear state feedback controller successfully drives the surface covariance of the closed-loop infinite-dimensional system of nonlinear KSE to the set-point value $\widetilde{\mathrm{Cov}}_{\mathrm{h}}$, which is within the range of the theoretical estimate (for the theoretical estimation of the surface covariance of the closed-loop infinite-dimensional nonlinear system under the nonlinear state feedback controller, see Theorem 1 in [62]).

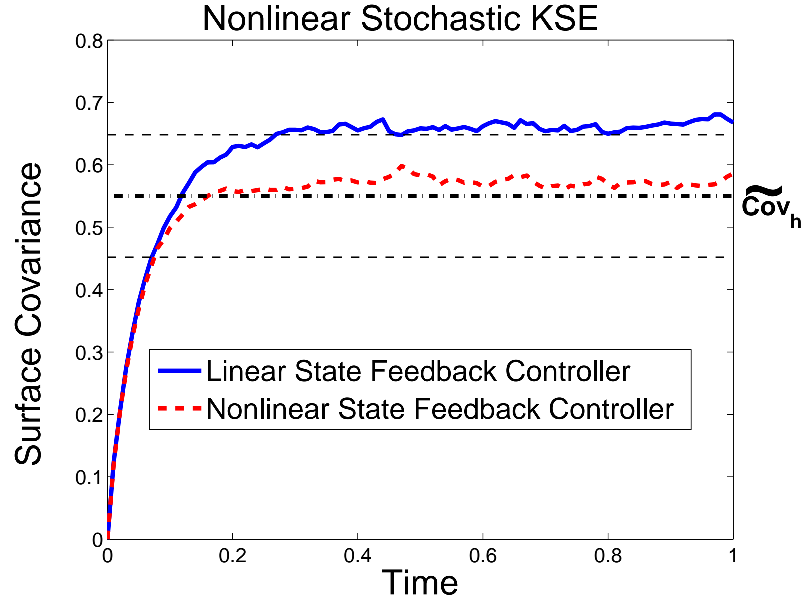

Figure 2.5: Comparison of the closed-loop surface covariance profiles of the nonlinear stochastic KSE under linear and nonlinear state feedback control. The horizontal dashed lines represent the range in which the surface covariance $\mathrm{Cov_h}$ is expected to be based on the theoretical estimates of Theorem 1 in [62].

The surface covariance under the linear state feedback controller falls outside of the range of the theoretical estimate. The improved performance of the nonlinear state feedback controller is due to the fact that the nonlinearity of the process model is explicitly accounted for in the controller design.

Nonlinear dynamic output feedback control of nonlinear stochastic KSE

In this subsection, we design a nonlinear dynamic output feedback controller by combining the nonlinear state feedback controller of Eq. (2.85) and a dynamic nonlinear

state estimator. An appropriate nonlinear state estimator considered of the form:

$$\frac{d\hat{x}_s}{dt} = \Lambda_s \hat{x}_s + f_s(\hat{x}_s, 0) + B_s u + K(y - C_s \hat{x}_s) \tag{2.86}$$

where the gain matrix, K, is determined by using Eq. (2.25).

The resulting nonlinear dynamic output feedback controller takes then the form:

$$\begin{aligned} \frac{d\hat{x}_s}{dt} &= \Lambda_s \hat{x}_s + f_s(\hat{x}_s, 0) + B_s u + K(y - C_s \hat{x}_s), \quad \hat{x}_s(0) = \hat{x}_{s0}, \\ u &= B_s^{-1} \left\{ (\Lambda_{cs} - \Lambda_s)\hat{x}_s - f_s(\hat{x}_s, 0) \right\}. \end{aligned} \tag{2.87}$$

Figure 2.6 shows the surface covariance profiles of the closed-loop system under nonlinear dynamic output feedback control with different numbers of measurement sensors. For comparison, the closed-loop surface covariance under the nonlinear state feedback controller is also shown in Figure 2.6. There are differences between the steady-state surface covariance under the nonlinear dynamic output feedback controller and under the state feedback controller. A higher number of measurement sensors leads to a smaller difference since more information of the surface is available to the state estimator. This is consistent with the fact that a higher number of measurement sensors is capable of achieving a lower closed-loop surface covariance under output feedback covariance control. Note that the state feedback controller gives the lowest steady-state surface covariance since there is no estimation error involved in its implementation.

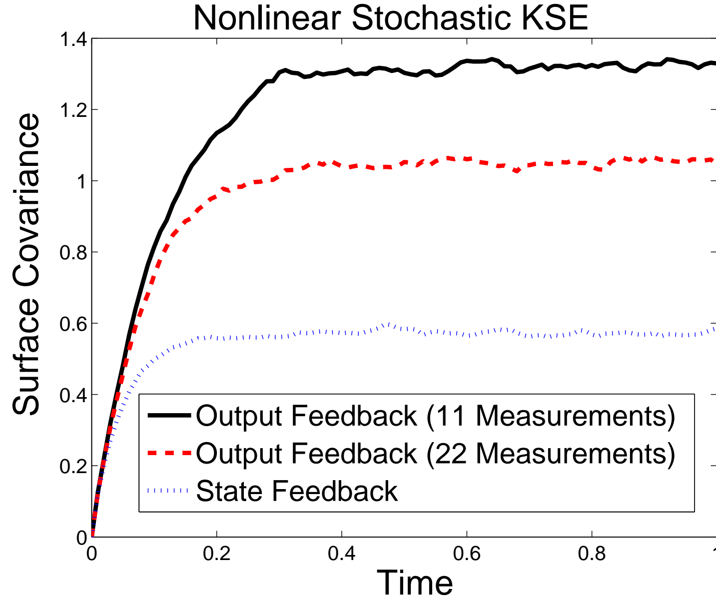

Figure 2.6: The surface covariance of nonlinear KSE under nonlinear dynamic output feedback controllers with different numbers of measurement sensors.

2.5 Conclusions

In this chapter, we developed a method for dynamic output feedback covariance control of the state covariance of linear dissipative stochastic PDEs using spatially distributed control actuation and sensing with measurement noise. The stochastic PDE was initially formulated into a system of infinite stochastic ODEs by using modal decomposition. A finite-dimensional approximation was then obtained to capture the dominant mode contribution to the surface roughness profile (i.e., the covariance of the surface height profile). Subsequently, a state feedback controller and a Kalman-Bucy filter were designed on the basis of the finite-dimensional approximation. The resulting linear dynamic output feedback controller is the one that couples the state

feedback controller and the state estimator. The steady-state expected surface covariance under the linear dynamic output feedback controller was then estimated on the basis of the closed-loop finite-dimensional system. An analysis was performed to obtain an estimate of the expected surface covariance of the closed-loop infinite-dimensional system. Applications of the linear dynamic output feedback controller to the linearized and nonlinear stochastic Kuramoto-Sivashinsky equations were presented. Finally, nonlinear state feedback controller and nonlinear output feedback controller designs were also presented and applied to the nonlinear KSE.

Chapter 3

Parameter Estimation for a Stochastic PDE Model of a Sputtering Process

3.1 Introduction

Following upon the state/output feedback covariance control design for linear and nonlinear stochastic PDEs of Chapter 2, this chapter focuses on a specific thin film manufacturing process (sputtering) and develops a method for the parameter estimation of nonlinear stochastic partial differential equation (PDE) systems. Sputtering processes are widely used in the thin film and semiconductor fabrication to remove materials from the surface of solids through the impact of energetic particles. In many

cases sputtering is used to smooth out surface features. The surface morphology of thin films after sputter erosion strongly depends on conditions such as incident ion energy, sputtered substrate temperature and material composition [66]. In a sputtering process, the surface is directly shaped by microscopic surface processes (e.g., erosion, diffusion and surface reaction), which are stochastic processes. Therefore, the stochastic nature of sputtering processes must be fully considered in the modeling and the parameters of the stochastic models need to be estimated from the simulation data or experimental data of such processes.

In this chapter, the sputtering process model involves two surface micro-processes: atom erosion and surface diffusion. This sputtering process is simulated using a kMC simulation method and its surface height evolution can be adequately described by the stochastic Kuramoto-Sivashinsky equation (KSE), a fourth-order nonlinear stochastic PDE. First, we estimate the four parameters of the stochastic KSE so that the expected surface roughness profile predicted by the stochastic KSE is close (in a least-square sense) to the profile of the kMC simulation of the sputtering process. To perform this model parameter estimation task, we initially formulate the nonlinear stochastic KSE into a system of infinite nonlinear stochastic ODEs. A finite-dimensional approximation of the stochastic KSE is then constructed that captures the dominant mode contribution to the state and the evolution of the state covariance of the stochastic ODE system is derived. Then, a kMC simulator is used to generate representative surface snapshots during process evolution to obtain values

of the state vector of the stochastic ODE system. Subsequently, the state covariance of the stochastic ODE system that corresponds to the sputtering process is computed based on the kMC simulation results. Finally, the model parameters of the nonlinear stochastic KSE are obtained by using least-squares methods so that the state covariance computed from the stochastic KSE process model matches that computed from kMC simulations. Subsequently, we use appropriate finite-dimensional approximations of the computed stochastic KSE model to design state and output feedback controllers, which are applied to the kMC model of the sputtering process. Extensive closed-loop system simulations demonstrate that the controllers reduce the expected surface roughness by 55% compared to the corresponding values under open-loop operation.

3.2 Preliminaries

3.2.1 Process description

We consider a one-dimensional (1-D) lattice representation of a crystalline surface of a sputtering process, which includes two surface micro-processes, atom erosion and surface diffusion. The solid-on-solid assumption is made which means that no defects or overhangs are allowed to be developed in the film. The microscopic rules under which atom erosion and surface diffusion take place are as follows: a site, i, is first randomly picked among the sites of the whole lattice and the particle at the top of

this site is subject to: a) erosion with probability $0 < f < 1$, or b) diffusion with probability $1 - f$.

If the particle at the top of site i is subject to erosion, the particle is removed from the site i with probability $P_{\mathrm{e}} Y(\phi_i)$. P_{e} is determined as $\frac{1}{7}$ times the number of occupied sites in a box of size 3×3 centered at the site i, which is shown in Figure 3.1. There are a total of nine sites in the box. The central one is the particle to be considered for erosion (the one marked by $\bullet$). Among the remaining eight sites, the site above the central site of interest must be vacant since the central site is a surface site. Therefore, only seven of the eight sites can be occupied and the maximum value of P_{e} is 1. $Y(\phi_i)$ is the sputtering yield function defined as follows:

$$Y(\phi_i) = y_0 + y_1 \phi_i^2 + y_2 \phi_i^4 \tag{3.1}$$

where y_0, y_1 and y_2 are constants. Following [26], the values of y_0, y_1 and y_2 can be chosen such that $Y(0) = 0.5$, $Y(\frac{\pi}{2}) = 0$ and $Y(1) = 1$, which corresponds to $y_0 = 0.5$, $y_1 = 1.0065$, and $y_2 = -0.5065$. The local slope, ϕ_i, is defined as follows:

$$\phi_i = \tan^{-1}\left(\frac{h_{i+1} - h_{i-1}}{2a}\right) \tag{3.2}$$

where a is the lattice parameter and h_{i+1} and h_{i-1} are the values of surface height at sites $i+1$ and $i-1$, respectively.

If the particle at the top of site i is subject to diffusion, one of its two nearest

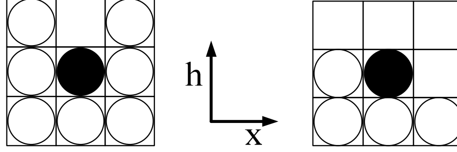

Figure 3.1: Schematic of the rule to determine $P_{\rm e}$. $P_{\rm e}$ is defined as $\dfrac{1}{7}$ times the number of occupied sites in a box of size 3×3 centered at the particle on the top of site i; $P_{\rm e} = 1$ in the left figure and $P_{\rm e} = \dfrac{4}{7}$ in the right figure, where the particle marked by $\bullet$ is on the top of site i.

neighbors, j ($j = i+1$ or $i-1$) is randomly chosen and the particle is moved to the nearest neighbor column with transition probability $w_{i\to j}$ as follows:

$$w_{i\to j} = \frac{1}{1+\exp\left(\beta \Delta H_{i\to j}\right)} \tag{3.3}$$

where $\Delta H_{i\to j}$ is the energy difference between the final and initial states of the move, $\beta = \dfrac{1}{k_{\rm B}T}$ and H is defined through the Hamiltonian of an unrestricted solid-on-solid model as follows:

$$H = \left(\frac{J}{a^n}\right) \sum_{k=1}^{N} (h_k - h_{k+1})^n \tag{3.4}$$

where J is the bond energy, N is the total number of sites in the lattice and n is a positive number. In the simulations presented in this chapter, we use $n = 2$ and $\beta J = 2$ [80].

3.2.2 KMC model of the sputtering process

To carry out kMC simulations of this sputtering process, the rates of surface micro-processes should be computed [32, 87]. The rates of both erosion and diffusion are site specific and can be obtained based on the process description as follows:

$$\begin{aligned} r_{\mathrm{e}}(i) &= \frac{f}{\tau} P_{\mathrm{e}}(i) Y(\phi_i) \quad , i = 1, 2, \ldots, N, \\ r_{\mathrm{d}}(i,j) &= \frac{1-f}{2\tau} w_{i \to j} \quad , i = 1, 2, \ldots, N, \end{aligned} \tag{3.5}$$

where $r_{\mathrm{e}}(i)$ is the erosion rate at site i and $r_{\mathrm{d}}(i,j)$ is the rate at which a surface particle hops from site i to site j. For the sputtering process considered, only nearest neighbor hopping is allowed, so $j = i \pm 1$. $P_{\mathrm{e}}(i)$ is determined by the box rule shown in Figure 3.1, $Y(\phi_i)$ is defined in Eqs. (3.1) and (3.2), and $w_{i \to j}$ is defined in Eqs. (3.3) and (3.4). τ is defined as the time scale [53] and is fixed at $1/sec$ for open-loop simulations.

After the rates of surface micro-processes are determined, kMC simulations can be carried out using an appropriate algorithm. In general, there are two groups of kMC algorithms which have been developed to simulate dynamical processes governed by the master equation: (a) the null-event algorithm [98], and (b) the continuous-time Monte Carlo method [88]. The null-event algorithm tries to execute Monte Carlo events on randomly selected sites with certain probabilities of success, while the continuous-time Monte Carlo method selects an event before the selection of the site on which the event is going to be executed. Upon a successful event, the time

passed during the event is computed based on the total rates of all the micro-processes in both the null-event algorithm and the continuous-time Monte Carlo algorithm [75].

A review and analysis on complexities and efficiencies of these algorithms can be found in [75]. Although the continuous-time Monte Carlo algorithms with lists of neighbors and local update are often used for simulating the dynamics of complex processes, they are not appropriate for the sputtering process considered in this chapter. The continues-time Monte Carlo method requires the construction of a set of classes for possible Monte Carlo events and associated surface sites so that the events in each class have exactly the same transition probabilities. Typically, the transition probabilities depend on the surface micro-environment of the surface site considered. The continues-time Monte Carlo method is efficient to simulate systems such as surface reactions and thin film growth processes in which the dependence of the transition probabilities on the surface micro-environment is simply the number of nearest neighbors. This type of dependence of the transition probability on surface micro-environment results in a small number of classes needed to run the simulation. For the sputtering process considered in this chapter, the dependence of both the erosion and diffusion rates on the surface micro-environment is very complex and essentially all surface sites have different erosion and diffusion rates. If a set of classes are constructed so that each class contains exactly the same transition probability, a large number of classes are required, which will result in an inefficient simulation scheme. With these considerations, we decide to simulate the sputtering process in

this chapter by using the null-event algorithm [98] so that the complex dependence of the transition probabilities on the surface micro-configuration in the sputtering process can be handled in an efficient way.

The following kMC simulation algorithm is used to simulate the sputtering process:

- The first integer random number, ζ_1 ($0 < \zeta_1 \leq N$, where ζ_1 is an integer and N is the total number of surface sites) is generated to pick a site, i, among all the sites on the 1-D lattice.

- The second real random number, ζ_2 in the $(0, 1)$ interval, is generated to decide whether the chosen site, i, is subject to erosion ($\zeta_2 < f$) or diffusion ($\zeta_2 > f$).

- If the chosen site is subject to erosion, P_e and $Y(\phi_i)$ are computed. Specifically, P_e is computed by using the box rule shown in Figure 3.1 where the center of the box is the surface particle on site i and $Y(\phi_i)$ is computed by using Eqs. (3.1) and (3.2). Then, another real random number $\zeta_{\mathrm{e}3}$ in the $(0, 1)$ interval is generated. If $\zeta_{\mathrm{e}3} < P_\mathrm{e} Y(\phi_i)$ the surface particle on site i is removed. Otherwise, no event is executed.

- If the chosen site is subject to diffusion, a side neighbor, j, ($j = i + 1$ or $i - 1$ in the case of a 1-D lattice) is randomly picked and the hopping rate, $w_{i \to j}$, is computed by using Eq. (3.3). Then, another real random number $\zeta_{\mathrm{d}3}$ in the $(0, 1)$ interval is generated. If $\zeta_{\mathrm{d}3} < w_{i \to j}$, the surface atom is moved to the new site. Otherwise no event is executed.

- Upon the execution of an event, a time increment, δt is computed by using the following expression:

$$\delta t = -\frac{\ln \zeta_4}{\frac{f}{\tau}\sum_{i=1}^{N}[P_{\mathrm{e}}(i)Y(\phi_i)] + \frac{1-f}{2\tau}\sum_{i=1}^{N}[w_{i\to i+1} + w_{i\to i-1}]} \quad (3.6)$$

where ζ_4 is a real random number in the $(0, 1)$ interval.

All random numbers, ζ_1, ζ_2, ζ_3 and ζ_4, follow a uniform probability distribution in their domains of definition.

Periodic boundary conditions (PBCs) are used in the kMC model of the sputtering process. Using PBCs, a particle that diffuses out of the simulation lattice at one boundary enters into the simulation lattice from the opposing side. Limited by the currently available computing power, the lattice size of a kMC simulation is much smaller than the size of a real process. Therefore, PBCs are widely used in molecular level simulations so that the statistical properties of a large scale stochastic process can be appropriately captured by kMC simulations carried out on a small simulation lattice [67].

Remark 3.1 *Note that the probability f in Eq. (3.5) is dependent on the operating conditions of the sputtering process. Based on the process description, the value of f affects the ratio of erosion and diffusion events on the surface. Since an erosion event is a direct consequence of the bombardment by incoming particles, a higher bombard-*

ment rate will result in a higher erosion rate, which implies a larger f. On the other hand, the surface diffusion rate, r_{d} in Eq. (3.5), should not depend on the bombardment rate of incoming particles. When spatially distributed control is implemented, the surface bombardment rate is a spatially distributed variable. Consequently, f is a spatially distributed variable that can be computed based on the surface bombardment rate.

3.2.3 Stochastic PDE model of the sputtering process

The sputtering process is a stochastic process. The height fluctuations of the surface in this sputtering process can be adequately described by the stochastic KSE, which is a fourth order, nonlinear stochastic PDE [26]. The stochastic KSE takes the following form:

$$\frac{\partial h}{\partial t} = -\nu \frac{\partial^2 h}{\partial x^2} - \kappa \frac{\partial^4 h}{\partial x^4} + \frac{\lambda}{2}\left(\frac{\partial h}{\partial x}\right)^2 + \xi(x,t) \tag{3.7}$$

subject to PBCs:

$$\frac{\partial^j h}{\partial x^j}(-\pi,t) = \frac{\partial^j h}{\partial x^j}(\pi,t), \quad j = 0,\ldots,3 \tag{3.8}$$

and the initial condition:

$$h(x,0) = h_0(x) \tag{3.9}$$

where ν, κ, and λ are parameters related to surface mechanisms [53], $x \in [-\pi,\pi]$ is the spatial coordinate, t is the time, $h(x,t)$ is the height of the surface at position x and time t. The PBCs are used so that the treatment of surface boundaries is

consistent to that of the kMC model where PBCs are also used. $\xi(x,t)$ is a Gaussian noise with the following expressions for its mean and covariance:

$$\begin{aligned} \langle \xi(x,t) \rangle &= 0, \\ \langle \xi(x,t)\xi(x',t') \rangle &= \sigma^2 \delta(x-x')\delta(t-t'), \end{aligned} \tag{3.10}$$

where σ is a constant, $\delta(\cdot)$ is the Dirac function, and $\langle \cdot \rangle$ denotes the expected value.

To study the dynamics of Eq. (3.7), we initially consider the eigenvalue problem of the linear operator of Eq. (3.7), which takes the form:

$$\begin{gathered} A\bar{\phi}_n(x) = -\nu \frac{d^2\bar{\phi}_n(x)}{dx^2} - \kappa \frac{d^4\bar{\phi}_n(x)}{dx^4} = \lambda_n \bar{\phi}_n(x), \\ \frac{d^j\bar{\phi}_n}{dx^j}(-\pi) = \frac{d^j\bar{\phi}_n}{dx^j}(\pi), \\ j = 0,1,2,3, \quad n = 1,2,\ldots,\infty, \end{gathered} \tag{3.11}$$

where λ_n denotes an eigenvalue and $\bar{\phi}_n$ denotes an eigenfunction. A direct computation of the solution of the above eigenvalue problem yields $\lambda_0 = 0$ with $\psi_0 = 1/\sqrt{2\pi}$, and $\lambda_n = \nu n^2 - \kappa n^4$ (λ_n is an eigenvalue of multiplicity two) with eigenfunctions $\phi_n = (1/\sqrt{\pi})\sin(nx)$ and $\psi_n = (1/\sqrt{\pi})\cos(nx)$ for $n = 1,\ldots,\infty$. Note that the $\bar{\phi}_n$ in Eq. (3.11) denotes either ϕ_n or ψ_n. From the expression of the eigenvalues, it follows that for fixed values of $\nu > 0$ and $\kappa > 0$, the number of unstable eigenvalues of the operator A in Eq. (3.11) is finite and the distance between two consecutive eigenvalues (i.e., λ_n and λ_{n+1}) increases as n increases.

To present the method that we use to estimate the parameters of the stochastic

KSE of Eq. (3.7) and design controllers, we first derive a nonlinear stochastic ODE approximation of Eq. (3.7) using Galerkin's method. To this end, we first expand the solution of Eq. (3.7) in an infinite series in terms of the eigenfunctions of the operator of Eq. (3.11) as follows:

$$h(x,t) = \sum_{n=1}^{\infty} \alpha_n(t)\phi_n(x) + \sum_{n=0}^{\infty} \beta_n(t)\psi_n(x) \tag{3.12}$$

where $\alpha_n(t)$, $\beta_n(t)$ are time-varying coefficients. Substituting the above expansion for the solution, $h(x,t)$, into Eq. (3.7) and taking the inner product with the adjoint eigenfunctions, $\phi_n^*(z) = (1/\sqrt{\pi})\sin(nz)$ and $\psi_n^*(z) = (1/\sqrt{\pi})\cos(nz)$, the following system of infinite nonlinear stochastic ODEs is obtained:

$$\begin{aligned} \frac{d\alpha_n}{dt} &= (\nu n^2 - \kappa n^4)\alpha_n + \lambda f_{n\alpha} + \xi_\alpha^n(t), \quad n = 1, 2, \ldots, \infty, \\ \frac{d\beta_n}{dt} &= (\nu n^2 - \kappa n^4)\beta_n + \lambda f_{n\beta} + \xi_\beta^n(t), \quad n = 0, 1, \ldots, \infty, \end{aligned} \tag{3.13}$$

where

$$\begin{aligned} f_{n\alpha} &= \frac{1}{2}\int_{-\pi}^{\pi} \phi_n^*(x) \left(\sum_{j=1}^{\infty} \alpha_j(t) \frac{d\phi_j}{dx}(x) + \sum_{j=0}^{\infty} \beta_j(t) \frac{d\psi_j}{dx}(x) \right)^2 dx, \\ f_{n\beta} &= \frac{1}{2}\int_{-\pi}^{\pi} \psi_n^*(x) \left(\sum_{j=1}^{\infty} \alpha_j(t) \frac{d\phi_j}{dx}(x) + \sum_{j=0}^{\infty} \beta_j(t) \frac{d\psi_j}{dx}(x) \right)^2 dx, \end{aligned} \tag{3.14}$$

and

$$\begin{aligned} \xi_\alpha^n(t) &= \int_{-\pi}^{\pi} \xi(x,t)\phi_n^*(x)dx, \\ \xi_\beta^n(t) &= \int_{-\pi}^{\pi} \xi(x,t)\psi_n^*(x)dx. \end{aligned} \tag{3.15}$$

Using Result 1, we obtain $\langle \xi_\alpha^n(t)\xi_\alpha^n(t')\rangle = \sigma^2\delta(t-t')$ and $\langle \xi_\beta^n(t)\xi_\beta^n(t')\rangle = \sigma^2\delta(t-t')$.

The surface roughness of the process is a variable of interest from a control point of view. The surface roughness, r, is represented by the standard deviation of the surface from its average height and is computed as follows:

$$r(t) = \sqrt{\frac{1}{2\pi}\int_{-\pi}^{\pi}[h(x,t)-\bar{h}(t)]^2 dx} \tag{3.16}$$

where $\bar{h}(t) = \dfrac{1}{2\pi}\displaystyle\int_{-\pi}^{\pi} h(x,t)dx$ is the average surface height. According to Eq. (3.12), we have $\bar{h}(t) = \beta_0(t)\psi_0$. Therefore, $\langle r^2(t)\rangle$ can be rewritten in terms of $\alpha_n(t)$ and $\beta_n(t)$:

$$\begin{aligned} \langle r^2(t)\rangle &= \frac{1}{2\pi}\left\langle \int_{-\pi}^{\pi}(h(x,t)-\bar{h}(t))^2 dx \right\rangle \\ &= \frac{1}{2\pi}\left\langle \int_{-\pi}^{\pi}\left[\sum_{i=1}^{\infty}\alpha_i(t)\phi_i(x) + \sum_{i=0}^{\infty}\beta_i(t)\psi_i(x) - \beta_0(t)\psi_0\right]^2 dx \right\rangle \\ &= \frac{1}{2\pi}\left\langle \int_{-\pi}^{\pi}\sum_{i=1}^{\infty}\left[\alpha_i^2(t)\phi_i(x)^2 + \beta_i^2(t)\psi_i(x)^2\right] dx \right\rangle \\ &= \frac{1}{2\pi}\left\langle \sum_{i=1}^{\infty}(\alpha_i^2(t)+\beta_i^2(t)) \right\rangle = \frac{1}{2\pi}\sum_{i=1}^{\infty}\left[\langle\alpha_i^2(t)\rangle + \langle\beta_i^2(t)\rangle\right]. \end{aligned} \tag{3.17}$$

Eq. (3.17) provides a direct link between the state covariance of the infinite stochastic

ODEs of Eq. (3.13) and the expected surface roughness of the sputtering process.

Remark 3.2 *The stochastic PDE model and the kMC model of the sputtering process are consistent. The stochastic PDE model for the sputtering processes can be derived based on the corresponding master equation, which describes the evolution of the probability that the surface is at a certain configuration (see, for example, [53, 90]). The kMC model is a first-principle model in the sense that the microscopic events that directly form the surface are explicitly considered in the model. Mathematically, kMC simulation methods provide an unbiased realization of the master equation. Therefore, the evolution of the surface configuration predicted by the closed-form stochastic PDE model is consistent to that predicted by the kMC model. As a result, a controller designed based on the stochastic PDE process model can be applied to the kMC model of the same process [61, 60, 71, 62]. However, the parameters of the stochastic KSE derived based on the corresponding master equation need to be carefully estimated. A continuum limit is used in the derivation of the stochastic KSE from the master equation, which requires an infinite number of lattice sites in the kMC model. From a practical point of view, a kMC model with a finite number of lattice sites is, however, used for the simulation of the sputtering process, thereby leading to a mismatch between the stochastic KSE and the kMC model. Therefore, it is necessary to estimate the parameters of the stochastic KSE based on the kMC data directly to ensure that the KSE model predictions are close to the ones of the kMC model.*

3.2.4 Model reduction

Owing to its infinite-dimensional nature, the system of Eq. (3.13) cannot be directly used as a basis for either parameter estimation or feedback controller design that can be implemented in practice (i.e., the practical implementation of such algorithms will require the computation of infinite sums which cannot be done by a computer). Instead, we will use finite-dimensional approximations of the system of Eq. (3.13).

Specifically, we rewrite the system of Eq. (3.13) as follows:

$$\begin{aligned} \frac{dx_{\mathrm{s}}}{dt} &= \Lambda_{\mathrm{s}} x_{\mathrm{s}} + \lambda f_{\mathrm{s}}(x_{\mathrm{s}}, x_{\mathrm{f}}) + \xi_{\mathrm{s}}, \\ \frac{dx_{\mathrm{f}}}{dt} &= \Lambda_{\mathrm{f}} x_{\mathrm{f}} + \lambda f_{\mathrm{f}}(x_{\mathrm{s}}, x_{\mathrm{f}}) + \xi_{\mathrm{f}}, \end{aligned} \tag{3.18}$$

where

$$\begin{aligned} x_{\mathrm{s}} &= [\alpha_1 \quad \dots \quad \alpha_m \quad \beta_1 \quad \dots \quad \beta_m]^T, \\ x_{\mathrm{f}} &= [\alpha_{m+1} \quad \beta_{m+1} \quad \alpha_{m+2} \quad \beta_{m+2} \quad \dots]^T, \\ \Lambda_{\mathrm{s}} &= \mathrm{diag}\,[\lambda_1 \quad \dots \quad \lambda_m \quad \lambda_1 \quad \dots \quad \lambda_m], \\ \Lambda_{\mathrm{f}} &= \mathrm{diag}\,[\lambda_{m+1} \quad \lambda_{m+1} \quad \lambda_{m+2} \quad \lambda_{m+2} \quad \dots], \\ f_{\mathrm{s}}(x_{\mathrm{s}}, x_{\mathrm{f}}) &= [f_{1\alpha}(x_{\mathrm{s}}, x_{\mathrm{f}}) \quad \dots \quad f_{m\alpha}(x_{\mathrm{s}}, x_{\mathrm{f}}) \quad f_{1\beta}(x_{\mathrm{s}}, x_{\mathrm{f}}) \quad \dots \quad f_{m\beta}(x_{\mathrm{s}}, x_{\mathrm{f}})]^T, \\ f_{\mathrm{f}}(x_{\mathrm{s}}, x_{\mathrm{f}}) &= \left[f_{(m+1)\alpha}(x_{\mathrm{s}}, x_{\mathrm{f}}) \quad f_{(m+1)\beta}(x_{\mathrm{s}}, x_{\mathrm{f}}) \quad f_{(m+2)\alpha}(x_{\mathrm{s}}, x_{\mathrm{f}}) \quad \dots\right]^T, \\ \xi_{\mathrm{s}} &= \left[\xi_\alpha^1 \quad \dots \quad \xi_\alpha^m \quad \xi_\beta^1 \quad \dots \quad \xi_\beta^m\right]^T, \\ \xi_{\mathrm{f}} &= \left[\xi_\alpha^{m+1} \quad \xi_\beta^{m+1} \quad \xi_\alpha^{m+2} \quad \xi_\beta^{m+2} \quad \dots\right]^T. \end{aligned} \tag{3.19}$$

The dimension of the x_s subsystem is $2m$ and the x_f subsystem is infinite-dimensional.

We note that the subsystem x_f in Eq. (3.18) is infinite-dimensional. Neglecting the x_f subsystem, the following $2m$-dimensional system is obtained:

$$\frac{d\tilde{x}_s}{dt} = \Lambda_s \tilde{x}_s + \lambda f_s(\tilde{x}_s, 0) + \xi_s \tag{3.20}$$

where the tilde symbol in $\tilde{x}_s$ denotes that this state variable is associated with a finite-dimensional system.

3.3 Parameter estimation of the nonlinear stochastic PDE model

While the parameters of stochastic PDE models for several deposition and sputtering processes can be derived based on the corresponding master equation, which describes the evolution of the probability that the surface is at a certain configuration; for all practical purposes, the stochastic PDE model parameters should be estimated by matching the prediction of the stochastic PDE model to that of kMC simulations due to the approximations made in the derivation of the stochastic PDE model from the master equation [36, 60].

In this section, we present a method to estimate the parameters of the nonlinear stochastic KSE model of the sputtering process by using data from the kMC simula-

tions of the process. The parameter estimation algorithm is developed on the basis of the finite dimensional system of Eq. (3.20).

3.3.1 System of deterministic ODEs for state covariance

The system of Eq. (3.20) is a finite-dimensional nonlinear stochastic ODE system including all four parameters, ν, κ, λ, and σ^2 of the stochastic KSE of Eq. (3.7). We first derive the system of deterministic ODEs that describes the dynamics of the covariance matrix of the state vector of Eq. (3.20), x_s, which is defined as $P_s = \langle x_s x_s^T \rangle$.

Consider the evolution of the state of Eq. (3.20) in a small time interval, $[t, t+\Delta t]$ as follows [47, 25]:

$$x_s(t+\Delta t) = (I_s + \Delta t \Lambda_s)\, x_s(t) + \Delta t \lambda f_s(x_s(t), 0) + \Delta t \xi_s(t) \tag{3.21}$$

where I_s is a $2m \times 2m$ identity matrix. To study the dynamics of P_s, we approximate the Dirac function, $\delta(\cdot)$ involved in the covariances of ξ_s by $\dfrac{1}{\Delta t}$, and neglect the terms of order Δt^2. When Eq. (3.21) is used to compute the numerical solution of $x_s(t)$, it is clear that $x_s(t)$ is only dependent on $\xi_s(\tau)$ (for $\tau \leq t - \Delta t$). Since $\xi_s(t)$ and $\xi_s(\tau)$ are mutually independent according to the definition of Gaussian noise of Eq. (3.10) and Result 1, $\xi_s(t)$ is also independent of $x_s(t)$. We, therefore, have $\langle \xi_s(t) x_s^T(t) \rangle = 0$ and $\langle x_s(t) \xi_s^T(t) \rangle = 0$. Consequently, the following equation for P_s can be obtained

from Eq. (3.21):

$$\begin{aligned} P_{\rm s}(t+\Delta t) = & \; P_{\rm s}(t) + \Delta t\{\Lambda_{\rm s} P_{\rm s}(t) + P_{\rm s}(t)\Lambda_{\rm s}^T\} \\ & + \Delta t\{\lambda \left\langle x_{\rm s}(t) f_{\rm s}(x_{\rm s}(t),0)^T + f_{\rm s}(x_{\rm s}(t),0) x_{\rm s}(t)^T \right\rangle + R_{\rm s}\} \end{aligned} \tag{3.22}$$

where $R_{\rm s}$ is the intensity of $\xi_{\rm s}$ and $R_{\rm s}\delta(t-t') = \langle \xi_{\rm s}(t)\xi_{\rm s}^T(t)\rangle$. In this chapter, $R_{\rm s} = \sigma^2 I_{2m\times 2m}$.

By bringing $P_{\rm s}(t)$ to the left hand side of Eq. (3.22), dividing both sides by Δt and setting $\Delta t \to 0$, we obtain the following nonlinear system of deterministic ODEs for the state covariance of the system of Eq. (3.18):

$$\frac{dP_{\rm s}(t)}{dt} = \Lambda_{\rm s} P_{\rm s}(t) + P_{\rm s}(t)\Lambda_{\rm s}^T + R_{\rm s} + \lambda \left\langle x_{\rm s}(t) f_{\rm s}(x_{\rm s}(t),0)^T + f_{\rm s}(x_{\rm s}(t),0) x_{\rm s}(t)^T \right\rangle . \tag{3.23}$$

Note that the linear part of Eq. (3.23) is the Lyapunov equation used in covariance controller design for linear systems [37]. We will use this deterministic ODE system as the basis for parameter estimation.

3.3.2 Parameter estimation

The four parameters of the stochastic PDE process model of Eq. (3.7) can be estimated from Eq. (3.23). Specifically, the parameters ν and κ are included in the matrix $\Lambda_{\rm s}$ of Eq. (3.23) and the parameter λ is associated with the nonlinear term of Eq. (3.23). To this end, we need to obtain $P_{\rm s}(t)$ and $\left\langle x_{\rm s}(t) f_{\rm s}(t)^T + f_{\rm s}(t) x_{\rm s}(t)^T \right\rangle$,

which are both functions of x_{s}, to perform the parameter estimation.

The data of $x_{\mathrm{s}} = [\alpha_1(t) \ \dots \ \alpha_m(t) \ \beta_1(t) \ \dots \ \beta_m(t)]^T$ can be obtained from kMC simulations of the sputtering process. Once x_{s} is obtained, $f_{\mathrm{s}}(x_{\mathrm{s}}, 0) = [f_{1\alpha}(x_{\mathrm{s}}, 0) \ \dots \ f_{m\alpha}(x_{\mathrm{s}}, 0) \ f_{1\beta}(x_{\mathrm{s}}, 0) \ \dots \ f_{m\beta}(x_{\mathrm{s}}, 0)]^T$ can be computed as follows:

$$
\begin{aligned}
f_{n\alpha}(x_{\mathrm{s}}(t), 0) &= \frac{1}{2}\int_{-\pi}^{\pi} \phi_n^*(x) \left(\sum_{j=1}^{m} \alpha_j(t) \frac{d\phi_j}{dx}(x) + \sum_{j=0}^{m} \beta_j(t) \frac{d\psi_j}{dx}(x) \right)^2 dx, \\
f_{n\beta}(x_{\mathrm{s}}(t), 0) &= \frac{1}{2}\int_{-\pi}^{\pi} \psi_n^*(x) \left(\sum_{j=1}^{m} \alpha_j(t) \frac{d\phi_j}{dx}(x) + \sum_{j=0}^{m} \beta_j(t) \frac{d\psi_j}{dx}(x) \right)^2 dx, \\
& n = 1, 2, \dots, m.
\end{aligned} \tag{3.24}
$$

To compute the expected values for $x_{\mathrm{s}}(t)x_{\mathrm{s}}(t)^T$ and $x_{\mathrm{s}}(t)f_{\mathrm{s}}(x_{\mathrm{s}}, 0)^T + f_{\mathrm{s}}(x_{\mathrm{s}}, 0)x_{\mathrm{s}}(t)$, multiple kMC simulation runs for the sputtering process should be performed and the profiles of $x_{\mathrm{s}}(t)x_{\mathrm{s}}(t)^T$ and $x_{\mathrm{s}}(t)f_{\mathrm{s}}(x_{\mathrm{s}}, 0)^T + f_{\mathrm{s}}(x_{\mathrm{s}}, 0)x_{\mathrm{s}}(t)$ should be averaged to obtain the expected values.

The time derivative of $P_{\mathrm{s}}(t)$ can be computed by the first-order approximation ($O(\Delta t)$) of the time derivative as follows:

$$
\frac{dP_{\mathrm{s}}(t)}{dt} = \frac{P_{\mathrm{s}}(t + \Delta t) - P_{\mathrm{s}}(t)}{\Delta t} \tag{3.25}
$$

where Δt is a small time interval.

When the values of $dP_{\mathrm{s}}(t)/dt$, $P_{\mathrm{s}}(t)$ and $\langle x_{\mathrm{s}}(t)f_{\mathrm{s}}(x_{\mathrm{s}}, 0)^T + f_{\mathrm{s}}(x_{\mathrm{s}}, 0)x_{\mathrm{s}}(t)^T \rangle$ are obtained through kMC simulation runs at a set of discrete time instants ($t = t_1, t_2, \dots, t_k$),

Eq. (3.23) becomes a system of linear algebraic equations for the four unknown model parameters. When the number of equations is larger than the number of parameters to be estimated, the least-squares method can be used to determine the model parameters.

Since P_s is a diagonally dominant matrix (see simulation part for a numerical verification), to make the parameter estimation algorithm insensitive to round-off errors, we propose to formulate the system of algebraic equations for least-squares fitting of the model parameters by using only the diagonal elements of the system of Eq. (3.23). The system of ODEs corresponding to the diagonal elements of Eq. (3.23) is as follows:

$$\begin{aligned}\frac{d\langle \alpha_n^2(t)\rangle}{dt} &= 2(\nu n^2 - \kappa n^4)\langle \alpha_n^2(t)\rangle + 2\lambda\langle \alpha_n(t) f_{n\alpha}(t)\rangle + \sigma^2, \quad n = 1, \ldots, m, \\ \frac{d\langle \beta_n^2(t)\rangle}{dt} &= 2(\nu n^2 - \kappa n^4)\langle \beta_n^2(t)\rangle + 2\lambda\langle \beta_n(t) f_{n\beta}(t)\rangle + \sigma^2, \quad n = 1, \ldots, m.\end{aligned} \tag{3.26}$$

The system of Eq. (3.26) is a linear system with respect to ν, κ, λ and σ^2 and it is straightforward to reformulate Eq. (3.26) in the form of the following linear system to estimate ν, κ, λ and σ^2 using the least-squares method:

$$b = A\theta \tag{3.27}$$

where $\theta = [\nu \quad \kappa \quad \lambda \quad \sigma^2]^T$,

$$A = \begin{bmatrix} 1^2 \times 2\langle\alpha_1^2(t_1)\rangle & 1^4 \times 2\langle\alpha_1^2(t_1)\rangle & 2\langle\alpha_1(t_1) f_{1\alpha}(t_1)\rangle & 1 \\ \vdots & \vdots & \vdots & \vdots \\ m^2 \times 2\langle\alpha_m^2(t_1)\rangle & m^4 \times 2\langle\alpha_m^2(t_1)\rangle & 2\langle\alpha_m(t_1) f_{m\alpha}(t_1)\rangle & 1 \\ 1^2 \times 2\langle\beta_1^2(t_1)\rangle & 1^4 \times 2\langle\beta_1^2(t_1)\rangle & 2\langle\beta_1(t_1) f_{1\beta}(t_1)\rangle & 1 \\ \vdots & \vdots & \vdots & \vdots \\ m^2 \times 2\langle\beta_m^2(t_1)\rangle & m^4 \times 2\langle\beta_m^2(t_1)\rangle & 2\langle\beta_m(t_1) f_{m\beta}(t_1)\rangle & 1 \\ \vdots & \vdots & \vdots & \vdots \\ 1^2 \times 2\langle\alpha_1^2(t_k)\rangle & 1^4 \times 2\langle\alpha_1^2(t_k)\rangle & 2\langle\alpha_1(t_k) f_{1\alpha}(t_k)\rangle & 1 \\ \vdots & \vdots & \vdots & \vdots \\ m^2 \times 2\langle\alpha_m^2(t_k)\rangle & m^4 \times 2\langle\alpha_m^2(t_k)\rangle & 2\langle\alpha_m(t_k) f_{m\alpha}(t_k)\rangle & 1 \\ 1^2 \times 2\langle\beta_1^2(t_k)\rangle & 1^4 \times 2\langle\beta_1^2(t_k)\rangle & 2\langle\beta_1(t_k) f_{1\beta}(t_k)\rangle & 1 \\ \vdots & \vdots & \vdots & \vdots \\ m^2 \times 2\langle\beta_m^2(t_k)\rangle & m^4 \times 2\langle\beta_m^2(t_k)\rangle & 2\langle\beta_m(t_k) f_{m\beta}(t_k)\rangle & 1 \end{bmatrix}, \tag{3.28}$$

and

$$b = \begin{bmatrix} b_1^T & b_2^T & \dots & b_k^T \end{bmatrix}^T \tag{3.29}$$

where

$$b_i = \left[\frac{d\langle\alpha_1^2(t_i)\rangle}{dt} \quad \dots \quad \frac{d\langle\alpha_m^2(t_i)\rangle}{dt} \quad \frac{d\langle\beta_1^2(t_i)\rangle}{dt} \quad \dots \quad \frac{d\langle\beta_m^2(t_i)\rangle}{dt} \right]^T, \quad i = 1, 2, \dots, k. \tag{3.30}$$

Note that all elements in b and A can be obtained through the kMC simulations of the thin film growth or sputtering process. The least-squares fitting of the model parameters can be obtained as follows:

$$\hat{\theta} = (A^T A)^{-1} A^T b. \tag{3.31}$$

Remark 3.3 *Different values of m are used in parameter estimation and controller design. For parameter estimation, the value of m should be large enough so that the finite-dimensional system of Eq. (3.27) includes all representative modes of the system. While for controller design, the value of m depends on the process and the requirement on the closed-loop performance. Specifically, m should be equal or larger than the number of unstable modes of the process to ensure closed-loop stability. Furthermore, according to Theorem 1 in [62], m should be large enough to have a sufficiently small ϵ so that the closed-loop surface roughness of the infinite-dimensional system is sufficiently close to the set-point value. However, a very large m should be avoided, since it requires a large number of actuators which may not be practical from a practical implementation point of view..*

Remark 3.4 *Note that it is important to appropriately collect the data set of surface snapshots from kMC simulations for parameter estimation. The data set should be representative so that the dynamics of the stochastic process can be adequately captured by the data set and reliable parameter estimation results can be obtained. Specifically,*

the condition number of the square matrix $A^T A$ *of Eq. (3.31) should be used as an indicator of the quality of the data set. The matrix* A *is constructed by using the data derived from the surface snapshots. The condition number measures the sensitivity of the solution to the perturbations in* A *and* b*. There is stochastic noise contained in the data used to construct the matrix* A *and the vector* b *in Eq. (3.31). This noise will perturb* A *and* b *from their true values. A low condition number of the square matrix* $A^T A$ *will ensure that the perturbations in* A *and* b *introduced by the noise will not result in significant errors in the estimated model parameters. According to the simulations, a low condition number between* 10 *to* 20 *can be achieved by appropriately selecting snapshots while a large condition number could be over* 1000*. Another good and practical criterion for a given situation is to compare the profiles of the expected surface roughness of the process and the stochastic PDE with estimated parameters. If they are matched consistently, the condition number of* $A^T A$ *is considered as a low number for that particular problem. The sampling time and the number of surface snapshots should be carefully selected so that the condition number of the square matrix* $A^T A$ *is small. Another effective way to decrease the condition number is to acquire as many representative surface snapshots of the process as possible, e. g., with different initial conditions.*

Remark 3.5 *Note that this chapter does not intent to develop a new model for the sputtering process and validate the model against experimental data from a process. Instead, the focus of this chapter is to estimate the parameters of a stochastic PDE*

model and compare the model output against that from a kMC model, which is considered as a more accurate process model. Therefore, if the kMC model for the sputtering process can capture the roughness evolution of a real process, our method results in a closed-form stochastic PDE model that possesses a very similar modeling capability. There is a large body of literature available for kMC simulations of various sputtering and thin film growth processes. This work can be readily extended to a variety of real world processes to construct stochastic PDE process models provided that an accurate kMC model is available for the process of interest.

3.4 Feedback control of surface roughness

In this section, we design a linear output feedback controller based on the stochastic KSE process model to regulate the expected surface roughness of the sputtering process to a desired level. A state feedback controller is initially designed by following the method developed in [60]. Then, a static state estimation scheme is constructed and the output feedback controller design is completed by combining the state feedback control law and the state estimation scheme.

3.4.1 Distributed control problem formulation

We consider the stochastic KSE with distributed control in the spatial domain $[-\pi, \pi]$:

$$\frac{\partial h}{\partial t} = -\nu \frac{\partial^2 h}{\partial x^2} - \kappa \frac{\partial^4 h}{\partial x^4} + \frac{\lambda}{2} \left(\frac{\partial h}{\partial x} \right)^2 + \sum_{i=1}^{p} b_i(x) u_i(t) + \xi(x,t) \tag{3.32}$$

subject to PBCs:

$$\frac{\partial^j h}{\partial x^j}(-\pi, t) = \frac{\partial^j h}{\partial x^j}(\pi, t), \quad j = 0, 1, 2, 3, \tag{3.33}$$

and the initial condition:

$$h(x, 0) = h_0(x) \tag{3.34}$$

where u_i is the ith manipulated input, p is the number of manipulated inputs and b_i is the ith actuator distribution function (i.e., b_i determines how the control action computed by the ith control actuator, u_i, is distributed (e.g., point or distributed actuation) in the spatial interval $[-\pi, \pi]$). The variables are defined in the same way as in Eq. (3.7) of Section 3.2.3. Following similar derivations to the ones of Section 3.2.3, the following system of infinite nonlinear stochastic ODEs with distributed control can be obtained:

$$\begin{aligned} \frac{d\alpha_n}{dt} &= (\nu n^2 - \kappa n^4)\alpha_n + \lambda f_{n\alpha} + \sum_{i=1}^{p} b_{i\alpha_n} u_i(t) + \xi_\alpha^n(t), \quad n = 1, \ldots, \infty, \\ \frac{d\beta_n}{dt} &= (\nu n^2 - \kappa n^4)\beta_n + \lambda f_{n\beta} + \sum_{i=1}^{p} b_{i\beta_n} u_i(t) + \xi_\beta^n(t), \quad n = 1, \ldots, \infty, \end{aligned} \tag{3.35}$$

where $f_{n\alpha}$ and $f_{n\beta}$ are defined in Eq. (3.14) and $\xi_\alpha^n(t)$ and $\xi_\beta^n(t)$ are defined in Eq. (3.15). $b_{i\alpha_n}$ and $b_{i\beta_n}$ are defined as follows:

$$
\begin{aligned}
b_{i\alpha_n} &= \int_{-\pi}^{\pi} \phi_n^*(x) b_i(x) dx, \\
b_{i\beta_n} &= \int_{-\pi}^{\pi} \psi_n^*(x) b_i(x) dx.
\end{aligned}
\tag{3.36}
$$

The system of Eq. (3.35) can be rewritten in the following form:

$$
\begin{aligned}
\frac{dx_\mathrm{s}}{dt} &= \Lambda_\mathrm{s} x_\mathrm{s} + f_\mathrm{s}(x_\mathrm{s}, x_\mathrm{f}) + B_\mathrm{s} u + \xi_\mathrm{s}, \\
\frac{dx_\mathrm{f}}{dt} &= \Lambda_\mathrm{f} x_\mathrm{f} + f_\mathrm{f}(x_\mathrm{s}, x_\mathrm{f}) + B_\mathrm{f} u + \xi_\mathrm{f},
\end{aligned}
\tag{3.37}
$$

where x_s, x_f, Λ_s, Λ_f, $f_\mathrm{s}(x_\mathrm{s}, x_\mathrm{f})$, $f_\mathrm{f}(x_\mathrm{s}, x_\mathrm{f})$, ξ_s and ξ_f are defined in Eq. (3.19), and

$$
B_\mathrm{s} = \begin{bmatrix}
b_{1\alpha_1} & \dots & b_{p\alpha_1} \\
\vdots & \ddots & \vdots \\
b_{1\alpha_m} & \dots & b_{p\alpha_m} \\
b_{1\beta_1} & \dots & b_{p\beta_1} \\
\vdots & \ddots & \vdots \\
b_{1\beta_m} & \dots & b_{p\beta_m}
\end{bmatrix}, \quad
B_\mathrm{f} = \begin{bmatrix}
b_{1\alpha_{m+1}} & \dots & b_{p\alpha_{m+1}} \\
b_{1\beta_{m+1}} & \dots & b_{p\beta_{m+1}} \\
b_{1\alpha_{m+2}} & \dots & b_{p\alpha_{m+2}} \\
b_{1\beta_{m+2}} & \dots & b_{p\beta_{m+2}} \\
\vdots & \vdots & \vdots
\end{bmatrix}.
\tag{3.38}
$$

Note that the dimension of the x_s subsystem is $2m$ and the x_f subsystem is infinite-dimensional. Neglecting the x_f subsystem, the following $2m$-dimensional system is

obtained:

$$\frac{d\tilde{x}_{\mathrm{s}}}{dt} = \Lambda_{\mathrm{s}}\tilde{x}_{\mathrm{s}} + \lambda f_{\mathrm{s}}(\tilde{x}_{\mathrm{s}}, 0) + B_{\mathrm{s}}u + \xi_{\mathrm{s}} \tag{3.39}$$

where the tilde symbol in $\tilde{x}_{\mathrm{s}}$ denotes that this state variable is associated with a finite-dimensional system.

We note here that the accuracy of the finite-dimensional system can be improved by including a finite-number of the x_{f} modes using the concept of approximate inertial manifolds [23, 6].

Remark 3.6 *Note that in practice, the control action, u_i, can be implemented by manipulating the gas composition across the surface in either a deposition process or a sputtering process. Spatially controllable CVD reactors have been developed to enable across-wafer spatial control of surface gas composition during deposition [18]. In such a control problem formulation, the rate that particles land on the surface or the rate that surface particles are eroded is spatially distributed and is computed by the controller. The parameters of the stochastic KSE model of Eq. (3.32) depend on both the temperature and the rate that particles land on the surface or that surface particles are eroded [53]. In this chapter, the temperature is assumed to be a constant. The rate that particles land on the surface or the rate that surface particles are eroded used to compute the stochastic KSE model parameters corresponds to that under open-loop operation, and thus, it is also a constant. The contribution of the spatially distributed rate that particles land on the surface or the rate that surface particles are eroded to*

the fluctuations of the surface height profile (e.g., the surface roughness) is captured by the term $\sum_{i=1}^{p} b_i(x)u_i(t)$. *This control problem formulation is further supported by our simulation results which demonstrate that the controller designed on the basis of the stochastic KSE model of a sputtering process can be successfully applied to the kMC model of the same sputtering process to control the surface roughness to desired levels (see simulation results in Section 3.5).*

3.4.2 State feedback control

Following the method presented in [60], we design a linear state feedback controller on the basis of the linearization of Eq. (3.39) around its zero solution. To simplify our development, we assume that $p = 2m$ (i.e., the number of control actuators is equal to the dimension of the finite-dimensional system) and pick the actuator distribution functions such that $B_{\rm s}^{-1}$ exists. The linear state feedback control law then takes the form:

$$u = B_{\rm s}^{-1}(\Lambda_{\rm cs} - \Lambda_{\rm s})\tilde{x}_{\rm s} \tag{3.40}$$

where the matrix $\Lambda_{\rm cs}$ contains the desired poles of the closed-loop system; $\Lambda_{\rm cs} = \mathrm{diag}[\lambda_{{\rm c}\alpha 1} \ \ldots \ \lambda_{{\rm c}\alpha m} \ \lambda_{{\rm c}\beta 1} \ \ldots \ \lambda_{{\rm c}\beta m}]$, $\lambda_{{\rm c}\alpha i}$ and $\lambda_{{\rm c}\beta i}$ $(1 \le i \le m)$ are desired poles of the closed-loop finite-dimensional system, which satisfy $Re\{\lambda_{{\rm c}\alpha i}\} < 0$ and $Re\{\lambda_{{\rm c}\beta i}\} < 0$ for $(1 \le i \le m)$ and can be determined from the desired closed-loop surface roughness level.

3.4.3 Output feedback control

The state feedback controller of Eq. (3.40) was derived under the assumption that measurements of the states $\tilde{x}_s$ are available, which implies that measurements of the surface height profile, $h(x,t)$, are available at all positions and time. However, from a practical point of view, measurements of the surface height profile are only available at a finite number of spatial positions. Motivated by this practical consideration, we address in this section the synthesis of an output feedback controller that uses measurements of the thin film surface height at distinct locations to enforce a desired surface roughness in the closed-loop kMC simulation model. The measured surface height profile can be expressed as follows:

$$y(t) = [h(x_1,t) \quad h(x_2,t) \quad \dots \quad h(x_q,t)]^T \tag{3.41}$$

where x_i $(i = 1, 2, \dots, q)$ denotes a location of a point measurement sensor and q is the number of measurement sensors. Since the height profile $h(x,t)$ can be expanded into an infinite series as shown in Eq. (3.12), the vector of output measurements of Eq. (3.41) can be written in terms of the state of the infinite-dimensional system, x_s

and x_{f}, as follows:

$$y(t) = \begin{bmatrix} \sum_{n=1}^{\infty} \alpha_n(t)\phi_n(x_1) + \sum_{n=1}^{\infty} \beta_n(t)\psi_n(x_1) + \beta_0(t)\psi_0 \\ \sum_{n=1}^{\infty} \alpha_n(t)\phi_n(x_2) + \sum_{n=1}^{\infty} \beta_n(t)\psi_n(x_2) + \beta_0(t)\psi_0 \\ \vdots \\ \sum_{n=1}^{\infty} \alpha_n(t)\phi_n(x_q) + \sum_{n=1}^{\infty} \beta_n(t)\psi_n(x_q) + \beta_0(t)\psi_0 \end{bmatrix} \tag{3.42}$$

$$= C_{\mathrm{s}} \begin{bmatrix} \beta_0(t) \\ x_{\mathrm{s}}(t) \end{bmatrix} + C_{\mathrm{f}} x_{\mathrm{f}}(t)$$

where

$$C_{\mathrm{s}}(t) = \begin{bmatrix} \psi_0 & \phi_1(x_1) & \phi_2(x_1) & \dots & \phi_m(x_1) & \psi_1(x_1) & \psi_2(x_1) & \dots & \psi_m(x_1) \\ \psi_0 & \phi_1(x_2) & \phi_2(x_2) & \dots & \phi_m(x_2) & \psi_1(x_2) & \psi_2(x_2) & \dots & \psi_m(x_2) \\ \vdots & \vdots & \vdots & \ddots & \vdots & \vdots & \vdots & \ddots & \vdots \\ \psi_0 & \phi_1(x_q) & \phi_2(x_q) & \dots & \phi_m(x_q) & \psi_1(x_q) & \psi_2(x_q) & \dots & \psi_m(x_q) \end{bmatrix} \tag{3.43}$$

and

$$C_{\mathrm{f}}(t) = \begin{bmatrix} \phi_{m+1}(x_1) & \psi_{m+1}(x_1) & \phi_{m+2}(x_1) & \psi_{m+2}(x_1) & \dots \\ \phi_{m+1}(x_2) & \psi_{m+1}(x_2) & \phi_{m+2}(x_2) & \psi_{m+2}(x_2) & \dots \\ \vdots & \vdots & \ddots & & \\ \phi_{m+1}(x_q) & \psi_{m+1}(x_q) & \phi_{m+2}(x_q) & \psi_{m+2}(x_q) & \dots \end{bmatrix}. \tag{3.44}$$

Neglecting the $x_{\rm f}$ component in the system of Eq. (3.37) and Eq. (3.42) and linearizing the resulting finite-dimensional system around its zero solution, the following linearized finite-dimensional system is obtained:

$$\begin{aligned} \frac{d\tilde{x}_{\rm s}}{dt} &= \Lambda_{\rm s}\tilde{x}_{\rm s} + B_{\rm s}u + \xi_{\rm s}, \\ \tilde{y} &= C_{\rm s}\begin{bmatrix} \tilde{\beta}_0(t) \\ \tilde{x}_{\rm s}(t) \end{bmatrix}. \end{aligned} \tag{3.45}$$

The system of Eq. (3.45) is used for the static output feedback control design. The general form of the output feedback control laws is as follows:

$$u = \mathcal{F}(y) \tag{3.46}$$

where $\mathcal{F}(y)$ is a vector function and y is the vector of measured outputs. The synthesis of the controller of Eq. (3.46) will be achieved by combining the state feedback controller of Eq. (3.40) with a procedure proposed in [22] for obtaining estimates for the states of the approximate ODE model of Eq. (3.45) from the measurements. To this end, we need to impose the following requirement on the number of measurements in order to obtain estimates of the states $x_{\rm s}$ of the finite-dimensional system of Eq. (3.39) from the measurements y.

Assumption 3.1 *$q = 2m+1$, and the inverse of $C_{\rm s}$ exists, so that $[\hat{\beta}_0 \ \hat{x}_{\rm s}^T]^T = C_{\rm s}^{-1}y$.*

We note that the requirement that the inverse of $C_{\rm s}$ exists can be achieved by

appropriate choice of the location of the measurement sensors. When point measurement sensors are used, this requirement can be verified by checking the invertibility of the matrix.

The output feedback control law of Eq. (3.46) is designed on the basis of Eq. (3.45) as follows:

$$u = \mathcal{F}(y) = B_{\rm s}^{-1}(\Lambda_{\rm cs} - \Lambda_{\rm s})\,[\mathbf{0} \quad I_{\rm s}]\,C_{\rm s}^{-1} y \tag{3.47}$$

where $[\mathbf{0} \quad I_{\rm s}]$ is used to extract estimated states $x_{\rm s}$ from $\begin{bmatrix} \hat{\beta}_0(t) \\ \hat{x}_{\rm s}(t) \end{bmatrix}$, $\mathbf{0}$ is a $2m \times 2m$ zero matrix and $I_{\rm s}$ is a $2m \times 2m$ elementary matrix.

Remark 3.7 *Note that although the stochastic KSE model of Eq. (3.7) for which we computed the parameters is a nonlinear model for the sputtering process, the state feedback controller of Eq. (3.40) and the output feedback controller of Eq. (3.47) are linear controllers that are designed based on a linearization of the stochastic KSE around its zero solution. Our decision to identify the nonlinear stochastic KSE model of the sputtering process but design the output feedback controller based on a linearized process model is made based on two considerations. First, from a modeling point of view, the sputtering process is a nonlinear process and a linear model is not sufficient to represent the time evolution of the surface height profile. Specifically, due to the existence of unstable eigenvalues of the linear operator of Eq. (3.11), the expected surface roughness predicted by a linear stochastic PDE model will go to infinity as* $t \rightarrow \infty$*, which is not true for the sputtering process due to the un-modeled nonlinearities*

of the process. Therefore, it is important to model the sputtering process using a nonlinear stochastic PDE model to appropriately capture the process dynamics. On the other hand, since the instability of the spatially uniform steady state comes from the linear part of the model, and the nonlinear part of the stochastic KSE helps bound the surface roughness, for control purposes, we only need to focus on the stabilization of the linear part of the stochastic KSE. This argument can be further supported by our simulation results, which demonstrate the effectiveness of the linear output feedback controller designed in this chapter.

Remark 3.8 *We note that a full-scale model of a sputtering process would consist of a two-dimensional lattice representation of the surface. Although we developed the method for output feedback control design based on a one-dimensional lattice representation of the surface, it is possible to extend the proposed method to control the surface roughness of material preparation processes taking place in two-dimensional domains. In a two-dimensional in space process, the feedback control design will be based on a two-dimensional extension of the model of Eq. (3.37). Moreover, Eq. (3.37) will be obtained by solving the eigenvalue/eigenfunction problem in the two-dimensional spatial domain subject to appropriate boundary conditions; this can be achieved in a similar way to that followed for the one-dimensional spatial domain (see the work by Ni and Christofides [71] for results on the solution of the eigenvalue/eigenfunction problem for a two-dimensional spatial domain). Once the modal representation of Eq. (3.37) corresponding to the two-dimensional stochastic PDE model is obtained,*

the method proposed in this chapter for controller design can be applied to control the surface roughness.

3.5 Numerical simulations

In this section, we present applications of the proposed model parameter estimation method and both of the state feedback and output feedback controllers to the kMC model of a sputtering process to demonstrate the effectiveness of the algorithms. Specifically, the model parameters of the stochastic KSE process model are first estimated by using data of surface snapshots obtained form kMC simulations. The identified KSE model is linearized and is consequently used as a basis for both state feedback control and output feedback control design. The controllers designed based on the stochastic KSE model are applied to the kMC model of the sputtering process to reduce the expected surface roughness to desired levels.

In all simulations, we consider a sputtering process that takes place on a lattice containing 200 sites. Therefore, $a = 0.0314$. The sputtering yield function, $Y(\phi_i)$ is a nonlinear function of ϕ_i, which takes the form of Eq. (3.1). y_0, y_1 and y_2 are chosen such that $Y(0) = 0.5$, $Y(\pi/2) = 0$ and $Y(1) = 1$ [26].

3.5.1 Model parameter estimation

We first compute the profiles of the state covariance and the expected values for $\alpha_n f_{n\alpha}$ and $\beta_n f_{n\beta}$ from kMC simulations of the sputtering process. Upon the execution of an event, the state of the stochastic KSE model (α_n or β_n) is updated. If the executed event is erosion, α_n or β_n can be updated as follows [60, 62]:

$$\begin{aligned} \alpha_n^{\text{new}} &= \alpha_n^{\text{old}} + \frac{a\left[\psi(n, z_i - a/2) - \psi(n, z_i + a/2)\right]}{n}, \\ \beta_n^{\text{new}} &= \beta_n^{\text{old}} + \frac{a\left[\phi(n, z_i + a/2) - \phi(n, z_i - a/2)\right]}{n}. \end{aligned} \tag{3.48}$$

If the executed event is diffusion from site i to site j, α_n or β_n are updated as follows:

$$\begin{aligned} \alpha_n^{\text{new}} = & \ \alpha_n^{\text{old}} + \frac{a\left[\psi(n, z_i - a/2) - \psi(n, z_i + a/2)\right]}{n} \\ & - \frac{a\left[\psi(n, z_j - a/2) - \psi(n, z_j + a/2)\right]}{n}, \\ \beta_n^{\text{new}} = & \ \beta_n^{\text{old}} + \frac{a\left[\phi(n, z_i + a/2) - \phi(n, z_i - a/2)\right]}{n} \\ & - \frac{a\left[\phi(n, z_j + a/2) - \phi(n, z_j - a/2)\right]}{n}, \end{aligned} \tag{3.49}$$

where a is the lattice parameter and z_i is the coordinate of the center of site i.

The terms $\alpha_n f_{n\alpha}$ and $\beta_n f_{n\beta}$ are computed by using Eq. (3.24) with $m = 10$ for $n = 1, 2, \ldots, 10$. The expected profiles are the averages of profiles obtained from 10000 independent kMC simulation runs. The covariance profiles of α_1, α_3, α_5, α_7, and α_9 are shown in Figure 3.2 and the profiles for the expected values of $\alpha_1 f_{1\alpha}$, $\alpha_3 f_{3\alpha}$, $\alpha_5 f_{5\alpha}$, $\alpha_7 f_{7\alpha}$, and $\alpha_9 f_{9\alpha}$ are shown in Figure 3.3. Similar profiles are observed

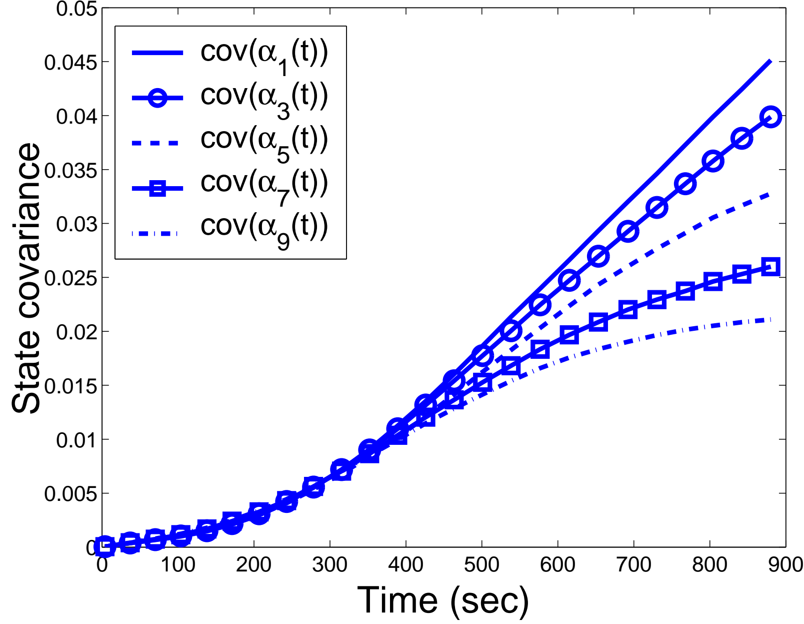

Figure 3.2: Profiles of the state covariance $\langle \alpha_n^2(t) \rangle$ for $n = 1$, 3, 5, 7, and 9.

for the covariance of β_n and $\beta_n f_{n\beta}$, and are omitted here for brevity.

Since we use $m = 10$, the first $2m = 20$ modes are used for parameter estimation. The three-dimensional profile of the covariance matrix for the first 20 states at the end of a simulation run is plotted in Figure 3.4. It is clear that the covariance matrix is diagonally dominant. Therefore, it is appropriate to use just the diagonal elements of the system of Eq. (3.23) for parameter estimation so that the estimation algorithm is insensitive to round-off errors. To formulate the least-squares fitting problem, $d\langle \alpha_n^2(t) \rangle/dt$, $d\langle \beta_n^2(t) \rangle/dt$, $\langle \alpha_n^2(t) \rangle$, $\langle \beta_n^2(t) \rangle$, $\langle \alpha_n(t) f_{n\alpha}(t) \rangle$, and $\langle \beta_n(t) f_{n\beta}(t) \rangle$ are evaluated at the first 150 available discrete time instants in the data obtained from kMC simulations. Therefore, in the least-squares fitting formulations of Eqs. (3.27) and (3.31), A is a 3000×4 matrix, b is a 3000×1 vector and $\theta = [\nu \ \kappa \ \lambda \ \sigma^2]^T$. The

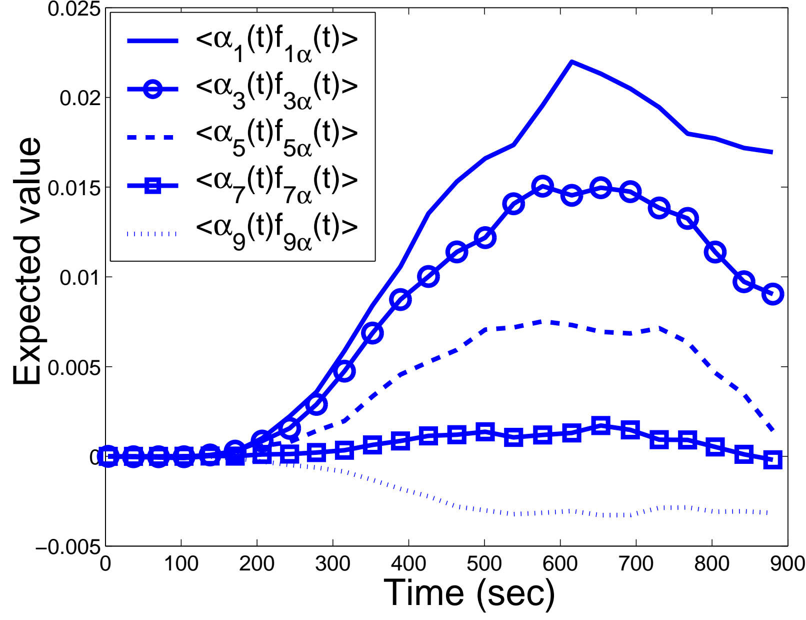

Figure 3.3: Profiles of the expected value for $\alpha_n f_{n\alpha}(t)$ for $n = 1$, 3, 5, 7, and 9.

values of the four parameters obtained from least-squares fitting are $\nu = 2.76 \times 10^{-5}$, $\kappa = 1.54 \times 10^{-7}$, $\lambda = 3.06 \times 10^{-3}$, and $\sigma^2 = 1.78 \times 10^{-5}$.

To validate the parameter estimation method, we first compute the expected open-loop surface roughness from the stochastic KSE model of Eq. (3.7) with the computed parameters. Then, the profile from the stochastic KSE with computed parameters is compared to that from the kMC model. The expected surface roughness is computed from the simulations of the stochastic KSE and the kMC model by averaging surface roughness profiles obtained from 100 and 10000 independent runs, respectively. The simulation result is shown in Figure 3.5. It is clear that the computed model parameters result in consistent expected surface roughness profiles from the stochastic KSE model of Eq. (3.7) and from the kMC simulator of the sputtering process. There

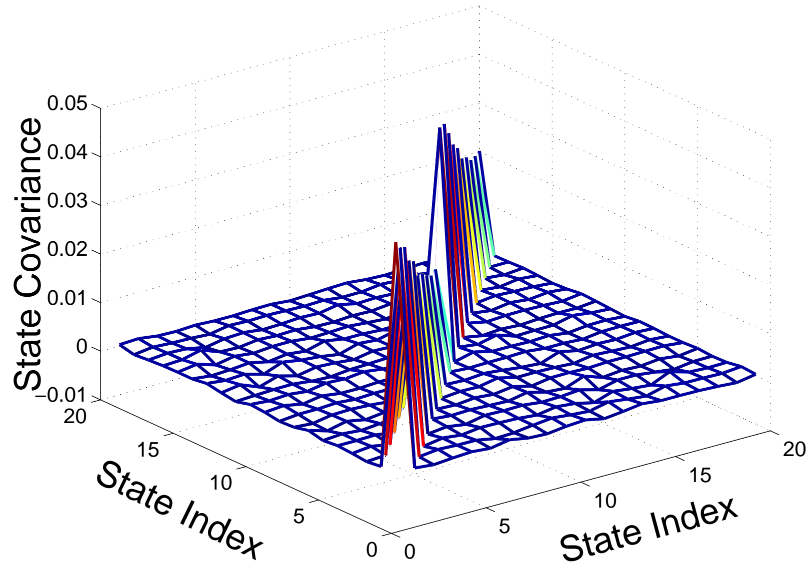

Figure 3.4: The covariance matrix for the first 20 states: a diagonally dominant matrix.

is observable difference between the two profiles, which indicates the existence of a slight mismatch of the identified model with the kMC model of the sputtering process. The mismatch between the profiles originates from the fact that the KSE model is derived from the master equation of the sputtering process with an assumption of infinitesimal lattice size, while in the kMC simulation a 200-lattice (finite-numbered) model is used.

3.5.2 Closed-loop simulation under state feedback control

We design a state feedback controller for the sputtering process based on the $2m$ order approximation of the stochastic ODE and apply the controller to the kMC model of the sputtering process to control the surface roughness to the desired level.

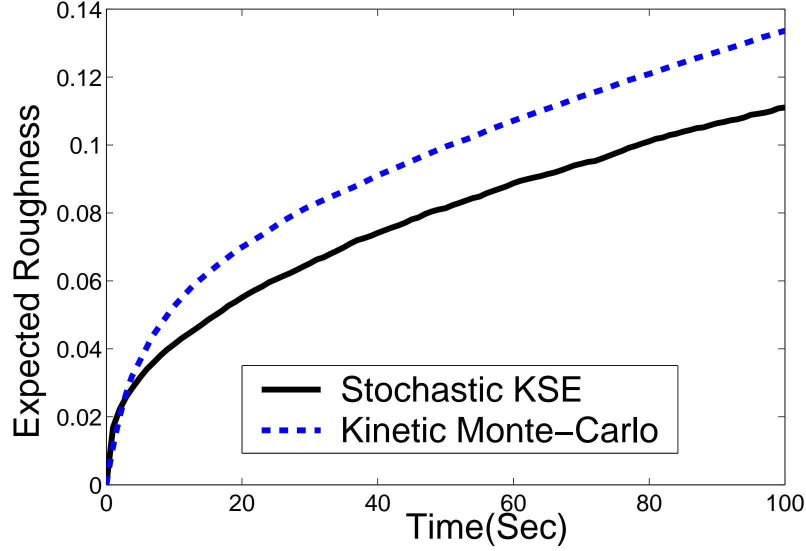

Figure 3.5: Comparison of the open-loop profile of the expected surface roughness of the sputtering process from the kMC simulator and that from the solution of the stochastic KSE using the estimated parameters.

The state feedback controller is designed using the computed KSE model parameters and $\Lambda_{\rm cs} = {\rm diag}[-0.01\ -0.01\ \ldots\ -0.01]$. $2m$ control actuators are used to control the system. The ith actuator distribution function is taken to be:

$$b_i(z) \quad = \quad \begin{cases} \dfrac{1}{\sqrt{\pi}}\sin(iz), & i = 1, \ldots, m, \\ \dfrac{1}{\sqrt{\pi}}\cos[(i-m)z], & i = m+1, \ldots, 2m. \end{cases} \tag{3.50}$$

The controller is implemented by manipulating the probability that a randomly selected site is subject to the erosion rule, f. From a practical point of view, a spatially distributed erosion probability can be realized by varying the gas composition across the substrate. Specifically, the bombardment rate of each surface site under feedback

control is $1/\tau = 1 + (\sum_{j=1}^{2m} b_j(z_i)u_j(t))/a$. Since the variation of the bombardment rate does not change the surface diffusion rate, according to the discussion in Remark 3.1, the f of site i should relate to the surface bombardment rate in a way that $(1-f)/\tau$ is a constant. Since in open-loop operation, $\bar{f} = 0.5$ and $1/\bar{\tau} = 1$, we have $(1-f)/\tau = (1-\bar{f})/\bar{\tau} = 0.5$. Therefore, f under feedback control is determined according to the following expression:

$$f(i) = \frac{\bar{f} + \left(\sum_{j=1}^{2m} b_j(z_i)u_j(t)\right)/a}{1 + \left(\sum_{j=1}^{2m} b_j(z_i)u_j(t)\right)/a} \tag{3.51}$$

where $\bar{f} = 0.5$ is the probability a selected surface site is subject to erosion, and $1/\bar{\tau} = 1$ is the bombardment rate of each surface site in open-loop operation.

The simulation algorithm used to run the kMC simulations for the closed-loop system is similar to the one for the open-loop system except that once an event is executed, the first $2m$ states ($\alpha_1, \ldots, \alpha_m$ and $\beta_1, \ldots, \beta_m$) are updated and new control actions are computed to update the value of f (defined in Eq. (3.51) for each surface site

The dimension of the reduced-order model, $2m$, needs to be appropriately determined. It should be large enough so that all unstable modes are included. The number of unstable modes is 26 according to the estimated model parameters of the sputtering process considered in this chapter. When $2m \geq 26$ and the desired closed-loop poles are negative, the linearized closed-loop system under the state feedback

control is stable. This is demonstrated by the simulation result with $2m = 40$.

The closed-loop system simulation result under the state feedback controller designed on the basis of a 40th-order approximation is shown in Figure 3.6 (the dash-dotted line labeled with $m = 20$). The other profiles in Figure 3.6 are under controllers of different orders and will be discussed later. The initial surface roughness is around 0.5. The expected surface roughness is computed by averaging the surface roughness profiles obtained from 100 independent runs. It is clear from Figure 3.6 that the state feedback controller effectively reduces the expected surface roughness and stabilizes it at about 0.3. For the purpose of comparison, an expected open-loop surface roughness profile, which is obtained by averaging 100 independent open-loop simulation runs, is shown in Figure 3.7. Under open-loop operation, the final steady-state surface roughness is around 0.7. Therefore, the state feedback controller reduces the expected surface roughness by 55%. This demonstrates the effectiveness of the state feedback control law. A snapshot of the surface configuration at the end of the closed-loop simulation is shown in Figure 3.9.

However, even when the size of the reduced-order system is smaller than the number of the unstable modes, the state feedback control law still reduces the surface roughness compared to the open-loop value. This is due to the nonlinearity of the stochastic KSE, which bounds the unstable linear terms and prevents the expected surface roughness from going to infinity. To demonstrate this and show that $m = 20$ is appropriate for the state feedback controller design, we compare several state feedback

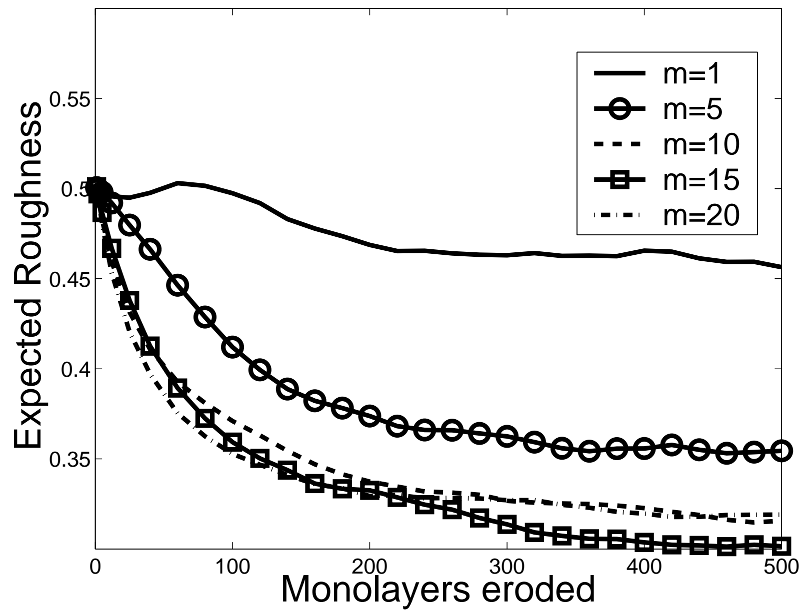

Figure 3.6: Closed-loop surface roughness profiles in the sputtering process under state feedback controllers of different order, m: initial surface roughness is 0.5.

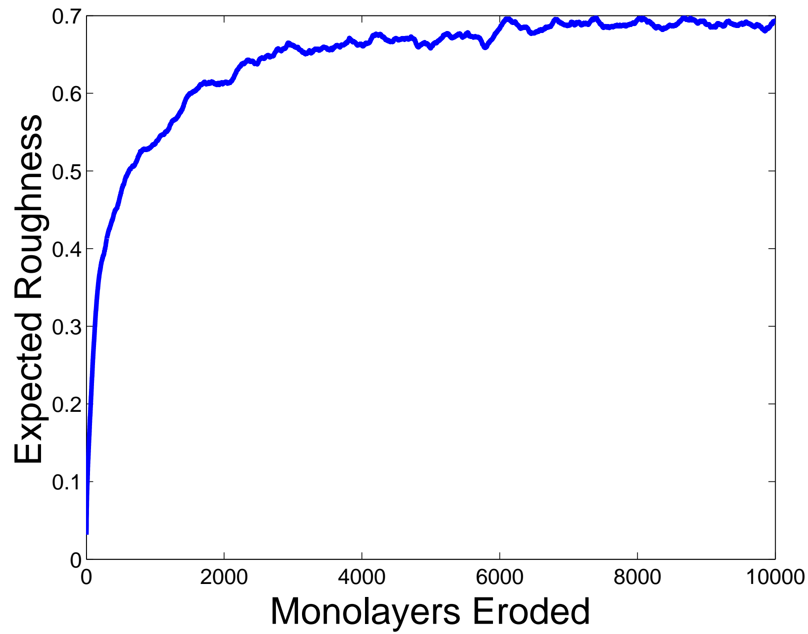

Figure 3.7: Profiles of the expected open-loop surface roughness of the sputtering process.

controllers based on the reduced-order systems with different dimensions, $m = 1$, 5, 10, 15 as well as $m = 20$. For each controller, the number of actuators is the same with the dimension of the reduced-order system and $\Lambda_{cs} = \text{diag}[-0.01\ -0.01\ \ldots\ -0.01]$. The expected surface roughness is the average of the surface roughness profiles obtained from 100 independent runs. The initial surface roughness for the close-loop simulation is fixed at 0.5 and 0, separately.

The closed-loop simulation results are shown in Figure 3.6 and Figure 3.8. Despite the use of different initial conditions, the expected surface roughness profiles of the closed-loop systems under the various state feedback controllers are stabilized at the same values, for the same m. It is also clear that all final expected closed-loop surface roughness values are lower compared to the open-loop simulation. The surface roughness is further reduced as m increases. However, there is no significant difference between the expected roughness of $m = 15$ and $m = 20$. Higher order controllers will not result in further reduction of the surface roughness. So it is concluded that $m = 20$ is an appropriate dimension of the reduced-order system for the state feedback controller.

3.5.3 Closed-Loop simulation under output feedback control

We also apply the output feedback controller of Eq. (3.47) to the kMC model of the sputtering process. The output feedback controller is designed based on the same order stochastic ODE approximation used in the design of the state feedback controller

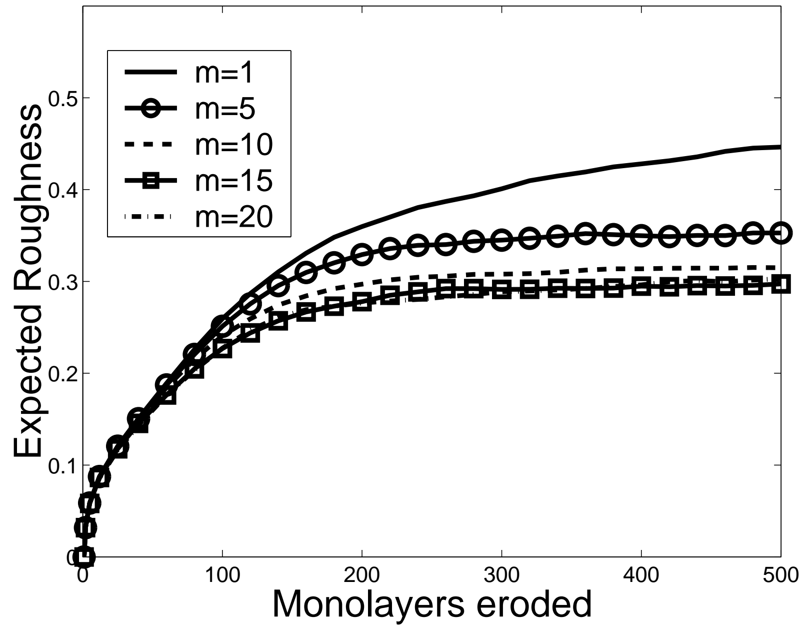

Figure 3.8: Closed-loop surface roughness profiles in the sputtering process under state feedback controllers of different order m: initial surface roughness is 0 (flat initial surface).

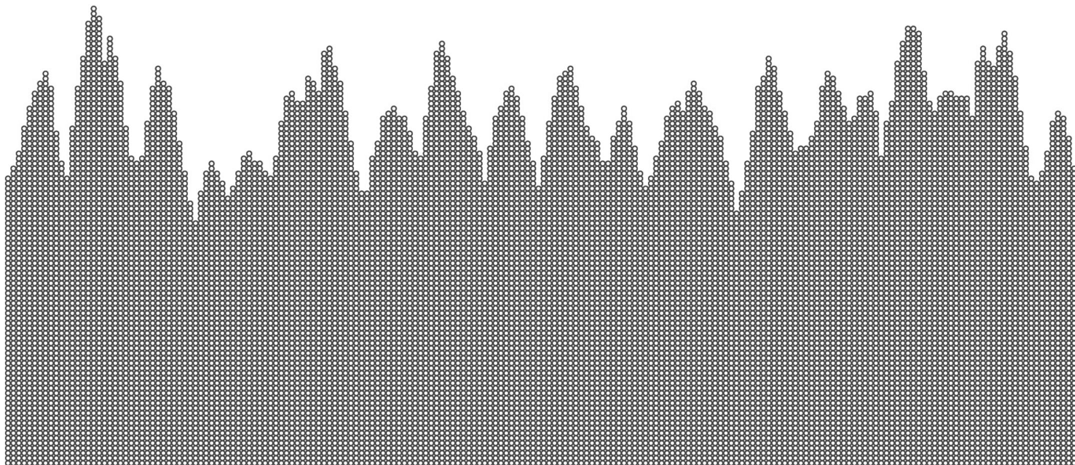

Figure 3.9: A snapshot of the surface configuration at the end of the closed-loop simulation under the 40th order state feedback controller: initial surface roughness is 0.5.

in Section 3.5.2. The positions of point measurements are evenly distributed on the surface lattice. The same control actuators are used to control the system as defined in Eq. (3.50).

The closed-loop system simulation result under the 40th order output feedback controller is shown in Figure 3.10. (the dash-dotted line labeled with $m = 20$). The expected surface roughness is the average of surface roughness profiles obtained from 100 independent runs. The initial surface roughness is fixed at 0.5. Similar to the closed-loop simulation result under state feedback control, the output feedback controller also reduces the expected surface roughness by 55% compared to the corresponding open-loop simulation value. A snapshot of the surface configuration at the end of the closed-loop simulation is shown in Figure 3.12.

For output feedback control, $m = 20$ is also an appropriate dimension for the reduced-order system. Simulations under output feedback control with different dimensions of the reduced-order system are compared in Figure 3.10 and Figure 3.11 with different initial surface conditions similarly to the comparison of the state feedback controller in Section 3.5.2. In these figures, we can see that the output feedback controllers stabilize the expected surface roughness, but are not as effective as the state feedback controllers, especially when the dimension, m, is relatively small. In Figure 3.10, the output feedback controller with $m = 1$ drives the expected surface roughness to a value which is higher than the one obtained under open-loop operation (see Figure 3.7). In Figure 3.10, we also observe that as the dimension (and thus the

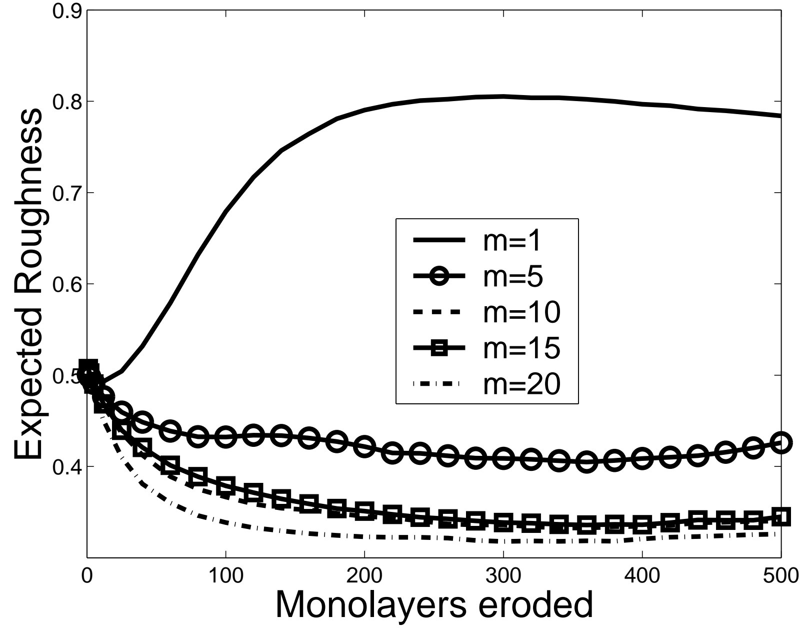

Figure 3.10: Closed-loop surface roughness profiles in the sputtering process under output feedback controllers of different order, m: initial surface roughness is 0.5.

number of sensors) of the model used for controller design increases, the difference between the output feedback controllers and the state feedback controllers decreases. This is due to the decreased error of the estimated state as the number of measurements increases. We therefore conclude that $m = 20$ is an appropriate value for the output feedback controller design.

3.6 Conclusions

In this chapter, we developed a method to estimate the parameters of the nonlinear stochastic KSE model and designed model-based state and output feedback controllers for a sputtering process, which includes two surface micro-processes and is simulated

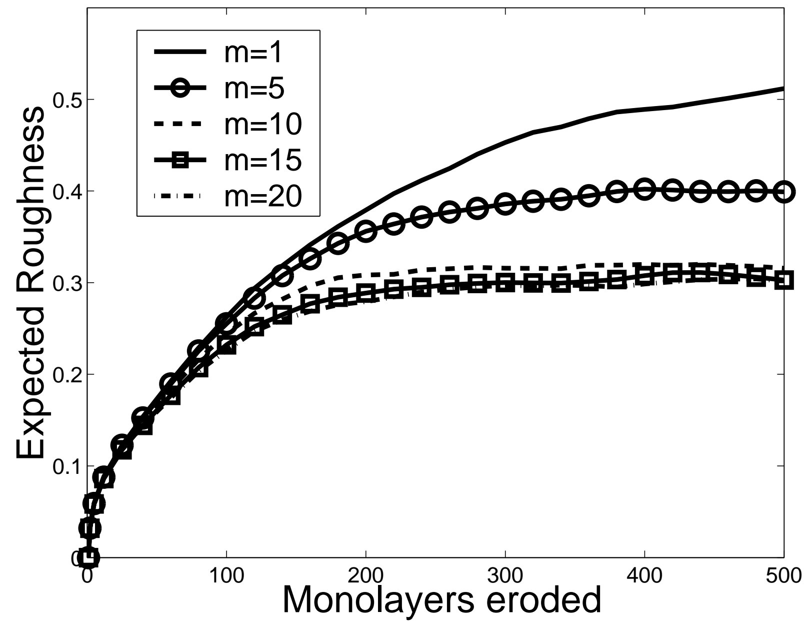

Figure 3.11: Closed-loop surface roughness profiles in the sputtering process under output feedback controllers of different order, m: initial surface roughness is 0 (flat initial surface).

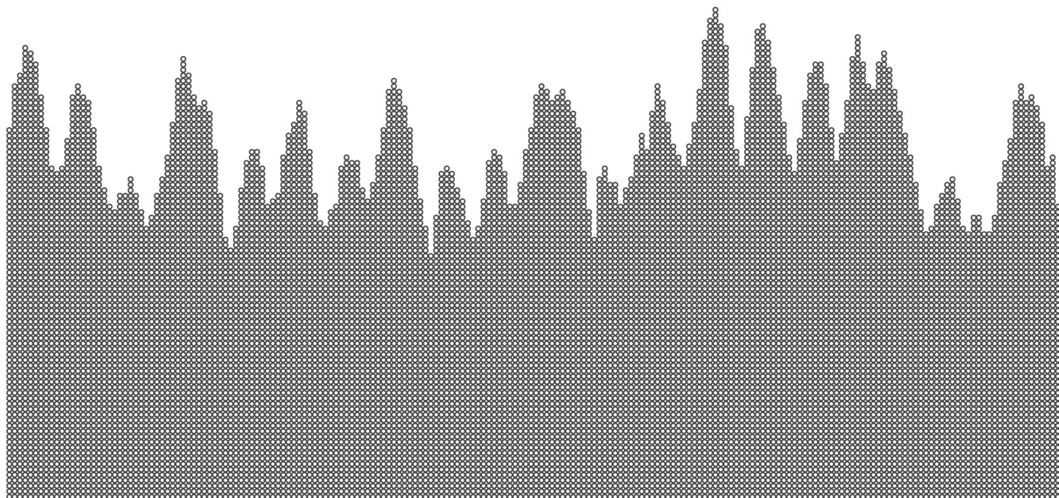

Figure 3.12: A snapshot of the surface configuration at the end of the closed-loop simulation under the 40th order output feedback controller: initial surface roughness is 0.5.

by a kMC model. Both parameter estimation and feedback control design began with formulation of the stochastic KSE into a system of infinite stochastic ODEs by using modal decomposition. A finite dimensional approximation was then obtained to capture the dominant mode contribution to the surface roughness profile. For parameter estimation purposes, a deterministic ODE model of the evolution of the state covariance was derived to eliminate the influence of fluctuations from the stochastic processes. Subsequently, a kMC simulator of the sputtering process was used to generate surface snapshots at different time instants during the process evolution to obtain the state and the state covariance of the stochastic ODE system. Finally, the model parameters of the nonlinear stochastic KSE were obtained using least-squares methods and validated by comparing the KSE open-loop simulation results with the kMC simulation results. With respect to feedback controller design, two schemes were developed and applied to the sputtering process: state feedback control and output feedback control. Both control laws were demonstrated to effectively reduce the expected surface roughness of the kMC simulation of the sputtering process compared to the open-loop operation.

Chapter 4

Model Predictive Control of Surface Roughness

4.1 Introduction

In this chapter, model predictive control (MPC) algorithms are developed on the basis of the identified stochastic PDE models for the thin film growth process to achieve desired surface morphology and film microstructure. First, a method for model predictive control of nonlinear stochastic PDEs is developed. The control objective is to regulate the state variance of the PDE, e.g., the roughness of a surface in a thin film growth process, to a desired level. To present this method, a nonlinear stochastic PDE is first formulated into a infinite-dimensional nonlinear stochastic ODE system by using Galerkin's method. A finite-dimensional approximation is then constructed

to capture the dominant mode contribution to the state variance. A model predictive control problem is formulated based on the finite-dimensional approximation. In the closed-loop system under the model predictive control, the control action is computed by minimizing an objective cost function, which includes both transient and terminal state penalty. An analysis of the closed-loop nonlinear infinite-dimensional system is performed to characterize the closed-loop performance enforced by the model predictive controller. Subsequently, numerical simulations are performed using the stochastic Kuramoto-Sivashinsky equation (KSE) to demonstrate the effectiveness of the proposed predictive controller. In addition, we consider the problem of surface roughness regulation in a one-dimensional ion-sputtering process described by a kMC model. We first demonstrate that the spatially distributed control configuration is more effective for surface roughness regulation compared to the spatially invariant control configuration. Then, a model predictive controller, which is designed based on an identified stochastic KSE surface model, is applied to the kMC model of the sputtering process and is demonstrated to successfully regulate the expected surface roughness to a desired level [63].

4.2 Nonlinear model predictive controller design

4.2.1 Preliminaries

We consider nonlinear dissipative stochastic PDEs with distributed control of the following form:

$$\frac{\partial h}{\partial t} = \mathcal{A}h + \mathcal{F}(h) + \sum_{i=1}^{p} b_i(x)u_i(t) + \xi(x,t) \tag{4.1}$$

subject to homogeneous boundary conditions and the initial condition $h(x,0) = h_0(x)$, where $x \in [-\pi, \pi]$ is the spatial coordinate, t is the time, $h(x,t)$ is the height of the surface at position x and time t, $\mathcal{A}$ is a dissipative spatial differential operator, $\mathcal{F}$ is a nonlinear function, $u_i(t)$ is the ith manipulated input, p is the number of manipulated inputs and $b_i(x)$ is the ith actuator distribution function (i.e., $b_i(x)$ determines how the control action computed by the ith control actuator, $u_i(t)$, is distributed (e.g., point or distributed actuation) in the spatial interval $[-\pi, \pi]$). $\xi(x,t)$ is a Gaussian white noise with the following expressions for its mean and covariance:

$$\begin{aligned} \langle \xi(x,t) \rangle &= 0, \\ \langle \xi(x,t)\xi(x',t') \rangle &= \sigma^2 \delta(x-x')\delta(t-t'), \end{aligned} \tag{4.2}$$

where σ is a real number, $\delta(\cdot)$ is the Dirac delta function, and $\langle \cdot \rangle$ denotes the expected value.

The eigenvalue problem for $\mathcal{A}$ is defined as

$$\mathcal{A}\phi_j = \lambda_j \phi_j, \quad j = 1, 2, \ldots, \infty, \tag{4.3}$$

where λ_j and ϕ_j denote the jth eigenvalue and eigenfunction, respectively. To simplify our development and motivated by most practical applications, we consider stochastic PDEs for which $\mathcal{A}$ is a highly dissipative operator (i.e., a second-order or fourth-order linear self-adjoint operator) and has eigenvalues which are real numbers. The eigenspectrum of $\mathcal{A}$, $\sigma(\mathcal{A})$, is defined as the set of all eigenvalues of $\mathcal{A}$, i.e., $\sigma(\mathcal{A}) = \{\lambda_1, \lambda_2, \ldots\}$. Assumption 4.1 states that the eigenspectrum of $\mathcal{A}$ can be partitioned into a finite-dimensional part consisting of m slow eigenvalues and a stable infinite-dimensional complement containing the remaining fast eigenvalues, the separation between the slow and fast eigenvalues of $\mathcal{A}$ is large, and that the infinite sum of $\sum_{i=1}^{\infty} \frac{1}{|\lambda_i|}$ converges to a finite positive number.

Assumption 4.1 *[23]: The eigenvalues of $\mathcal{A}$ satisfy the following:*

1. $\lambda_1 \geq \lambda_2 \geq \ldots$.

2. *$\sigma(\mathcal{A})$ can be partitioned as $\sigma(\mathcal{A}) = \sigma_1(\mathcal{A}) + \sigma_2(\mathcal{A})$, where $\sigma_1(\mathcal{A})$ consists of the first m (with m finite) eigenvalues, i.e., $\sigma_1(\mathcal{A}) = \{\lambda_1, \lambda_2, \ldots, \lambda_m\}$. $\lambda_{m+1} < 0$ and $\frac{|\lambda_1|}{|\lambda_{m+1}|} = O(\epsilon)$ where $\epsilon < 1$ is a small positive number.*

3. *There exists a positive number, $\gamma > 0$, such that $\sum_{i=1}^{\infty} \frac{1}{|\lambda_i|} < \gamma$.*

Note that the eigenvalue problem of the stochastic PDE of Eq. (4.1) is formulated in the same way as that of deterministic PDEs. The assumption of finite number of unstable eigenvalues and discrete eigenspectrum are always satisfied for parabolic PDE systems defined in finite spatial domains [19], while the assumption of existence of only a few dominant modes that capture the dominant dynamics of the stochastic parabolic PDE system and the convergence of the infinite sum $\sum_{i=1}^{\infty} \frac{1}{|\lambda_i|}$ to a finite positive number are usually satisfied by the majority of materials processes (see the example of the sputtering process described by the stochastic KSE in the Section 4.3).

The inner product and norm in the Hilbert space $\mathcal{H}$ are defined as

$$(\omega_1, \omega_2) \ = \ \int_{\Omega} (\omega_1(z), \omega_2(z))_{\mathbb{R}^n} dz, \quad \|\omega_1\|_2 \ = \ (\omega_1, \omega_1)^{1/2}, \tag{4.4}$$

where ω_1, ω_2 are two elements of $\mathcal{H}$, Ω is the domain of definition of the process, and the notation $(\cdot, \cdot)_{\mathbb{R}^n}$ denotes the standard inner product in $\mathbb{R}^n$.

4.2.2 Model reduction

We apply Galerkin's method (see [19] for a detailed discussion on the standard Galerkin's method) to the system of Eq. (4.1) to derive an approximate finite-dimensional system. First, the solution of Eq. (4.1) is expanded into an infinite series in terms of

the eigenfunctions of the operator of Eq. (4.3) as follows:

$$h(x,t) = \sum_{n=1}^{\infty} \alpha_n(t)\phi_n(x) \tag{4.5}$$

where $\alpha_n(t)$ are time-varying coefficients. Substituting the above expansion for the solution, $h(x,t)$, into Eq. (4.1) and taking the inner product with the adjoint eigenfunctions, $\phi_n^*(x)$, the following system of infinite nonlinear stochastic ODEs is obtained:

$$\frac{d\alpha_n}{dt} = \lambda_n \alpha_n + f_{n\alpha} + \sum_{i=1}^{p} b_{i\alpha_n} u_i(t) + \xi_\alpha^n(t), \quad n = 1, \ldots, \infty, \tag{4.6}$$

where

$$b_{i\alpha_n} = \int_{-\pi}^{\pi} \phi_n^*(x) b_i(x) dx, \quad \xi_\alpha^n(t) = \int_{-\pi}^{\pi} \xi(x,t)\phi_n^*(x) dx, \tag{4.7}$$

and

$$f_{n\alpha} = \int_{-\pi}^{\pi} \phi_n^*(x)\mathcal{F}(h) dx. \tag{4.8}$$

Using Result 1, the covariance of $\xi_\alpha^n(t)$ can be obtained as $\langle \xi_\alpha^n(t)\xi_\alpha^n(t')\rangle = \sigma^2\delta(t - t')$.

Owing to its infinite-dimensional nature, the system of Eq. (4.6) cannot be directly used for the design of controllers that can be implemented in practice (i.e., the practical implementation of controllers which are designed on the basis of this system will require the computation of infinite sums which cannot be done by a computer). Instead, we will base the controller design on a finite-dimensional approximation of

this system. Subsequently, we will show that the resulting controller will enforce the desired control objective in the closed-loop infinite-dimensional system. Specifically, we rewrite the system of Eq. (4.6) as follows:

$$\begin{aligned} \frac{dx_{\rm s}}{dt} &= \mathcal{A}_{\rm s}x_{\rm s} + \mathcal{F}_{\rm s}(x_{\rm s}, x_{\rm f}) + \mathcal{B}_{\rm s}u + \xi_{\rm s}, \\ \frac{dx_{\rm f}}{dt} &= \mathcal{A}_{\rm f}x_{\rm f} + \mathcal{F}_{\rm f}(x_{\rm s}, x_{\rm f}) + \mathcal{B}_{\rm f}u + \xi_{\rm f}, \end{aligned} \tag{4.9}$$

where $x_{\rm s} = [\alpha_1 \quad \alpha_2 \quad \dots \quad \alpha_m]^T$, $x_{\rm f} = [\alpha_{m+1} \quad \alpha_{m+2} \quad \dots]^T$, $\mathcal{A}_{\rm s} = \text{diag}[\lambda_1 \quad \lambda_2 \quad \dots \quad \lambda_m]$, $\mathcal{A}_{\rm f} = \text{diag}\,[\lambda_{m+1}\ \lambda_{m+2}\ \dots]$, $\mathcal{F}_{\rm s}(x_{\rm s}, x_{\rm f}) = [f_{1\alpha}(x_{\rm s}, x_{\rm f}) \quad f_{2\alpha}(x_{\rm s}, x_{\rm f}) \quad \dots \quad f_{m\alpha}(x_{\rm s}, x_{\rm f})]^T$, $\mathcal{F}_{\rm f}(x_{\rm s}, x_{\rm f}) = [\ f_{m+1\alpha}(x_{\rm s}, x_{\rm f})\ f_{m+2\alpha}(x_{\rm s}, x_{\rm f})\ \dots]^T$, $u = [u_1 \quad u_2 \quad \dots \quad u_p]$, $\xi_{\rm s} = [\xi_\alpha^1 \quad \dots \quad \xi_\alpha^m]$, $\xi_{\rm f} = [\xi_\alpha^{m+1} \quad \xi_\alpha^{m+2} \quad \dots]$,

$$\mathcal{B}_{\rm s} = \begin{bmatrix} b_{1_{\alpha_1}} & \dots & b_{p_{\alpha_1}} \\ \vdots & \ddots & \vdots \\ b_{1_{\alpha_m}} & \dots & b_{p_{\alpha_m}} \end{bmatrix}, \quad \text{and } \mathcal{B}_{\rm f} = \begin{bmatrix} b_{1_{\alpha_{m+1}}} & \dots & b_{p_{\alpha_{m+1}}} \\ b_{1_{\alpha_{m+2}}} & \dots & b_{p_{\alpha_{m+2}}} \\ \vdots & \vdots & \vdots \end{bmatrix}. \tag{4.10}$$

The standard Galerkin's method is to approximate the solution $h(x,t)$ of the system of Eq. (4.1) by $\tilde{x}_{\rm s}(t)$, which is given by the following $m-$dimensional system:

$$\frac{d\tilde{x}_{\rm s}}{dt} = \mathcal{A}_{\rm s}\tilde{x}_{\rm s} + \mathcal{F}_{\rm s}(\tilde{x}_{\rm s}, 0) + \mathcal{B}_s u + \xi_{\rm s} \tag{4.11}$$

where the tilde symbol in $\tilde{x}_{\rm s}$ denotes that this state variable is associated with a finite-dimensional system. We note that there are a variety of other methods/concepts

available for model reduction of nonlinear distributed parameter systems. For example, the concept of approximate inertial manifolds [23, 19, 6] can be employed to obtain improved approximations of the finite-dimensional system of Eq. (4.11) and proper orthogonal decomposition (POD) [9, 6] can be used to derive empirical eigenfunctions based on process model solutions which can be employed as basis functions in Galerkin's method.

4.2.3 Model predictive controller design

In this section, we design a nonlinear model predictive controller based on the finite-dimensional stochastic ODE system of Eq. (4.11). In our development, we will need the following notation for the full state, $X = [x_{\mathrm{s}}^T \ x_{\mathrm{f}}^T]^T = [\alpha_1 \ \alpha_2 \ \ldots \ \alpha_m \ \alpha_{m+1} \ \ldots]^T$. The variances of x_{s}, x_{f} and X are defined as:

$$\begin{aligned} \mathrm{var}(x_{\mathrm{s}}(t)) &= \left[\langle \alpha_1^2(t) \rangle \quad \ldots \quad \langle \alpha_m^2(t) \rangle\right]^T, \\ \mathrm{var}(x_{\mathrm{f}}(t)) &= \left[\langle \alpha_{m+1}^2(t) \rangle \quad \langle \alpha_{m+2}^2(t) \rangle \quad \ldots\right]^T, \\ \mathrm{var}(X(t)) &= \left[\mathrm{var}(x_{\mathrm{s}}(t))^T \quad \mathrm{var}(x_{\mathrm{f}}(t))^T\right]^T, \end{aligned} \tag{4.12}$$

where $\langle \cdot \rangle$ denotes the expected value. The 2-norms of a finite-dimensional vector, $y_{\mathrm{s}}(t) = [y_1(t) \ y_2(t) \ \ldots \ y_m(t)]^T$ and an infinite-dimensional vector, $y_{\mathrm{f}}(t) = [y_1(t) \ y_2(t) \ \ldots]^T$ are defined as follows:

$$\|y_{\mathrm{s}}(t)\| = \sqrt{\sum_{j=1}^{m} y_j^2(t)}, \quad \|y_{\mathrm{f}}(t)\| = \sqrt{\sum_{j=1}^{\infty} y_j^2(t)}. \tag{4.13}$$

Accordingly, we have the following for the norms of the vectors $\text{var}(x_{\rm s})$, $\text{var}(x_{\rm f})$ and $\text{var}(X)$:

$$\begin{aligned} \|\text{var}(x_{\rm s}(t))\|^2 &= \sum_{j=1}^{m} \langle \alpha_j^2(t) \rangle^2, \\ \|\text{var}(x_{\rm f}(t))\|^2 &= \sum_{j=m+1}^{\infty} \langle \alpha_j^2(t) \rangle^2, \\ \|\text{var}(X(t))\|^2 &= \sum_{j=1}^{\infty} \langle \alpha_j^2(t) \rangle^2. \end{aligned} \tag{4.14}$$

MPC formulation based on the infinite-dimensional system

In this section, we consider the problem of control of the norm of the state variance of the nonlinear stochastic infinite-dimensional system of Eq. (4.1) to a desired level. This problem will be addressed within a model predictive control framework, where the control, at a time t and state $x(t)$, is obtained by solving a finite-horizon optimal control problem. Since the system of infinite stochastic ODEs of Eq. (4.9) is mathematically equivalent to the stochastic PDE of Eq. (4.1), the MPC problem is formulated based on the system of infinite stochastic ODEs of Eq. (4.9) in the following form:

$$\begin{gathered} \min_{u} \{ J(X(t), t, u(\cdot)) | u(\cdot) \in S \} \\ \text{subject to} \\ \frac{dx_{\rm s}}{dt} = \mathcal{A}_{\rm s} x_{\rm s} + \mathcal{F}_{\rm s}(x_{\rm s}, x_{\rm f}) + \mathcal{B}_{\rm s} u + \xi_{\rm s}, \\ \frac{dx_{\rm f}}{dt} = \mathcal{A}_{\rm f} x_{\rm f} + \mathcal{F}_{\rm f}(x_{\rm s}, x_{\rm f}) + \mathcal{B}_{\rm f} u + \xi_{\rm f}, \end{gathered} \tag{4.15}$$

where $S = S(t, T_{\rm p})$ is the family of piecewise functions, with period Δ, mapping $[t, t+T_{\rm p}]$ into $\mathcal{U} = \{u(t) \in \mathbb{R}^l\}$ and $T_{\rm p}$ is a specified prediction horizon. The control $u(\cdot)$ in S is characterized by the sequence $u[k]$, where $u[k] = u(t + k\Delta)$ and satisfies that $u(t) = u[k]$ for all $t \in [t+k\Delta, t+(k+1)\Delta]$. Note that by selecting an appropriate S, input constraints can be readily included in the control problem formulation. The objective function, $J(X(t), t, u(\cdot))$ is, in general, given by:

$$\begin{aligned} J(X, t, u(\cdot)) = & \int_t^{t+T_{\rm p}} Q\|\mathrm{var}(X^{\rm u}(\tau)) - \mathrm{var}(X^*(\tau))\|^2 d\tau \\ & + Q_{\rm f}\|\mathrm{var}(X(t+T_{\rm p})) - \mathrm{var}(X^*(t+T_{\rm p}))\|^2 \end{aligned} \tag{4.16}$$

where $\mathrm{var}(X^*(\tau))$ is the reference trajectory describing the variance of the desired state for the infinite-dimensional system, $\mathrm{var}(X^{\rm u}(\tau))$ denotes the variance of the state X that is due to the control $u(t)$, with initial state $X(t)$ at a time t in the closed-loop system of Eq. (4.1), Q and $Q_{\rm f}$ are positive real numbers, and $T_{\rm p}$ is the prediction horizon. We note that the cost function of Eq. (4.16) does not include a penalty on the control action. Yet, we do impose an implicit penalty on the control action by imposing appropriate bounds on the eigenvalues of the closed-loop system (see optimization formulation of Eq. (4.21) below). The minimizing control $u^0(\cdot) = \{u(t), u(t+\Delta), u(t+2\Delta), \dots\} \in S$ is then applied to the system over the interval $[t, t+\Delta]$ and the procedure is repeated at $t+\Delta$ until a terminal time is

reached. This defines an implicit model predictive control law as follows:

$$u(t) \;=\; M(X(t)) \;=\; u^0(\Delta; X(t), t) \tag{4.17}$$

in which $M(x(t))$ denotes the nonlinear map between the state and control.

MPC formulation and solution based on the reduced-order model

Note that the predictive control formulation shown in Eq. (4.15) is developed on the basis of an infinite-dimensional stochastic system. Therefore, it leads to a predictive controller that is of infinite order and cannot be realized in practice. To address this issue, we provide a predictive control formulation that is on the basis of the finite-dimensional system of Eq. (4.11) and computes the control action by minimizing an objective function including the distance between the predicted state variance and a reference trajectory and a terminal penalty.

Consider a vector of reference trajectories describing the desired trajectories for each element of the variance of x_{s}, $\mathrm{var}(x_{\mathrm{s}}^*(t)) = [\langle x_1^*(t)^2\rangle \, \ldots \, \langle x_m^*(t)^2\rangle]^T$. The control action, $u(t)$, can be obtained by solving, in a receding horizon fashion, the following

optimization problem:

$$\min_{u} \int_{t}^{t+T_{\rm p}} Q\|\mathrm{var}(\tilde{x}_{\rm s}^{\rm u}) - \mathrm{var}(x_{\rm s}^{*})\|^{2} d\tau + Q_{\rm f}\|\mathrm{var}(\tilde{x}_{\rm s}^{\rm u}(t+T_{\rm p})) - \mathrm{var}(x_{\rm s}^{*}(t+T_{\rm p}))\|^{2}$$

subject to

$$\frac{d\tilde{x}_{\rm s}}{dt} = \mathcal{A}_{\rm s}\tilde{x}_{\rm s} + \mathcal{F}_{\rm s}(\tilde{x}_{\rm s}, 0) + \mathcal{B}_{s}u + \xi_{\rm s} \tag{4.18}$$

where $\tilde{x}_{\rm s}^{\rm u}$ is the solution of Eq. (4.11) that is due to the control $u(\tau)$, with an initial condition $\tilde{x}_{\rm s}(t)$ at a time t.

A challenge for the design of a predictive controller for a stochastic process is to predict the state variance, $\mathrm{var}(x_{\rm s}(t))$, in a computationally efficient way. Although a realization of the future evolution of state variance can be solved through numerical integrations of the stochastic process model of Eq. (4.18), due to the stochastic nature of the process, numerical solutions from different simulation runs of the same stochastic process are not identical. The state variance should be computed by averaging the numerical solutions of the stochastic process from a large number of individual simulation runs. The prediction of state variance using brute force numerical integration of a nonlinear stochastic system is, therefore, extremely computationally expensive and is not appropriate for the design of predictive controllers to be implemented in real-time.

As an alternative, an analytical solution of the state variance based on the process model, if available, provides a feasible way for MPC design and implementation. For linear stochastic PDEs, the analytical solution of the state variance is readily

available, which results in efficient design of a model predictive controller for surface variance regulation [71]. However, analytical solutions of the state variance for nonlinear stochastic PDEs are, in general, not available. To this end, we focus on the construction of a nonlinear feedback controller that can induce a linear structure in the closed-loop finite-dimensional stochastic system of Eq. (4.11). Therefore, the analytical solution of the state variance under the proposed controller structure can be obtained. Consequently, the control action is computed by solving an optimization problem in a receding horizon fashion and computationally efficient way.

Specifically, under the assumption that the number of control actuators is equal to the dimension of the $\tilde{x}_s$-subsystem and the matrix B_s is invertible, the control law takes the following form:

$$u(t) \;=\; \mathcal{B}_s^{-1}\left\{\left(\mathcal{A}_{cs}(t)-\mathcal{A}_s\right)\tilde{x}_s(t)-\mathcal{F}_s(\tilde{x}_s(t),0)\right\} \tag{4.19}$$

where $\mathcal{A}_{cs}(t) = \mathrm{diag}[\lambda_{c1}(t) \;\ldots\; \lambda_{cm}(t)]$ and $\lambda_{ci}(t)$, $i = 1,\, 2,\, \ldots,\, m$, are time-varying, desired poles of the closed-loop finite-dimensional system. Note that in the proposed controller structure of Eq. (4.19), the desired poles are not fixed values but will be computed in real-time by solving an on-line optimization problem in a receding horizon fashion. This is a fundamental difference from the nonlinear feedback controller proposed in [62].

Replacing the u of Eq. (4.11) by Eq. (4.19), we have the following closed-loop

system:

$$\frac{d\tilde{x}_{\rm s}(t)}{dt} = \mathcal{A}_{\rm cs}(t)\tilde{x}_{\rm s}(t) + \xi_{\rm s} \tag{4.20}$$

In this control problem formulation, the computation of the control action, $u(t)$, is equivalent to the computation of $\mathcal{A}_{\rm cs}(t)$, or the values of $\lambda_{{\rm c}i}(t)$ for $i = 1, 2, \ldots, m$, by solving the following optimization problem:

$$\begin{gathered}
\min_{\mathcal{A}_{\rm cs}(t)} \int_t^{t+T_{\rm p}} Q\|\text{var}(\tilde{x}_{\rm s}) - \text{var}(x_{\rm s}^*)\|^2 d\tau + Q_{\rm f}\|\text{var}(\tilde{x}_{\rm s}(t+T_{\rm p})) - \text{var}(x_{\rm s}^*(t+T_{\rm p}))\|^2 \\
\text{subject to} \\
\frac{d\tilde{x}_{\rm s}}{dt} = \mathcal{A}_{\rm cs}(t)\tilde{x}_{\rm s} + \xi_{\rm s}, \\
a_i < \lambda_{{\rm c}i}(t) < b_i < 0, \quad i = 1, 2, \ldots, m.
\end{gathered} \tag{4.21}$$

Note that in the optimization problem of Eq. (4.21), $\mathcal{A}_{\rm cs}(t)$ does not change during the optimization time interval $t < \tau < t + T_{\rm p}$. Therefore, the optimization problem of Eq. (4.21), which does not include penalty on the control action, is a quadratic problem with linear constraints for which the existence of the optimal solution is guaranteed and unique. The control action, u, is computed using Eq. (4.19), in which $\mathcal{A}_{\rm cs}(t)$ is obtained from the solution of the constrained optimization problem of Eq. (4.21). Since the poles of the closed-loop finite dimensional system, $\lambda_{{\rm c}i}(t)$, are constrained, u is not explicitly included in the objective function. The analytical

solution of the state variance of Eq. (4.20) can be obtained as follows:

$$\tilde{x}_n(\tau) = e^{\lambda_{cn}(\tau - t)}\tilde{x}_n(t) + \int_t^{\tau} e^{\lambda_{cn}(t+T_{\rm p}-\mu)}\xi_{\rm s}^n(\mu)d\mu, \quad n = 1, 2, \dots, m. \tag{4.22}$$

The expected value (the first stochastic moment) and the variance (the second stochastic moment) of the state of Eq. (4.20) can be computed as follows [60, 71]:

$$\begin{aligned} \langle \tilde{x}_n(\tau) \rangle &= e^{\lambda_{cn}(\tau - t)}\tilde{x}_n(t), & n = 1, 2, \dots, m, \\ \langle \tilde{x}_n(\tau)^2 \rangle &= \frac{e^{2\lambda_{cn}(\tau - t)} - 1}{2\lambda_{cn}} + \langle \tilde{x}_n(t) \rangle^2, & n = 1, 2, \dots, m. \end{aligned} \tag{4.23}$$

Eq. (4.23) also gives the analytical solution of $\mathrm{var}(\tilde{x}_{\rm s}(t))$ in the closed-loop finite-dimensional system of Eq. (4.11). Using Eq. (4.23), the optimization problem of Eq. (4.21) can be subsequently formulated as a minimization of a nonlinear algebraic equation, which can be readily solved by using standard unconstrained or constrained multidimensional nonlinear minimization algorithms (for example, Nelder-Mead method or golden section search [16, 52]). The computational cost of these optimization algorithms grows with the number of variables and the computation involves only standard numerical operations such as function evaluation and comparison. The optimization problems can be solved fast relative to the time scale of process evolution using currently available computing power.

Remark 4.1 *Note that input and state constraints could be incorporated into the predictive control formulation of Eq. (4.18). In a stochastic process, the value of*

either the input or the state at a specific time is not predictable and its evolution can only be described by its statistical moments. Therefore, the state constraints should be incorporated into the predictive control formulation in the form of their statistical moments. Of particular interest are their second-order moments (covariance) because the state covariance represents the expected surface roughness of a thin film [60, 61] and the input covariance can be related to control energy [82]. However, systematic handling of input and/or state constraints in predictive control of stochastic PDEs also requires an efficient way to compute the state and/or input covariance, which is, in general, very challenging for nonlinear stochastic PDEs and is outside of the scope of the present work.

4.2.4 Analysis of the closed-loop infinite-dimensional system

In this section, we analyze the state variance of the infinite dimensional system under the predictive controller of Eq. (4.21). To ensure exponential stability of the closed-loop finite-dimensional system, the upper-bounds of the closed-loop poles in Eq. (4.21), b_i, $i = 1, 2, \ldots, m$, are all negative. Under this condition, a Lyapunov function can be constructed to prove the exponential stability of the closed-loop finite-dimensional system with time-varying matrix $\mathcal{A}_{\rm cs}(t)$ in Eq. (4.21) (note that $\mathcal{A}_{\rm cs}(t)$ is a diagonal matrix). To this end, we can design the predictive controller of Eq. (4.21) to successfully drive the variance of $\tilde{x}_{\rm s}$ of the system of Eq. (4.20) to the desired value, e.g., $\|{\rm var}(x_{\rm s}(t))\|^2 = \|{\rm var}(x_{\rm s}^*(t))\|^2$. By applying the controller of

Eqs. (4.19) and (4.21) to the infinite-dimensional system of Eq. (4.9), and using that $\epsilon = \dfrac{|\lambda_1|}{|\lambda_{m+1}|}$, the closed-loop system takes the form:

$$
\begin{aligned}
\frac{dx_{\rm s}}{dt} &= \mathcal{A}_{\rm cs}x_{\rm s} + (\mathcal{F}_{\rm s}(x_{\rm s}, x_{\rm f}) - \mathcal{F}_{\rm s}(x_{\rm s}, 0)) + \xi_{\rm s}, \\
\epsilon\frac{dx_{\rm f}}{dt} &= \mathcal{A}_{{\rm f}\epsilon}x_{\rm f} + \epsilon\mathcal{B}_{\rm f}\mathcal{B}_{\rm s}^{-1}(\mathcal{A}_{\rm cs} - \mathcal{A}_{\rm s})\tilde{x}_{\rm s} \\
&\quad + \epsilon\mathcal{F}_{\rm f}(x_{\rm s}, x_{\rm f}) - \epsilon\mathcal{B}_{\rm f}\mathcal{B}_{\rm s}^{-1}\mathcal{F}_{\rm s}(\tilde{x}_{\rm s}, 0) + \epsilon\xi_{\rm f},
\end{aligned}
\tag{4.24}
$$

where λ_1 and λ_{m+1} are the first and the $(m+1)$th eigenvalues of the linear operator in Eq. (4.9), and $\mathcal{A}_{{\rm f}\epsilon} = {\rm diag}[\lambda_{\epsilon 1}\ \lambda_{\epsilon 2}\ \ldots]$ is an infinite-dimensional matrix defined as $\mathcal{A}_{{\rm f}\epsilon} = \epsilon\mathcal{A}_{\rm f}$.

We now proceed to characterize the accuracy with which the variance of $x = [x_{\rm s}^T\ x_{\rm f}^T]^T$ is controlled in the closed-loop infinite-dimensional system. Theorem 4.1 provides estimates of the variances of $x_{\rm s}$ and $x_{\rm f}$ of the closed-loop system of Eq. (4.24) and a characterization of the variance of x enforced by the controller of Eqs. (4.19) and (4.21) in the closed-loop infinite dimensional system. The proof of Theorem 4.1 is given below.

Theorem 4.1 *Consider the infinite-dimensional closed-loop system of Eq. (4.24) and the definition of* $\|{\rm var}(x_{\rm s})\|^2$, $\|{\rm var}(x_{\rm f})\|^2$, *and* $\|{\rm var}(X)\|^2$ *shown in Eq. (4.14). Then, there exist* $\mu^* > 0$ *and* $\epsilon^* > 0$ *such that if* $\|x_{\rm f0}\| + \|x_{\rm s0}\| \leq \mu^*$ *and* $\epsilon \in (0, \epsilon^*]$,

$\|\mathrm{var}(x_{\mathrm{s}}(t_{\mathrm{f}}))\|^2$, $\|\mathrm{var}(x_{\mathrm{f}}(t_{\mathrm{f}}))\|^2$, *and* $\|\mathrm{var}(x(t_{\mathrm{f}}))\|^2$ *satisfy:*

$$\|\mathrm{var}(x_{\mathrm{f}}(t))\|^2 = O(\epsilon), \tag{4.25}$$

$$\|\mathrm{var}(x_{\mathrm{s}}(t))\|^2 = \|\mathrm{var}(x_{\mathrm{s}}^*(t))\|^2 + O(\sqrt{\epsilon}), \tag{4.26}$$

$$\|\mathrm{var}(X(t))\|^2 = \|\mathrm{var}(x_{\mathrm{s}}^*(t))\|^2 + O(\sqrt{\epsilon}), \tag{4.27}$$

where x_{f0} *and* x_{s0} *are the initial conditions for* x_{f} *and* x_{s} *in Eq. (4.24), respectively.*

Proof of Theorem 4.1. The proof of Theorem 4.1 includes several steps. First, we prove that the closed-loop infinite-dimensional system is asymptotically stable for a sufficiently small ϵ. Second, we compute the $\|\mathrm{var}(x_{\mathrm{f}})\|^2$ using the x_{f} subsystem of Eq. (4.24) and prove Eq. (4.25) in Theorem 4.1. Then, we compute $\|\mathrm{var}(x_{\mathrm{s}})^2\|$ using the x_{s} subsystem of Eq. (4.24) and prove Eq. (4.26) in Theorem 4.1. Finally, the proof of Theorem 4.1 is completed by proving Eq. (4.27) based on the results in Eqs. (4.25) and (4.26).

Closed-loop infinite-dimensional system stability. Let $u(t) = M(x_{\mathrm{s}})$ be the general expression of the control law corresponding to the predictive control formulation of Eq. (4.18). The infinite-dimensional closed-loop system of Eq. (4.24) can be re-written

as follows:

$$\begin{aligned} \frac{dx_{\rm s}}{dt} &= \mathcal{A}_{\rm s}x_{\rm s} + \mathcal{F}_{\rm s}(x_{\rm s}, x_{\rm f}) + \mathcal{B}_{\rm s}M(x_{\rm s}) + \xi_{\rm s}, \\ \epsilon\frac{dx_{\rm f}}{dt} &= \mathcal{A}_{\rm f\epsilon}x_{\rm f} + \epsilon\mathcal{F}_{\rm f}(x_{\rm s}, x_{\rm f}) + \epsilon\mathcal{B}_{\rm f}M(x_{\rm s}) + \epsilon\xi_{\rm f}, \end{aligned} \tag{4.28}$$

where $x_{\rm f}$ subsystem is a fast subsystem due to the eigenspectrum of $\mathcal{A}_{\rm f\epsilon}$. Rewriting the system of Eq. (4.28) in the fast-time-scale $\tau = t/\epsilon$ and setting $\epsilon = 0$, the $x_{\rm f}$ subsystem of Eq. (4.28) takes the form:

$$\frac{d\bar{x}_{\rm f}}{d\tau} = \mathcal{A}_{\rm f\epsilon}\bar{x}_{\rm f} \tag{4.29}$$

where $\bar{x}_{\rm f}$ denotes the state of the $x_{\rm f}$ subsystem after neglecting the three terms. According to Assumption 4.1 for the eigenspectrum of the linear operator $\mathcal{A}$, all eigenvalues of $\mathcal{A}_{\rm f\epsilon}$ have negative real parts. Thus, the system of Eq. (4.29) is exponentially stable. Setting $\epsilon = 0$ in the system of Eq. (4.28), the following closed-loop finite-dimensional system is obtained:

$$\begin{aligned} \frac{d\tilde{x}_{\rm s}}{dt} &= \mathcal{A}_{\rm s}\tilde{x}_{\rm s} + \mathcal{F}_{\rm s}(\tilde{x}_{\rm s}, 0) + \mathcal{B}_{\rm s}M(\tilde{x}_{\rm s}) + \xi_{\rm s} \\ &= \mathcal{A}_{\rm cs}\tilde{x}_{\rm s} + \xi_{\rm s} \end{aligned} \tag{4.30}$$

which is locally exponentially stable by the design of the predictive controller of Eq. (4.21). Therefore, there exists a positive real number $\hat{\epsilon}$ such that $\forall \epsilon \in (0, \hat{\epsilon}]$, the zero solution of the closed-loop infinite-dimensional system of Eq. (4.24) is locally asymptotically stable.

Proof of Eq. (4.25) in Theorem 4.1. Consider the closed-loop system of Eq. (4.24) and note that the terms in the right-hand-side of the x_{f} subsystem constitute an $O(\epsilon)$ approximation to the term $\mathcal{A}_{\mathrm{f}\epsilon}x_{\mathrm{f}}$. Consider also the following linear stochastic system:

$$\epsilon\frac{d\bar{x}_{\mathrm{f}}}{dt} \;=\; \mathcal{A}_{\mathrm{f}\epsilon}\bar{x}_{\mathrm{f}} + \epsilon\xi_{\mathrm{f}}. \tag{4.31}$$

Following a similar approach to the one employed in the proof of Theorem A.1 in [49, p. 361], we have that there exists an $\hat{\epsilon}^* > 0$ such that for all $\epsilon \in (0, \hat{\epsilon}^*]$, we have that:

$$x_{\mathrm{f}}(t) = \bar{x}_{\mathrm{f}}(t) + O(\sqrt{\epsilon}). \tag{4.32}$$

Based on the definition of $\|\mathrm{var}(x_{\mathrm{f}})\|^2$ in Eq. (4.14), we have the following estimate for $\|\mathrm{var}(x_{\mathrm{f}}(t))\|^2$:

$$\|\mathrm{var}(x_{\mathrm{f}}(t))\|^2 = \|\mathrm{var}(\bar{x}_{\mathrm{f}}(t) + O(\sqrt{\epsilon}))\|^2 \leq 2\|\mathrm{var}(\bar{x}_{\mathrm{f}}(t))\|^2 + O(\epsilon). \tag{4.33}$$

Furthermore, $\|\mathrm{var}(x_{\mathrm{f}}(t))\|^2$ and $\|\mathrm{var}(\bar{x}_{\mathrm{f}}(t))\|^2$ are equal to the traces of the covariance matrices of $x_{\mathrm{f}}(t)$ and $\bar{x}_{\mathrm{f}}(t)$, $P_{\mathrm{f}}(t) = \langle x_{\mathrm{f}}(t)x_{\mathrm{f}}(t)^T\rangle$ and $\bar{P}_{\mathrm{f}}(t) = \langle \bar{x}_{\mathrm{f}}(t)\bar{x}_{\mathrm{f}}(t)^T\rangle$, respectively. Finally, for $t > t_{\mathrm{b}}$ (where t_b is the time needed for $P_{\mathrm{f}}(t)$ and $\bar{P}_{\mathrm{f}}(t)$ to converge to their stead-state values and $t_b \to 0$ as $\epsilon \to 0$), $P_{\mathrm{f}}(t)$ and $\bar{P}_{\mathrm{f}}(t)$ converge to $P_{\mathrm{f}}(\infty)$ and $\bar{P}_{\mathrm{f}}(\infty)$, respectively (both $P_{\mathrm{f}}(\infty)$ and $\bar{P}_{\mathrm{f}}(\infty)$ are bounded quantities which follows from closed-loop stability). Because $\mathcal{A}_{\mathrm{f}\epsilon}$ is a diagonal matrix, the trace of matrix $\bar{P}_{\mathrm{f}}$

can be computed as follows [60]:

$$Tr\{\bar{P}_{\rm f}\} = \frac{\epsilon}{2}\sum_{i=1}^{\infty}\left|\frac{1}{\lambda_{\epsilon i}}\right| \tag{4.34}$$

where $\lambda_{\epsilon i}$ ($i = 1, 2, \ldots, \infty$) are the eigenvalues of the matrix $\mathcal{A}_{{\rm f}\epsilon}$ in Eq. (4.31). According to Assumption 4.1, $\sum_{i=1}^{\infty}\left|\frac{1}{\lambda_{\epsilon i}}\right|$ converges to a finite positive number, and thus, there exists a positive real number $k_{{\rm f}\epsilon}$ such that

$$Tr\{\bar{P}_{\rm f}\} < \frac{\epsilon}{2}k_{{\rm f}\epsilon}. \tag{4.35}$$

Therefore, it follows that

$$Tr\{\bar{P}_{\rm f}\} = \|{\rm var}(\bar{x}_{\rm f})\|^2 = O(\epsilon). \tag{4.36}$$

According to Eq. (4.33), it follows that the $\|{\rm var}(x_{\rm f})\|^2$ is $O(\epsilon)$. This completes the proof of Eq. (4.25) in Theorem 4.1. □

Proof of Eq. (4.26) in Theorem 4.1. Consider the $x_{\rm s}$ subsystem of the closed-loop system of Eq. (4.24). First, we note that there exists a positive real number k_{1s} such that [23, 19]

$$\|\mathcal{F}_{\rm s}(x_{\rm s}, x_{\rm f}) - \mathcal{F}_{\rm s}(x_{\rm s}, 0)\| < k_{1s}\|x_{\rm f}\| \tag{4.37}$$

where the definition of the vector norm can be found in Eq. (4.13). From Eq. (4.32), we have the following estimate for $\|x_{\rm f}\|$ for $t \geq t_{\rm b}$ (where $t_{\rm b}$ is the time needed for

$\|\bar{x}_{\mathrm{f}}(t)\|$ to approach zero and $t_b \to 0$ as $\epsilon \to 0$):

$$\|x_{\mathrm{f}}(t)\| = O(\sqrt{\epsilon}). \tag{4.38}$$

This implies that we have the following estimate for $\|\mathcal{F}_{\mathrm{s}}(x_{\mathrm{s}}, x_{\mathrm{f}}) - \mathcal{F}_{\mathrm{s}}(x_{\mathrm{s}}, 0)\|$ for $t \geq t_{\mathrm{b}}$:

$$\|\mathcal{F}_{\mathrm{s}}(x_{\mathrm{s}}, x_{\mathrm{f}}) - \mathcal{F}_{\mathrm{s}}(x_{\mathrm{s}}, 0)\| = O(\sqrt{\epsilon}). \tag{4.39}$$

Therefore, the solution of the following system consists an $O(\sqrt{\epsilon})$ approximation of the x_{s} of Eq. (4.24) [49, Theorem A.1, p. 361]:

$$\frac{d\bar{x}_{\mathrm{s}}}{dt} = \mathcal{A}_{\mathrm{cs}}\bar{x}_{\mathrm{s}} + \xi_{\mathrm{s}}. \tag{4.40}$$

In particular, there exists an $\hat{\epsilon}^{**} > 0$ such that for all $\epsilon \in (0, \hat{\epsilon}^{**}]$, it holds that:

$$x_{\mathrm{s}}(t) - \bar{x}_{\mathrm{s}}(t) = O(\sqrt{\epsilon}) \tag{4.41}$$

and

$$\begin{aligned} \|\mathrm{var}(x_{\mathrm{s}}(t))\|^2 - \|\mathrm{var}(\bar{x}_{\mathrm{s}}(t))\|^2 &= \langle \|x_{\mathrm{s}}(t)\|^2 - \|\bar{x}_{\mathrm{s}}(t)\|^2 \rangle \\ &= \langle (\|x_{\mathrm{s}}(t)\| - \|\bar{x}_{\mathrm{s}}(t)\|)(\|x_{\mathrm{s}}(t)\| + \|\bar{x}_{\mathrm{s}}(t)\|) \rangle \\ &= O(\sqrt{\epsilon}). \end{aligned} \tag{4.42}$$

Note that it is assumed that the controller of Eqs. (4.19) and (4.21) can successfully

drive the norm of the variance of x_{s} of the system of Eq. (4.20) to track the reference trajectory, which means the following equation holds:

$$\|\mathrm{var}(\bar{x}_{\mathrm{s}}(t))\|^2 = \|\mathrm{var}(x_{\mathrm{s}}^*(t))\|^2 \tag{4.43}$$

Based on Eqs. (4.42) and (4.43), we immediately have that in the closed-loop infinite-dimensional system of Eq. (4.24), the following holds:

$$\|\mathrm{var}(x_{\mathrm{s}}(t))\|^2 = \|\mathrm{var}(x_{\mathrm{s}}^*(t))\|^2 + O(\sqrt{\epsilon}). \tag{4.44}$$

This completes the proof of Eq. (4.26) in Theorem 4.1. □

Proof of Eq. (4.27) in Theorem 4.1. According to Eq. (4.14), we have the following equation for $\|\mathrm{var}(x(t))\|^2$ in Eq. (4.24):

$$\|\mathrm{var}(X(t))\|^2 = \|\mathrm{var}(x_{\mathrm{s}}(t))\|^2 + \|\mathrm{var}(x_{\mathrm{f}}(t))\|^2. \tag{4.45}$$

Using Eqs. (4.25) and (4.26), we have:

$$\|\mathrm{var}(X(t))\|^2 = \|\mathrm{var}(x_{\mathrm{s}}^*(t))\|^2 + O(\sqrt{\epsilon}) + O(\epsilon). \tag{4.46}$$

Since as $\epsilon \longrightarrow 0$, it holds that:

$$\frac{O(\epsilon)}{O(\sqrt{\epsilon})} \longrightarrow 0. \tag{4.47}$$

The $O(\epsilon)$ term in Eq. (4.46) is very small relative to the term $O(\sqrt{\epsilon})$ and can be neglected. Thus, there exists an $\epsilon^* = min(\hat{\epsilon}^*, \hat{\epsilon}^{**})$ such that if $\epsilon \in (0, \epsilon^*]$, then

$$\|\text{var}(X(t))\|^2 = \|\text{var}(x_s^*(t))\|^2 + O(\sqrt{\epsilon}). \tag{4.48}$$

This completes the proof of Theorem 4.1. ■

4.3 Simulation results

In this section, we present applications of the proposed model predictive controller to both the stochastic PDE model and the kinetic Monte Carlo model of a sputtering process. Since the physical interpretation of the state variance of a stochastic PDE is the expected roughness of the surface modeled by the stochastic PDE, we will use the expected surface roughness as the control objective in the simulation study. By applying the MPC to the stochastic KSE, we demonstrate that the nonlinear MPC is able to regulate the expected surface roughness of the process modeled by the stochastic KSE to a desired level and the proposed predictive controller possesses good robustness properties against model uncertainties. To demonstrate the applicability of the proposed predictive control method to control surfaces directly formed by microscopic events, we also apply the predictive controller to the kinetic Monte Carlo model of a sputtering process to demonstrate that the controller designed based on the stochastic KSE model of the process can regulate the surface roughness of the

kinetic Monte Carlo model of the same process to a desired level.

4.3.1 Model predictive control of the stochastic Kuramoto-Sivashinsky equation

In this section, we present applications of the proposed predictive controller to a stochastic KSE. The stochastic KSE is a fourth-order nonlinear stochastic partial differential equation that describes the evolution of the height fluctuation for surfaces in a variety of material preparation processes including surface erosion by ion sputtering [26, 53] and surface smoothing by energetic clusters [42]. We consider the following stochastic KSE with spatially distributed control:

$$\frac{\partial h}{\partial t} = -\nu \frac{\partial^2 h}{\partial x^2} - \kappa \frac{\partial^4 h}{\partial x^4} + \frac{\lambda}{2}\left(\frac{\partial h}{\partial x}\right)^2 + \sum_{i=1}^{p} \hat{b}_i(x) u_i(t) + \xi'(x,t) \tag{4.49}$$

where u_i is the ith manipulated input, p is the number of manipulated inputs, $\hat{b}_i$ is the ith actuator distribution function (i.e., $\hat{b}_i$ determines how the control action computed by the ith control actuator, u_i, is distributed (e.g., point or distributed actuation) in the spatial interval $[-\pi, \pi]$), $\nu = 1.975 \times 10^{-4}$, $\kappa = 1.58 \times 10^{-4}$, $\lambda = 1.975 \times 10^{-4}$, $x \in [-\pi, \pi]$ is the spatial coordinate, t is the time, $h(x,t)$ is the height of the surface at position x and time t and $\xi'(x,t)$ is a Gaussian white noise with zero mean and unit covariance:

$$\langle \xi'(x,t)\xi'(x',t')\rangle = \delta(x-x')\delta(t-t'). \tag{4.50}$$

Eq. (4.49) is subject to periodic boundary conditions (PBCs):

$$\frac{\partial^j h}{\partial x^j}(-\pi, t) = \frac{\partial^j h}{\partial x^j}(\pi, t), \quad j = 0, 1, 2, 3, \tag{4.51}$$

and the initial condition $h(x, 0) = 0$. The parameters of the KSE are selected such that $\kappa < \nu$ so that there is one positive eigenvalue of the linear operator and the zero solution of the open-loop system is unstable. Note that although a uniform initial condition is used in this simulation, non-uniform initial conditions can be handled by the MPC formulation proposed in this chapter in the same way. A 200th order stochastic ODE of Eq. (4.49) obtained via Galerkin's method is used to simulate the process (the use of higher-order approximations led to identical numerical results, thereby implying that the following simulation runs are independent of the discretization). The Dirac delta function involved in the covariances of ξ_α^n and ξ_β^n is approximated by $\frac{1}{\Delta t}$, where Δt is the integration time step.

Eigenvalue problem

To study the dynamics of Eq. (4.49), we initially consider the eigenvalue problem of the linear operator of Eq. (4.49), which takes the form:

$$\begin{gathered} A\bar{\phi}_n(x) = -\nu \frac{d^2\bar{\phi}_n(x)}{dx^2} - \kappa \frac{d^4\bar{\phi}_n(x)}{dx^4} = \lambda_n \bar{\phi}_n(x), \\ \frac{d^j\bar{\phi}_n}{dx^j}(-\pi) = \frac{d^j\bar{\phi}_n}{dx^j}(\pi), \\ j = 0, 1, 2, 3, \quad n = 1, 2, \ldots, \infty, \end{gathered} \tag{4.52}$$

where λ_n denotes an eigenvalue and $\bar{\phi}_n$ denotes an eigenfunction. A direct computation of the solution of the above eigenvalue problem yields $\lambda_0 = 0$ with $\psi_0 = 1/\sqrt{2\pi}$, and $\lambda_n = \nu n^2 - \kappa n^4$ (λ_n is an eigenvalue of multiplicity two) with eigenfunctions $\phi_n = (1/\sqrt{\pi})\sin(nx)$ and $\psi_n = (1/\sqrt{\pi})\cos(nx)$ for $n = 1, \ldots, \infty$. Note that the $\bar{\phi}_n$ in Eq. (4.52) denotes either ϕ_n or ψ_n. From the expression of the eigenvalues, it follows that for fixed values of $\nu > 0$ and $\kappa > 0$, the number of unstable eigenvalues of the operator A in Eq. (4.52) is finite and the distance between two consecutive eigenvalues (i.e., λ_n and λ_{n+1}) increases as n increases.

We then derive nonlinear stochastic ODE formulations of Eq. (4.49) using Galerkin's method. By substituting the expansion of $h(x,t)$ in terms of the eigenfunctions into Eq. (4.49) and taking the inner product with the adjoint eigenfunctions, the following system of infinite nonlinear stochastic ODEs is obtained:

$$\begin{aligned} \frac{d\alpha_n}{dt} &= (\nu n^2 - \kappa n^4)\alpha_n + f_{n\alpha} + \sum_{i=1}^{p} b_{i\alpha_n} u_i(t) + \xi_\alpha^n(t), \quad n = 1, 2, \ldots, \infty, \\ \frac{d\beta_n}{dt} &= (\nu n^2 - \kappa n^4)\beta_n + f_{n\beta} + \sum_{i=1}^{p} b_{i\beta_n} u_i(t) + \xi_\beta^n(t), \quad n = 0, 1, \ldots, \infty. \end{aligned} \tag{4.53}$$

The control objective is the expected value of the surface roughness, r, which is modeled by the stochastic KSE and is represented by the standard deviation of the surface from its average height and is computed as follows:

$$\langle r^2(t) \rangle = \left\langle \frac{1}{2\pi} \int_{-\pi}^{\pi} [h(x,t) - \bar{h}(t)]^2 dx \right\rangle \tag{4.54}$$

where $\bar{h}(t) = \frac{1}{2\pi}\int_{-\pi}^{\pi} h(x,t)dx$ is the average surface height. The expected surface roughness, $\langle r^2(t)\rangle$ can be rewritten in terms of $\alpha_n(t)$ and $\beta_n(t)$ as follows:

$$\begin{aligned}
\langle r^2(t)\rangle &= \frac{1}{2\pi}\left\langle \int_{-\pi}^{\pi} (h(x,t)-\bar{h}(t))^2 dx \right\rangle \\
&= \frac{1}{2\pi}\left\langle \int_{-\pi}^{\pi} \left[\sum_{i=1}^{\infty}\alpha_i(t)\phi_i(x) + \sum_{i=0}^{\infty}\beta_i(t)\psi_i(x) - \beta_0(t)\psi_0\right]^2 dx \right\rangle \\
&= \frac{1}{2\pi}\left\langle \int_{-\pi}^{\pi} \sum_{i=1}^{\infty}\left[\alpha_i^2(t)\phi_i(x)^2 + \beta_i^2(t)\psi_i(x)^2\right] dx \right\rangle \\
&= \frac{1}{2\pi}\left\langle \sum_{i=1}^{\infty}(\alpha_i^2(t)+\beta_i^2(t)) \right\rangle = \frac{1}{2\pi}\sum_{i=1}^{\infty}\left[\langle\alpha_i^2(t)\rangle + \langle\beta_i^2(t)\rangle\right].
\end{aligned} \tag{4.55}$$

Therefore, the control problem of the expected surface roughness is equivalent to the state covariance control of the stochastic KSE. The proposed predictive control method can be applied to regulate the expected surface roughness.

Open-loop dynamics of the stochastic KSE

In the first simulation, we compute the expected value of open-loop surface roughness profile from the solution of the stochastic KSE of Eq. (4.49) by setting $u_i(t) = 0$ for $i = 1, \dots, p$. For $\nu = 1.975 \times 10^{-4}$ and $\kappa = 1.58 \times 10^{-4}$, the stochastic KSE possesses one positive eigenvalue. Therefore, the zero solution of the open-loop system is unstable. Surface roughness profiles obtained from 100 independent simulation runs using the same parameters are averaged and the resulting surface roughness profile is shown in Figure 4.1. The value of the open-loop surface roughness increases due to the

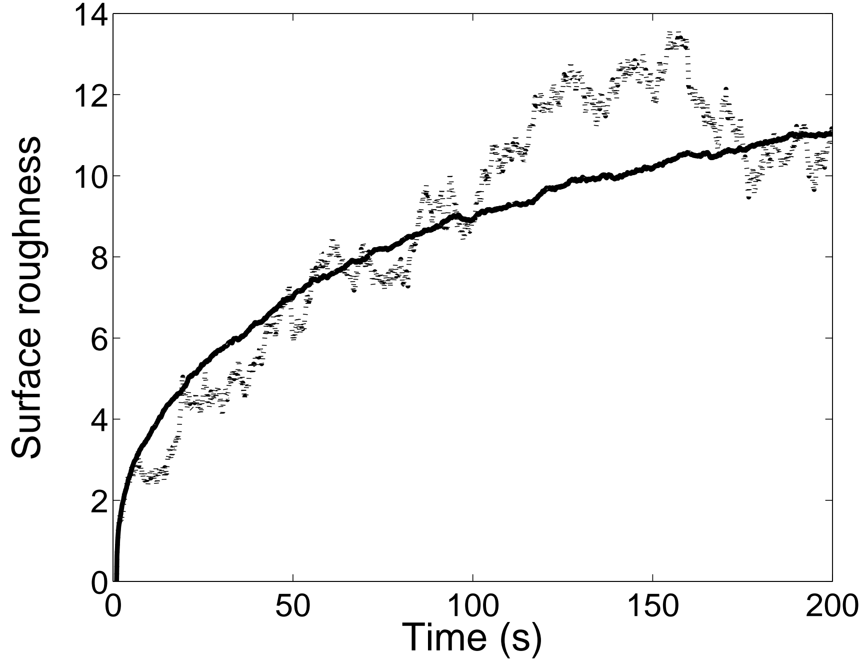

Figure 4.1: Comparison of the open-loop expected surface roughness profile computed by averaging 100 independent simulation runs (solid line) and that from a single simulation run (dotted line) of the stochastic KSE of Eq. (4.49).

open-loop instability of the zero solution. On the other hand, due to the existence of the nonlinear term, the open-loop surface roughness does not increase exponentially but it is bounded.

Model reduction

Following the same way of model reduction of Eq. (4.9), we rewrite the system of Eq. (4.53) as follows:

$$
\begin{aligned}
\frac{dx_{\mathrm{s}}}{dt} &= \Lambda_{\mathrm{s}} x_{\mathrm{s}} + f_{\mathrm{s}}(x_{\mathrm{s}}, x_{\mathrm{f}}) + B_{\mathrm{s}} u + \xi_{\mathrm{s}}, \\
\frac{dx_{\mathrm{f}}}{dt} &= \Lambda_{\mathrm{f}} x_{\mathrm{f}} + f_{\mathrm{f}}(x_{\mathrm{s}}, x_{\mathrm{f}}) + B_{\mathrm{f}} u + \xi_{\mathrm{f}},
\end{aligned}
\tag{4.56}
$$

where $x_{\rm s} = [\alpha_1 \ \ldots \ \alpha_m \ \beta_1 \ \ldots \ \beta_m]^T$, $x_{\rm f}$=$[\alpha_{m+1} \ \beta_{m+1} \ \ldots \ ]^T$, $\Lambda_{\rm s}$=diag$[\lambda_1 \ \ldots \ \lambda_m \ \lambda_1 \ \ldots \ \lambda_m]$, $\Lambda_{\rm f}$ = diag$[\lambda_{m+1} \ \lambda_{m+1} \ \lambda_{m+2} \ \lambda_{m+2} \ \ldots]$, $f_{\rm s}(x_{\rm s}, x_{\rm f}) = [f_{1\alpha}(x_{\rm s}, x_{\rm f}) \ \ldots \ f_{m\alpha}(x_{\rm s}, x_{\rm f}) \ f_{1\beta}(x_{\rm s}, x_{\rm f}) \ \ldots \ f_{m\beta}(x_{\rm s}, x_{\rm f})]^T$, $f_{\rm f}(x_{\rm s}, x_{\rm f}) = [f_{m+1\alpha}(x_{\rm s}, x_{\rm f}) \ f_{m+1\beta}(x_{\rm s}, x_{\rm f}) \ \ldots \ ]^T$, $u = [u_1 \ \ldots \ u_p]$, $\xi_{\rm s} = [\xi_\alpha^1 \ \ldots \ \xi_\alpha^m \ \xi_\beta^1 \ \ldots \ \xi_\beta^m]$, and $\xi_{\rm f} = [\xi_\alpha^{m+1} \ \xi_\beta^{m+1} \ \ldots]$,

$$B_{\rm s} = \begin{bmatrix} b_{1_{\alpha_1}} & \ldots & b_{p_{\alpha_1}} \\ \vdots & \ddots & \vdots \\ b_{1_{\alpha_m}} & \ldots & b_{p_{\alpha_m}} \\ b_{1_{\beta_1}} & \ldots & b_{p_{\beta_1}} \\ \vdots & \ddots & \vdots \\ b_{1_{\beta_m}} & \ldots & b_{p_{\beta_m}} \end{bmatrix}, \quad B_{\rm f} = \begin{bmatrix} b_{1_{\alpha_{m+1}}} & \ldots & b_{p_{\alpha_{m+1}}} \\ b_{1_{\beta_{m+1}}} & \ldots & b_{p_{\beta_{m+1}}} \\ b_{1_{\alpha_{m+2}}} & \ldots & b_{p_{\alpha_{m+2}}} \\ b_{1_{\beta_{m+2}}} & \ldots & b_{p_{\beta_{m+2}}} \\ \vdots & \vdots & \vdots \end{bmatrix}. \tag{4.57}$$

We note that the subsystem $x_{\rm f}$ in Eq. (4.56) is infinite-dimensional. Neglecting the $x_{\rm f}$ subsystem, the following $2m$-dimensional system is obtained:

$$\frac{d\tilde{x}_{\rm s}}{dt} = \Lambda_{\rm s}\tilde{x}_{\rm s} + f_{\rm s}(\tilde{x}_{\rm s}, 0) + B_{\rm s}u + \xi_{\rm s} \tag{4.58}$$

where the tilde symbol in $\tilde{x}_{\rm s}$ denotes that this state variable is associated with a finite-dimensional system.

Nonlinear predictive control of the stochastic KSE

In this closed-loop simulation, we design a predictive controller based on a 10th order stochastic ODE approximation constructed by using the first 10 eigenmodes of the system of Eq. (4.49). Ten control actuators are used to control the system. The ith actuator distribution function is taken to be:

$$b_i(z) = \begin{cases} \frac{1}{\sqrt{\pi}} \sin(iz), & i = 1, \dots, 5, \\ \frac{1}{\sqrt{\pi}} \cos[(i-5)z], & i = 6, \dots, 10. \end{cases} \tag{4.59}$$

Under this control problem formulation, $m = 5$ and the value of $\epsilon = |\lambda_1|/|\lambda_{11}| = 4.21 \times 10^{-4}$. Our desired expected value of the surface roughness is 4.28. A reference trajectory for the expected surface roughness is constructed and is shown by the dotted line in Figure 4.2. Closed-loop simulations are performed to study the evolution of the expected value of the surface roughness under predictive control. To further simplify the computation, the predictive controller is solved by assuming that all the closed-loop poles of the finite-dimensional system are equal to each other. Closed-loop surface roughness profiles obtained from 100 independent simulation runs using the same simulation parameters are averaged and the resulting surface roughness profile is shown in Figure 4.2 (solid line) and it is compared with the reference trajectory (dotted line). We can see that the controller successfully drives the surface roughness to the desired level, which is lower than that corresponding to open-loop operation ($u_i(t) = 0$, $i = 1, \dots, 10$) shown in Figure 4.1.

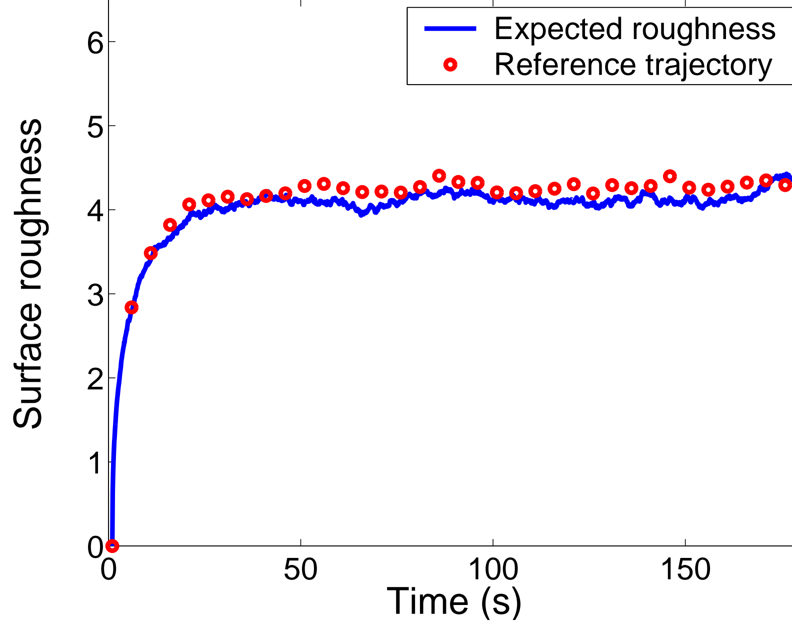

Figure 4.2: The closed-loop profile of the expected value of the surface roughness of the nonlinear KSE under predictive control (solid line) versus the reference trajectory.

Robustness properties of the predictive controller

In this subsection, we demonstrate the good robustness properties of the model predictive controller against parameter uncertainties of the stochastic KSE process model. To this end, we consider significant uncertainty in the parameters of the stochastic KSE process model. Specifically, the controller is designed based on the stochastic KSE model with the following parameters, $\nu_m = 1.975 \times 10^{-4}$, $\kappa_m = 1.58 \times 10^{-4}$, and $\lambda_m = 1.975 \times 10^{-4}$, where the subscript m denotes that the parameter is used by the model predictive controller design. However, the parameters of the stochastic KSE to which the predictive controller is applied are, $\nu = 1.5\nu_m$, $\kappa = 0.5\kappa_m$, and $\lambda = 1.2\lambda_m$, which correspond to a 50% uncertainty associated with ν and κ and a 20% uncertainty associated with λ. Both the proposed predictive controller and the

pole placement covariance controller proposed in [62] are applied to the stochastic KSE model with the model uncertainties, and the simulation results are shown in Figure 4.3. It is clear that the pole placement covariance controller developed in [62] fails to regulate the expected surface roughness to the desired level, but the predictive controller successfully regulates the expected surface roughness to the desired level in the presence of significant model uncertainties.

Remark 4.2 *Note that in the pole placement covariance controller [62], the closed-loop poles are determined based on the stochastic KSE model and the desired expected surface roughness through an off-line design procedure. When there are model errors, the errors will propagate to the closed-loop poles of the controller which results in a deteriorated closed-loop performance. In the proposed predictive controller, the closed-loop poles are computed by solving an on-line optimization problem. The on-line solution of the optimization problem provides a feedback mechanism which compensates for the effect of model errors on the performance of the closed-loop system.*

4.3.2 Model predictive control of an ion-sputtering process

In this section, we apply the MPC algorithm to an ion-sputtering process, of which the dynamics can be described by the stochastic KSE. The detailed process description of the sputtering process is given in Section 3.2.1 in Chapter 3.

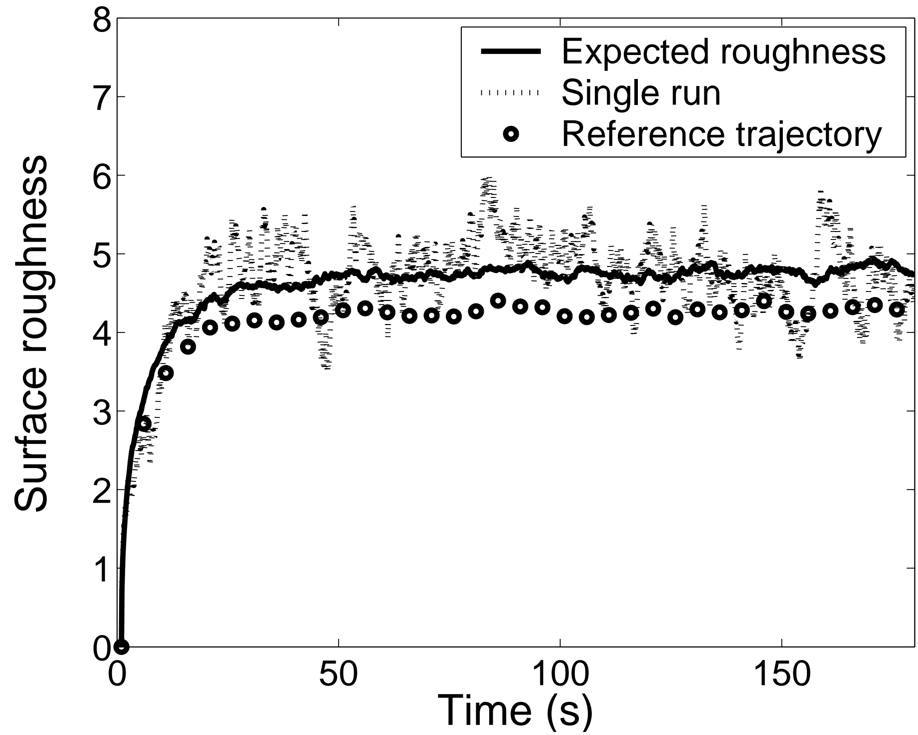

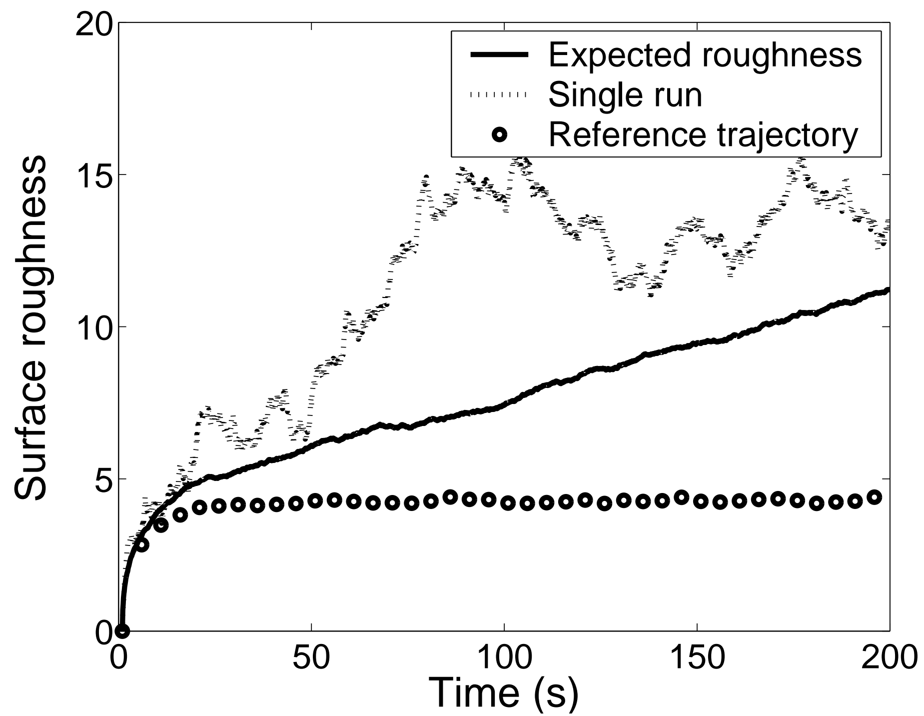

Figure 4.3: Comparison of the expected closed-loop surface roughness of the nonlinear KSE under the proposed predictive controller (top figure) and under the nonlinear pole placement controller developed in [62] (bottom figure). Effect of model uncertainty.

Necessity of spatially distributed control

Both spatially distributed control configuration [61, 60, 62] and spatially invariant control configuration [57, 58, 71] could be used to control the surface roughness of various material preparation processes. However, the selection of control configurations in the previous works was largely arbitrary and was not guided by the characteristics of the specific process considered. In this section, we investigate the necessity and effectiveness of spatially distributed control configuration in the context of control of processes described by nonlinear stochastic PDEs.

For the ion-sputtering process considered in this section, we consider the manipulated input as either the surface bombardment rate or the substrate temperature. We will demonstrate through the kMC simulation of the sputtering process that a desired expected surface roughness value, 0.3, cannot be achieved by manipulating either the substrate temperature or the surface bombardment rate as a spatially invariant process input, but can be achieved by manipulating the surface bombardment rate as a spatially distributed process input.

In the first set of simulation runs, we compute the expected surface roughness profiles of the sputtering process during the erosion of the first 1000 monolayers under different substrate temperature. In all simulation runs, $f = 0.5$ and $\beta J = J/k_{\mathrm{B}}T$ changes from 0.05 to 5. Note that in each simulation run, the substrate temperature is spatially invariant and constant. The surface roughness is calculated as the standard deviation of the surface height profile. In the kMC simulation, the formula to compute

the surface roughness is as follows

$$r = \sqrt{\frac{1}{L}\sum_{i=1}^{L}(h_i - \bar{h})^2} \tag{4.60}$$

where L denotes the number of the lattice sites on the lateral direction and $\bar{h}$ denotes the averaged value of the surface height among all lattice sites.The expected surface roughness is the average of surface roughness profiles obtained from 100 independent runs.

Figure 4.4 shows a comparison of the expected surface roughness profiles under different temperatures. It is clear that although the expected surface roughness can be reduced by decreasing the temperature (or increasing the value of βJ), the reduction is quite limited. Furthermore, it can be observed that the minimum expected surface roughness that can be achieved by manipulating the substrate temperature as a spatially invariant process input is around 0.5, which is much higher than the desired surface roughness of 0.3 in this case study.

In the second set of simulation runs, we compute the expected surface roughness profiles of the sputtering process during the erosion of the first 1000 monolayers under different values of the erosion probability, f. In all simulation runs, the substrate temperature is fixed such that $\beta J = 2$ and the probability that a selected surface particle is subjected to erosion, f, changes from 0.1 to 0.6. Note that in each simulation run, the value of f is fixed. The erosion probability can be changed by varying the surface

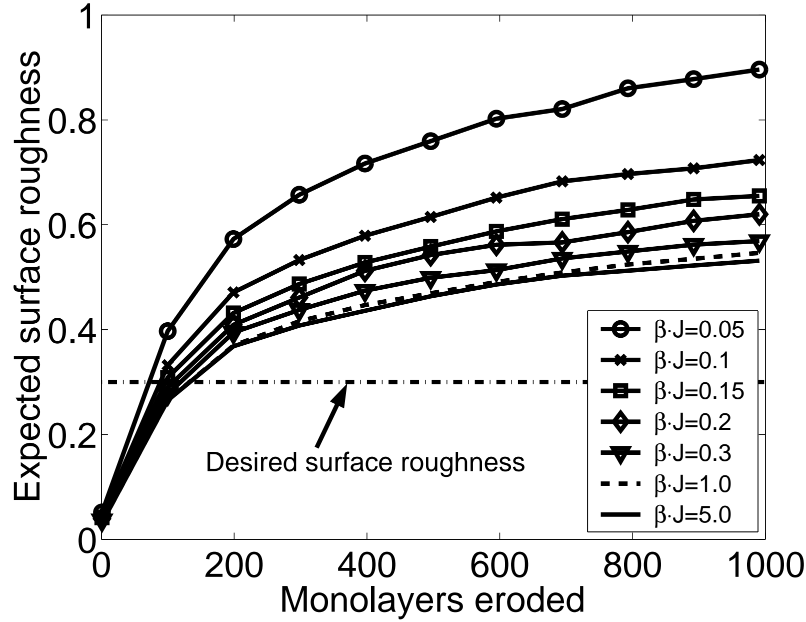

Figure 4.4: Comparison of the open-loop profile of the expected surface roughness from the kMC simulator when $f = 0.5$ and βJ varies from 0.05 to 5.

bombardment rate [39]. In this study, the change of f from 0.1 to 0.6 corresponds to the change of surface bombardment rate from 0.1 $s^{-1}site^{-1}$ to 1.5 $s^{-1}site^{-1}$.

Figure 4.5 shows the comparison of the expected surface roughness profiles under different values of f. Again, although the expected surface roughness can be reduced by decreasing the value of f, the reduction is quite limited. It can be observed that the minimum expected surface roughness that can be achieved by manipulating the surface bombardment rate as a spatially invariant process input is around 0.5, which is higher than the desired surface roughness of 0.3 in this case study.

Finally, we consider a case where f is spatially invariant but is time-varying. Specifically, for each monolayer eroded, $f = 0.1$ for the first half monolayer and $f = 0.6$ for another half monolayer. We compute the expected surface roughness profiles

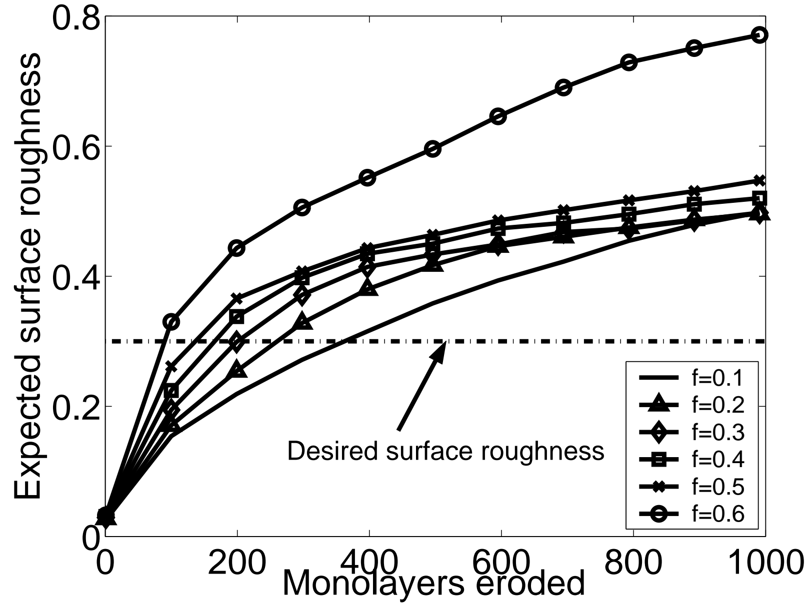

Figure 4.5: Comparison of the open-loop profile of the expected surface roughness from the kMC simulator when $\beta J = 2$ and f varies from 0.1 to 0.6.

of the sputtering process during the erosion of the first 800 monolayers under this time-varying erosion probability, f. In all simulation runs, the substrate temperature is fixed such that $\beta J = 2$. Figure 4.6 shows the profile of the expected surface roughness under this operation. The profile is also compared to those under fixed values of f ($f = 0.1$ and $f = 0.6$). It can be observed that when f is time-varying between 0.1 and 0.6, the resulted expected surface roughness profile is between the profiles obtained under fixed values of $f = 0.1$ and $f = 0.6$. Although time-varying inputs are useful for surface processing in certain applications, they are not effective in reducing the surface roughness of the sputtering process considered in this chapter. The surface roughness obtained from this time-varying input is around 0.5 and is also higher than the desired surface roughness of 0.3.

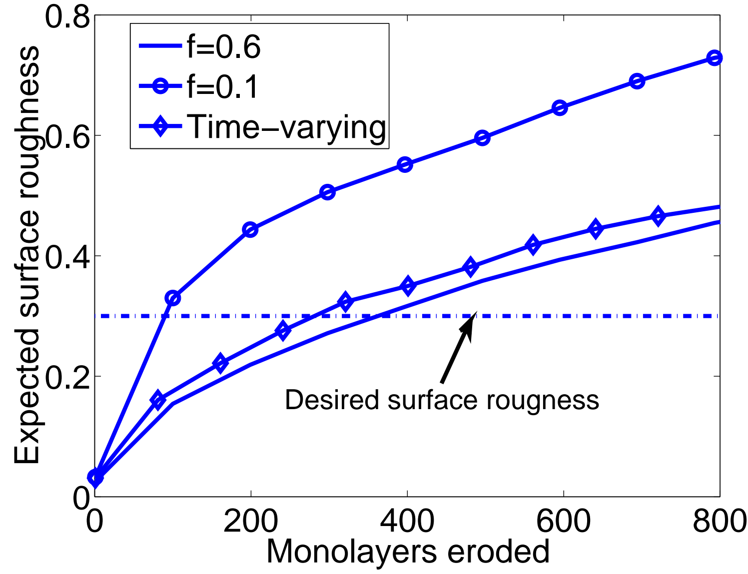

Figure 4.6: Comparison of open-loop profiles of the expected surface roughness from the kMC simulator when $\beta J = 2$ and f is 1) $f = 0.6$, 2) $f = 0.1$, and 3) time-varying.

Based on the simulation results shown in this subsection, it can be concluded that reduction of the expected surface roughness of the sputtering process by manipulation either of the substrate temperature or of the surface bombardment rate as a spatially invariant process input is very limited, and, in the case studies, the desired surface roughness which is 0.3, cannot be achieved. In the following subsection, we will demonstrate that this limitation can be overcome by the proposed nonlinear controller designed based on the stochastic KSE process model, which uses spatially distributed control actuation. To this end, we consider a sputtering process with fixed substrate temperature ($\beta J = 2$) and control the expected surface roughness to the desired value by manipulating the spatially distributed surface bombardment rate across the surface.

Remark 4.3 *Note that we focus on the predictive control of surface roughness in processes that can be modeled by nonlinear stochastic PDEs so that a pre-specified surface roughness can be achieved. For a specific material preparation process, the desired surface roughness should be determined based on the process characteristics and the product specifications. Detailed discussion on the selection of desired surface roughness for a variety of existing thin film deposition and sputtering processes is beyond the scope of this work.*

The stochastic KSE model with spatially distributed control

In the remainder of this section, a stochastic KSE model will be identified using surface snapshots generated by the kMC simulation of the sputtering process and the spatially distributed control action will be computed using the proposed model predictive controller designed on the basis of the identified stochastic KSE model.

The equation for the height fluctuations of the surface in this sputtering process was derived in [53] and is a stochastic KSE of the form of Eq. (4.61):

$$\frac{\partial h}{\partial t} = -\nu \frac{\partial^2 h}{\partial x^2} - \kappa \frac{\partial^4 h}{\partial x^4} + \frac{\lambda}{2}\left(\frac{\partial h}{\partial x}\right)^2 + \xi(x,t) \tag{4.61}$$

where $x \in [-\pi, \pi]$ is the spatial coordinate, t is the time, $h(x,t)$ is the height of the surface at position x and time t, and $\xi(x,t)$ is a Gaussian noise with zero mean and covariance:

$$\langle \xi(x,t)\xi(x',t')\rangle = \sigma^2 \delta(x-x')\delta(t-t') \tag{4.62}$$

where σ is a constant. We note that this stochastic KSE representation for the surface morphological evolution in sputtering processes is limited to surface morphologies that do not involve re-entrant features; the re-entrant features could arise under certain sputtering conditions and are catastrophic for the surface. The values of the four parameters are obtained via least-squares fitting methods presented in Chapter 3: $\nu = 2.76 \times 10^{-5}$, $\kappa = 1.54 \times 10^{-7}$, $\lambda = 3.06 \times 10^{-3}$, and $\sigma^2 = 1.78 \times 10^{-5}$.

Model predictive control with distributed control action

In the closed-loop simulation, we design a predictive controller based on a 20th order stochastic ODE approximation constructed by using the first 20 eigenmodes of the linearized (around zero solution) stochastic PDE of Eq. (4.61). First we design a linear state feedback controller as follows:

$$u(t) \;=\; \mathcal{B}_{\mathrm{s}}^{-1}\left\{\left(\mathcal{A}_{\mathrm{cs}}(t)-\mathcal{A}_{\mathrm{s}}\right)\tilde{x}_{\mathrm{s}}(t)\right\} \tag{4.63}$$

where $\mathcal{A}_{\mathrm{cs}}(t) = \mathrm{diag}[\lambda_{\mathrm{c}1}(t)\ \ldots\ \lambda_{cm}(t)]$. $\lambda_{\mathrm{c}i}(t)$, $i = 1, 2, \ldots, m$ are time-varying, desired poles of the closed-loop finite-dimensional system and the poles $\lambda_{\mathrm{c}i}(t)$ are computed

by solving the following optimization problem:

$$\min_{\mathcal{A}_{\rm cs}(t)} \int_t^{t+T_{\rm p}} Q\|\mathrm{var}(x_{\rm s}) - \mathrm{var}(x_{\rm s}^*)\|^2 d\tau + Q_{\rm f}\|\mathrm{var}(x_{\rm s}(t+T_{\rm p})) - \mathrm{var}(x_{\rm s}^*(t+T_{\rm p}))\|^2$$

$$\text{subject to}$$

$$\frac{dx_{\rm s}}{dt} = \mathcal{A}_{\rm cs}(t)x_{\rm s} + \xi_{\rm s},$$

$$a_i < \lambda_i < b_i < 0, \quad i = 1, 2, \ldots, m. \tag{4.64}$$

Twenty control actuators are used to control the system. The ith actuator distribution function is taken to be:

$$b_i(z) = \begin{cases} \frac{1}{\sqrt{\pi}}\sin(iz), & i = 1, \ldots, 10, \\ \frac{1}{\sqrt{\pi}}\cos[(i-10)z], & i = 11, \ldots, 20. \end{cases} \tag{4.65}$$

Under this control problem formulation, $m = 10$ and the value of $\epsilon = |\lambda_1|/|\lambda_{21}| = 0.02$. Our desired expected value of the surface roughness is 0.3. To further simplify the computation, the predictive controller is solved by assuming that all the closed-loop poles of the finite-dimensional system are equal to each other. Note that the predictive controller of Eqs. (4.63) – (4.64) is the linearization around the zero solution of the predictive controller of Eqs. (4.19) – (4.21).

Then, we apply the designed predictive controller to the kMC model of the sputtering process to control the surface roughness to the desired level. In this simulation, the initial surface roughness is about 0.5 and the microstructure of the initial surface is shown in Figure 4.7. The controller is implemented by manipulating the probability

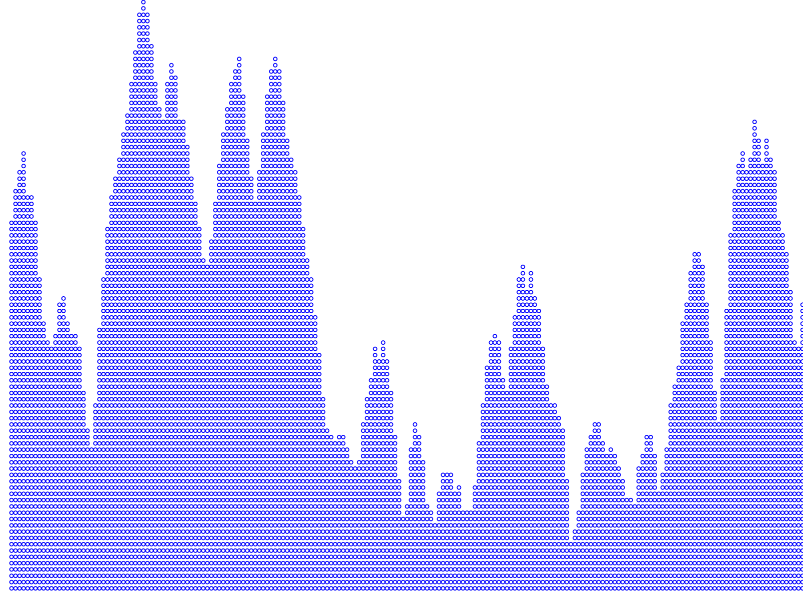

Figure 4.7: Surface micro-configuration at the beginning of the closed-loop simulation run. The initial surface roughness is 0.5.

that a randomly selected site is subject to erosion rule, f. Specifically, the f of site i is determined according to the following expression:

$$f(i) = \frac{\bar{f} + \left(\sum_{j=1}^{20} b_j(z_i)u_j(t)\right)/a}{1 + \left(\sum_{j=1}^{20} b_j(z_i)u_j(t)\right)/a}. \tag{4.66}$$

Closed-loop surface roughness profiles obtained from 100 independent simulation runs using the same simulation parameters are averaged and the resulting expected surface roughness profile is shown in Figure 4.8. We can see that the predictive controller drives the surface roughness very close to the desired level, which is lower than the surface roughness that can be achieved by manipulating the surface bombardment

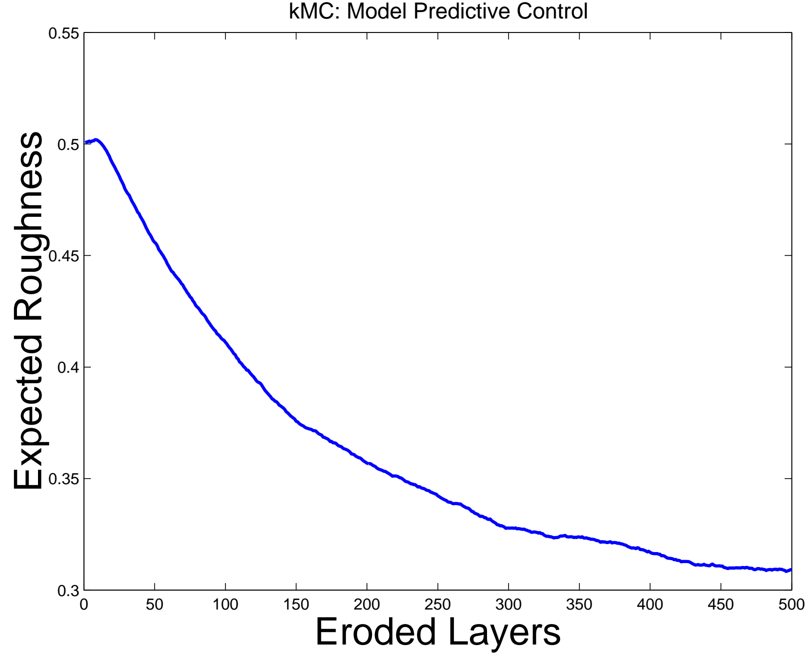

Figure 4.8: The closed-loop profile of the expected value of the surface roughness under predictive control.

rate in a spatially invariant manner.

The microstructure of the surface at the end of the closed-loop system simulation run is shown in Figure 4.9. It is clear that the proposed model predictive control results in a smoother closed-loop surface.

Remark 4.4 *Note that although the stochastic KSE model of Eq. (4.61) is a nonlinear model for the sputtering process, the linearization of the stochastic KSE around its zero solution is used to design the predictive controller of Eqs. (4.63) – (4.64). This is based on the following argument. Since the instability of the spatially uniform steady state comes from the linear part of the model, and the nonlinear part of the stochastic KSE helps bound the surface roughness, for control purposes, we only need*

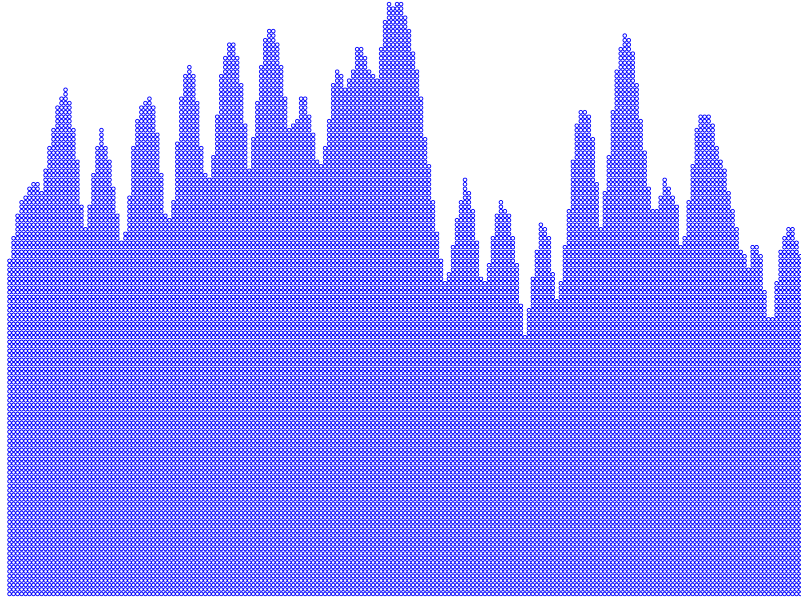

Figure 4.9: Surface micro-configuration at the end of the closed-loop simulation run under predictive control. The final surface roughness is around 0.3.

to focus on the stabilization of the linear part of the stochastic KSE. This argument is further supported by our simulation results, which demonstrate the effectiveness of the predictive controller designed in this chapter.

4.4 Conclusions

In this chapter, we presented a method for model predictive control of nonlinear stochastic PDEs to regulate the state variance to a desired level. Initially, a system of infinite nonlinear stochastic ODEs was derived from the nonlinear stochastic PDE by using Galerkin's method. To capture the dominant mode contribution, a finite-dimensional approximation of the stochastic ODE system was then derived. A model predictive control problem was formulated based on the approximation. This

enabled computationally efficient prediction of state variance of the finite-dimensional system. The control action was computed by minimizing an objective penalty function. To characterize the closed-loop performance enforced by the model predictive controller, an analysis of the closed-loop nonlinear infinite-dimensional system was provided. The predictive controller was initially applied to the stochastic KSE and resulted in successful control of the norm of the state variance to a desired level in the presence of significant model parameter uncertainties. In addition, the problem of surface roughness regulation in a one-dimensional ion-sputtering process including two surface micro-processes, diffusion and erosion, was considered. We established, through kMC simulations, that the spatially distributed control configuration was more effective for surface roughness regulation compared to the spatially invariant control configuration for this process. Then, we designed a model predictive controller based on an identified stochastic KSE surface model to control the surface roughness of the sputtering process by manipulating the surface bombardment rate in a spatially distributed manner. The predictive controller successfully regulated the expected surface roughness to a desired level in the kMC model of the sputtering process.

Chapter 5

Modeling and Control of Film Porosity

5.1 Introduction

In the previous chapters, our research work has focused on modeling and control of surface roughness (surface covariance). In this chapter, systematic methodologies are developed for modeling and control of film porosity in thin film deposition processes. Initially, a thin film deposition process which involves atom adsorption and migration is introduced and is modeled using a triangular lattice-based kMC simulator which allows porosity, vacancies and overhangs to develop and leads to the deposition of a porous film. Subsequently, appropriate definitions of film site occupancy ratio (SOR), i.e., fraction of film sites occupied by particles over total number of film sites, and

its fluctuations are introduced to describe film porosity. Then, deterministic and stochastic ODE models are derived that describe the time evolution of film SOR and its fluctuation. The coefficients of the ODE models are estimated on the basis of data obtained from the kMC simulator of the deposition process using least-square methods and their dependence on substrate temperature is determined. The developed ODE models are used as the basis for the design of model predictive control (MPC) algorithms that include penalty on the film SOR and its variance to regulate the expected value of film SOR at a desired level and reduce run-to-run fluctuations. Simulation results demonstrate the applicability and effectiveness of the proposed film porosity modeling and control methods in the context of the deposition process under consideration.

5.2 Thin film deposition process description and modeling

This section presents the description of the kMC algorithm of a thin film deposition process. Two microscopic processes are considered; atom adsorption and surface migration. Vacancies and overhangs are allowed in the kMC model to introduce porosity during the thin film growth. Substrate temperature and deposition rate are the macroscopic parameters which control the deposition process.

5.2.1 On-lattice kinetic Monte Carlo model of film growth

The thin film growth process considered in this chapter includes two microscopic processes: an adsorption process, in which particles are incorporated into the film from the gas phase, and a migration process, in which surface particles move to adjacent sites [56, 55, 92, 95]. Solid-on-solid (SOS) deposition models, in which vacancies and overhangs are forbidden, are frequently used to model thin film deposition processes [70, 62] and investigate the surface evolution of thin films. However, vacancies and overhangs must be incorporated in the process model to account for film porosity. Since SOS models are inadequate to model the evolution of thin film internal microstructure, a deposition process taking place in a triangular lattice is considered.

Specifically, the thin film growth model used in this chapter is an on-lattice kMC model in which all particles occupy discrete lattice sites. The on-lattice kMC model is valid for temperatures $T < 0.5T_{\rm m}$, where $T_{\rm m}$ is the melting point of the crystal. At high temperatures ($T \lesssim T_{\rm m}$), the particles cannot be assumed to be constrained on the lattice sites and the on-lattice model is not valid. In this chapter, a triangular lattice is selected to represent the crystalline structure of the film, as shown in Figure 5.1. All particles are modeled as identical hard disks and the centers of the particles deposited on the film are located on the lattice sites. The diameter of the particles equals the distance between two neighboring sites. The width of the lattice is fixed so that the lattice contains a fixed number of sites in the lateral direction. The new particles are always deposited from the top side of the lattice where the gas phase is located;

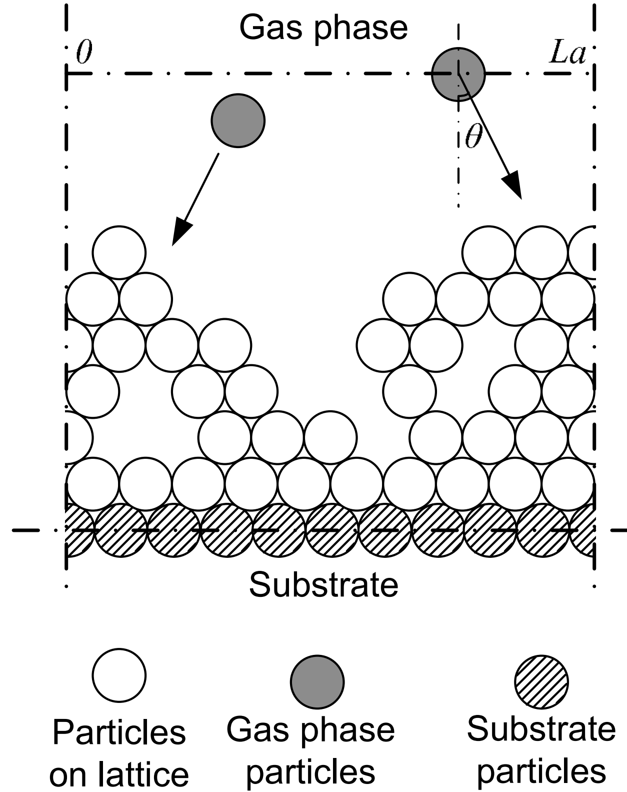

Figure 5.1: Thin film growth process on a triangular lattice.

see Figure 5.1. Particle deposition results in film growth in the direction normal to the lateral direction. The direction normal to the lateral direction is thus designated as the growth direction. The number of sites in the lateral direction is defined as the lattice size and is denoted by L. The lattice parameter, a, which is defined as the distance between two neighboring sites and equals the diameter of a particle (all particles have the same diameter), determines the lateral extent of the lattice, La.

The number of nearest neighbors of a site ranges from zero to six, the coordination number of the triangular lattice. A site with no nearest neighbors indicates an unadsorbed particle in the gas phase (i.e., a particle which has not been deposited

on the film yet). A particle with six nearest neighbors is associated with an interior particle that is fully surrounded by other particles and cannot migrate. A particle with one to five nearest neighbors is possible to diffuse to an unoccupied neighboring site with a probability that depends on its local environment. In the triangular lattice, a particle with only one nearest neighbor is considered unstable and is subject to instantaneous surface relaxation. Details of particle surface relaxation and migration will be discussed in Section 5.2.2 and 5.2.3 below.

In the simulation, a bottom layer in the lattice is initially set to be fully packed and fixed, as shown in Figure 5.1. There are no vacancies in this layer and the particles in this layer cannot migrate. This layer acts as the substrate for the deposition and is not counted in the computation of the number of the deposited particles, i.e., this fixed layer does not influence the film porosity (see Section 5.3 below).

Two types of microscopic processes (Monte Carlo events) are considered, an adsorption process and a migration process. These Monte Carlo events are assumed to be Poisson processes. All events occur randomly with probabilities proportional to their respective rates. The events are executed instantaneously upon selection and the state of the lattice remains unchanged between two consecutive events.

5.2.2 Adsorption process

In an adsorption process, an incident particle comes in contact with the film and is incorporated onto the film. The microscopic adsorption rate, W, which is in units

of layers per unit time, depends on the gas phase concentration. The layers in the unit of adsorption rate are densely packed layers, which contain L particles. With this definition, W is independent of L. In this chapter, the macroscopic adsorption rate, W, is treated as a process parameter. For the entire deposition process, the microscopic adsorption rate in terms of incident particles per unit time, which is denoted as r_{a}, is related to W as follows:

$$r_{\mathrm{a}} = LW \tag{5.1}$$

The incident particles are initially placed at random positions above the film lattice and move toward the lattice in random directions, as shown in Figure 5.1. The initial particle position, x_0, which is the center of an incident particle, is uniformly distributed in the continuous domain, $(0,\ La)$. The incident angle, θ, is defined as the angle between the incident direction and the direction normal to the film, with a positive value assigned to the down-right incident direction and a negative value assigned to the down-left incident direction. Probability distribution functions of the incident angle may vary from a Dirac delta function to a cosine function, for different deposition processes. In this chapter, the probability distribution of the angle of incidence is chosen to be uniform in the interval $(-0.5\pi,\ 0.5\pi)$.

The procedure of an adsorption process is illustrated in Figure 5.2. After the initial position and incident angle are determined, the incident particle, A, travels

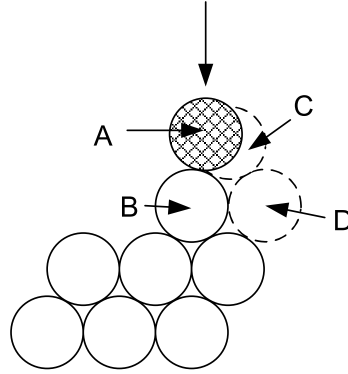

Figure 5.2: Schematic of the adsorption event with surface relaxation. In this event, particle A is the incident particle, particle B is the surface particle that is first hit by particle A, site C is the nearest vacant site to particle A among the sites that neighbor particle B, and site D is a stable site where particle A relaxes.

along a straight line toward the film until contacting the first particle, B, on the film. Upon contact, particle A stops and sticks to particle B at the contacting position; see Figure 5.2. Then, particle A moves (relaxes) to the nearest vacant site, C, among the neighboring sites of particle B. Surface relaxation is conducted if site C is unstable, i.e., site C has only one neighboring particle, as shown in Figure 5.2. When a particle is subject to surface relaxation, the particle moves to its most stable neighboring vacant site, which is defined as the site with the most nearest neighbors. In the case of multiple neighboring vacant sites with the same number of nearest neighbors, a random one is chosen from these sites with equal probability as the objective of the particle surface relaxation process. Note that particle surface relaxation is considered as part of the deposition event, and thus, it does not contribute to the process simulation time. There is also only one relaxation event per incident particle.

5.2.3 Migration process

In a migration process, a particle overcomes the energy barrier of the site and jumps to its vacant neighboring site. The migration rate (probability) of a particle follows an Arrhenius-type law with a pre-calculated activation energy barrier that depends on the local environment of the particle, i.e., the number of the nearest neighbors of the particle chosen for a migration event. The migration rate of the ith particle is calculated as follows:

$$r_{\mathrm{m},i} = \nu_0 \exp\left(-\frac{n_i E_0}{k_{\mathrm{B}} T}\right) \tag{5.2}$$

where ν_0 denotes the pre-exponential factor, n_i is the number of the nearest neighbors of the ith particle and can take the values of 2, 3, 4 and 5 ($r_{\mathrm{m},i}$ is zero when $n_i = 6$ since this particle is fully surrounded by other particles and cannot migrate), E_0 is the contribution to the activation energy barrier from each nearest neighbor, k_{B} is the Boltzmann's constant and T is the substrate temperature of the thin film. Since the film is thin, the temperature is assumed to be uniform throughout the film and is treated as a time-varying but spatially invariant process parameter. In this chapter, the factor and energy barrier contribution in Eq. (5.2) take the following values $\nu_0 = 10^{13}$ s^{-1} and $E_0 = 0.6$ eV, which are appropriate for a silicon film [46].

When a particle is subject to migration, it can jump to either of its vacant neighboring sites with equal probability, unless the vacant neighboring site has no nearest neighbors, i.e., the surface particle cannot jump off the film and it can only migrate

on the surface.

5.2.4 Simulation algorithm

After the rates of surface micro-processes are determined, kMC simulations can be carried out using an appropriate algorithm. A comparison between two basic Monte Carlo simulation algorithms, the null-event algorithm [98] and the continuous-time Monte Carlo method [88], can be found in [75]. The null-event algorithm tries to execute Monte Carlo events on randomly selected sites with certain probabilities, while the continuous-time Monte Carlo (CTMC) method selects an event before the selection of the site on which the event is going to be executed. The existence of null tests makes the null-event algorithm inefficient compared to the CTMC algorithm, especially when the rates of the events are close to zero. From this chapter, the CTMC method is chosen as the kMC algorithm. With the assumption that all microscopic processes are Poisson processes, the time increment upon the execution of a successful event is computed based on the total rates of all the micro-processes, which can be listed and calculated from the current state of the lattice. To further improve the computational efficiency, a grouping algorithm is also used in the selection of the particle that is subject to migration [68]. In the grouping algorithm, the events are pre-grouped to improve the execution speed. The layer of the film emerges as a natural grouping criterion, i.e., all particles in the same layer are considered to be part of one group.

With these considerations, the following kMC simulation algorithm is used to simulate the deposition process:

1. A triangular lattice of lateral extent La, is created to represent the crystalline structure of the film. All particles in the film are constrained to be on the discrete sites of the lattice. A substrate layer, which is fully packed and fixed, is added at the bottom of the lattice at the beginning ($t = 0$ s) of the simulation.

2. A list of events is created (or updated) for all possible events including adsorption and migration. The rate for each event is calculated based on the process parameters, i.e., the substrate temperature and the deposition rate.

3. A random number $\zeta_1 \in (0, r_\mathrm{a} + \sum_{i=1}^{N} r_{\mathrm{m},i})$ is generated to determine whether the next event is an adsorption event ($0 < \zeta_1 < r_\mathrm{a}$) or a migration event ($r_\mathrm{a} < \zeta_1 < r_\mathrm{a} + \sum_{i=1}^{N} r_{\mathrm{m},i}$), where N is the total number of deposited particles on the lattice at the specific time instant. Note that the particles being present in the substrate layer are not counted as deposited particles.

4. If the next event is an adsorption event, an incident particle initiates from the gas phase above the film. Two random numbers, $\zeta_{21} \in (0, La)$ and $\zeta_{22} \in (-0.5\pi, 0.5\pi)$, are generated following a uniform probability distribution to determine the initial particle position and incident angle, respectively. The incident particle is incorporated into the film following the microscopic rules for adsorption events discussed in Section 5.2.2.

5. If the next event is a migration event, a random number $\zeta_3 \in (0, \sum_{i=1}^{N} r_{\mathrm{m},i})$ is generated to determine which particle is subject to migration. The migrating particle is found from the following rule: $\sum_{i=1}^{n-1} r_{\mathrm{m},i} < \zeta_3 < \sum_{i=1}^{n} r_{\mathrm{m},i}$, where n indicates the nth particle that is subject to migration. The migrating particle jumps to its neighboring vacant site following the microscopic rules for migration events discussed in Section 5.2.3.

6. Upon the execution of an event, a time increment, δt, is computed by using the following expression:

$$\delta t = -\frac{\ln \zeta_4}{r_{\mathrm{a}} + \sum_{i=1}^{N} r_{\mathrm{m},i}} \tag{5.3}$$

where ζ_4 is a real random number in the $(0, 1)$ interval.

7. If t exceeds a preset deposition duration time, t_d, the kMC simulation is terminated. Otherwise the kMC algorithm is repeated starting from Step 2.

To simulate the process with limited-size lattice and reduce the boundary effects, periodic boundary conditions (PBCs) are applied to the kMC model of the deposition process. Note that PBCs are widely used in molecular level simulations, e.g.,[67], so that the statistical properties of a large scale stochastic process can be appropriately captured by kMC simulations carried out on a finite-size lattice.

5.3 Open-loop simulations

In this section, simulations of the kMC model of a silicon thin film growth process using the methodology described in the previous section are presented with the process parameters being kept constant (i.e., open-loop simulation). Appropriate definitions of film SOR are also introduced to describe the film porosity and its fluctuation.

5.3.1 Definition of film site occupancy ratio

Since film porosity is the main objective of modeling and control design of this chapter, a new variable, film SOR, is introduced to represent the extent of the porosity inside the thin film as follows:

$$\rho = \frac{N}{LH} \tag{5.4}$$

where ρ denotes the film SOR, N is the total number of deposited particles on the lattice, L is the lattice size (i.e., number of sites in one layer) and H denotes the number of deposited layers. Note that the deposited layers are the layers that contain deposited particles and do not include the initial substrate layer. The concept of packing density, which represents the occupancy ratio of space for a specific packing method, is not the same as the film SOR defined in Eq. (5.4), and thus, it cannot be used to characterize the evolution of film porosity.

Figure 5.3 gives an example showing how film SOR is defined. Since each layer contains L sites, the total number of sites in the film is LH. Film SOR is the ratio

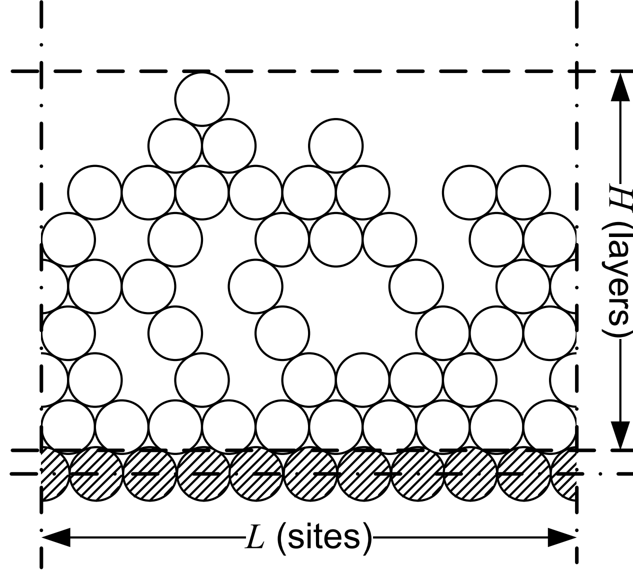

Figure 5.3: Illustration of the definition of film SOR of Eq. (5.4).

between the number of deposited particles, N, and the total number of sites, LH. With this definition, film SOR ranges from 0 to 1. Specifically, $\rho = 1$ denotes a film whose sites are fully occupied and has a flat surface. At the beginning of the deposition process when there are no particles deposited on the lattice and only the substrate layer is present, N and H are both zeros and the ratio $N/(LH)$ is not defined, and thus, a zero value is assigned to the film SOR at this state.

Due to the stochastic nature of kMC models of thin film growth processes, the film SOR, ρ, fluctuates about a mean value, $\langle\rho\rangle$, at all times. A quantitative measure of the SOR fluctuations is provided by the variance of the film SOR as follows:

$$\mathrm{Var}(\rho) = \left\langle (\rho - \langle\rho\rangle)^2 \right\rangle \tag{5.5}$$

where $\langle \cdot \rangle$ denotes the average (mean) value.

5.3.2 Film site occupancy ratio evolution profile

In this subsection, the thin film deposition process is simulated according to the algorithm described in Section 5.2. The evolution of film SOR and its variance are computed from Eqs. (5.4) and (5.5), respectively. The lattice size L is equal to 100 throughout this chapter. The choice of lattice size is determined from a balance between statistical accuracy and reasonable requirements for computing power. 1000 independent simulation runs are carried out to obtain the expected value and the variance of the film SOR. The simulation time is 1000 s. All simulations start with an identical flat initial condition, i.e., only a substrate layer is present on the lattice without any deposited particles. Figure 5.4 shows the evolution profiles of the expected value and the variance of the film SOR during the deposition process for the following process parameters: $T = 600$ K and $W = 1$ layer/s. In Figure 5.4, the film SOR is initially 0 and as particles begin to deposit on the film, the film SOR increases with respect to time and quickly reaches a steady-state value. Snapshots of the thin film microstructure at different times, $t = 100$ s, 400 s, 700 s, and 1000 s, of the open-loop simulation are shown in Figure 5.5.

In the snapshots of the microstructure, columnar structures are observed, which is due to the effect of nonlocal shadowing of the existing particles, which prevents incident particles from adsorbing to the film sites that are blocked by the particles

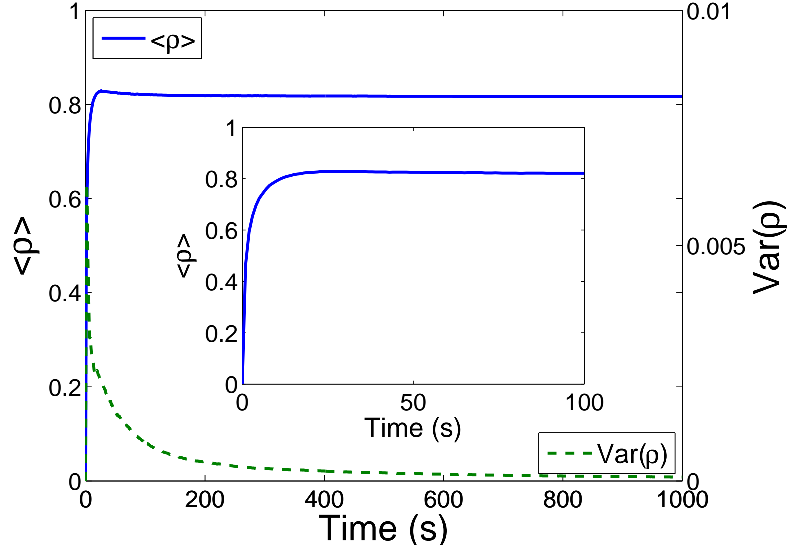

Figure 5.4: Mean value (solid lines) and variance (dashed line) of the complete film SOR versus time for a 1000 s open-loop deposition process with substrate temperature $T = 600$ K and deposition rate $W = 1$ layer/s.

at higher positions. Such columnar structures are also observed both in the experiments and in simulations with similar microscopic rules [56, 55, 92, 97]. Within the columnar structure, there exist small pores in the microstructure that contribute to the film porosity. Such a structure (columns with few pores) is the result of certain deposition conditions, i.e., the substrate temperature and the adsorption rate considered. Different conditions may result in different microstructure. For example, at the low-temperature region (below 500 K), the deposited thin film shows a tree-like structure with a large number of small pores.

The evolution profile of the variance starts at zero and jumps to a peak, after which the variance decays with respect to time. The variance is used to represent the extent of fluctuation of the film SOR at a given time. Since all simulations start at the

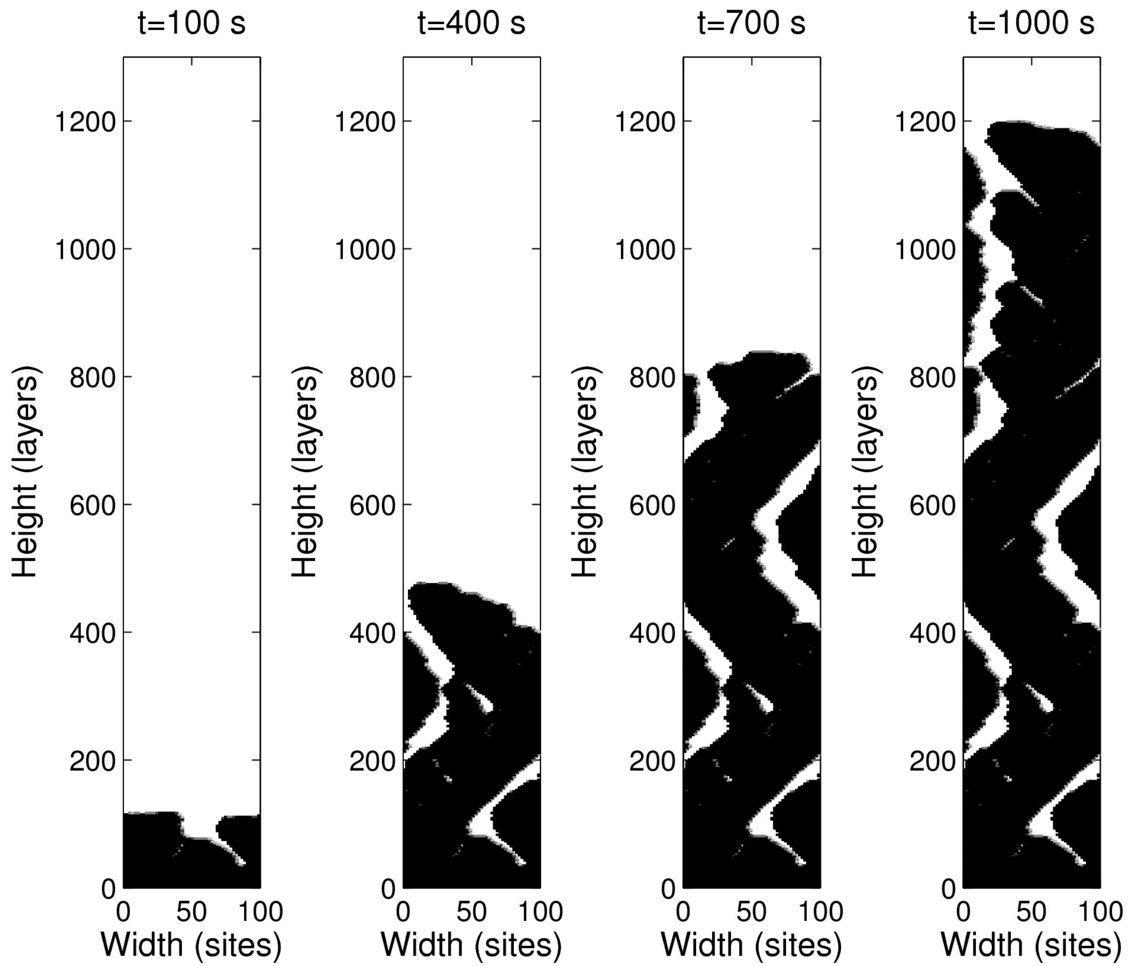

Figure 5.5: Snapshots of the film microstructure at $t = 100$ s, 400 s, 700 s, and 1000 s of the open-loop deposition process with substrate temperature $T = 600$ K and deposition rate $W = 1$ layer/s.

same initial condition, the initial variance is zero (by convention) at time $t = 0$ s. As particles begin to deposit on the film, the variance of the film SOR, $\text{Var}(\rho)$, increases at short times and it subsequently decreases to zero at large times. Note that the film SOR is a cumulative property since it accounts for all the deposited layers and particles on the film. In other words, the film SOR from each individual simulation run approaches its expected value at large times. Thus, at large times, SOR fluctuations decrease as more layers are included into the film. It is evident from Figure 5.4 that the SOR variance decays and approaches zero at large times. Figure 5.6 shows the probability distribution functions of the film SOR at different time instants. It can be clearly seen in Figure 5.6 that, as time increases, the probability distribution functions become sharper and closer to its mean value, which shows the fact that the fluctuation of film SOR is diminishing (i.e., smaller variance) at large times. Thus, the film SOR of Eq. (5.4) and its variance of Eq. (5.5) are not suitable variables for the purposes of modeling and control of film porosity fluctuations. Another variable must be introduced to represent the fluctuation of the film porosity.

5.3.3 Partial film site occupancy ratio

In this subsection, a new concept of film SOR is introduced, termed partial film SOR, which is the film SOR calculated by accounting only for the top H_{p} layers of the film.

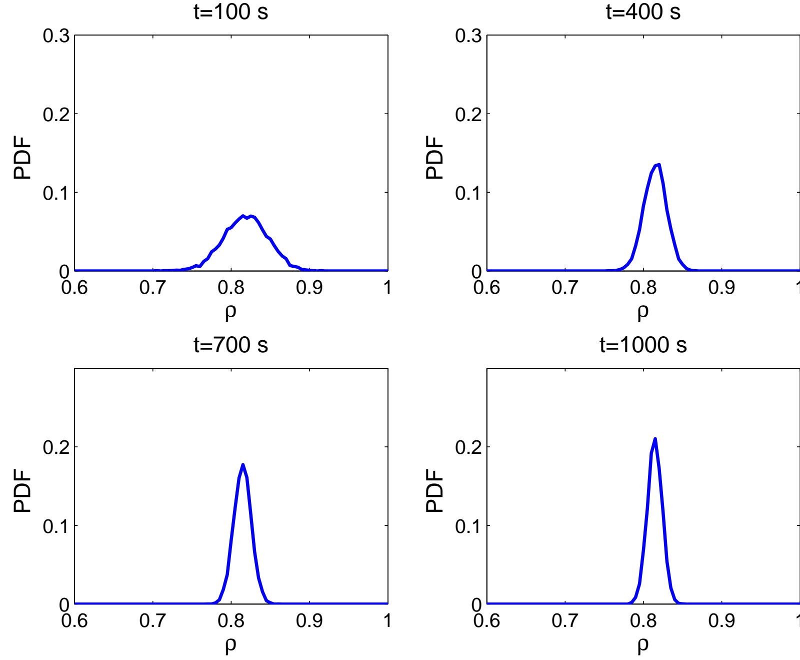

Figure 5.6: Probability distribution functions (PDF) of film SOR at $t = 100$ s, 400 s, 700 s, and 1000 s of the open-loop deposition process.

Mathematically, the partial film SOR is defined as follows:

$$\rho_{\mathrm{p}} = \frac{N_{\mathrm{p}}}{LH_{\mathrm{p}}} \tag{5.6}$$

where ρ_{p} denotes the partial film SOR and N_{p} denotes the number of particles in the top H_{p} layers and H_{p} denotes the number of top layers of the film included in the computation of the partial film SOR. The definition of the partial film SOR is shown schematically in Figure 5.7. To calculate the partial film SOR of Eq. (5.6), the number of top H_{p} layers must first be determined. As shown in Figure 5.7, the top H_{p} layers start from the top layer of the lattice and include the $(H_{\mathrm{p}} - 1)$ layers

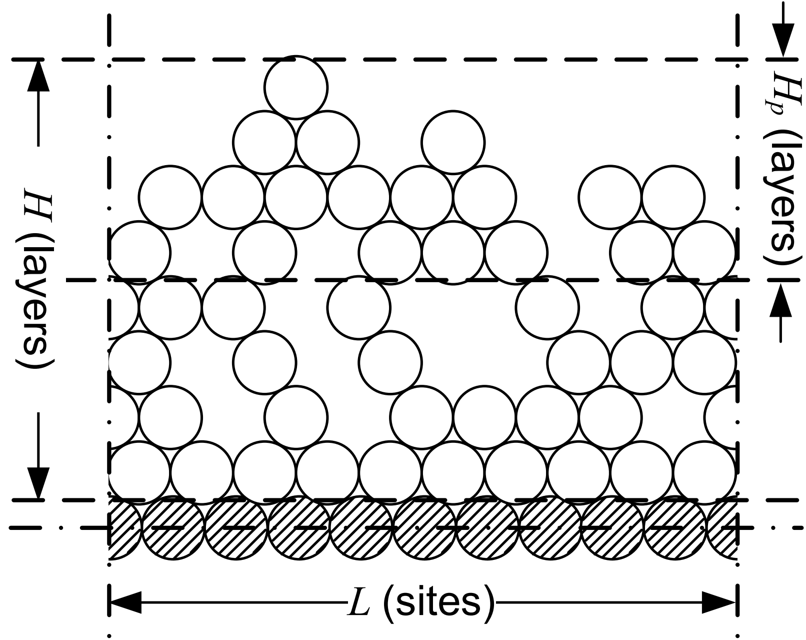

Figure 5.7: Illustration of the definition of partial film SOR of Eq. (5.6).

below the top layer. The number of particles in the top H_p layers is denoted by N_p. The partial film SOR, ρ_p, is then calculated as the ratio between N_p and the total number of sites in the top H_p layers, LH_p. Similar to ρ, ρ_p is ranging from 0 to 1. $\rho_\mathrm{p} = 1$ denotes fully occupied top H_p layers.

The choice of H_p affects the value of the partial film SOR, ρ_p, and furthermore, it results in different modeling results and controller performance. Specifically, the partial film SOR cannot be correctly calculated without the existence of H_p layers in the film. This problem is bypassed by assuming the existence of H_p fully-packed substrate layers in the film before the deposition process begins. These substrate layers are used in the calculation of ρ_p when $H < H_\mathrm{p}$. This assumption does not affect the deposition process since the particles in the substrate layers neither migrate

nor affect the adsorption or migration processes of the deposited particles. Therefore, at the beginning of deposition, the partial film SOR starts from unity since all H_p layers are substrate layers and are fully occupied. There also exist alternative choices of H_p at the beginning of deposition, e.g., equating H_p with H and hence having $\rho_\mathrm{p} = \rho$ when $H < H_\mathrm{p}$. Different choices of H_p affect the computation of ρ_p at the initial stages and result in different initial values. However, the main dynamics of the partial film SOR remains unchanged, especially at large times.

Although complete film SOR and partial film SOR are defined similarly, they are different variables, which are used to describe different aspects of the film. The most notable difference is the denominator of the fractions. In the complete film SOR, the denominator of the ratio is the number of the sites in the entire deposited film, and thus, it increases with respect to time, due to the deposition of new particles. This cumulative property of the complete film SOR averages the fluctuations of the porosity from different layers of the film and results in the decay of the variance of the complete film SOR to zero with respect to time. For the partial film SOR, on the contrary, the denominator of the ratio is fixed at LH_p, and thus, ρ_p only accounts for the porosity of the newly deposited H_p layers of the film. Another difference lies in the mechanism of the deposition process. Due to particle migration, particles in the film interior have a higher probability of achieving closed packed configurations than particles in the top layers. However, newly deposited particles in the top layers have not experienced enough migration events and are more active for migrating. For the

above reasons, the fluctuation of ρ_p does not decay with respect to time and is much larger than the fluctuation of ρ at large times. Thus, the variance of ρ_p is selected to represent the porosity fluctuations and is used for modeling and control design. The partial film SOR variance, $\mathrm{Var}(\rho_\mathrm{p})$, is computed by the following expression

$$\mathrm{Var}(\rho_\mathrm{p}) = \big\langle (\rho_\mathrm{p} - \langle \rho_\mathrm{p} \rangle)^2 \big\rangle. \tag{5.7}$$

The evolution profiles of the expected partial film SOR and the variance of partial film SOR are shown in Figure 5.8 for the same process parameters as in Figure 5.4. The top 100 layers are chosen in the calculation of the partial film SOR, i.e., $H_\mathrm{p} = 100$ in Eq. (5.6). The choice of H_p depends on the process requirements. Too few layers result in dramatic fluctuations of the partial film SOR. For a deposition process of about 1000 deposited layers, it is found through extensive simulation tests that 100 top layers constitute a suitable choice for modeling and control design. The magnitude of the variance of the partial film SOR depends on the choice of H_p. For problems with different lattice sizes, a different H_p may be selected to produce a representative magnitude of the variance.

As shown in Figure 5.8, the mean partial film SOR, $\langle \rho_\mathrm{p} \rangle$, starts from 1 as a result from the use of the initial substrate layer. Then, $\langle \rho_\mathrm{p} \rangle$ decreases with respect to time and reaches a steady-state value at large times. Compared to the expected film SOR in Figure 5.4, the expected partial film SOR is smaller at steady state, since the top

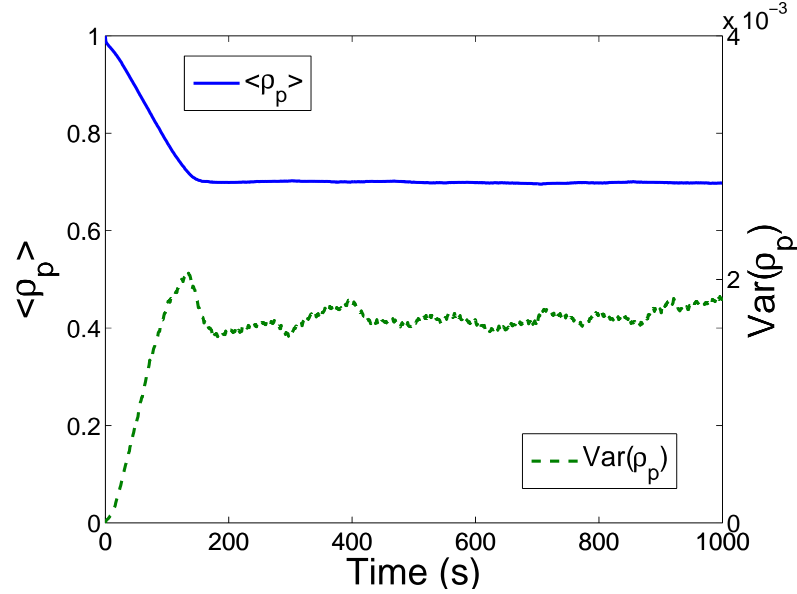

Figure 5.8: Profiles of mean value (solid line) and variance (dashed line) of the partial film SOR in a 1000 s open-loop deposition process with substrate temperature $T =$ 600 K and deposition rate $W = 1$ layer/s.

layers of the film are newly formed and are more active for particle migration than the bulk layers, which are already deposited for a longer time and are stabilized.

The evolution profile of the variance of partial film SOR, $\text{Var}(\rho_{\text{p}})$, is different from the one of the complete film SOR, $\text{Var}(\rho)$, which decays to zero at large times. Similar to the evolution of $\text{Var}(\rho)$, $\text{Var}(\rho_{\text{p}})$ starts from zero due to an identical deterministic initial condition applied to all simulations. However, $\text{Var}(\rho_{\text{p}})$ does not decay to zero with respect to time, but reaches a steady-state non-zero value. This steady-state non-zero value can be seen from Figure 5.9, which shows the probability distribution functions of the partial film SOR at different time instants. As time increases, the probability distribution function of the partial film SOR remains steadily shaped

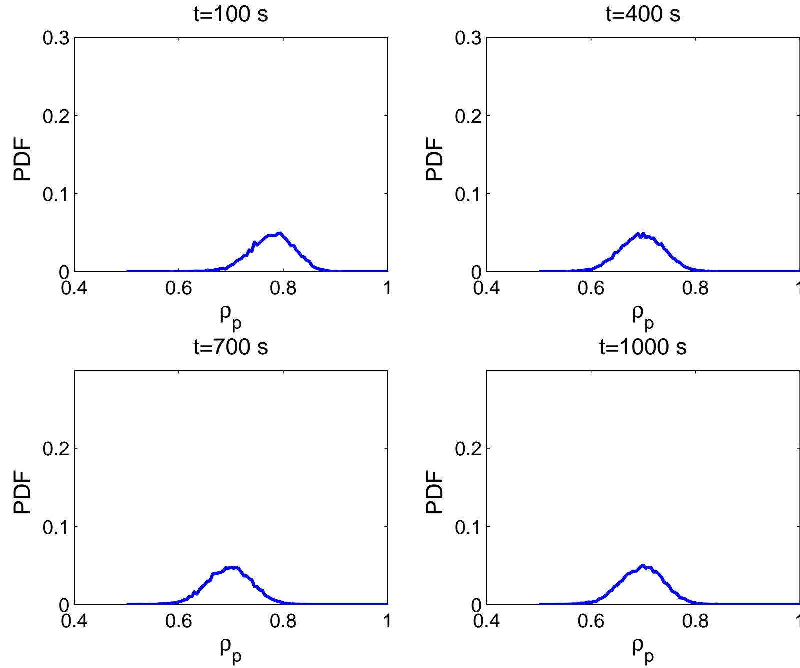

Figure 5.9: Probability distribution functions (PDF) of partial film SOR at $t = 100$ s, 400 s, 700 s, and 1000 s of the open-loop deposition process.

(i.e., steady-state value of variance) instead of becoming sharper as the one of the film SOR shown in Figure 5.8. Therefore, the variance of partial film SOR is chosen as the representation of the run-to-run fluctuation of film porosity. Finally, we note that a careful inspection of Figures 5.4 and 5.8 indicates that the variances of the film SOR are two orders of magnitude less than the corresponding mean values, i.e., the mean value of the film SORs $\sim O(1)$ and the variance of the film SORs $\sim O(10^{-3})$.

5.4 Construction of ODE models for complete and partial film site occupancy ratio

For control purposes, dynamic models are required that describe how the film porosity expressed in terms of complete and partial film SOR varies with respect to potential manipulated input variables like temperature and deposition rate. In this section, deterministic and stochastic linear ODE models are derived to describe the evolution of film SOR. The derivation of these ODE models and the computation of their parameters is done on the basis of data obtained from the kMC model of the deposition process.

5.4.1 Deterministic dynamic model of complete film site occupancy ratio

From the open-loop simulation results, the dynamics of the expected value of the complete film SOR evolution can be approximately described by a first-order ODE model. Therefore, a linear first-order deterministic ODE is chosen to describe the dynamics of the complete film SOR as follows:

$$\tau \frac{d \langle \rho(t) \rangle}{dt} = \rho^{\text{ss}} - \langle \rho(t) \rangle \tag{5.8}$$

where t is the time, τ is the time constant and ρ^{ss} is the steady-state value of the complete film SOR. The deterministic ODE system of Eq. (5.10) is subject to the following initial condition:

$$\langle \rho(t_0) \rangle = \rho_0 \tag{5.9}$$

where t_0 is the initial time and ρ_0 is the initial value of the complete film SOR. Note that ρ_0 is a deterministic variable, since ρ_0 refers to the expected value of the complete film SOR at $t = t_0$. From Eqs. (5.8) and (5.9), it follows that

$$\langle \rho(t) \rangle = \rho^{\text{ss}} + (\rho_0 - \rho^{\text{ss}})\, e^{-(t-t_0)/\tau}. \tag{5.10}$$

The model parameters, τ and ρ^{ss}, depend on substrate temperature. This dependence will be mathematically expressed in Section 5.4.3 below.

5.4.2 Stochastic dynamic model of partial film site occupancy ratio

To regulate the variance of the partial film SOR, a stochastic model must be used. For simplicity, a linear stochastic ODE is used to model the dynamics of the partial film SOR. Similarly to the deterministic ODE model for the expected complete film SOR of Eq. (5.8), a first-order stochastic ODE is chosen for the computation of the

partial film SOR as follows:

$$\tau_{\rm p}\frac{d\rho_{\rm p}(t)}{dt} = \rho_{\rm p}^{\rm ss} - \rho_{\rm p}(t) + \xi_{\rm p}(t) \tag{5.11}$$

where $\rho_{\rm p}^{\rm ss}$ and $\tau_{\rm p}$ are the two model parameters which denote the steady-state value of the partial film SOR and the time constant, respectively, and $\xi_{\rm p}(t)$ is a Gaussian white noise with the following expressions for its mean and covariance:

$$\begin{aligned} \langle \xi_{\rm p}(t) \rangle &= 0, \\ \langle \xi_{\rm p}(t)\xi_{\rm p}(t') \rangle &= \sigma_{\rm p}^2 \delta(t - t'), \end{aligned} \tag{5.12}$$

where $\sigma_{\rm p}$ is a parameter which measures the intensity of the Gaussian white noise and $\delta(\cdot)$ denotes the standard Dirac delta function. The model parameters $\rho_{\rm p}^{\rm ss}$, $\tau_{\rm p}$ and $\sigma_{\rm p}$ are functions of the substrate temperature. We note that $\xi_{\rm p}(t)$ is taken to be a Gaussian white noise because the values of $\rho_{\rm p}$ obtained from $10,000$ independent kMC simulations of the deposition process at large times are in closed accord with a Gaussian distribution law: see Figure 5.10 for the histogram of the partial film SOR at $t = 1000$ s.

The stochastic ODE system of Eq. (5.11) is subject to the following initial condition:

$$\rho_{\rm p}(t_0) = \rho_{\rm p0} \tag{5.13}$$

where $\rho_{\rm p0}$ is the initial value of the partial film SOR. Note that $\rho_{\rm p0}$ is a random

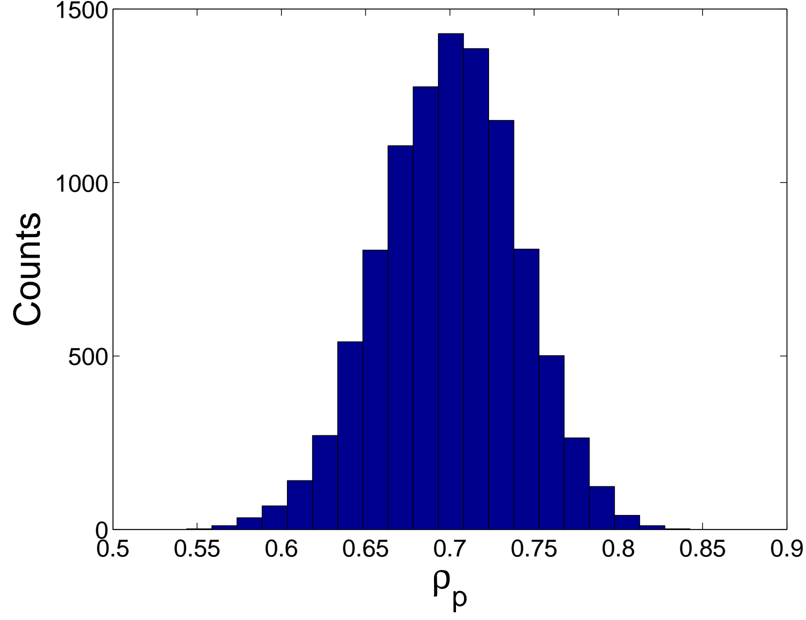

Figure 5.10: Histogram from 10000 simulation runs of the partial film SOR at the end ($t = 1000$ s) of the open-loop deposition process with substrate temperature $T = 600$ K and deposition rate $W = 1$ layer/s.

number, which follows a Gaussian distribution.

The following analytical solution to Eq. (5.11) can be obtained from a direct computation as follows:

$$\rho_{\mathrm{p}}(t) = \rho_{\mathrm{p}}^{\mathrm{ss}} + \left(\rho_{\mathrm{p}0} - \rho_{\mathrm{p}}^{\mathrm{ss}}\right) e^{-(t-t_0)/\tau_{\mathrm{p}}} + \int_{t_0}^{t} e^{-(s-t_0)/\tau_{\mathrm{p}}} \xi_{\mathrm{p}} ds. \tag{5.14}$$

In Eq. (5.14), $\rho_{\mathrm{p}}(t)$ is a random process, the expected value of which, $\langle \rho_{\mathrm{p}}(t) \rangle$, can be obtained as follows:

$$\langle \rho_{\mathrm{p}}(t) \rangle = \rho_{\mathrm{p}}^{\mathrm{ss}} + \left(\langle \rho_{\mathrm{p}0} \rangle - \rho_{\mathrm{p}}^{\mathrm{ss}}\right) e^{-(t-t_0)/\tau_{\mathrm{p}}}. \tag{5.15}$$

The analytical solution to $\mathrm{Var}(\rho_\mathrm{p})$ can be obtained from the solution of Eq. (5.14) using Result 1 as follows:

$$\mathrm{Var}(\rho_\mathrm{p}(t)) = \frac{\tau_\mathrm{p}\sigma_\mathrm{p}^2}{2} + \left(\mathrm{Var}(\rho_{\mathrm{p}0}) - \frac{\tau_\mathrm{p}\sigma_\mathrm{p}^2}{2}\right) e^{-2(t-t_0)/\tau_\mathrm{p}} \tag{5.16}$$

where $\mathrm{Var}(\rho_{\mathrm{p}0})$ is the variance of the partial film SOR at time $t = 0$ s, which is calculated as follows:

$$\mathrm{Var}(\rho_{\mathrm{p}0}) = \left\langle (\rho_{\mathrm{p}0} - \langle \rho_{\mathrm{p}0} \rangle)^2 \right\rangle. \tag{5.17}$$

A new model parameter, $\mathrm{Var}_\mathrm{p}^\mathrm{ss}$, is introduced to simplify the solution of $\mathrm{Var}(\rho_\mathrm{p})$ in Eq. (5.16) as follows:

$$\mathrm{Var}_\mathrm{p}^\mathrm{ss} = \frac{\tau_\mathrm{p}\sigma_\mathrm{p}^2}{2} \tag{5.18}$$

where $\mathrm{Var}_\mathrm{p}^\mathrm{ss}$ stands for the steady-state value of the variance of the partial film SOR. With the introduction of this new model parameter, the solution of the variance of the partial film SOR, $\mathrm{Var}(\rho_\mathrm{p})$, can be rewritten in the following form:

$$\mathrm{Var}(\rho_\mathrm{p}(t)) = \mathrm{Var}_\mathrm{p}^\mathrm{ss} + \left(\mathrm{Var}(\rho_{\mathrm{p}0}) - \mathrm{Var}_\mathrm{p}^\mathrm{ss}\right) e^{-2(t-t_0)/\tau_\mathrm{p}}. \tag{5.19}$$

5.4.3 Parameter estimation and dependence

Referring to the deterministic and stochastic ODE models of Eqs. (5.8) and (5.11), we note that they include five parameters, ρ^ss, τ, $\rho_\mathrm{p}^\mathrm{ss}$, τ_s and $\mathrm{Var}_\mathrm{p}^\mathrm{ss}$. The five parameters

describe the dynamics of the film SOR accounting for the effect of fluctuations. These parameters must be estimated by comparing the predicted evolution profiles from the ODE models and the ones from the kMC simulation of the deposition process. Least-square methods are used to estimate the model parameters so that the ODE model predictions are close in a least-square sense to the kMC simulation data.

Parameter estimation

Since the ODE models of Eqs. (5.8) and (5.11) are linear, the five parameters, ρ^{ss}, τ, $\rho_{\mathrm{p}}^{\mathrm{ss}}$, τ_{p} and $\mathrm{Var}_{\mathrm{p}}^{\mathrm{ss}}$, can be estimated from the solutions to Eqs. (5.10) and (5.15). Specifically, the parameters $\rho_{\mathrm{p}}^{\mathrm{ss}}$ and τ_{p} are estimated using Eq. (5.10) and the parameters $\rho_{\mathrm{p}}^{\mathrm{ss}}$, τ_{p} and $\mathrm{Var}_{\mathrm{p}}^{\mathrm{ss}}$ are estimated using Eq. (5.15), solving two separate least-square problems. Specifically, the two least-square problems can be solved independently to obtain the first four model parameters. The steady-state variance, $\mathrm{Var}_{\mathrm{p}}^{\mathrm{ss}}$, is obtained from the values of the variance evolution profiles at large times.

The parameters ρ^{ss} and τ are estimated by minimizing the sum of the squared difference between the evolution profiles from the ODE model prediction and the kMC simulation at different time instants as follows:

$$\min_{\rho^{\mathrm{ss}},\tau} \sum_{i=1}^{m} \left[\langle \rho(t_i) \rangle - \left(\rho^{\mathrm{ss}} + (\rho_0 - \rho^{\mathrm{ss}})\, e^{-(t-t_0)/\tau} \right) \right]^2 \tag{5.20}$$

where m is the number of the data pairs, $(t_i,\ \langle \rho(t_i) \rangle)$, from the kMC simulations. Similarly, $\rho_{\mathrm{p}}^{\mathrm{ss}}$ and τ_{p} can be obtained by solving the following least-square optimization

problem expressed in terms of the expected partial film SOR:

$$\min_{\rho_{\mathrm{p}}^{\mathrm{ss}},\tau_{\mathrm{p}}} \sum_{i=1}^{m} \left[\langle \rho_{\mathrm{p}}(t_i) \rangle - \left(\rho_{\mathrm{p}}^{\mathrm{ss}} + \left(\rho_{\mathrm{p}0} - \rho_{\mathrm{p}}^{\mathrm{ss}} \right) e^{-(t-t_0)/\tau_{\mathrm{p}}} \right) \right]^2. \tag{5.21}$$

The data used for the parameter estimation are obtained from the open-loop kMC simulation of the thin film growth process. The process parameters are fixed during each open-loop simulation so that the dependence of the model parameters on the process parameters can be obtained for fixed operation conditions. The complete film SOR and the partial film SOR are calculated on the basis of the deposited film at specific time instants. Due to the stochastic nature of the process, multiple independent simulation runs are performed to obtain the expected values of the complete film SOR and of the partial film SOR as well as of the variance of the partial film SOR.

The above parameter estimation process is applied to the open-loop simulation results. First, the open-loop evolution profiles of the complete film SOR and of the partial film SOR are obtained from 1000 independent kMC simulation runs with substrate temperature $T = 600$ K and deposition rate $W = 1$ layer/s. Subsequently, the deterministic and stochastic ODE models of Eqs. (5.8) and (5.11) are compared with the open-loop kMC simulation data to compute the model parameters using least square methods. Figures 5.11 and 5.12 show the open-loop profiles and the predicted profiles of $\langle \rho \rangle$, $\langle \rho_{\mathrm{p}} \rangle$ and $\mathrm{Var}(\rho_{\mathrm{p}})$ from the ODE models with the estimated

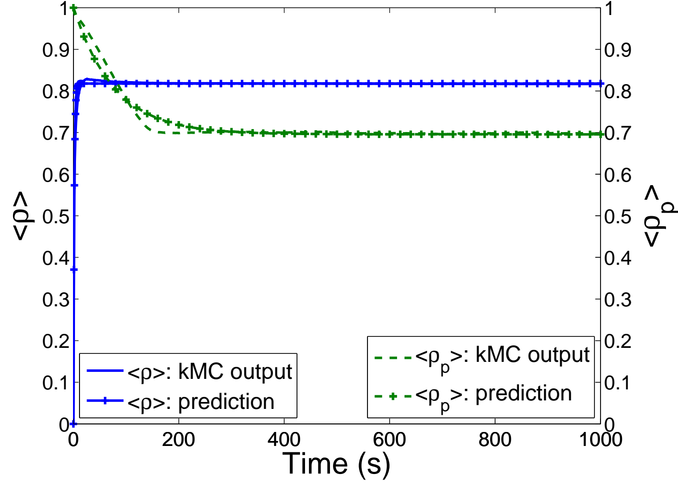

Figure 5.11: Profiles of the expected complete film SOR (solid line) and of the expected partial film SOR (dashed line) in a 1000 s open-loop deposition process and predictions from the deterministic ODE model (solid line with '+') and the stochastic ODE model (dashed line with '+') with estimated parameters; $T = 600$ K, $W = 1$ layer/s.

parameters as follows:

$$\begin{aligned} &\rho^{\mathrm{ss}} = 0.8178, \quad \tau = 1.6564 \text{ s}, \\ &\rho_p^{\mathrm{ss}} = 0.6957, \quad \tau_{\mathrm{p}} = 77.2702 \text{ s}, \quad \mathrm{Var}_{\mathrm{p}}^{\mathrm{ss}} = 1.6937 \times 10^{-3}. \end{aligned} \tag{5.22}$$

The predictions from the ODE models are very close to the open-loop kMC simulation profiles, which indicates that the dynamics of the film SOR can be adequately described by first-order ODEs. There is, however, some mismatch of the predicted ODE-based profiles from the kMC data, especially for the expected value of the complete film SOR. This is because the dynamics of the complete film SOR depend on the total height of the film. A film at initial stages is very thin and the complete film SOR changes significantly as more layers are deposited, while a film at large

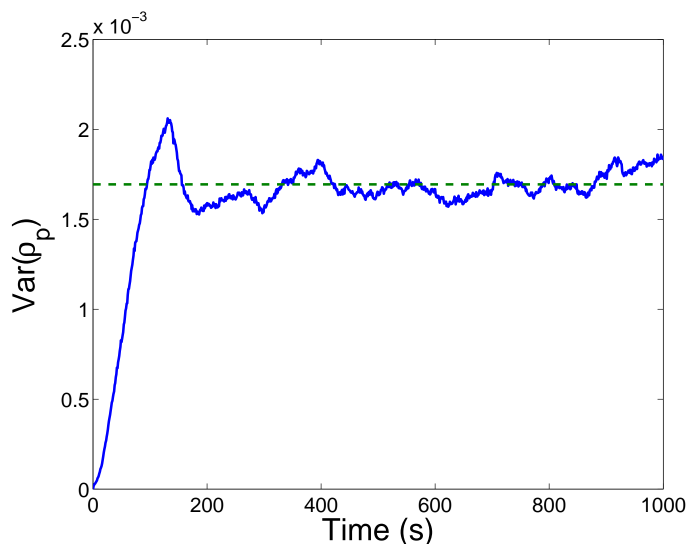

Figure 5.12: Variance of the partial film SOR with respect to time for a 1000 s open-loop deposition process (solid line) and the estimated steady-state level (dashed line); $T = 600$ K, $W = 1$ layer/s.

times is much thicker and the complete film SOR is relatively insensitive to the newly deposited layers. Since a first-order ODE model is used to capture the dynamics of the complete film SOR, the time constant, τ, is chosen to strike a balance between the initial and final stages of the film growth. Therefore, the predictions from the ODE model cannot match the open-loop profiles, obtained from the kMC models, perfectly at all times. Overall, the computed first-order ODE models approximate well the dynamics of the film SOR and its fluctuation, and thus, they can be used for the purpose of feedback control design. The closed-loop system simulation results using these first-order models will be discussed in Section 5.5.3 below.

The lattice size dependence of the steady-state value of the complete film SOR is shown in Figure 5.13. It can be clearly seen that the film SOR depends on the

lattice size. To achieve near lattice-size independence, a very large lattice size is required and cannot be simulated using the available amount of computing power. The purpose of the proposed modeling method is to identify the film SOR models from the output of the given deposition process, which can be from either a kMC simulator or experimental deposition process data. Note that the applicability of the proposed modeling method is not limited to any specific lattice size. In this chapter, a model with lattice size of 100 captures the film SOR dynamics and allows obtaining sufficient statistical accuracy in terms of computing expected values and variances of film SORs.

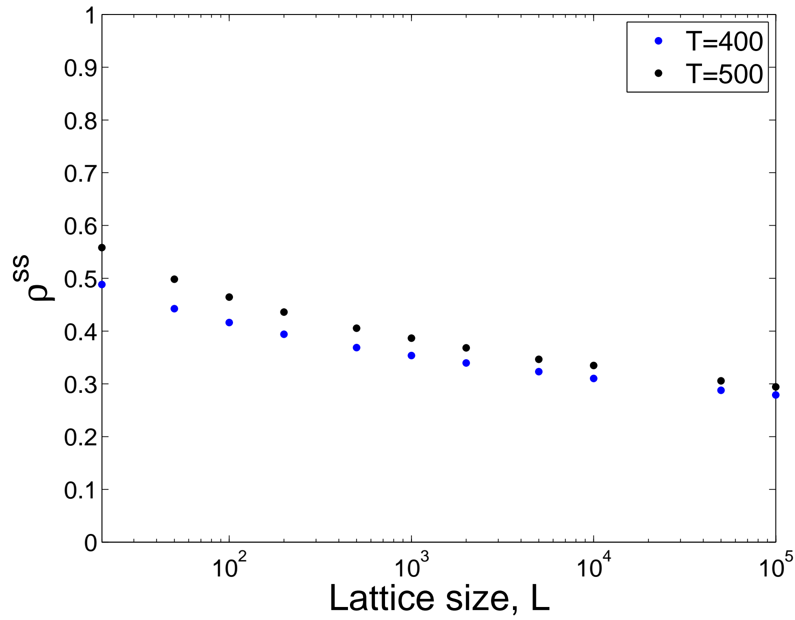

Figure 5.13: Dependence of steady-state values of film SOR, ρ^{ss}, on the lattice size for different temperatures.

Dependence of model parameters on process parameters

The model parameters of the ODE models of Eqs. (5.8) and (5.11) depend on two process parameters, temperature and deposition rate. This dependence is used in the formulation of the model predictive control design in the next section when solving the optimization problem. Thus, parameter estimation from open-loop kMC simulation results of the thin film growth process for a variety of process parameters is performed to obtain the relationship between the model parameters and the process parameters. In this chapter, the deposition rate for all simulations is fixed at 1 layer/s and the only manipulated input considered is the substrate temperature, T. The range of T is between 300 K and 800 K, which is from room temperature to the upper limit of the allowable temperature for a valid on-lattice kMC model of silicon film. The dependence of the model parameters on the substrate temperature is shown in Figures 5.14, 5.15 and 5.16. In these figures, it can be clearly seen that the dependence of the model parameters on temperature is highly nonlinear. For most model parameters, there are asymptotes at the low temperature region due to the limited surface migration rates at low temperatures. However, at high temperatures, ρ^{ss} and $\rho_{\text{p}}^{\text{ss}}$ approach unity, which corresponds to a fully packed film, i.e., all film sites are occupied by particles.

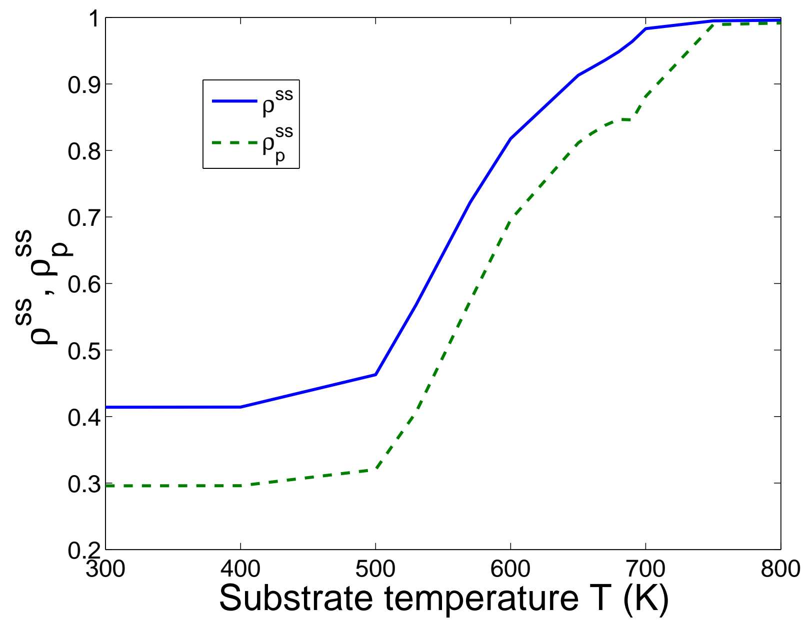

Figure 5.14: Dependence of ρ^{ss} and $\rho_{\mathrm{p}}^{\mathrm{ss}}$ on the substrate temperature with deposition rate $W = 1$ layer/s.

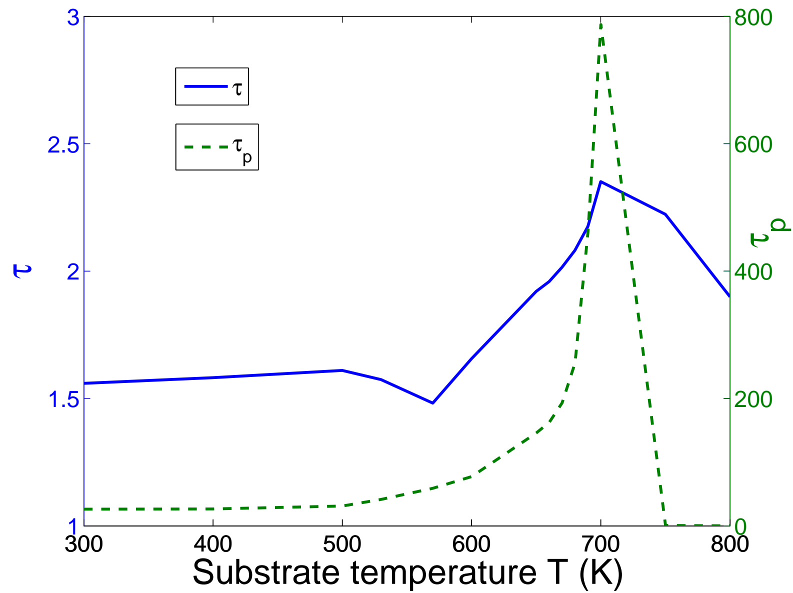

Figure 5.15: Dependence of τ and τ_{p} on the substrate temperature with deposition rate $W = 1$ layer/s.

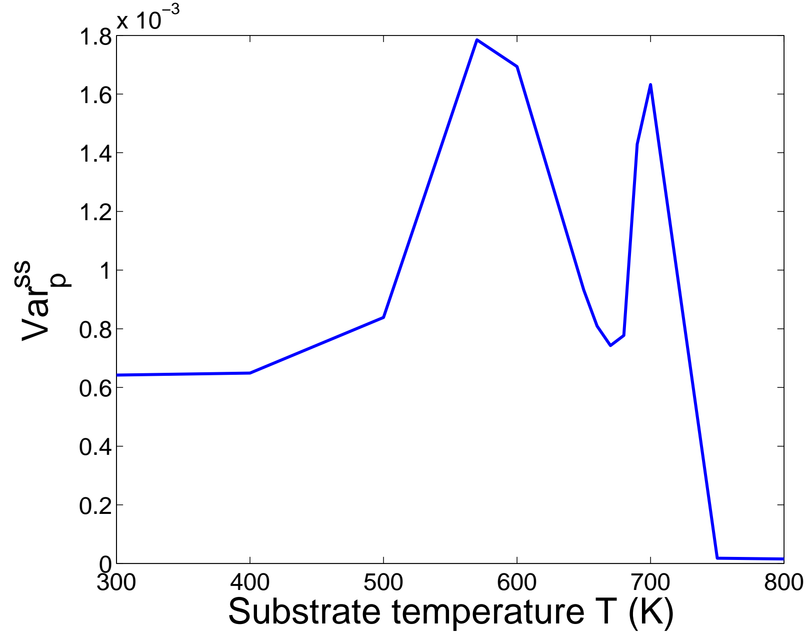

Figure 5.16: Dependence of $\mathrm{Var}_{\mathrm{p}}^{\mathrm{ss}}$ on the substrate temperature with deposition rate $W = 1$ layer/s.

5.5 Model predictive control design

In this section, we design model predictive controllers based on the deterministic and stochastic ODE models of Eqs. (5.8) and (5.11) to simultaneously control the complete film SOR of the deposition process to a desired level and minimize the variance of the partial film SOR. State feedback controllers are considered in this chapter, i.e., the values of the complete film SOR and of the partial film SOR are assumed to be available for feedback control. Real-time film SOR can be estimated from *in situ* thin film thickness measurements [17] in combination with off-line film porosity measurements.

5.5.1 Regulation of complete film site occupancy ratio

Since the film porosity is the main control objective in this chapter, we first consider the problem of regulation of the expected complete film SOR to a desired level, ρ_{set}, within a model predictive control framework. The substrate temperature is used as the manipulated input and the deposition rate is fixed at a certain value, W_0, during the entire closed-loop simulation. To account for a number of practical considerations, several constraints are added to the control problem. First, there is a constraint on the range of variation of the substrate temperature. This constraint ensures validity of the on-lattice kMC model. Another constraint is imposed on the rate of change of the substrate temperature to account for actuator limitations.

We note that classical control schemes like proportional-integral (PI) control cannot be designed to explicitly account for input/state constraints, optimality considerations and the batch nature of the deposition process, and thus, their use will not be pursued. Furthermore, dynamic open-loop optimization may be used but it does not provide robustness against the model inaccuracies and the fluctuations in the deposition process. In the case where feedback porosity control cannot be attained, dynamic optimization may be used instead; this is naturally included in the proposed model predictive control framework.

The control action, at a time t and state ρ, is obtained by solving a finite-horizon optimal control problem. The optimal temperature profile is calculated by solving a finite-dimensional optimization problem in a receding horizon fashion. Specifically,

the MPC problem is formulated based on the deterministic ODE of Eq. (5.8) as follows:

$$
\begin{gathered}
\min_{T_1,\ldots,T_i,\ldots,T_p} J(\rho(t)) = \sum_{i=1}^{p} q_{\mathrm{sp},i} \left[\rho_{\mathrm{set}} - \langle \rho(t+i\Delta) \rangle\right]^2 \\
\text{subject} \quad \text{to} \\
\langle \rho(t+i\Delta) \rangle = \rho^{\mathrm{ss}}(T_i, W_0) + \left(\langle \rho(t+(i-1)\Delta) \rangle - \rho^{\mathrm{ss}}(T_i, W_0)\right) e^{-\Delta/\tau(T_i, W_0)}, \\
T_{\min} < T_i < T_{\max}, \quad \left| \frac{T_{i+1} - T_i}{\Delta} \right| \leq L_{\mathrm{T}}, \\
i = 1, 2, \ldots, p,
\end{gathered}
\tag{5.23}
$$

where t is the current time, Δ is the sampling time, p is the number of prediction steps, $p\Delta$ is the specified prediction horizon, T_i, $i = 1, 2, \ldots, p$, is the substrate temperature at the ith step ($T_i = T(t + i\Delta)$), respectively, W_0 is the fixed deposition rate, $q_{\mathrm{sp},i}$, $i = 1, 2, \ldots, p$, are the weighting penalty factors for the error of the complete film SOR at the ith prediction step, $T_{\min}$ and $T_{\max}$ are the lower and upper bounds on the substrate temperature, respectively, and L_{T} is the limit on the rate of change of the substrate temperature. In the MPC formulation of Eq. (5.23), J is the cost function, which contains penalty on the squared difference between the desired value of the complete film SOR, ρ_{set}, and the predicted values of this variable at all time steps.

The dynamics of the expected value of the complete film SOR are described by the deterministic first-order ODE of Eq. (5.10). The dependence of model parameters on process parameters is obtained from the parameter estimation at a variety of

conditions. Due to the availability of analytical solutions of the linear ODE model of Eq. (5.10), these analytical solutions can be used directly in the MPC formulation of Eq. (5.23) for the prediction of $\langle \rho(t) \rangle$. The system state, $\rho(t)$, is the complete film SOR at time t. Note that $\rho(t)$, which is obtained directly from the simulation in real-time, is considered as the expected complete film SOR and can be used as an initial condition for the solution of the deterministic ODE of Eq. (5.10). In the closed-loop simulations, the instantaneous values of ρ and ρ_{p} are made available to the controller at each sampling time; however, no statistical information, e.g., the expected value of complete/partial film SOR, is available for feedback. The optimal set of control actions, $(T_1, T_2, \ldots, T_p)$, is obtained from the solution of the multi-variable optimization problem of Eq. (5.23), and only the first value of the manipulated input trajectory, T_1, is applied to the deposition process during the time interval $(t, t+\Delta)$. At time $t+\Delta$, a new measurement of ρ is received and the MPC problem of Eq. (5.23) is solved for the next control input trajectory.

5.5.2 Fluctuation regulation of partial film site occupancy ratio

Reduction of run-to-run variability is another goal in process control of a thin film growth process. In this chapter, the fluctuation of film SOR is represented by the variance of partial film SOR, $\mathrm{Var}(\rho_{\mathrm{p}})$. Ideally, a zero value means no fluctuation from run to run. However, it is impossible to achieve zero variance of partial film

SOR due to the stochastic nature of the thin film growth process. Thus, the control objective of fluctuation regulation is to minimize the variance by manipulating the process parameters.

In this chapter, the fluctuation is included into the cost function together with the error of the complete film SOR. Specifically, the MPC formulation with penalty on the error of the expected complete film SOR and penalty on the variance of the partial film SOR is given as follows:

$$
\begin{aligned}
\min_{T_1,\ldots,T_i,\ldots,T_p} J(\rho(t)) = \sum_{i=1}^{p} \left\{ q_{\mathrm{sp},i} \left[\rho_{\mathrm{set}} - \langle \rho(t+i\Delta)\rangle\right]^2 + q_{\mathrm{var},i} \mathrm{Var}[\rho_{\mathrm{p}}(t+i\Delta)] \right\} \\
\text{subject} \quad \text{to} \\
\langle \rho(t+i\Delta)\rangle = \rho^{\mathrm{ss}}(T_i, W_0) + \left(\langle \rho(t+(i-1)\Delta)\rangle - \rho^{\mathrm{ss}}(T_i, W_0)\right) e^{-\Delta/\tau(T_i,W_0)}, \\
\mathrm{Var}(\rho_{\mathrm{p}}(t+i\Delta)) = \ \mathrm{Var}_{\mathrm{p}}^{\mathrm{ss}}(T_i, W_0) \\
+ \left(\mathrm{Var}\left[\rho_{\mathrm{p}}(t+(i-1)\Delta)\right] - \mathrm{Var}_{\mathrm{p}}^{\mathrm{ss}}(T_i, W_0)\right) e^{-2\Delta/\tau_{\mathrm{p}}(T_i,W_0)}, \\
T_{\min} < T_i < T_{\max}, \quad \left|\frac{T_{i+1} - T_i}{\Delta}\right| \leq L_{\mathrm{T}}, \\
i = 1, 2, \ldots, p,
\end{aligned}
\tag{5.24}
$$

where $q_{\mathrm{sp},i}$ and $q_{\mathrm{var},i}$, $i = 1, 2, \ldots, p$, are weighting penalty factors on the error of the complete film SOR and of the variance of the partial film SOR, respectively. Other variables in Eq. (5.24) are defined similar to the ones in Eq. (5.23). The same constraints as in Eq. (5.23) are imposed on the MPC formulation of Eq. (5.24). Due to the unavailability of statistical information of the partial film SOR in real-time, the

initial condition of the partial film SOR is regarded as a deterministic variable and the initial condition for $\mathrm{Var}(\rho_{\mathrm{p}}(t))$ is considered to be zero in the MPC formulation.

5.5.3 Closed-loop simulations

In this section, the model predictive controllers of Eqs. (5.23) and (5.24) are applied to the kMC model of the thin film growth process described in Section 5.2. The value of the substrate temperature is obtained from the solution to the problem of Eqs. (5.23) and (5.24) at each sampling time and is applied to the closed-loop system until the next sampling time. The complete film SOR and the partial film SOR are obtained directly from the kMC model of the thin film at each sampling time as the state of the system and are fed into the controllers. The sampling time is fixed in all closed-loop simulations to be $\Delta = 5$ s, which is in the same order of magnitude of the time constant of the dynamics of the complete film SOR, τ. The optimization problems in the MPC formulations of Eqs. (5.23) and (5.24) are solved using a local constrained minimization algorithm.

The constraint on the rate of change of the substrate temperature is imposed onto the optimization problem, which is realized in the optimization process in the following way:

$$\left|\frac{T_{i+1}-T_i}{\Delta}\right| \le L_{\mathrm{T}} \Rightarrow |T_{i+1}-T_i| \le L_{\mathrm{T}}\Delta \Rightarrow T_i - L_{\mathrm{T}}\Delta \le T_{i+1} \le T_i + L_{\mathrm{T}}\Delta, \quad i = 1, 2, \ldots, p. \tag{5.25}$$

The desired value (set-point) for the complete film SOR in the closed-loop simulations is 0.9. The number of prediction steps is 5. The deposition rate is fixed at 1 layer/s and all closed-loop simulations are initialized with an initial temperature of 300 K. The maximal rate of change of the temperature is 10 K/s. Expected values and variances are calculated from 1000 independent simulation runs.

Regulation of complete film site occupancy ratio

First, the closed-loop simulation results of complete film SOR regulation using the model predictive control formulation of Eq. (5.23) are provided. In this MPC formulation, the cost function contains only penalty on the difference of the complete film SOR from the set-point value. Specifically, the optimization problem is formulated to minimize the difference between the complete film SOR set-point and the prediction of the expected complete film SOR at the end of each prediction step. All weighting penalty factors, $q_{\mathrm{sp},i}$, $i = 1, 2, \ldots, p$, are assigned to be equal. Figure 5.17 shows the profiles of the expected value of the complete film SOR in the closed-loop system simulation. The profiles of the complete film SOR and of the substrate temperature from a single simulation run are also included in Figure 5.17.

In Figure 5.17, the substrate temperature increases linearly at the initial stages due to the constraint on the rate of change, and it approaches to a value around 650 K, which is calculated from the optimization problem based on the current complete film SOR. The expected complete film SOR reaches the value of 0.87 at the end

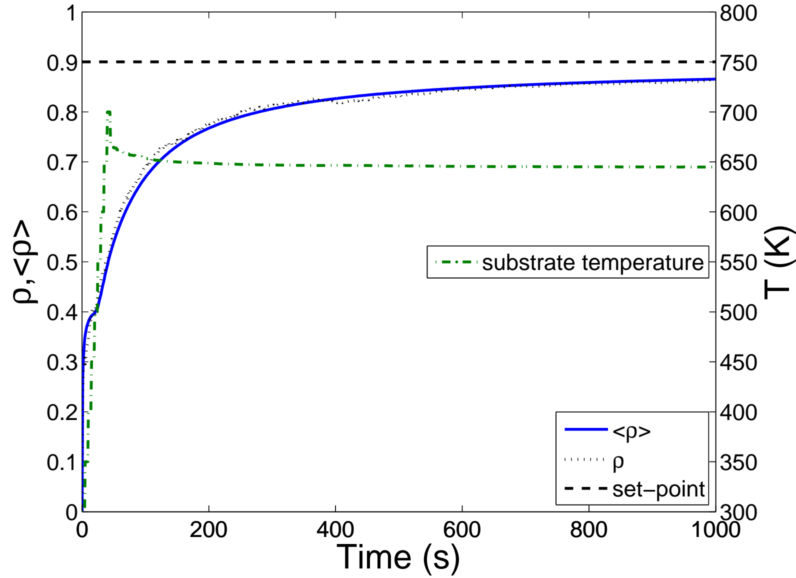

Figure 5.17: Closed-loop profiles of the complete film SOR (solid line) and of the expected value of the complete film SOR (dotted line) under the controller of Eq. (5.23). The profile of the substrate temperature is also included (dash-dotted line).

of the simulation. There is a difference of 0.03 from the set point, which is due to the fact that the first-order ODE model is not an exact description of the film SOR dynamics, but rather an approximation. However, for the purpose of control design, the first-order ODE model is acceptable. Another reason for the difference is the cumulative nature of the complete film SOR. Since the initial temperature, 300 K, is far below the optimal temperature for the desired film SOR, it takes some time for the substrate temperature to reach the optimal temperature. The initial condition of the substrate temperature results in a period of low temperature at the initial stages. In this period, layers with higher porosity are deposited onto the film and, as a result, the complete film SOR is lowered. Thus, it takes longer time for the complete film SOR to reach its steady-state value. The difference between the set-

point and the closed-loop steady-state value can be overcome by pre-setting a higher initial substrate temperature. Another possible method to improve the closed-loop performance is to replace the quadratic cost function that penalizes the deviation of the SORs from the desired values with other functions, since quadratic terms slow down the convergence speed in the vicinity of the set point. Snapshots of the film microstructure at different times, $t = 100$ s, 400 s, 700 s, and 1000 s, of the closed-loop simulation are shown in Figure 5.18.

Fluctuation regulation of partial film site occupancy ratio

To reduce the run-to-run variability of the film porosity, the variance of the partial film SOR is added into the cost function in the model predictive controller of Eq. (5.24). There are two weighting factors, $q_{\text{sp},i}$ and $q_{\text{var},i}$, which represent the weights on the complete film SOR and on the variance of the partial film SOR prediction, respectively. Figure 5.19 shows the profiles of the expected complete film SOR and of the substrate temperature in the closed-loop simulation, with the following values assigned to the weighting factors:

$$q_{\text{sp},i} = 1, \quad q_{\text{var},i} = 10, \quad i = 1, 2, 3, 4, \text{ and } 5. \tag{5.26}$$

As shown in Figure 5.19, the complete film SOR and the substrate temperature evolve similarly as in Figure 5.17. However, with the cost function including penalty on the variance of the partial film SOR, the optimal temperature is higher than the

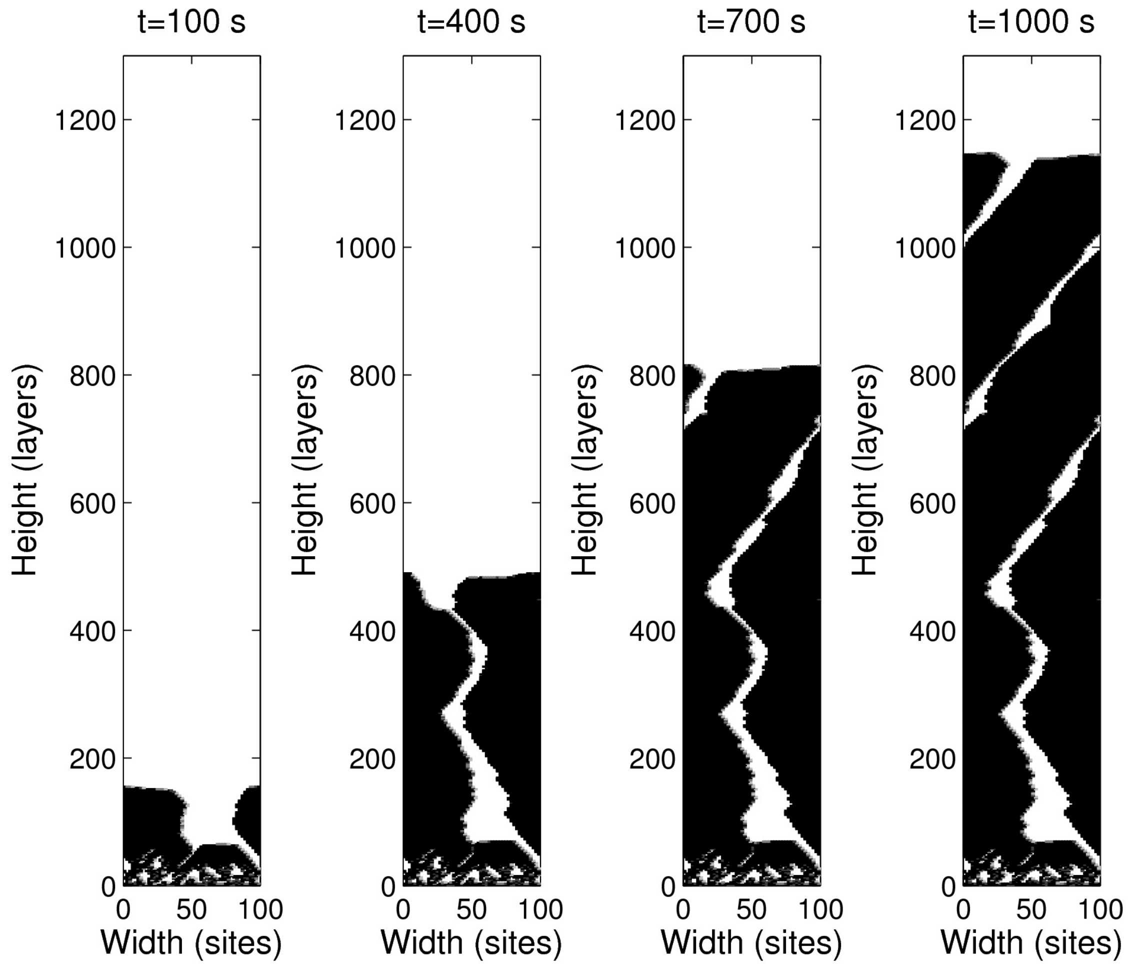

Figure 5.18: Snapshots of the film microstructure at t = 100 s, 400 s, 700 s, and 1000 s of the closed-loop simulation under the feedback controller of Eq. (5.23) with $q_{\text{sp},i} = 1$, $i = 1, \ldots, 5$.

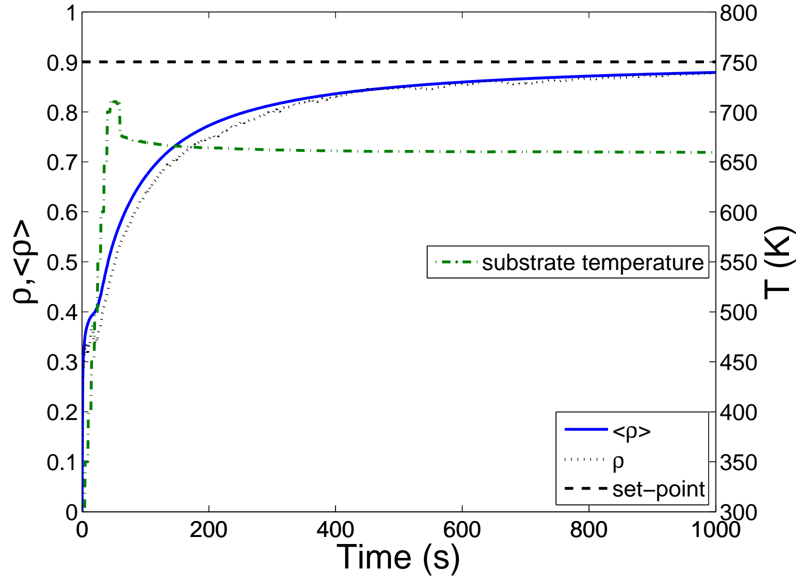

Figure 5.19: Closed-loop profiles of the complete film SOR (solid line) and of the expected value of the complete film SOR (dotted line) under the controller of Eq. (5.24). The profile of the substrate temperature is also included (dash-dotted line).

one in Figure 5.17, since a higher substrate temperature is in favor of decreasing run-to-run fluctuations. Figure 5.20 shows a comparison of the variance of the partial film SOR between the two model predictive controllers with $q_{\text{var},i} = 0$ and $q_{\text{var},i} = 10$, $i = 1, 2, 3, 4,$ and 5. It can be seen that the variance of the partial film SOR is lowered with penalty on this variable included into the cost function of the MPC formulation. Snapshots of the film microstructure at different times, $t = 100$ s, 400 s, 700 s, and 1000 s, of the closed-loop simulation are shown in Figure 5.21.

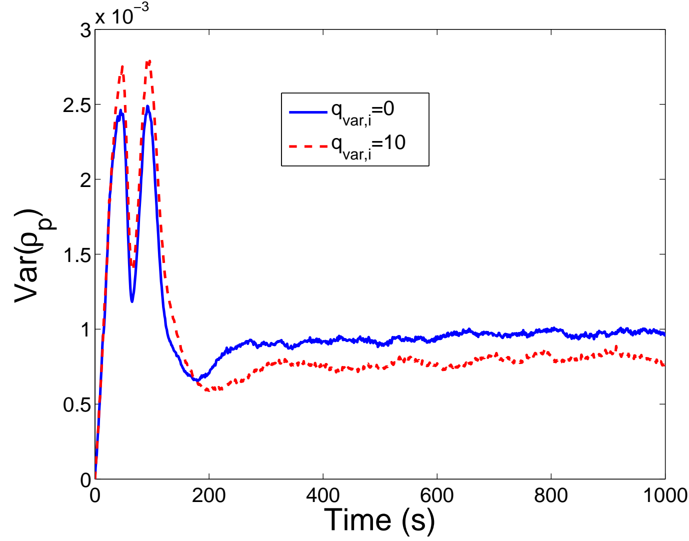

Figure 5.20: Comparison of the variance of the partial film SOR for different weights: $q_{\text{var},i} = 0$ (solid line) and $q_{\text{var},i} = 10$ (dashed line).

5.6 Conclusions

In this chapter, systematic methodologies were developed for modeling and control of film porosity in thin film deposition. A thin film deposition process which involves atom adsorption and migration was introduced and was modeled using a triangular lattice-based kMC simulator which allows porosity, vacancies and overhangs to develop and leads to the deposition of a porous film. Appropriate definitions of film SOR and its fluctuation were introduced to describe film porosity. Deterministic and stochastic ODE models were derived that describe the time evolution of film SOR and its fluctuation. The coefficients of the ODE models were estimated on the basis of data obtained from the kMC simulator of the deposition process using least-square methods and their dependence on substrate temperature was determined. The de-

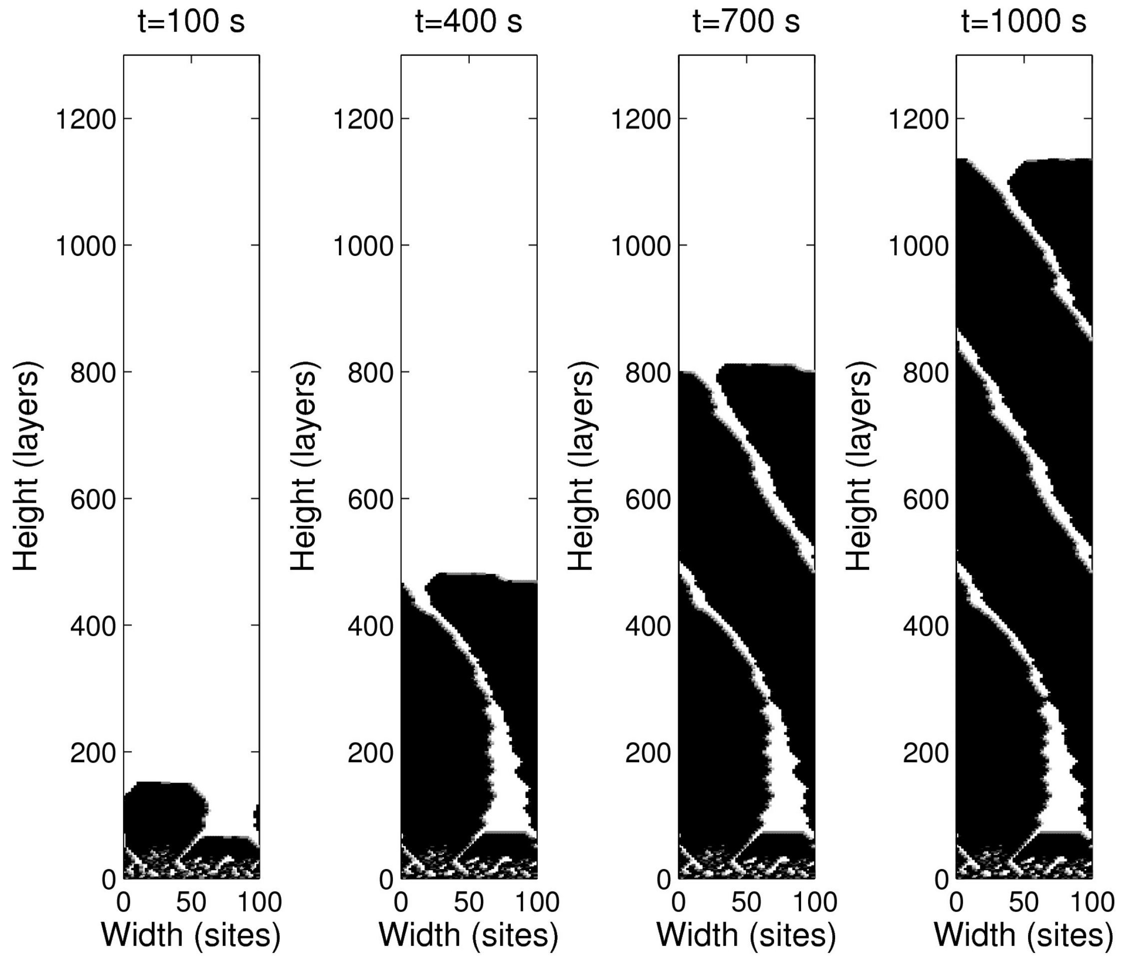

Figure 5.21: Snapshots of the film microstructure at $t = 100$ s, 400 s, 700 s, and 1000 s of the closed-loop simulation under the feedback controller of Eq. (5.24) with $q_{\text{sp},i} = 1$, $q_{\text{var},i} = 10$, $i = 1, \ldots, 5$.

veloped ODE models were used as the basis for the design of MPC algorithms that include penalty on the film SOR and its variance to regulate the expected value of film SOR at a desired level and reduce run-to-run fluctuations. The applicability and effectiveness of the proposed modeling and control methods were demonstrated by simulation results in the context of the deposition process under consideration.

Chapter 6

Simultaneous Regulation of Surface Roughness and Porosity

6.1 Introduction

This chapter further focuses on stochastic modeling and simultaneous regulation of surface roughness and film porosity in a porous thin film deposition process modeled via kMC simulation on a triangular lattice. The microscopic model of the thin film growth process includes adsorption and migration processes. Vacancies and overhangs are allowed inside the film for the purpose of modeling thin film porosity. The definition of surface height profile is first introduced for a porous thin film deposition taking place in a triangular lattice. The dynamics of surface height of the thin film are described by an Edward-Wilkinson (EW)-type equation, which is a second-order

linear stochastic PDE model. The root mean square (RMS) surface roughness is chosen as one of the controlled variables. Subsequently, an appropriate definition of film site occupancy ratio (SOR) is introduced to represent the extent of porosity inside the film and is chosen as the second to-be-controlled variable. A deterministic ODE model is postulated to describe the time evolution of film SOR. The coefficients of the EW equation of surface height and of the deterministic ODE model of film SOR are estimated on the basis of data obtained from the kMC simulator of the deposition process using least-square methods and their dependence on substrate temperature is determined. The developed dynamic models are used as the basis for the design of a model predictive control algorithm that includes penalty on the deviation of surface roughness square and film SOR from their respective set-point values. Simulation results demonstrate the applicability and effectiveness of the proposed modeling and control approach in the context of the deposition process under consideration.

6.2 Thin film deposition process

6.2.1 Description and modeling

The thin film growth process considered in this chapter is similar to the deposition process introduced in Chapter 5, which includes an adsorption process and a migration process. However, a vertical incidence in the adsorption process is considered in this chapter for the purposes of modeling and control of surface height profile and surface

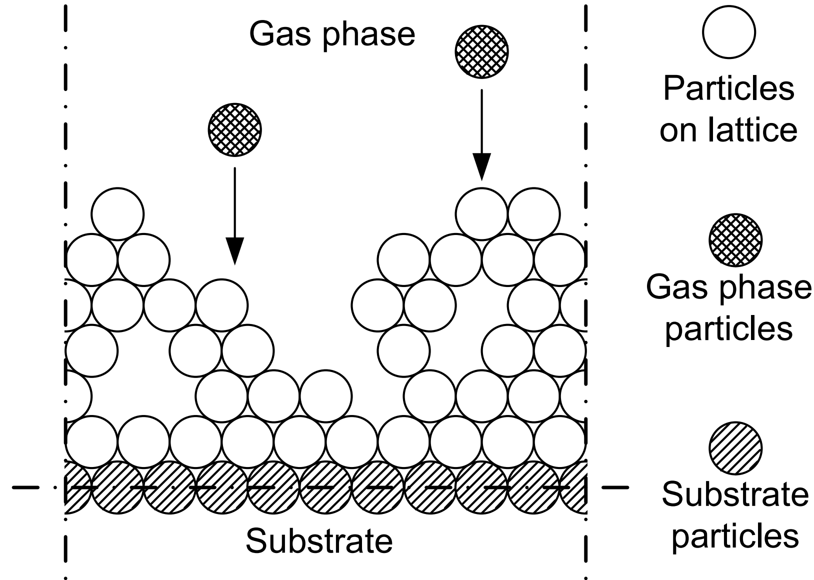

Figure 6.1: Thin film growth process on a triangular lattice with vertically incident particles from gas phase.

roughness. The deposition process with vertical incident particles is shown in in Figure 6.1.

In the adsorption process, an vertically incident particle is incorporated on the film; as illustrated in Figure 6.2. After the initial position is determined, the incident particle, A, travels along a straight line vertically towards the film until contacting the first particle, B, on the film. Upon contact, particle A stops and sticks to particle B at the contacting position; see Figure 6.2. Then, particle A moves (relaxes) to the nearest vacant site, C, among the neighboring sites of particle B. Surface relaxation is conducted if site C is unstable, i.e., site C has only one neighboring particle, as shown in Figure 6.2. When a particle is subject to surface relaxation, the particle moves to its most stable neighboring vacant site, which is defined as the site with

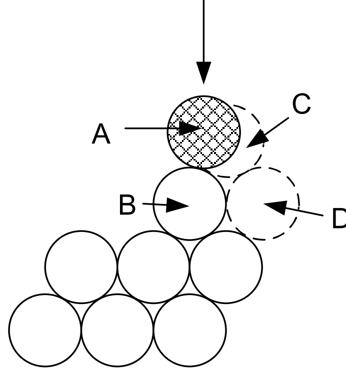

Figure 6.2: Schematic of the adsorption event with surface relaxation. In this event, particle A is the vertically incident particle, particle B is the surface particle that is first hit by particle A, site C is the nearest vacant site to particle A among the sites that neighbor particle B, and site D is a stable site where particle A relaxes.

the most nearest neighbors. In the case of multiple neighboring vacant sites with the same number of nearest neighbors, a random one is chosen from these sites with equal probability as the objective of the particle surface relaxation process. Note that particle surface relaxation is considered as part of the deposition event, and thus, it does not contribute to the process simulation time. There is also only one relaxation event per incident particle.

In the migration process, a particle overcomes the energy barrier of the site and jumps to its vacant neighboring site. The migration rate of the ith particle follows an Arrhenius-type law as follows:

$$r_{\mathrm{m},i} = \nu_0 \ \exp\left(-\frac{n_i E_0}{k_{\mathrm{B}} T}\right). \tag{6.1}$$

In this chapter, the same factor and energy barrier contribution in Eq. (6.1), $\nu_0 = 10^{13}$

s^{-1} and $E_0 = 0.6$ eV, are used as in Chapter 5.

6.2.2 Definitions of surface morphology and film porosity

Utilizing the continuous-time Monte Carlo algorithm, simulations of the kMC model of a porous silicon thin film growth process are carried out. Snapshots of film microstructure, i.e., the configurations of particles within the triangular lattice, are obtained from the kMC model at various time instants during process evolution. To quantitatively evaluate the thin film microstructure, two variables, surface roughness and film porosity, are introduced in this subsection.

Surface roughness, which measures the texture of thin film surface, is represented by the root mean square (RMS) of the surface height profile of the thin film. Determination of surface height profile is different in the triangular lattice model compared to a SOS model. In the SOS model, the surface of a thin film is naturally described by the positions of the top particles of each column. In the triangular lattice model, however, due to the existence of vacancies and overhangs, the definition of film surface needs further clarification. Specifically, taking into account practical considerations of surface roughness measurements, the surface height profile of a triangular lattice model is defined based on the particles that can be reached in the vertical direction, as shown in Figure 6.3. In this definition, a particle is considered as a surface particle only if it is not blocked by the particles of both of its neighboring columns. Therefore, the surface height profile of a porous thin film is the line that connects the sites

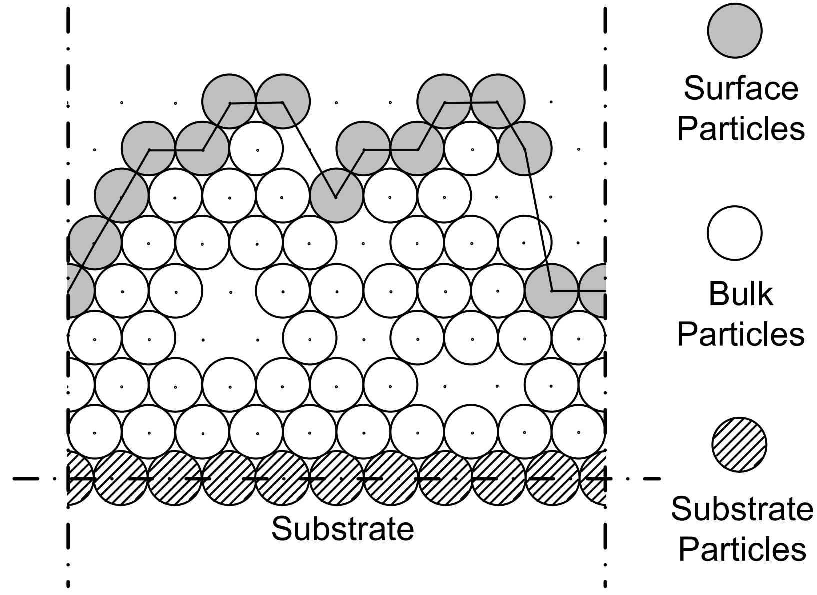

Figure 6.3: Definition of surface height profile. A surface particle is a particle that is not blocked by particles from both of its neighboring columns in the vertical direction.

that are occupied by the surface particles. With this definition, the surface height profile can be treated as a function of the spatial coordinate. Surface roughness, as a measurement of the surface texture, is defined as the standard deviation of the surface height profile from its average height. The mathematical expression of surface roughness is given later in Section 6.3.1.

In addition to film surface roughness, the film SOR is introduced to represent the extent of the porosity inside the thin film. The mathematical expression of film SOR is defined as follows:

$$\rho = \frac{N}{LH} \tag{6.2}$$

where ρ denotes the film SOR, N is the total number of deposited particles on the

lattice, L is the lattice size, and H denotes the number of deposited layers. Note that the deposited layers are the layers that contain only deposited particles and do not include the initial substrate layers. The variables in the definition expression of Eq. (6.2) can be found in Figure 5.3. Since each layer contains L sites, the total number of sites in the film that can be contained within the H layers is LH. Thus, film SOR is the ratio of the occupied lattice sites, N, over the total number of available sites, LH. Film SOR ranges from 0 to 1. Specifically, $\rho = 1$ denotes a fully occupied film with a flat surface. The value of zero is assigned to ρ at the beginning of the deposition process since there are no particles deposited on the lattice.

It is important to note that film surface roughness and porosity are correlated to some extent in the deposition process. A film with lower porosity tends to have a smoother surface, since the conditions to produce a dense film (higher substrate temperature or lower adsorption rate) also help reduce the surface roughness and vice versa. However, even though they are related to each other, roughness and porosity are separate variables that describe different aspects of the thin film. Films with same film SORs may have different surface roughness.

6.3 Dynamic models construction and parameter estimation

6.3.1 Edward-Wilkinson-type equation of surface height

An EW-type equation, a second-order stochastic PDE, can be used to describe the surface height evolution in many microscopic processes that involve thermal balance between adsorption (deposition) and migration (diffusion). An EW-type equation is chosen to describe the dynamics of the fluctuation of surface height (the validation of this choice will be made clear below):

$$\frac{\partial h}{\partial t} = r_{\mathrm{h}} + \nu \frac{\partial^2 h}{\partial x^2} + \xi(x,t) \tag{6.3}$$

subject to PBCs:

$$h(-\pi,t) = h(\pi,t), \quad \frac{\partial h}{\partial x}(-\pi,t) = \frac{\partial h}{\partial x}(\pi,t), \tag{6.4}$$

and the initial condition:

$$h(x,0) = h_0(x) \tag{6.5}$$

where $x \in [-\pi, \pi]$ is the projected spatial coordinate, t is the time, r_{h} and ν are the model parameters, and $\xi(x,t)$ is a Gaussian white noise with the following expressions

for its mean and covariance:

$$
\begin{aligned}
\langle \xi(x,t) \rangle &= 0, \\
\langle \xi(x,t)\xi(x',t') \rangle &= \sigma^2 \delta(x-x')\delta(t-t'),
\end{aligned}
\tag{6.6}
$$

where σ^2 is a parameter which measures the intensity of the Gaussian white noise and $\delta(\cdot)$ denotes the standard Dirac delta function. To validate the choice of $\xi(x,t)$ as Gaussian white noise, uncorrelated in both time and space, we present in Figures 6.4 and 6.5 the histograms of surface height, obtained from 10000 independent open-loop simulation runs at sufficiently large simulation times, at different positions and times. Specifically, Figure 6.4 shows the histogram of surface height at different sites ($x = 0a$, $25a$, $50a$, $75a$) at $t = 400$ s, and Figure 6.5 shows the histogram of surface height at $x = 50a$ for different time instants ($t = 100$ s, 200 s, 300 s, 400 s). It can be clearly seen in Figures 6.4 and 6.5 that the surface height follows Gaussian probability distribution at sufficiently large times and that the noise is uncorrelated in both time and space, which indicates that the choice of white noise is a reasonable one.

To proceed with model parameter estimation and control design, a stochastic ODE approximation of Eq. (6.3) is first derived using Galerkin's method. Consider

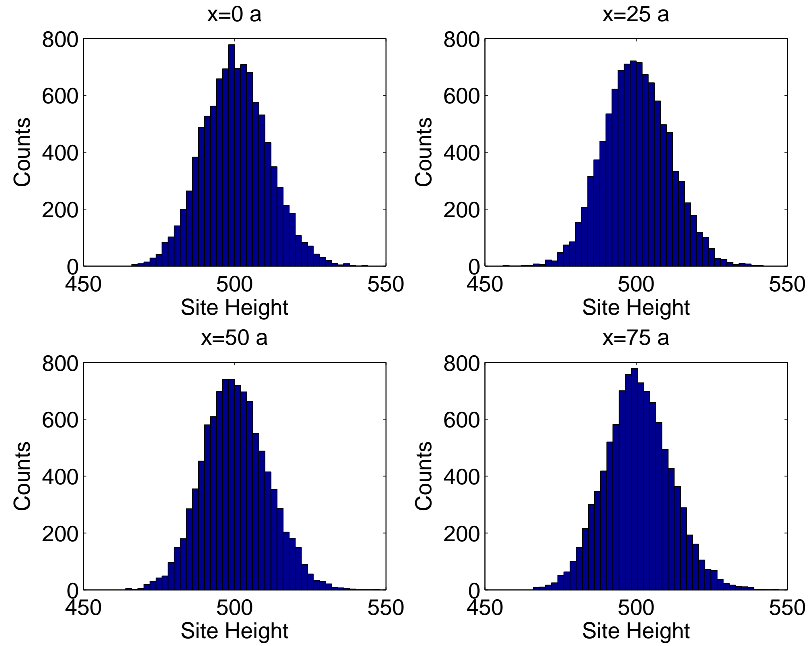

Figure 6.4: Histogram of surface height at $t = 400$ s for different sites ($x = 0a$, $25a$, $50a$, $75a$).

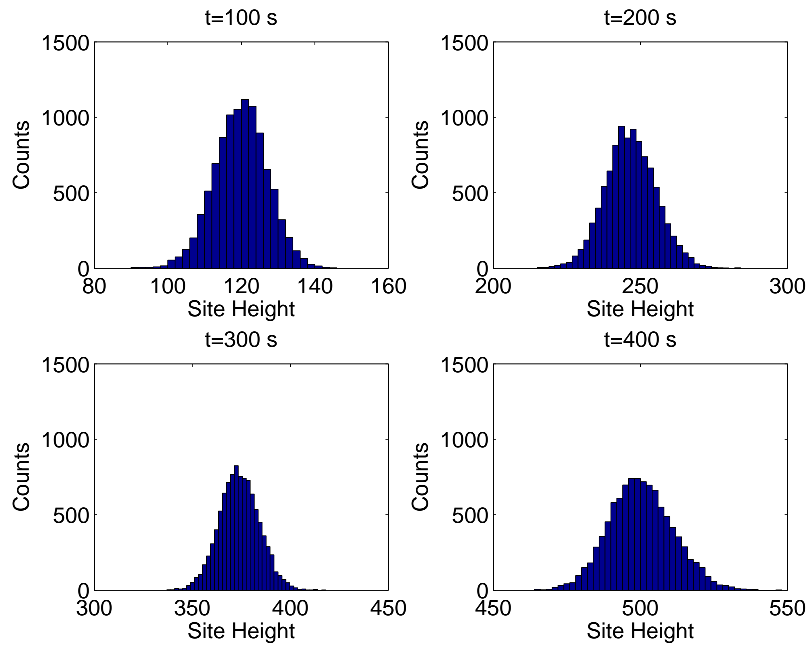

Figure 6.5: Histogram of surface height at $x = 50a$ for different time instants ($t = 100$ s, 200 s, 300 s, 400 s).

the eigenvalue problem of the linear operator of Eq. (6.3), which takes the form:

$$
\begin{aligned}
A\bar{\phi}_n(x) &= \nu \frac{d^2\bar{\phi}_n(x)}{dx^2} = \lambda_n \bar{\phi}_n(x), \\
\bar{\phi}_n(-\pi) = \bar{\phi}_n(\pi), &\quad \frac{d\bar{\phi}_n}{dx}(-\pi) = \frac{d\bar{\phi}_n}{dx}(\pi),
\end{aligned}
\tag{6.7}
$$

where λ_n denotes an eigenvalue and $\bar{\phi}_n$ denotes an eigenfunction. A direct computation of the solution of the above eigenvalue problem yields $\lambda_0 = 0$ with $\psi_0 = 1/\sqrt{2\pi}$, and $\lambda_n = -\nu n^2$ (λ_n is an eigenvalue of multiplicity two) with eigenfunctions $\phi_n = (1/\sqrt{\pi})\sin(nx)$ and $\psi_n = (1/\sqrt{\pi})\cos(nx)$ for $n = 1, \ldots, \infty$. Note that the $\bar{\phi}_n$ in Eq. (6.7) denotes either ϕ_n or ψ_n. For a fixed positive value of ν, all eigenvalues (except the zeroth eigenvalue) are negative and the distance between two consecutive eigenvalues (i.e., λ_n and λ_{n+1}) increases as n increases.

To this end, the solution of Eq. (6.3) is expanded in an infinite series in terms of the eigenfunctions of the operator of Eq. (6.7) as follows:

$$
h(x,t) = \sum_{n=1}^{\infty} \alpha_n(t)\phi_n(x) + \sum_{n=0}^{\infty} \beta_n(t)\psi_n(x) \tag{6.8}
$$

where $\alpha_n(t)$, $\beta_n(t)$ are time-varying coefficients. Substituting the above expansion for the solution, $h(x,t)$, into Eq. (6.3) and taking the inner product with the adjoint eigenfunctions, $\phi_n^*(x) = (1/\sqrt{\pi})\sin(nx)$ and $\psi_n^*(x) = (1/\sqrt{\pi})\cos(nx)$, the following

system of infinite stochastic ODEs is obtained:

$$\begin{aligned}
\frac{d\beta_0}{dt} &= \sqrt{2\pi} r_{\mathrm{h}} + \xi_{\beta}^{0}(t), \\
\frac{d\alpha_n}{dt} &= \lambda_n \alpha_n + \xi_{\alpha}^{n}(t), \quad n = 1, \ldots, \infty, \\
\frac{d\beta_n}{dt} &= \lambda_n \beta_n + \xi_{\beta}^{n}(t), \quad n = 1, \ldots, \infty,
\end{aligned} \tag{6.9}$$

where

$$\begin{aligned}
\xi_{\alpha}^{n}(t) &= \int_{-\pi}^{\pi} \xi(x,t) \phi_n^*(x) dx, \\
\xi_{\beta}^{n}(t) &= \int_{-\pi}^{\pi} \xi(x,t) \psi_n^*(x) dx.
\end{aligned} \tag{6.10}$$

Using Result 1, we obtain $\langle \xi_{\alpha}^{n}(t) \xi_{\alpha}^{n}(t') \rangle = \sigma^2 \delta(t-t')$ and $\left\langle \xi_{\beta}^{n}(t) \xi_{\beta}^{n}(t') \right\rangle = \sigma^2 \delta(t-t')$.

Since the stochastic ODE system is linear, the analytical solution of state variance can be obtained from a direct computation as follows:

$$\begin{aligned}
\left\langle \alpha_n^2(t) \right\rangle &= \frac{\sigma^2}{2\nu n^2} + \left(\left\langle \alpha_n^2(t_0) \right\rangle - \frac{\sigma^2}{2\nu n^2} \right) e^{-2\nu n^2 (t-t_0)}, \quad n = 1, 2, \ldots, \infty, \\
\left\langle \beta_n^2(t) \right\rangle &= \frac{\sigma^2}{2\nu n^2} + \left(\left\langle \beta_n^2(t_0) \right\rangle - \frac{\sigma^2}{2\nu n^2} \right) e^{-2\nu n^2 (t-t_0)}, \quad n = 1, 2, \ldots, \infty,
\end{aligned} \tag{6.11}$$

where $\langle \alpha_n^2(t_0) \rangle$ and $\langle \beta_n^2(t_0) \rangle$ are the state variances at time t_0. The analytical solution of state variance of Eq. (6.11) will be used in the parameter estimation and the MPC design in sections 6.3.3 and 6.4.2

When the dynamic model of surface height profile is determined, surface roughness of the thin film is defined as the standard deviation of the surface height profile from

its average height and is computed as follows:

$$r(t) = \sqrt{\frac{1}{2\pi}\int_{-\pi}^{\pi}[h(x,t) - \bar{h}(t)]^2 dx} \tag{6.12}$$

where $\bar{h}(t) = \dfrac{1}{2\pi}\displaystyle\int_{-\pi}^{\pi} h(x,t)dx$ is the average surface height. According to Eq. (6.8), we have $\bar{h}(t) = \beta_0(t)\psi_0$. Therefore, $\langle r^2(t)\rangle$ can be rewritten in terms of $\langle \alpha_n^2(t)\rangle$ and $\langle \beta_n^2(t)\rangle$ as follows:

$$\begin{aligned}
\langle r^2(t)\rangle &= \frac{1}{2\pi}\left\langle \int_{-\pi}^{\pi}(h(x,t) - \bar{h}(t))^2 dx \right\rangle \\
&= \frac{1}{2\pi}\left\langle \int_{-\pi}^{\pi}\left[\sum_{i=1}^{\infty}\alpha_i(t)\phi_i(x) + \sum_{i=0}^{\infty}\beta_i(t)\psi_i(x) - \beta_0(t)\psi_0\right]^2 dx \right\rangle \\
&= \frac{1}{2\pi}\left\langle \int_{-\pi}^{\pi}\sum_{i=1}^{\infty}\left[\alpha_i^2(t)\phi_i^2(x) + \beta_i^2(t)\psi_i^2(x)\right] dx \right\rangle \\
&= \frac{1}{2\pi}\left\langle \sum_{i=1}^{\infty}(\alpha_i^2(t) + \beta_i^2(t)) \right\rangle = \frac{1}{2\pi}\sum_{i=1}^{\infty}\left[\langle \alpha_i^2(t)\rangle + \langle \beta_i^2(t)\rangle\right].
\end{aligned} \tag{6.13}$$

Thus, Eq. (6.13) provides a direct link between the state variance of the infinite stochastic ODEs of Eq. (6.9) and the expected surface roughness of the thin film. Note that the model parameter r_{h} does not appear in the expression of surface roughness, since the zeroth state, β_0, is only affected by r_{h} but this state is not included in the computation of the expected surface roughness square of Eq. (6.13).

6.3.2 Deterministic dynamic model of film site occupancy ratio

Since film porosity is another control objective, a dynamic model is necessary in the MPC formulation to describe the evolution of film porosity, which is represented by the film SOR of Eq. (6.2). The dynamics of the expected value of the film SOR evolution are approximately described by a linear first-order deterministic ODE as follows [40]:

$$\tau \frac{d \langle \rho(t) \rangle}{dt} = \rho^{\mathrm{ss}} - \langle \rho(t) \rangle \tag{6.14}$$

where t is the time, τ is the time constant and ρ^{ss} is the steady-state value of the film SOR. The deterministic ODE system of Eq. (6.14) is subject to the following initial condition:

$$\langle \rho(t_0) \rangle = \rho_0 \tag{6.15}$$

where t_0 is the initial time and ρ_0 is the initial value of the film SOR. Note that ρ_0 is a deterministic variable, since ρ_0 refers to the film SOR at $t = t_0$. From Eqs. (6.14) and (6.15), it follows that

$$\langle \rho(t) \rangle = \rho^{\mathrm{ss}} + (\rho_0 - \rho^{\mathrm{ss}})\, e^{-(t-t_0)/\tau}. \tag{6.16}$$

The choice of a deterministic linear ODE for $\langle \rho(t) \rangle$ in Eq. (6.14) made based on open-loop process data and it adequately describes the dynamics of the film SOR.

Validation of the linear model of Eq. (6.14) is provided in Chapter 5.

6.3.3 Parameter estimation

Referring to the EW equation of Eq. (6.3) and the deterministic ODE model of Eq. (6.14), there are several model parameters, ν, σ^2, $\rho^{\rm ss}$ and τ, that need to be determined as functions of the substrate temperature. These parameters describe the dynamics of surface height and of film SOR and can be estimated by comparing the predicted evolution profiles for roughness and SOR from the dynamic models of Eq. (6.3) and Eq. (6.14) and the ones from the kMC simulation of the deposition process. Least-square methods are used to estimate the model parameters so that the model predictions are close in a least-square sense to the kMC simulation data.

Since surface roughness is a control objective, we choose the expected surface roughness square as the output for the parameter estimation of the EW equation of Eq. (6.3). Thus, the model coefficients, ν and σ^2 can be obtained by solving the problem of minimizing the prediction of the expected surface roughness square of Eq. (6.13) to the one from the kMC simulation at different time instants as follows:

$$\min_{\nu,\sigma^2} \sum_{k=1}^{n_1} \left[\left\langle r^2(t_k) \right\rangle - \frac{1}{2\pi} \sum_{i=1}^{\infty} \left(\left\langle \alpha_i^2(t_k) \right\rangle + \left\langle \beta_i^2(t_k) \right\rangle \right) \right]^2 \tag{6.17}$$

where n_1 is the number of the data samplings of surface height profile and surface roughness from the kMC simulations. The predictions of model state variance,

$\langle \alpha_i^2(t_k) \rangle$ and $\langle \beta_i^2(t_k) \rangle$, can be solved from the analytical solution of Eq. (6.11).

With respect to the parameters of the equation for film porosity, since the ODE model of Eq. (6.14) is linear, ρ^{ss} and τ can be estimated from the solutions of Eq. (6.16) by minimizing the sum of the squared difference between the evolution profiles from the ODE model prediction and the kMC simulation at different time instants as follows:

$$\min_{\rho^{\text{ss}},\tau} \sum_{k=1}^{n_2} \left[\langle \rho(t_k) \rangle - \left(\rho^{\text{ss}} + (\rho_0 - \rho^{\text{ss}})\, e^{-(k-t_0)/\tau} \right) \right]^2 \tag{6.18}$$

where n_2 is the number of the data pairs, $(t_k,\ \langle \rho(t_k) \rangle)$, from the kMC simulations.

The data used for the parameter estimation are obtained from the open-loop kMC simulation of the thin film growth process. The process parameters are fixed during each open-loop simulation so that the dependence of the model parameters on the process parameters can be obtained. Due to the stochastic nature of the process, multiple independent simulation runs are performed to obtain the expected values of surface roughness and film SOR.

The above parameter estimation process is applied to the open-loop simulation results with 100 lattice size. First, the open-loop evolution profiles of surface roughness and film SOR are obtained from 1000 independent kMC simulation runs with substrate temperature $T = 600$ K and deposition rate $W = 1$ layer/s. Model coefficients are estimated by solving the least square problems of Eqs. (6.17) and (6.18) as

follows:

$$\rho^{\rm ss} = 0.9823, \quad \tau = 2.9746 \text{ s}, \quad \nu = 2.6570 \times 10^{-4}, \quad \sigma^2 = 0.1757. \tag{6.19}$$

The EW-type equation with parameters estimated under time-invariant operating conditions is suitable for the purpose of MPC design. This is because the control input in the MPC formulation is piecewise, i.e., the manipulated substrate temperature remains constant between two consecutive sampling times, and thus, the dynamics of the microscopic process can be predicted using the dynamic models with estimated parameters. Eventually, the validation of the constructed models is demonstrated via closed-loop simulations (where the controller which utilizes the approximate models is applied to the kMC simulation of the process) which demonstrate that the desired control objectives are achieved. The simulation results will be shown in Section 6.5 below.

The dependence of the model coefficients on substrate temperature is used in the formulation of the model predictive controller in the next section. Thus, parameter estimation from open-loop kMC simulation results of the thin film growth process for a variety of operation conditions is performed to obtain the dependence of the model coefficients on substrate temperature. In this chapter, the deposition rate for all simulations is fixed at 1 layer/s. The range of T is between 300 K and 800 K, which is from room temperature to the upper limit of the allowable temperature for a

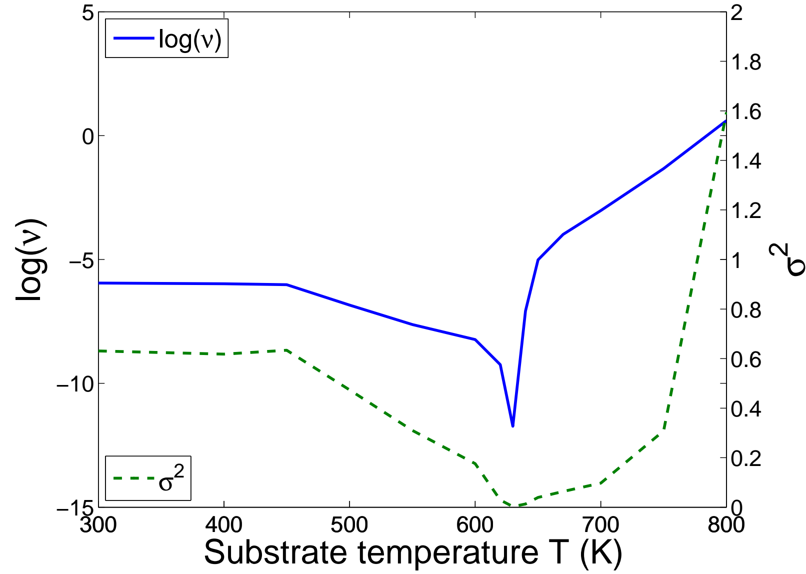

Figure 6.6: Dependence of $\ln(\nu)$ and σ^2 on the substrate temperature with deposition rate $W = 1$ layer/s.

valid on-lattice kMC model of silicon film. The dependence of the model parameters on the substrate temperature is shown in Figures 6.6 and 6.7. In these figures, it can be clearly seen that the dependence of the model parameters on temperature is highly nonlinear. Specifically, as substrate temperature increases, the migration rate becomes larger due to the Arrhenius type dependence of the migration rate on temperature. Thus, higher temperature tends to result in a thin film with less pores (higher film SOR) and a smoother surface (lower surface roughness).

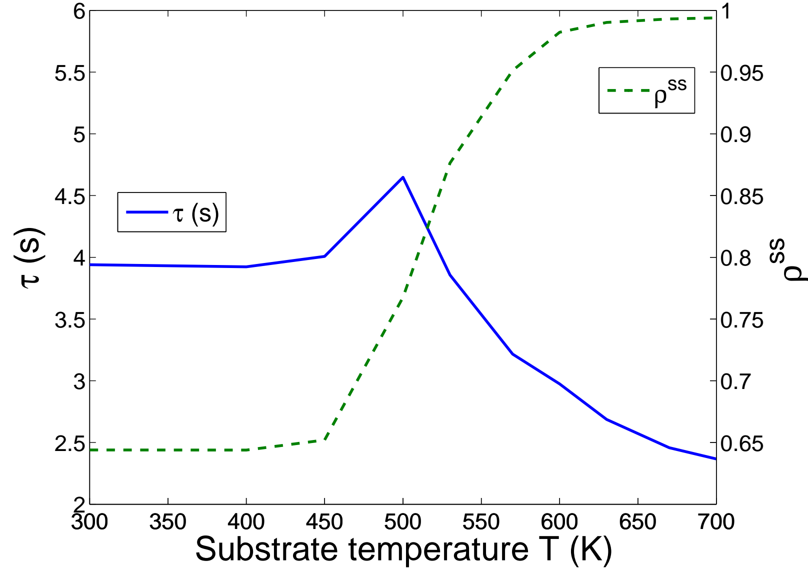

Figure 6.7: Dependence of ρ^{ss} and τ on the substrate temperature with deposition rate $W = 1$ layer/s.

6.4 Model predictive control

In this section, we design a model predictive controller based on the dynamic models of surface roughness and film SOR to simultaneously control the expected values of roughness square and film SOR to a desired level. The dynamics of surface roughness of the thin film are described by the EW equation of the surface height of Eq. (6.3) with appropriately computed parameters. Film SOR is modeled by a first-order deterministic ODE model. State feedback control is considered in this chapter, i.e., the surface height profile and the value of film SOR are assumed to be available to the controller and no sensor noise is introduced. Measurements of the film may be obtained in real-time through a combination of real-time gas phase measurements and empirical models that predict film porosity from gas phase measurements.

6.4.1 MPC formulation for regulation of roughness and porosity

We consider the problem of regulation of surface roughness and of film SOR to desired levels within a model predictive control framework. Since surface roughness and film SOR are stochastic variables, the expected values, $\langle r^2(t) \rangle$ and $\langle \rho \rangle$, are chosen as the control objectives. The substrate temperature is used as the manipulated input and the deposition rate is fixed at a certain value, W_0, during the entire closed-loop simulation. To account for a number of practical considerations, several constraints are added to the control problem. First, there is a constraint on the range of variation of the substrate temperature. This constraint ensures validity of the on-lattice kMC model. Another constraint is imposed on the rate of change of the substrate temperature to account for actuator limitations. The control action at time t is obtained by solving a finite-horizon optimal control problem. The cost function in the optimal control problem includes penalty on the deviation of $\langle r^2 \rangle$ and $\langle \rho \rangle$ from their respective set-point values. Different weighting factors are assigned to the penalties of the surface roughness and of the film SOR. Surface roughness and film SOR have very different magnitudes, ($\langle r^2 \rangle$ ranges from 1 to 10^2 and $\langle \rho \rangle$ ranges from 0 to 1). Therefore, relative deviations are used in the formulation of the cost function to make the magnitude of the two terms comparable. The optimization problem is subject to the dynamics of the surface height of Eq. (6.3) of and of the film SOR of Eq. (6.14). The optimal temperature profile is calculated by solving a finite-dimensional optimization

problem in a receding horizon fashion. Specifically, the MPC problem is formulated as follows:

$$
\begin{gathered}
\min_{T_1,\ldots,T_i,\ldots,T_p} J = \sum_{i=1}^{p} \left\{ q_{\mathrm{r}^2,i} \left[\frac{r_{\mathrm{set}}^2 - \langle r^2(t_i) \rangle}{r_{\mathrm{set}}^2} \right]^2 + q_{\rho,i} \left[\frac{\rho_{\mathrm{set}} - \langle \rho(t_i) \rangle}{\rho_{\mathrm{set}}} \right]^2 \right\} \\
\text{subject} \quad \text{to} \\
\frac{\partial h}{\partial t} = r_{\mathrm{h}} + \nu \frac{\partial^2 h}{\partial x^2} + \xi(x,t), \\
\tau \frac{d\,\langle \rho(t) \rangle}{dt} = \rho^{\mathrm{ss}} - \langle \rho(t) \rangle, \\
T_{\min} < T_i < T_{\max}, \quad \left| \frac{T_{i+1} - T_i}{\Delta} \right| \leq L_{\mathrm{T}}, \\
i = 1, 2, \ldots, p,
\end{gathered}
\tag{6.20}
$$

where t is the current time, Δ is the sampling time, p is the number of prediction steps, $p\Delta$ is the specified prediction horizon, t_i, $i = 1, 2, \ldots, p$, is the time of the ith prediction step ($t_i = t + i\Delta$), respectively, T_i, $i = 1, 2, \ldots, p$, is the substrate temperature at the ith step ($T_i = T(t + i\Delta)$), respectively, W_0 is the fixed deposition rate, $q_{\mathrm{r}^2,i}$ and $q_{\rho,i}$, $i = 1, 2, \ldots, p$, are the weighting penalty factors for the deviations of $\langle r^2 \rangle$ and $\langle \rho \rangle$ from their respective set-points at the ith prediction step, $T_{\min}$ and $T_{\max}$ are the lower and upper bounds on the substrate temperature, respectively, and L_{T} is the limit on the rate of change of the substrate temperature.

The optimal set of control actions, (T_1, T_2, $\ldots$, T_p), is obtained from the solution of the multi-variable optimization problem of Eq. (6.20), and only the first value of the manipulated input trajectory, T_1, is applied to the deposition process (i.e., kMC

model) during the time interval $(t, t+\Delta)$. At time $t+\Delta$, new measurements of ρ are received and the MPC problem of Eq. (6.20) is solved for the next control input trajectory.

6.4.2 MPC formulation based on reduced-order model

The MPC formulation proposed in Eq. (6.20) is developed on the basis of the EW equation of surface height and the deterministic ODE model of the film SOR. The EW equation, which is a distributed parameter dynamic model, contains infinite dimensional stochastic states. Therefore, it leads to a model predictive controller of infinite order that cannot be realized in practice (i.e., the practical implementation of such a control algorithm will require the computation of infinite sums which cannot be done by a computer). To this end, a finite dimensional approximation of the EW equation of order $2m$ is used; this approximation is obtained by using the first $2m$ modes in Eq. (6.9).

Due to the structure of the eigenspectrum of the linear operator of the EW equation of Eq. (6.3), the dynamics of the EW equation are characterized by a finite number of dominant modes. By neglecting the high-order modes ($n \geq m+1$), we rewrite the system of Eq. (6.9) into a finite-dimensional approximation as follows:

$$
\begin{aligned}
\frac{d\alpha_n}{dt} &= \lambda_n \alpha_n + \xi_\alpha^n(t), \quad n = 1, \ldots, m, \\
\frac{d\beta_n}{dt} &= \lambda_n \beta_n + \xi_\beta^n(t), \quad n = 1, \ldots, m.
\end{aligned}
\tag{6.21}
$$

Using the finite-dimensional system of Eq. (6.21), the expected surface roughness square, $\langle r^2(t)\rangle$, can be approximated with the finite-dimensional state variance as follows:

$$\left\langle \tilde{r}^2(t)\right\rangle = \frac{1}{2\pi}\sum_{i=1}^{m}\left[\left\langle \alpha_i^2(t)\right\rangle + \left\langle \beta_i^2(t)\right\rangle\right] \tag{6.22}$$

where the tilde symbol in $\langle \tilde{r}^2(t)\rangle$ denotes its association with a finite-dimensional system.

Thus, the MPC formulation on the basis of the finite-dimensional system of Eq. (6.21) and of the expected film SOR of Eq. (6.16) is shown as follows:

$$\begin{gathered}
\min_{T_1,\ldots,T_i,\ldots,T_p} J = \sum_{i=1}^{p}\left\{ q_{\mathrm{r}^2,i}\left[\frac{r_{\mathrm{set}}^2 - \langle \tilde{r}^2(t_i)\rangle}{r_{\mathrm{set}}^2}\right]^2 + q_{\rho,i}\left[\frac{\rho_{\mathrm{set}} - \langle \rho(t_i)\rangle}{\rho_{\mathrm{set}}}\right]^2\right\} \\
\text{subject to} \\
\left\langle \alpha_n^2(t_i)\right\rangle = \frac{\sigma^2}{2\nu n^2} + \left(\left\langle \alpha_n^2(t_{i-1})\right\rangle - \frac{\sigma^2}{2\nu n^2}\right) e^{-2\nu n^2 \Delta}, \\
\left\langle \beta_n^2(t_i)\right\rangle = \frac{\sigma^2}{2\nu n^2} + \left(\left\langle \beta_n^2(t_{i-1})\right\rangle - \frac{\sigma^2}{2\nu n^2}\right) e^{-2\nu n^2 \Delta}, \\
\langle \rho(t_i)\rangle = \rho^{\mathrm{ss}} + \left(\langle \rho(t_{i-1})\rangle - \rho^{\mathrm{ss}}\right) e^{-\Delta/\tau}, \\
T_{\min} < T_i < T_{\max}, \quad \left|\frac{T_{i+1} - T_i}{\Delta}\right| \le L_{\mathrm{T}}, \\
n = 1, 2, \ldots, m, \quad i = 1, 2, \ldots, p.
\end{gathered} \tag{6.23}$$

In the MPC formulation based on the reduced-order model of Eq. (6.23), the expected value of film SOR, $\langle \rho\rangle$, and the variance of the modal states, $\langle \alpha_n^2(t)\rangle$ and $\langle \beta_n^2(t)\rangle$, are needed to calculate the variables included in the cost over the prediction horizon. In the closed-loop simulations, the instantaneous values of ρ, $\alpha_n^2(t)$ and $\beta_n^2(t)$ are made

available to the controller at each sampling time; however, no statistical information, e.g., the expected value and variances, is available for feedback. Therefore, these instantaneous values at the sampling times, which are obtained directly from the simulation in real-time, are considered as the expected value of film SOR and surface height and the variances of the modal states and can be used as an initial conditions for the solution of the dynamic models employed in the MPC formulation of Eq. (6.23). Specifically, $\alpha_n^2(t)$ and $\beta_n^2(t)$ are computed from the surface height profile by taking the inner product with the adjoint eigenfunctions as follows:

$$\begin{aligned} \alpha_n(t) &= \int_{-\pi}^{\pi} h(x,t)\phi_n^*(x)dx, \quad n = 1, 2, \ldots, m, \\ \beta_n(t) &= \int_{-\pi}^{\pi} h(x,t)\psi_n^*(x)dx, \quad n = 1, 2, \ldots, m, \end{aligned} \tag{6.24}$$

where $h(x,t)$ is obtained at each sampling time from the kMC simulation.

6.5 Simulation results

In this section, the proposed model predictive controller of Eq. (6.23) is applied to the kMC model of the thin film growth process described in Section 6.2. The value of the substrate temperature is obtained from the solution of the problem of Eq. (6.23) at each sampling time and is applied to the closed-loop system until the next sampling time. The optimization problem in the MPC formulation of Eq. (6.23) is solved via a local constrained minimization algorithm using a broad set of initial guesses.

The constraint on the rate of change of the substrate temperature is imposed onto the optimization problem, which is realized in the optimization process in the following way:

$$\left|\frac{T_{i+1} - T_i}{\Delta}\right| \leq L_{\mathrm{T}} \Rightarrow |T_{i+1} - T_i| \leq L_{\mathrm{T}}\Delta \Rightarrow T_i - L_{\mathrm{T}}\Delta \leq T_{i+1} \leq T_i + L_{\mathrm{T}}\Delta, \quad i = 1, 2, \ldots, p. \tag{6.25}$$

The desired values (set-point values) in the closed-loop simulations are $r^2_{\mathrm{set}} = 10$ and $\rho_{\mathrm{set}} = 0.95$. The order of finite-dimensional approximation of the EW equation in the MPC formulation is $m = 20$. The deposition rate is fixed at 1 layer/s and an initial temperature of 600 K is used. The variation of temperature is from 400 K to 700 K. The maximum rate of change of the temperature is $L_{\mathrm{T}} = 10$ K/s. The sampling time is fixed at $\Delta = 1$ s. The number of prediction steps is set to be $p = 5$. The closed-loop simulation duration is 1000 s. All expected values are obtained from 1000 independent simulation runs.

The estimated parameters and the dependence of the parameters on substrate temperature is used in the model predictive control design, which is applied to the kMC simulations with the same lattice size, $L = 100$. We note that 100 lattice size in the kMC simulations is small compared to real wafers in the deposition process. However, it is not possible with currently available computing power to simulate molecular processes covering a realistic wafer size. However, developing modeling and control techniques for regulating thin film microstructure (surface roughness and

porosity) is an important research area because we need to understand how to regulate film surface roughness and porosity in industrial systems. The proposed modeling and control methods can be applied to any lattice size. Furthermore, the dynamic models used in the controller can be constructed directly from experimental surface roughness and porosity measurements.

Closed-loop simulations of separately regulating film surface roughness and porosity are first carried out. In these control problems, the control objective is to regulate one of the control variables, i.e., either surface roughness or film SOR, to a desired level. The cost functions of these problems contain only penalty on the error of the expected surface roughness square or of the expected film SOR from their set-point values. The corresponding MPC formulations can be realized by assigning different values to the penalty weighting factors, $q_{\mathrm{r}^2,i}$ and $q_{\rho,i}$.

In the roughness-only control problem, the weighting factors take the following values: $q_{\mathrm{r}^2,i} = 1$ and $q_{\rho,i} = 0$, $i = 1, 2, \ldots, p$. Figures 6.8 and 6.9 show the closed-loop simulation results of the roughness-only control problem. From Figure 6.8, we can see that the expected surface roughness square is successfully regulated at the desire level, 10. Since no penalty is included on the error of the expected film SOR, the final value of expected film SOR at the end of the simulation, $t = 1000$ s, is 0.988, which is far from the desired film SOR, 0.95.

In the SOR-only control problem, the weighting factors are assigned as: $q_{\mathrm{r}^2,i} = 0$ and $q_{\rho,i} = 1$, $i = 1, 2, \ldots, p$. Figures 6.10 and 6.11 show the closed-loop simulation

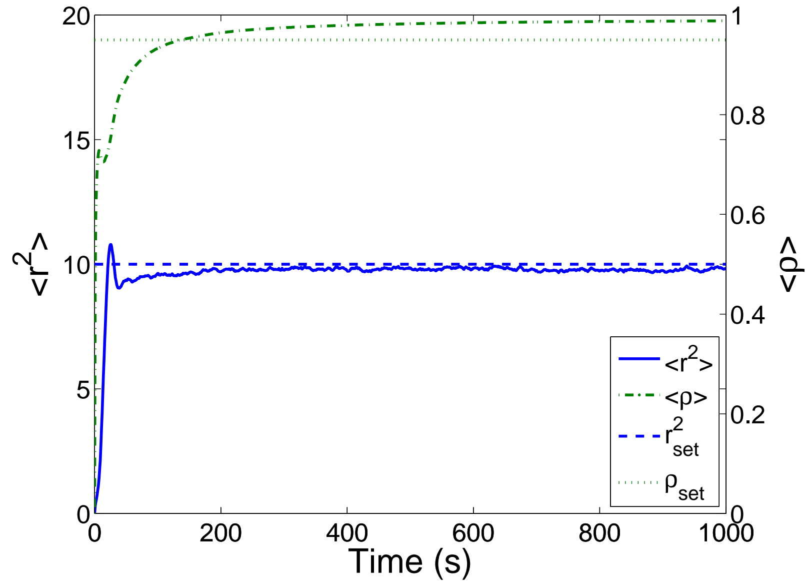

Figure 6.8: Profiles of the expected values of surface roughness square (solid line) and of the film SOR (dash-dotted line) under closed-loop operation with cost function including only penalty on surface roughness.

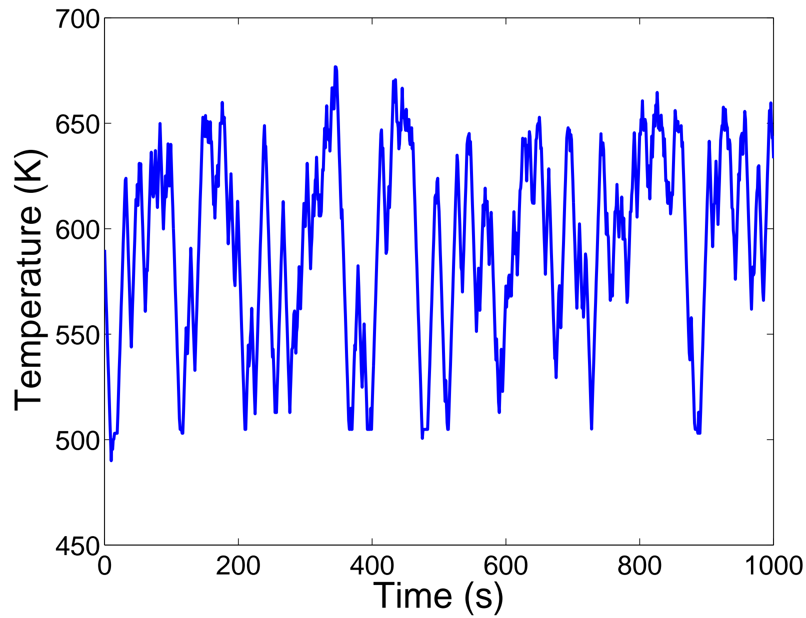

Figure 6.9: Profile of the instantaneous values of substrate temperature under closed-loop operation with cost function including only penalty on surface roughness.

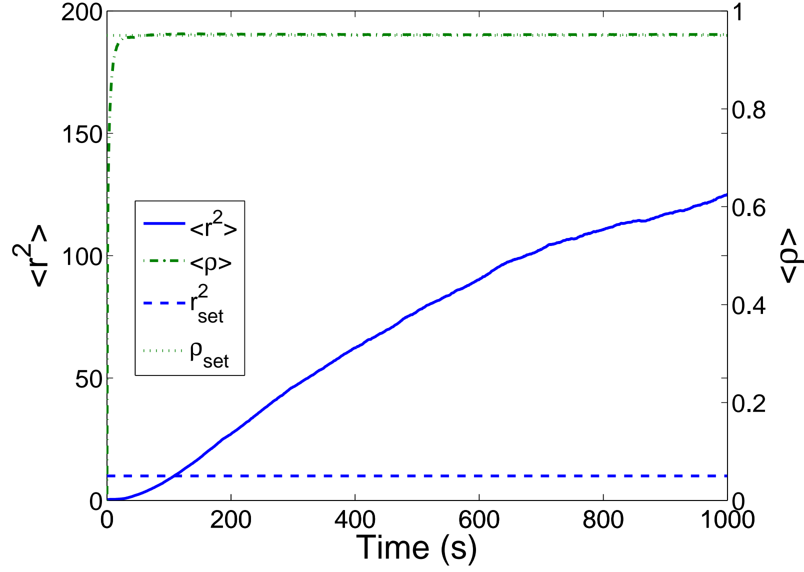

Figure 6.10: Profiles of the expected values of surface roughness square (solid line) and of the film SOR (dash-dotted line) under closed-loop operation with cost function including only penalty on the film SOR.

results of the SOR-only control problem. Similar to the results of the roughness-only control problem, the desired value of expected film SOR, 0.95, is approached at large times. However, since the error from the expected surface roughness square is not considered in the cost function, $\langle r^2 \rangle$ reaches a very high level around 125 at the end of the simulation.

Finally, closed-loop simulations of simultaneous regulation of surface roughness and film SOR are carried out by assigning non-zero values to both penalty weighting factors. Specifically, $q_{\mathrm{r}^2,1} = q_{\mathrm{r}^2,2} = \cdots = q_{\mathrm{r}^2,p} = 1$ and $q_{\rho,1} = q_{\rho,2} = \cdots = q_{\rho,p} = q_{\mathrm{SOR}}$ and q_{SOR} varies from 1 to 10^4. Since substrate temperature is the only manipulated input, the desired-values of r^2_{set} and ρ_{set} cannot be achieved simultaneously. With different assignments of penalty weighting factors, the model predictive controller of

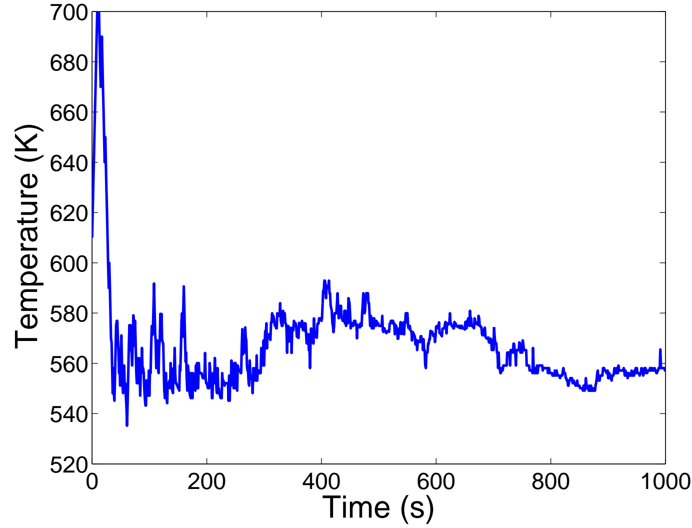

Figure 6.11: Profile of the instantaneous value of substrate temperature under closed-loop operation with cost function including only penalty on the film SOR.

Eq. (6.23) evaluates and strikes a balance between the two set-points. Figure 6.12 shows the expected values of r^2_{set} and ρ_{set} at the end of closed-loop simulations of the simultaneous control problem with respect to different weighting factors. It is clear from Figure 6.12 that as the weighting on expected film SOR increases, the expected film SOR approaches its set-point value of 0.95, while the expected surface roughness square deviates from its set-point value of 10.

Snapshots of the film microstructure at the end of the simulations (i.e., $t = 1000$ s) under open-loop and closed-loop operations are shown in Figure 6.13. The open-loop simulation is carried out at fixed process parameters of substrate temperature of 500 K and adsorption rate of 1 layer/s. The thin film obtained at the end of the open-loop simulation has higher surface roughness and film porosity, with the expected values of surface roughness square at 106 and film SOR at 0.78. Columnar/pillar structures can

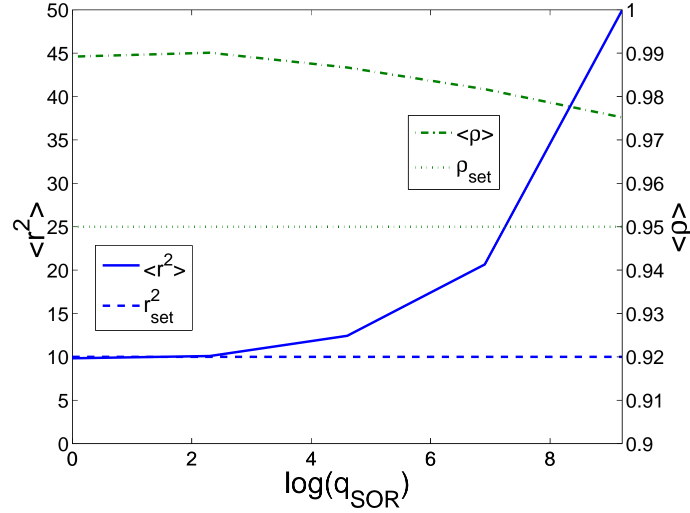

Figure 6.12: Profiles of the expected values of surface roughness square (solid line) and of the film SOR (dash-dotted line) at the end of the closed-loop simulations ($t = 1000$ s) with the following penalty weighting factors: $q_{r^2,i}$ fixed at 1 for all i and for different values of q_{SOR}.

be seen in the film microstructure in the open-loop simulation (Figure 6.13). Similar columnar structures have been also reported by other researchers in kMC simulations with triangular lattice and similar microscopic rules as well as in experimental works [95, 94, 56].

In the closed-loop simulations shown in Figure 6.13, three control schemes are compared: roughness-only control (I), SOR-only control (II) and simultaneous regulation of both roughness and porosity (III). As it was demonstrated by the evolution profiles of surface roughness and film SOR of the closed-loop simulations in Figures 6.8 and 6.10, the film microstructure under roughness-only control (I) has the lowest surface roughness square, which is close to the set-point value of 10, but the corresponding film SOR is 0.99, which is far from the desired value of 0.95. On the other hand, the

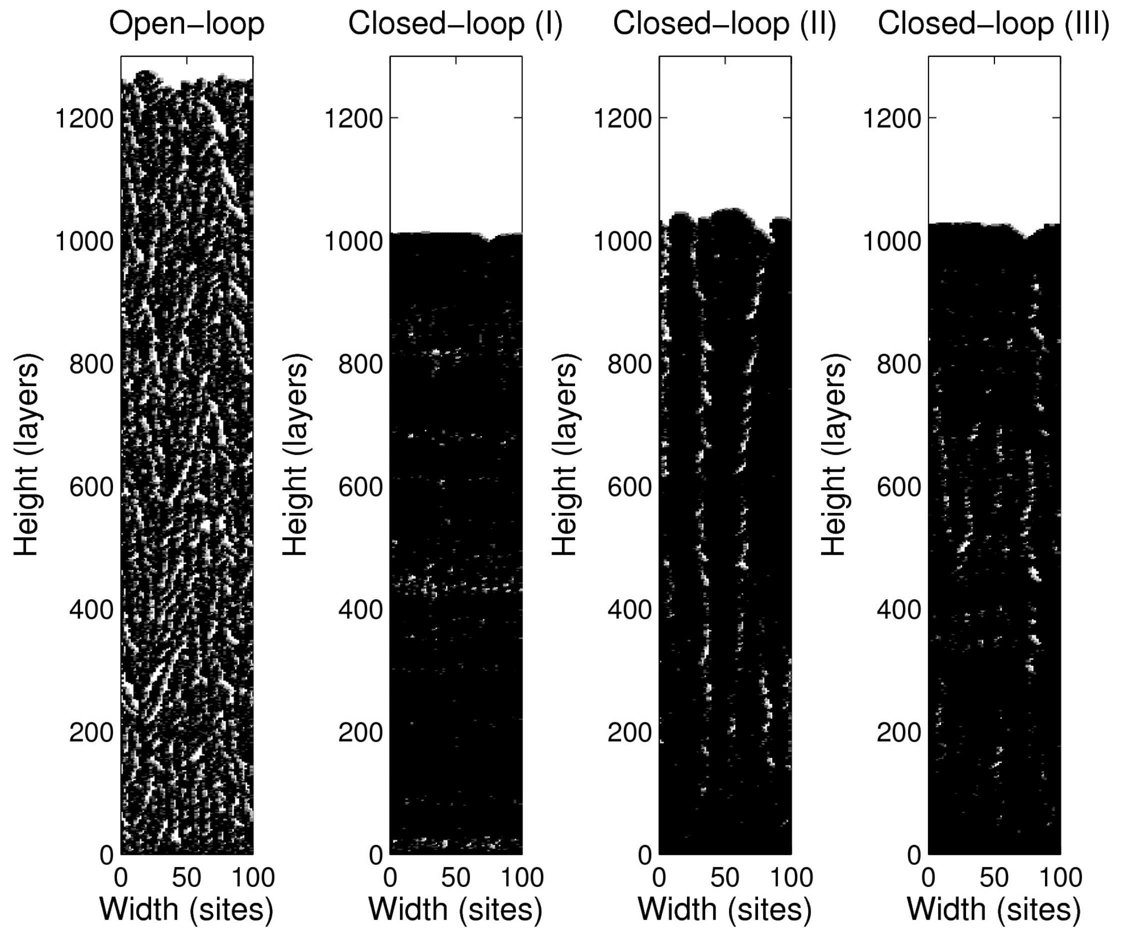

Figure 6.13: Snapshots of film microstructure at $t = 1000$ s of simulations under open-loop and closed-loop operations. Open-loop simulation is carried out at $T = 500$ K and $W = 1$ layer/s. Closed-loop simulations are carried out under three different control schemes: (I) roughness-only control; (II) SOR-only control; (III) simultaneous regulation of surface roughness and film SOR with $q_{\mathrm{r}^2,i} = 1$ and $q_{\mathrm{SOR}} = 10^4$.

film SOR under SOR-only control (II) is lower than under roughness-only control (I) and reaches the set-point of 0.95, which can be also seen by comparing the porosity of the thin film under closed-loop control (I) and (II) in Figure 6.13. However, the surface roughness square under SOR-only control (II) is much higher than the set-point value of 10 since no penalty is included on the deviation of surface roughness square from the set-point value in this case, and thus, the snapshot of the film microstructure has the roughest surface. Finally, under the control scheme (III), surface roughness and film porosity strike a balance from their respective set-points by including penalty on both deviations of surface roughness square and film SOR.

6.6 Conclusions

In this chapter, stochastic modeling and simultaneous regulation of surface roughness and film porosity was studied for a porous thin film deposition process modeled via kMC simulation on a triangular lattice with two microscopic processes. The definition of surface height profile of a porous thin film in a triangular lattice was first introduced. An EW-type equation was used to describe the dynamics of surface height and the evolution of the RMS surface roughness, which is one of the controlled variables. Subsequently, an appropriate definition of film SOR was introduced to represent the extent of porosity inside the film and was used as the second to-be-controlled variable. A deterministic ODE model was postulated to describe the time evolution of film SOR. The coefficients of the EW equation of surface height and of

the deterministic ODE model of the film SOR were estimated on the basis of data obtained from the kMC simulator of the deposition process using least-square methods and their dependence on substrate temperature was determined. The developed dynamic models were used as the basis for the design of a model predictive control algorithm that includes penalty on the deviation of surface roughness square and film SOR from their respective set-point values. Simulation results demonstrated the applicability and effectiveness of the proposed modeling and control approach in the context of the deposition process under consideration. When simultaneous control of surface roughness and porosity was carried out, a balanced trade-off was obtained in the closed-loop system between the two control objectives of surface roughness and porosity regulation.

Chapter 7

Simultaneous Regulation of Film Surface Roughness, Porosity, and Thickness Using Deposition Rate

7.1 Introduction

In Chapters 5 and 6, substrate temperature was used as the manipulated variable to regulate surface roughness and film porosity in the thin film deposition process. However, the weak dependence of the film thickness on the substrate temperature does not allow regulation of the film thickness at the end of the deposition process by manipulation of the substrate temperature. A good manipulated input candidate for the control of film thickness [58] (and for film surface roughness and porosity as

well) is the deposition rate, which has a direct influence on the growth rate of the film. Motivated by this consideration, this chapter focuses on distributed control of film thickness, surface roughness and porosity in a porous thin film deposition process using the deposition rate as the manipulated input. The deposition process includes adsorption and migration processes and it is modeled via kinetic Monte Carlo simulation on a triangular lattice with vacancies and overhangs allowed to develop inside the film. A distributed parameter (partial differential equation) dynamic model is derived to describe the evolution of the surface height profile of the thin film accounting for the effect of deposition rate. The dynamics of film porosity, evaluated as film site occupancy ratio (SOR), are described by an ordinary differential equation. The developed dynamic models are then used as the basis for the design of a model predictive control algorithm that includes penalty on the deviation of film thickness, surface roughness and film porosity from their respective set-point values. Simulation results demonstrate the applicability and effectiveness of the proposed modeling and control approach in the context of the deposition process under consideration.

7.2 Preliminaries

7.2.1 On-lattice kinetic Monte Carlo model of film growth

The deposition process is simulated using an on-lattice kMC model which is constructed on a two-dimensional triangular lattice (one dimensional on the growth di-

rection) [41], as shown in Figure 6.1. The on-lattice kMC model is valid for a low temperature region, $T < 0.5T_{\mathrm{m}}$ (T_{m} is the melting point of the crystalline material), where the particles can be assumed to be constrained on the lattice sites [56]. The lattice contains a fixed number of sites in the lateral direction. The new particles are always deposited from the gas phase which is located above the lattice; see Figure 6.1. The growth direction, along which the thin film keeps growing, is normal to the lateral direction. The number of sites in the lateral direction is defined as the lattice size and is denoted by L.

The number of nearest neighbors of a site ranges from zero to six, (six is the coordination number of the triangular lattice). A site with no nearest neighbors indicates an unadsorbed particle in the gas phase, i.e., a particle which has not been deposited on the film yet. A particle with six nearest neighbors is associated with an interior particle that is fully surrounded by other particles and cannot migrate. A particle with one to five nearest neighbors is possible to diffuse to an unoccupied neighboring site with a probability that depends on its local environment. In the triangular lattice, a particle with only one nearest neighbor is considered unstable and is subject to instantaneous surface relaxation.

In the simulation, a bottom layer in the lattice is initially set to be fully packed and fixed, as shown in Figure 6.1. There are no vacancies in this layer and the particles in this layer cannot migrate. This layer acts as the substrate for the deposition and is not counted in the computation of the number of the deposited particles, i.e.,

this fixed layer does not influence the film porosity (see Section 7.2.2 below). Two types of microscopic processes (Monte Carlo events) are considered in the kMC model [56, 55, 92, 95]: an adsorption process, in which particles are incorporated into the film from the gas phase, and a migration process, in which surface particles move to adjacent sites. These Monte Carlo events are assumed to be Poisson processes. All events occur randomly with probabilities proportional to their respective rates. The events are executed instantaneously upon selection and the state of the lattice remains unchanged between two consecutive events.

In the adsorption process, an incident particle comes in contact with the film and is incorporated onto the film, subject to instantaneous surface relaxation when the lattice site is unstable. The macroscopic adsorption rate (deposition rate), W, which is in units of layers per unit time, depends on the gas phase concentration. The layers in the unit of adsorption rate are densely packed layers, which contain L particles. With this definition, W is independent of L and is treated as a process parameter and will be used as the manipulated input. For the entire deposition process, the microscopic adsorption rate (deposition rate) in terms of incident particles per unit time, which is denoted as r_{a}, is related to W as follows:

$$r_{\mathrm{a}} = LW \tag{7.1}$$

The incident particles are initially placed at random positions above the film lattice

and move toward the lattice in the vertical direction. The random initial particle position, x_0, which is the center of an incident particle, follows a uniform probability distribution in the continuous spatial domain. Note that different distributions of the incident angle may be selected, e.g., a uniform or cosine distribution, for different film growth processes [40, 94].

In the migration process, a particle overcomes the energy barrier of the site and jumps to its vacant neighboring site. The migration rate (probability) of a particle follows an Arrhenius-type law with a pre-calculated activation energy barrier that depends on the local environment of the particle, i.e., the number of the nearest neighbors of the particle chosen for a migration event. The migration rate of the ith particle is calculated as follows:

$$r_{\mathrm{m},i} = \nu_0 \exp\left(-\frac{n_i E_0}{k_{\mathrm{B}} T}\right) \tag{7.2}$$

where ν_0 denotes the pre-exponential factor, n_i is the number of the nearest neighbors of the ith particle and can take the values of 2, 3, 4 and 5 ($r_{\mathrm{m},i}$ is zero when $n_i = 6$ since this particle is fully surrounded by other particles and cannot migrate), E_0 is the contribution to the activation energy barrier from each nearest neighbor, k_{B} is the Boltzmann's constant and T is the substrate temperature of the thin film. Since the film is thin, the temperature is assumed to be uniform throughout the film and is treated as a time-varying but spatially-invariant process parameter. The factor and energy barrier contribution in Eq. (7.2) take the following values $\nu_0 = 10^{13}$ s^{-1} and

$E_0 = 0.9$ eV. These values are appropriate for a silicon film [46]. Here we note that the contributions to the activation energy barrier from the second nearest neighbors are added into the contributions from the nearest neighbors. When a particle is subject to migration, it can jump to either of its vacant neighboring sites with equal probability, unless the vacant neighboring site has no nearest neighbors, i.e., the surface particle cannot jump off the film and it can only migrate on the surface.

7.2.2 Definitions of thin film microstructure

Utilizing the continuous-time Monte Carlo algorithm, simulations of the kMC model of a porous silicon thin film growth process can be carried out. Snapshots of film microstructure, i.e., the configurations of particles within the triangular lattice, are obtained from the kMC model at various time instants during process evolution. To quantitatively evaluate the thin film microstructure, two variables, surface roughness and film porosity, are introduced in this subsection.

Surface roughness, which measures the texture of thin film surface, is represented by the root mean square (RMS) of the surface height profile of the thin film. Determination of surface height profile is slightly different in the triangular lattice model compared to a solid-on-solid (SOS) model. In the SOS model, the surface of thin film is naturally described by the positions of the top particles of each column. In the triangular lattice model, however, due to the existence of vacancies and overhangs, the definition of film surface needs further clarification. Specifically, taking

into account practical considerations of surface roughness measurements, the surface height profile of a triangular lattice model is defined based on the particles that can be reached in the vertical direction, as shown in Figure 6.3. In this definition, a particle is considered as a surface particle only if it is not blocked by the particles in the neighboring columns. Therefore, the surface height profile of a porous thin film is the line that connects the sites that are occupied by the surface particles. With this definition, the surface height profile can be treated as a function of the spatial coordinate. Surface roughness, as a measurement of the surface texture, is defined as the standard deviation of the surface height profile from its average height. The definition expression of surface roughness is given later in Section 7.3.1.

In addition to film surface roughness, the film SOR is introduced to represent the extent of the porosity inside the thin film. The mathematical expression of film SOR is defined as follows:

$$\rho = \frac{N}{LH} \tag{7.3}$$

where ρ denotes the film SOR, N is the total number of deposited particles on the lattice, L is the lattice size, and H denotes the number of deposited layers. Note that the deposited layers are the layers that contain only deposited particles and do not include the initial substrate layers. The variables in the definition expression of Eq. (7.3) can be found in Figure 5.3. Since each layer contains L sites, the total number of sites in the film that can be contained within the H layers is LH. Thus, film SOR is the ratio of the occupied lattice sites, N, over the total number of available

sites, LH. Film SOR ranges from 0 to 1. Specifically, $\rho = 1$ denotes a fully occupied film with a flat surface. The value of zero is assigned to ρ at the beginning of the deposition process since there are no particles deposited on the lattice.

The definition of film SOR is different from the concept of packing density which is used to denote the fraction of a volume filled by a given collection of solids, and thus, packing density cannot be used to characterize the evolution of the porosity. Another important point is the correlation of film surface roughness and film porosity. These two properties of thin films are correlated to some extent in the deposition process. The conditions that produce a dense film, i.e., higher substrate temperature or lower deposition rate, also generate a smoother surface. However, even though there is correlation between the film surface roughness and porosity, films with the same surface roughness may have quite different film SORs.

7.3 Dynamic model construction and parameter estimation

7.3.1 Edwards-Wilkinson-type equation of surface height using deposition rate as manipulated input

An Edwards-Wilkinson (EW)-type equation, a second-order stochastic partial differential equation (PDE), can be used to describe the surface height evolution in many

microscopic processes that involve thermal balance between adsorption (deposition) and migration (diffusion) [61]. An EW-type equation is chosen to describe the dynamics of the fluctuation of surface height (the validation of this choice will be made clear below) of the form:

$$\frac{\partial h}{\partial t} = r_{\mathrm{h}} + \nu \frac{\partial^2 h}{\partial x^2} + \xi(x,t) \tag{7.4}$$

subject to PBCs:

$$h(-\pi,t) = h(\pi,t), \quad \frac{\partial h}{\partial x}(-\pi,t) = \frac{\partial h}{\partial x}(\pi,t), \tag{7.5}$$

and the initial condition:

$$h(x,0) = h_0(x) \tag{7.6}$$

where $x \in [-\pi,\pi]$ is the spatial coordinate, t is the time, r_{h} and ν are the model parameters, and $\xi(x,t)$ is a Gaussian white noise with the following mean and covariance:

$$\begin{aligned} \langle \xi(x,t) \rangle &= 0, \\ \langle \xi(x,t)\xi(x',t') \rangle &= \sigma^2 \delta(x-x')\delta(t-t'), \end{aligned} \tag{7.7}$$

where σ^2 is a parameter which measures the intensity of the Gaussian white noise and $\delta(\cdot)$ denotes the standard Dirac delta function. We note that the parameters r_{h}, ν and σ^2 are functions of the deposition rate, W, and this dependence will be estimated and discussed in Section 7.3.3 below.

To proceed with model parameter estimation and control design, a stochastic ODE

approximation of Eq. (7.4) is first derived using model decomposition. Consider the eigenvalue problem of the linear operator of Eq. (7.4), which takes the form:

$$
\begin{gathered}
A\bar{\phi}_n(x) = \nu \frac{d^2\bar{\phi}_n(x)}{dx^2} = \lambda_n \bar{\phi}_n(x), \\
\bar{\phi}_n(-\pi) = \bar{\phi}_n(\pi), \quad \frac{d\bar{\phi}_n}{dx}(-\pi) = \frac{d\bar{\phi}_n}{dx}(\pi),
\end{gathered} \tag{7.8}
$$

where λ_n denotes an eigenvalue and $\bar{\phi}_n$ denotes an eigenfunction. A direct computation of the solution of the above eigenvalue problem yields $\lambda_0 = 0$ with $\psi_0 = 1/\sqrt{2\pi}$, and $\lambda_n = -\nu n^2$ (λ_n is an eigenvalue of multiplicity two) with eigenfunctions $\phi_n = (1/\sqrt{\pi})\sin(nx)$ and $\psi_n = (1/\sqrt{\pi})\cos(nx)$ for $n = 1, \ldots, \infty$. Note that the $\bar{\phi}_n$ in Eq. (7.8) denotes either ϕ_n or ψ_n. For a fixed positive value of ν, all eigenvalues (except the zeroth eigenvalue) are negative and the distance between two consecutive eigenvalues (i.e., λ_n and λ_{n+1}) increases as n increases.

The solution of Eq. (7.4) is expanded in an infinite series in terms of the eigenfunctions of the operator of Eq. (7.8) as follows:

$$
h(x,t) = \sum_{n=1}^{\infty} \alpha_n(t)\phi_n(x) + \sum_{n=0}^{\infty} \beta_n(t)\psi_n(x) \tag{7.9}
$$

where $\alpha_n(t)$, $\beta_n(t)$ are time-varying coefficients. Substituting the above expansion for the solution, $h(x,t)$, into Eq. (7.4) and taking the inner product with the adjoint eigenfunctions, $\phi_n^*(x) = (1/\sqrt{\pi})\sin(nx)$ and $\psi_n^*(x) = (1/\sqrt{\pi})\cos(nx)$, the following

system of infinite stochastic ODEs is obtained:

$$
\begin{aligned}
\frac{d\beta_0}{dt} &= \sqrt{2\pi} r_{\mathrm{h}} + \xi_{\beta}^{0}(t), \\
\frac{d\alpha_n}{dt} &= \lambda_n \alpha_n + \xi_{\alpha}^{n}(t), \quad n = 1, \ldots, \infty, \\
\frac{d\beta_n}{dt} &= \lambda_n \beta_n + \xi_{\beta}^{n}(t), \quad n = 1, \ldots, \infty,
\end{aligned}
\tag{7.10}
$$

where

$$
\xi_{\alpha}^{n}(t) = \int_{-\pi}^{\pi} \xi(x,t) \phi_n^*(x) dx, \quad \xi_{\beta}^{n}(t) = \int_{-\pi}^{\pi} \xi(x,t) \psi_n^*(x) dx. \tag{7.11}
$$

The covariances of $\xi_{\alpha}^{n}(t)$ and $\xi_{\beta}^{n}(t)$ can be obtained: $\langle \xi_{\alpha}^{n}(t) \xi_{\alpha}^{n}(t') \rangle = \sigma^2 \delta(t-t')$ and $\left\langle \xi_{\beta}^{n}(t) \xi_{\beta}^{n}(t') \right\rangle = \sigma^2 \delta(t-t')$. Due to the orthogonality of the eigenfunctions of the operator in the EW equation of Eq. (7.4), $\xi_{\alpha}^{n}(t)$ and $\xi_{\beta}^{n}(t)$, $n = 0, 1, \ldots$, are stochastically independent.

Since the stochastic ODE system is linear, the analytical solution of state variance can be obtained from a direct computation as follows:

$$
\begin{aligned}
\left\langle \alpha_n^2(t) \right\rangle &= \frac{\sigma^2}{2\nu n^2} + \left(\left\langle \alpha_n^2(t_0) \right\rangle - \frac{\sigma^2}{2\nu n^2} \right) e^{-2\nu n^2 (t-t_0)} \quad n = 1, 2, \ldots, \infty, \\
\left\langle \beta_n^2(t) \right\rangle &= \frac{\sigma^2}{2\nu n^2} + \left(\left\langle \beta_n^2(t_0) \right\rangle - \frac{\sigma^2}{2\nu n^2} \right) e^{-2\nu n^2 (t-t_0)} \quad n = 0, 1, \ldots, \infty,
\end{aligned}
\tag{7.12}
$$

where $\langle \alpha_n^2(t_0) \rangle$ and $\langle \beta_n^2(t_0) \rangle$ are the state variances at time t_0. The analytical solution of state variance of Eq. (7.12) will be used in the parameter estimation and the MPC design.

When the dynamic model of surface height profile is determined, surface roughness of the thin film is defined as the standard deviation of the surface height profile from its average height and is computed as follows:

$$r(t) = \sqrt{\frac{1}{2\pi}\int_{-\pi}^{\pi}[h(x,t) - \bar{h}(t)]^2 dx} \tag{7.13}$$

where $\bar{h}(t) = \dfrac{1}{2\pi}\displaystyle\int_{-\pi}^{\pi} h(x,t)dx$ is the average surface height. According to Eq. (7.9), we have $\bar{h}(t) = \beta_0(t)\psi_0$. Therefore, $\langle r^2(t)\rangle$ can be rewritten in terms of $\langle \alpha_n^2(t)\rangle$ and $\langle \beta_n^2(t)\rangle$ as follows:

$$\begin{aligned}
\langle r^2(t)\rangle &= \frac{1}{2\pi}\left\langle \int_{-\pi}^{\pi}(h(x,t) - \bar{h}(t))^2 dx \right\rangle \\
&= \frac{1}{2\pi}\left\langle \sum_{i=1}^{\infty}(\alpha_i^2(t) + \beta_i^2(t)) \right\rangle = \frac{1}{2\pi}\sum_{i=1}^{\infty}\left[\langle \alpha_i^2(t)\rangle + \langle \beta_i^2(t)\rangle\right].
\end{aligned} \tag{7.14}$$

Thus, Eq. (7.14) provides a direct link between the state variance of the infinite stochastic ODEs of Eq. (7.10) and the expected surface roughness of the thin film. Note that the parameter r_h does not appear in the expression of surface roughness, since only the zeroth state, β_0, is affected by r_h but this state is not included in the computation of the expected surface roughness square of Eq. (7.14).

Film thickness, which is represented by the average of surface height, $\bar{h}$, is another control objective here. The dynamics of the expected value of average surface height can be obtained from the analytical solution of the zeroth state, β_0, from Eq. (7.10),

as follows:

$$\frac{d\left\langle \bar{h}\right\rangle}{dt} = r_{\text{h}} \tag{7.15}$$

subject to the initial condition

$$\left\langle \bar{h}(t_0)\right\rangle = \frac{1}{2\pi}\int_{-\pi}^{\pi} h(x,t_0)dx. \tag{7.16}$$

Here we need to point out that full knowledge of surface height profile throughout the spatial domain is necessary for the computation of the initial values of the film thickness, $\left\langle \bar{h}(t_0)\right\rangle$.

Eq. (7.15) implies that $\bar{h}$ can be directly controlled by manipulating the deposition rate. Finally, the analytical solution of expected value of film thickness, $\left\langle \bar{h}\right\rangle$, which will be used for parameter estimation (r_{h} dependence on W) and control purposes below, can be obtained directly from Eq. (7.15) as follows:

$$\left\langle \bar{h}(t)\right\rangle = \left\langle \bar{h}(t_0)\right\rangle + r_{\text{h}}(t-t_0). \tag{7.17}$$

7.3.2 Dynamic model of film site occupancy ratio

Film SOR is used to characterize film porosity. According to the definition of film SOR of Eq. (7.3), film SOR accounts for all deposited layers during the entire deposition process. Thus, film SOR is a cumulative property, the evolution of which can be characterized by an integral form. Before further derivation of the dynamic model of

film SOR, a concept of instantaneous film SOR of the film layers deposited between time t and $t + \Delta t$, denoted by ρ_{d}, is first introduced as the spatial derivative of the number of deposited particles in the growing direction as follows:

$$\rho_{\mathrm{d}} = \frac{dN}{d(HL)}. \tag{7.18}$$

In Eq. (7.18), the lattice size L is a constant and the derivative dH can be written as a linear function of time derivative dt as follows:

$$dH = r_{\mathrm{H}} dt \tag{7.19}$$

where r_{H} is the growth rate of the thin film from the top layer point of view. Note that r_{H} is different from the model coefficient r_{h} in Eq. (7.4). Thus, the expressions of N and H can be obtained by integrating Eqs. (7.18) and (7.19) as follows:

$$\begin{aligned} N(t) &= L \int_0^t \rho_{\mathrm{d}} r_{\mathrm{H}} ds, \\ H(t) &= \int_0^t \rho_{\mathrm{d}} ds. \end{aligned} \tag{7.20}$$

With the definition of ρ of Eq. (7.3) and the expressions of N and H of Eq. (7.20, the film SOR of Eq. (7.3) can be rewritten in an integral form as follows:

$$\rho = \frac{\int_0^t \rho_{\mathrm{d}} r_{\mathrm{H}} ds}{\int_0^t r_{\mathrm{H}} ds}. \tag{7.21}$$

To simplify the subsequent development and develop an SOR model that is suitable for control purposes, we assume (this assumption will be verified in the closed-loop simulation results below where the performance of the controller will be evaluated) that the dynamics of the instantaneous film SOR, ρ_{d}, can be approximated by a first-order process, i.e.:

$$\tau \frac{d\rho_{\mathrm{d}}(t)}{dt} = \rho_{\mathrm{d}}^{\mathrm{ss}} - \rho_{\mathrm{d}}(t) \tag{7.22}$$

where τ is the time constant and $\rho_{\mathrm{d}}^{\mathrm{ss}}$ is the steady-state value of the instantaneous film SOR. We note that the first-order ODE model of Eq. (7.22) was introduced and justified with numerical results in [40] for the modeling of the partial film SOR, which is defined to characterize the evolution of the film porosity of layers that are close to the film surface. In this chapter, the instantaneous film SOR is a similar concept to the partial film SOR, because it also describes the contribution to the bulk film porosity of the newly deposited layers. Therefore, the first-order ODE model is a suitable choice to describe the evolution of the instantaneous film SOR.

From Eq. (7.21), it follows that at large times as ρ_{d} approaches $\rho_{\mathrm{d}}^{\mathrm{ss}}$, the steady-state film SOR (ρ^{ss}) approaches the steady-state value of the instantaneous film SOR (i.e., $\rho^{\mathrm{ss}} = \rho_{\mathrm{d}}^{\mathrm{ss}}$). The deterministic ODE system of Eq. (7.22) is subject to the following initial condition:

$$\rho_{\mathrm{d}}(t_0) = \rho_{\mathrm{d0}} \tag{7.23}$$

where t_0 is the initial time and ρ_{d0} is the initial value of the instantaneous film SOR.

From Eqs. (7.22) and (7.23) and the fact that $\rho^{\text{ss}} = \rho_{\text{d}}^{\text{ss}}$ at large times, it follows that

$$\rho_{\text{d}}(t) = \rho^{\text{ss}} + (\rho_{\text{d0}} - \rho^{\text{ss}})\, e^{-(t-t_0)/\tau}. \tag{7.24}$$

For controller implementation purposes, the expression of the film SOR can be derived as follows:

$$\begin{aligned} \rho(t) &= \frac{\int_0^{t_0} \rho_{\text{d}} r_{\text{H}} ds + \int_{t_0}^{t} \rho_{\text{d}} r_{\text{H}} ds}{\int_0^{t_0} r_{\text{H}} ds + \int_{t_0}^{t} r_{\text{H}} ds}, \\ &= \frac{\rho(t_0)H(t_0) + \int_{t_0}^{t} \rho_{\text{d}} r_{\text{H}} ds}{H(t_0) + \int_{t_0}^{t} r_{\text{H}} ds}, \end{aligned} \tag{7.25}$$

where t_0 is the current time, $\rho(t_0)$ and $H(t_0)$ are film SOR and film height at time t_0, respectively.

Substituting the solution of ρ_{d} of Eq. (7.24) into Eq. (7.25) and assuming that r_{H} is constant for $t > \tau > t_0$, which is taken to be the case in the parameter estimation and the MPC formulations below, the analytical solution of film SOR at time t can be obtained as follows:

$$\rho = \frac{\rho(t_0)H(t_0) + r_{\text{H}}\left[\rho^{\text{ss}}(t-t_0) + (\rho^{\text{ss}} - \rho(t_0))\tau(e^{-(t-t_0)/\tau} - 1)\right]}{H(t_0) + r_{\text{H}}(t-t_0)} \tag{7.26}$$

which is directly utilized in the model predictive control formulation of Eq. (7.29) below.

7.3.3 Parameter estimation

In the dynamic models of Eqs. (7.4), (7.15) and (7.22), there are five model parameters that need to be obtained from kMC data of the deposition process. These model parameters can be estimated on the basis of the open-loop simulation data at fixed operation conditions, i.e., substrate temperature and deposition rate, from the kMC model introduced in Section 7.2 by using least square methods [40, 41]. In the parameter estimation, the predicted evolution profiles from the dynamic models and the ones from the kMC simulation of the deposition process are compared in a least-square sense to find the best model parameters.

Different operating conditions strongly affect the deposition process and result in different dynamics of the surface height profile and of the film SOR. Thus, the model parameters are functions of the operating conditions. In this chapter, we choose the deposition rate, W, as the manipulated input and keep the substrate temperature fixed at $T = 850$ K. The dependence of the model parameters on the deposition rate, W, can be obtained by performing the parameter estimation procedure discussed above for a variety of deposition rate values (ranging from 0.1 to 1 layer/s); see Figures 7.1, 7.2 and 7.3 for the dependence of the model parameters on the deposition rate. Simulation results from 1000 independent simulation runs are used for the parameter estimation under each deposition rate condition. It can be clearly seen that the model parameters are strong functions of the deposition rate and this dependence is the basis for using W to simultaneously control film thickness, roughness and

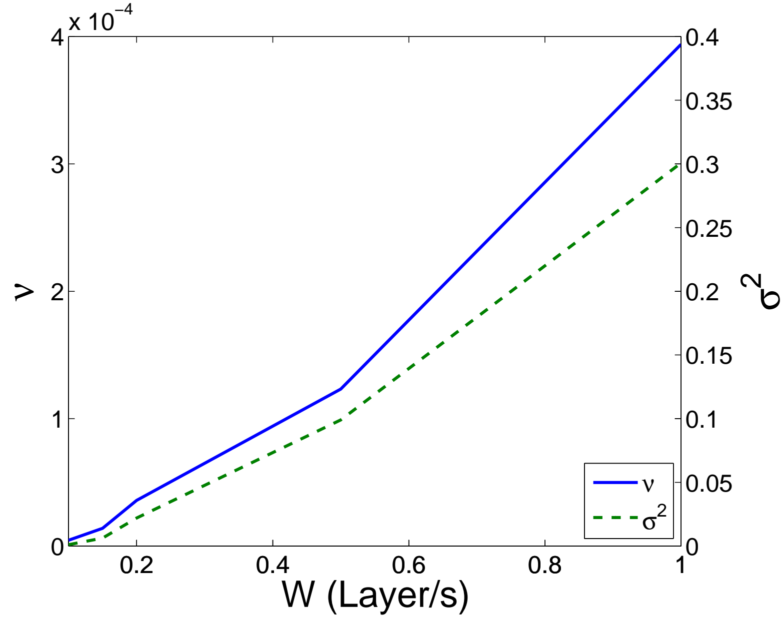

Figure 7.1: Dependence of ν and σ^2 on the deposition rate with substrate temperature $T = 850$ K.

porosity.

7.4 Model predictive controller design

In this section, a model predictive controller is designed based on the dynamic models of surface height and film SOR to regulate the expected values of surface roughness and film SOR to desired levels by manipulating the deposition rate. A desired minimum of film thickness is also included in the cost function in the MPC formulation. A reduced-order model of EW equation is used in the MPC formulation to approximate the dynamics of the surface roughness. The surface height profile and the value of film SOR are assumed to be available to the controller. In practice, these data can

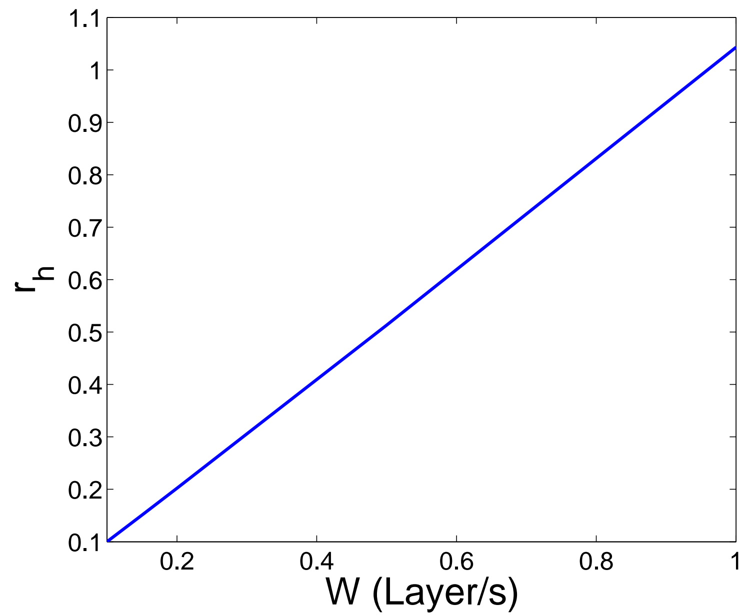

Figure 7.2: Dependence of r_{h} on the deposition rate with substrate temperature $T = 850$ K.

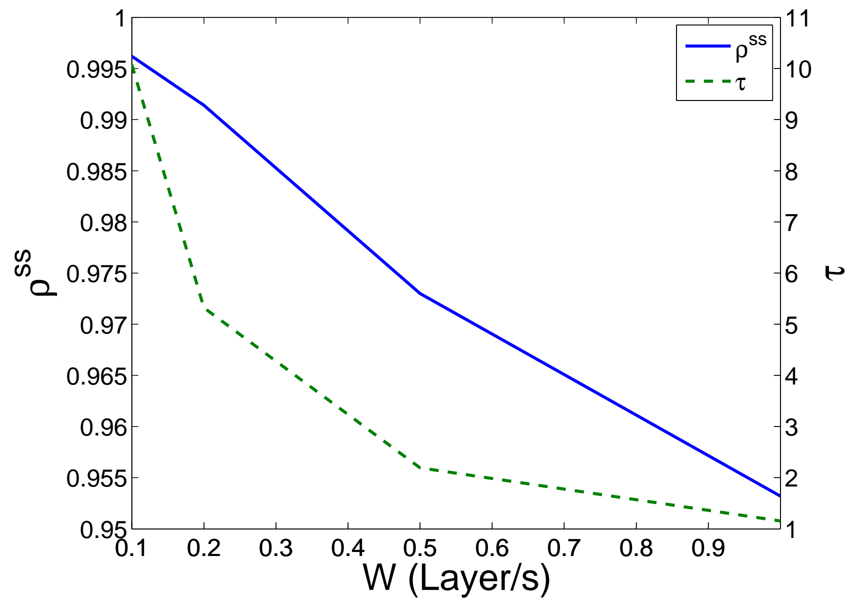

Figure 7.3: Dependence of ρ^{ss} and τ on the deposition rate with substrate temperature $T = 850$ K.

be obtained from *in situ* gas phase and thin film surface measurements (on-line film porosity may be obtained by a model that links the off-line film porosity and *in situ* gas phase measurements).

With respect to the choice of MPC for the controller design, we note that classical control schemes like proportional-integral (PI) control cannot be designed to explicitly account for input/state constraints, optimality considerations and the batch nature of the deposition process. Furthermore, dynamic open-loop optimization may be used but it does not provide robustness against model inaccuracies and fluctuations in the deposition process. In the case where feedback control cannot be attained, dynamic open-loop optimization may be used instead to regulate W; this is naturally included in the MPC framework employed here. The robustness of the MPC approach against model parameter uncertainty can be also improved by including adaptation schemes; see [15, 51] for results on adaptive control of PDEs.

7.4.1 Reduced-order model for surface roughness

In model predictive control formulation, the expected surface roughness is computed from the EW equation of Eq. (7.4). The EW equation, which is a distributed parameter dynamic model, contains infinite dimensional stochastic states. Therefore, it leads to a model predictive controller of infinite order that cannot be realized in practice (i.e., the practical implementation of a control algorithm based on such an system will require the computation of infinite sums which cannot be done by a com-

puter). To this end, a reduced-order model of the infinite dimensional ODE model of Eq. (7.10) is instead included and is used to calculate the prediction of expected surface roughness in the model predictive controller.

Due to the structure of the eigenspectrum of the linear operator of the EW equation of Eq. (7.4), the dynamics of the EW equation are characterized by a finite number of dominant modes. By neglecting the high-order modes ($n \geq m+1$), the system of Eq. (7.10) can be approximated by a finite-dimensional system as follows:

$$\begin{aligned} \frac{d\alpha_n}{dt} &= \lambda_n \alpha_n + \xi_\alpha^n(t), \quad n = 1, \dots, m, \\ \frac{d\beta_n}{dt} &= \lambda_n \beta_n + \xi_\beta^n(t), \quad n = 1, \dots, m. \end{aligned} \tag{7.27}$$

Note that the ODE for the zeroth state is also neglected, since the zeroth state does not contribute to surface roughness.

Using the finite-dimensional system of Eq. (7.27), the expected surface roughness square, $\langle r^2(t) \rangle$, can be approximated with the finite-dimensional state variance as follows:

$$\left\langle \tilde{r}^2(t) \right\rangle = \frac{1}{2\pi} \sum_{i=1}^{m} \left[\left\langle \alpha_i^2(t) \right\rangle + \left\langle \beta_i^2(t) \right\rangle \right] \tag{7.28}$$

where the tilde symbol in $\langle \tilde{r}^2(t) \rangle$ denotes its association with a finite-dimensional system.

7.4.2 MPC formulation

We consider the control problem of film thickness, surface roughness and film porosity regulation by using a model predictive control design. The expected values, $\langle \bar{h} \rangle$, $\langle r^2 \rangle$ and ρ, are chosen as the control objectives. The deposition rate is used as the manipulated input. The substrate temperature is fixed at a certain value, T_0, during all closed-loop simulations. We note here that the proposed modeling and control methods do no depend on the specific number of the manipulated variables and can be easily extended to the case of multi-inputs. To account for a number of practical considerations, several constraints are added to the control problem. First, there is a constraint on the range of variation of the deposition rate. This constraint ensures validity of the on-lattice kMC model. Another constraint is imposed on the rate of change of the deposition rate to account for actuator limitations. The control action at time t is obtained by solving a finite-horizon optimal control problem.

The cost function in the optimal control problem includes penalty on the deviation of $\langle r^2 \rangle$ and ρ from their respective set-point values. Since the manipulated variable is the deposition rate and the film deposition process is a batch operation (i.e., the film growth process is terminated within a certain time), a desired minimum of the film thickness is also required to prevent an undergrown thin film at the end of the deposition process. The minimal film thickness is regarded as the set-point value of the film thickness in the MPC formulation, i.e., the deviation of the film thickness from the minimum is included in the cost function. However, only the negative deviation

(when the film thickness is less than the minimum) is counted; no penalty is imposed on the deviation when the thin film exceeds the minimal thickness. Different weighting factors are assigned to the penalties on the deviations of the surface roughness and of the film SOR (and of the film thickness as well). Relative deviations are used in the formulation of the cost function to make the magnitude of the different terms used in the cost comparable for numerical calculation purposes. The optimization problem is subject to the dynamics of the reduced-order model of surface roughness of Eq. (7.27), the dynamics of the film thickness of Eq. (7.15), and the dynamics of the film SOR of Eq. (7.21). The optimal profile of the deposition rate is calculated by solving a finite-dimensional optimization problem in a receding horizon fashion.

Specifically, the MPC problem is formulated as follows:

$$
\begin{gathered}
\min_{W_1,\ldots,W_i,\ldots,W_p} J = \sum_{i=1}^{p} \left(q_{\mathrm{r}^2,i} F_{\mathrm{r}^2,i} + q_{\mathrm{h},i} F_{\mathrm{h},i} + q_{\rho,i} F_{\rho,i} \right) \\
\text{subject to} \\
F_{\mathrm{r}^2,i} = \left[\frac{r_{\mathrm{set}}^2 - \langle \tilde{r}^2(t_i) \rangle}{r_{\mathrm{set}}^2} \right]^2, \\
F_{\mathrm{h},i} = \begin{cases} \left[\dfrac{h_{\min} - \left\langle \bar{h}(t_i) \right\rangle}{h_{\min}} \right]^2, & h_{\min} > \left\langle \bar{h}(t_i) \right\rangle, \\ 0, & h_{\min} \leq \left\langle \bar{h}(t_i) \right\rangle, \end{cases} \\
F_{\rho,i} = \left[\frac{\rho_{\mathrm{set}} - \rho(t_i)}{\rho_{\mathrm{set}}} \right]^2, \\
\left\langle \alpha_n^2(t_i) \right\rangle = \frac{\sigma^2}{2\nu n^2} + \left(\left\langle \alpha_n^2(t_{i-1}) \right\rangle - \frac{\sigma^2}{2\nu n^2} \right) e^{-2\nu n^2 \Delta}, \\
\left\langle \beta_n^2(t_i) \right\rangle = \frac{\sigma^2}{2\nu n^2} + \left(\left\langle \beta_n^2(t_{i-1}) \right\rangle - \frac{\sigma^2}{2\nu n^2} \right) e^{-2\nu n^2 \Delta}, \\
\left\langle \bar{h}(t_i) \right\rangle = \left\langle \bar{h}(t_{i-1}) \right\rangle + r_{\mathrm{h}} \Delta, \\
\rho(t_i) = \frac{\left\{ \rho(t_{i-1}) \left\langle \bar{h}(t_{i-1}) \right\rangle + r_{\mathrm{h}} \left[\rho^{\mathrm{ss}} \Delta + (\rho^{\mathrm{ss}} - \rho(t_{i-1})) \tau (e^{-\Delta/\tau} - 1) \right] \right\}}{\left\langle \bar{h}(t_{i-1}) \right\rangle + r_{\mathrm{h}} \Delta}, \\
W_{\min} < W_i < W_{\max}, \quad \left| \frac{W_{i+1} - W_i}{\Delta} \right| \leq L_{\mathrm{W}}, \\
n = 1, 2, \ldots, m, \quad i = 1, 2, \ldots, p,
\end{gathered}
\tag{7.29}
$$

where t is the current time, Δ is the sampling time, p is the number of prediction steps, $p\Delta$ is the specified prediction horizon, t_i, $i = 1, 2, \ldots, p$, is the time of the ith prediction step ($t_i = t + i\Delta$), respectively, W_i, $i = 1, 2, \ldots, p$, is the deposition rate at the ith step ($W_i = W(t + i\Delta)$), respectively, $q_{\mathrm{r}^2,i}$, $q_{\mathrm{h},i}$, and $q_{\rho,i}$, $i = 1, 2, \ldots, p$, are the

weighting penalty factors for the deviations of $\langle r^2 \rangle$ and ρ from their respective set-points $r^2_{\rm set}$ and $\rho_{\rm set}$, and $\langle \bar{h} \rangle$ from its desired minimum, $h_{\rm min}$, at the ith prediction step, $W_{\rm min}$ and $W_{\rm max}$ are the lower and upper bounds on the deposition rate, respectively, and $L_{\rm W}$ is the limit on the rate of change of the deposition rate. Note that we choose $\langle \bar{h} \rangle$, $r_{\rm h}$ and $\rho(t_0)$ to replace H, $r_{\rm H}$ and $\rho_{\rm d0}$ in the MPC formulation of Eq. (7.29), respectively.

The optimal set of control actions, $(W_1, W_2, \ldots, W_p)$, is obtained from the solution of the multi-variable optimization problem of Eq. (7.29), and only the first value of the manipulated input trajectory, W_1, is applied to the deposition process from time t until the next sampling time, when new measurements are received and the MPC problem of Eq. (7.29) is solved for the computation of the next optimal input trajectory.

The dependence of the model parameters, $r_{\rm h}$, ν, σ^2, $\rho^{\rm ss}$, and τ, on the deposition rate, W, is used in the formulation of the model predictive controller of Eq. (7.29). The parameters estimated under time-invariant operating conditions are suitable for the purpose of MPC design because the control input in the MPC formulation is piecewise constant, i.e., the manipulated deposition rate remains constant between two consecutive sampling times, and thus, the dynamics of the microscopic process can be predicted using the dynamic models with estimated parameters.

7.5 Simulation results

In this section, the proposed model predictive controller of Eq. (7.29) is applied to the kMC model of the thin film growth process described in Section 7.2. The value of the deposition rate is obtained from the solution of the problem of Eq. (7.29) at each sampling time and is applied to the closed-loop system until the next sampling time. The optimization problem in the MPC formulation of Eq. (7.29) is solved via a local constrained minimization algorithm using a broad set of initial guesses. Since the state variables of the system are accessed or measured only at the sampling times in the closed-loop simulations, no statistical information, e.g., the expected complete film SOR, is available for feedback control. Thus, instantaneous values of the surface height profile and film SOR are used as the initial conditions for the dynamic models in the MPC formulation of Eq. (7.29).

The desired values (set-point values) in the closed-loop simulations are $r^2_{\rm set} = 100$ layer^2 and $\rho_{\rm set} = 0.96$, with a desired minimum of film thickness of $h_{\rm min} = 1000$ layer. The substrate temperature is fixed at 850 K and the initial deposition rate is 0.2 layer/s. The variation of deposition rate is from 0.1 layer/s to 1 layer/s. The maximum rate of change of the deposition rate is $L_{\rm W} = 10$ layer/s^2. All penalty factors, $q_{{\rm r}^2,i}$, $q_{{\rm h},i}$, and $q_{\rho,i}$, are set to be either zero or one. The number of prediction steps is set to be $p = 5$. The prediction horizon of each step is fixed at $\Delta = 200$ s. The time interval between two samplings is 5 s. The computational time that is used to solve the optimization problem with the current available computing power

is negligible (within 10 milliseconds) with respect to the sampling time interval. The closed-loop simulation duration is 1500 s. All expected values are obtained from 1000 independent simulation runs.

7.5.1 Regulation of surface roughness with/without constrained film thickness

Closed-loop simulations of separately regulating film surface roughness with desired minimum of film thickness (roughness control problem) are first carried out. In these control problems, the control objective is to regulate the expected surface roughness square to the desired value (100 layer^2) with a desired minimum of expected film thickness (1000 layers). Thus, the cost functions of these problems contain penalties on the deviations of the expected surface roughness square from the set-point value and of the expected film thickness from its desired minimum.

Figure 7.4 shows the closed-loop simulation results of the roughness-thickness control problem. From Figure 7.4, it can be seen that the model predictive controller drives the expected surface roughness square close to the desired value, 100 layer^2, at the end of the simulation. However, due to the existence of desired minimum of film thickness, 1000 layers, the controller computes a higher deposition rate, and thus, it results in a higher expected surface roughness square at the end of the closed-loop simulation. The effect of the minimum of film thickness can be observed by comparing Figure 7.4 to Figure 7.5, which shows the closed-loop simulation results without

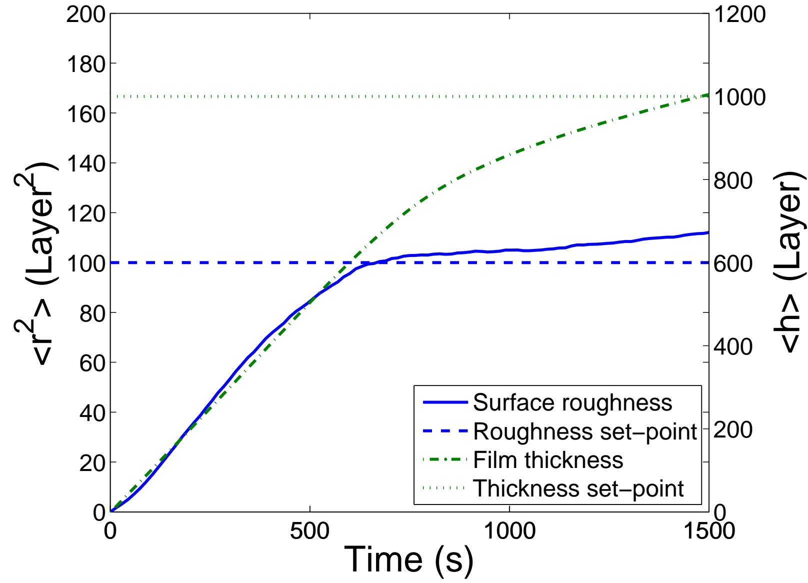

Figure 7.4: Profiles of the expected values of surface roughness square (solid line) and of the expected values of the film thickness (dash-dotted line) under closed-loop operation; roughness control problem with desired minimum of film thickness.

desired minimum of film thickness. It can be clearly seen that, without penalty on the deviation of film thickness, the expected surface roughness square approaches the set-point value at the end of the simulation, while the expected film thickness falls under the desired minimum. Figure 7.6 shows the comparison between the profiles of deposition rate with and without desired minimum of film thickness included in the cost function. In Figure 7.6, it can be seen that the thickness constraint results in a higher deposition rate so that the desired minimum of film thickness can be achieved at the end of the closed-loop simulations.

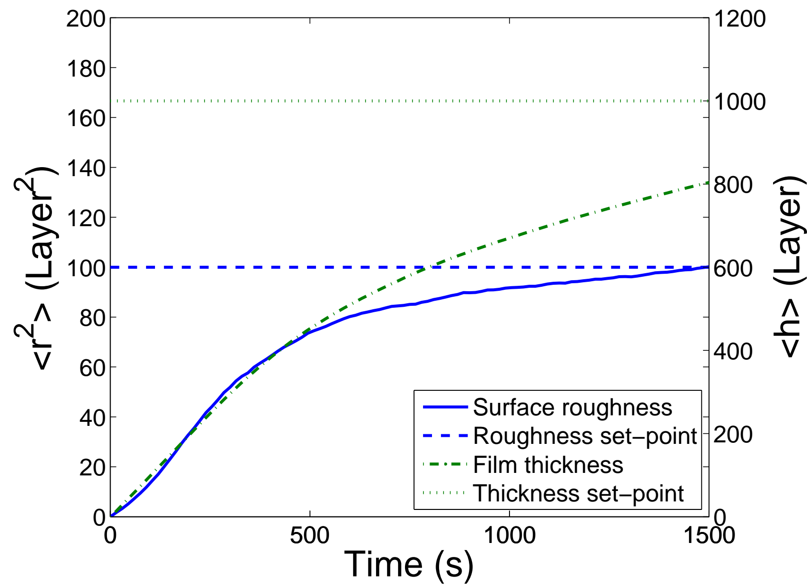

Figure 7.5: Profiles of the expected values of surface roughness square (solid line) and of the film thickness (dash-dotted line) under closed-loop operation; roughness control problem without desired minimum of film thickness.

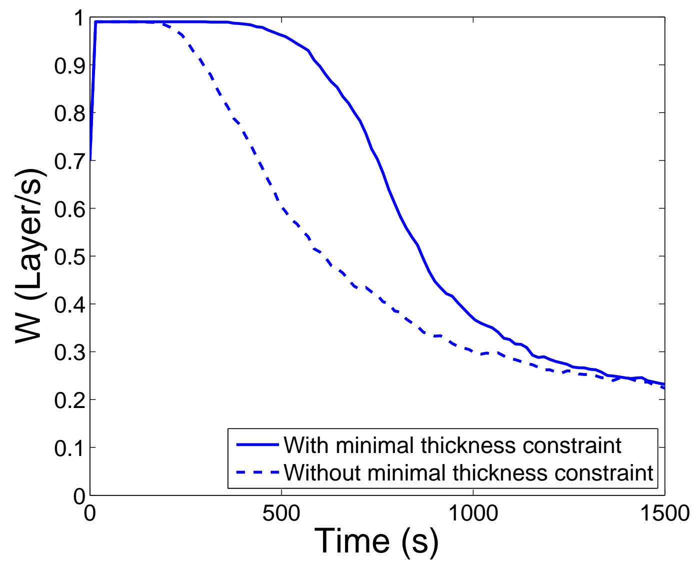

Figure 7.6: Profiles of the expected values of deposition rate under closed-loop operation with (solid line) and without (dashed line) desired minimum of film thickness; roughness control problem.

7.5.2 Regulation of film porosity by manipulating deposition rate

In this subsection, film SOR is the control objective (porosity control problem). In the porosity control problem, the cost function in the MPC formulation includes only penalty on the deviation of the film SOR from the set-point value, 0.96. Figure 7.7 shows the evolution profile of the film SOR from the closed-loop simulation of the porosity control problem. The model predictive controller successfully drives the expected film SOR to the set-point value and stabilizes it at the steady state. There is no offset from the set-point at large times compared to the closed-loop simulation results under a model predictive controller that utilizes a deterministic linear ODE model for the film SOR [40]. The elimination of offset demonstrates that the dynamic models of Eqs. (7.21) and (7.22), which are postulated in Section 7.3.2, are suitable for the purpose of porosity control. The corresponding profile of the deposition rate W is also shown in Figure 7.7 (dash-dotted line).

7.5.3 Simultaneous regulation of surface roughness and film porosity with constrained film thickness

Finally, closed-loop simulations of simultaneous regulation of film thickness, surface roughness and film SOR are carried out. Since the deposition rate is the only manipulated input, the desired values of r^2_{set} and ρ_{set} cannot be achieved simultaneously,

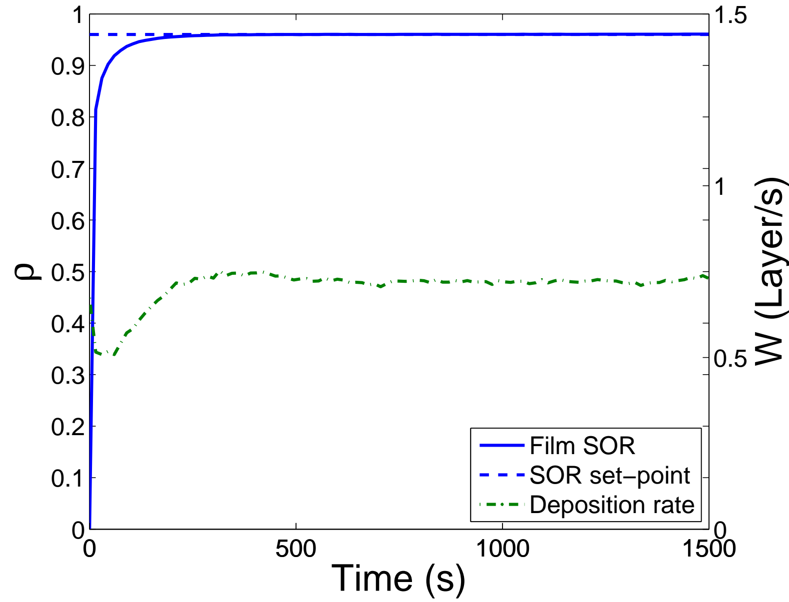

Figure 7.7: Profiles of the expected values of film SOR (solid line) and of the deposition rate (dash-dotted line) under closed-loop operation; porosity-only control.

i.e., the corresponding adsorption rates for the desired surface roughness and film thickness are not the same. Therefore, a trade-off between the two set-points is made by the controller. Figures 7.8 and 7.9 show the simulation results. The expected values of both surface roughness square and film SOR approach their corresponding set-points with the minimal film thickness achieved. The simulation profiles of expected surface roughness square and film thickness are close to the profiles from the roughness control problem in Section 7.5.1. The close profiles are due to the fact that the film SOR is not sensitive to the variation of the deposition rate, and thus, the controller tries to regulate the surface roughness square to its set-point.

Figures 7.10 and 7.11 show the instantaneous values of surface roughness square and film SOR in the closed-loop simulation. The instantaneous values are obtained

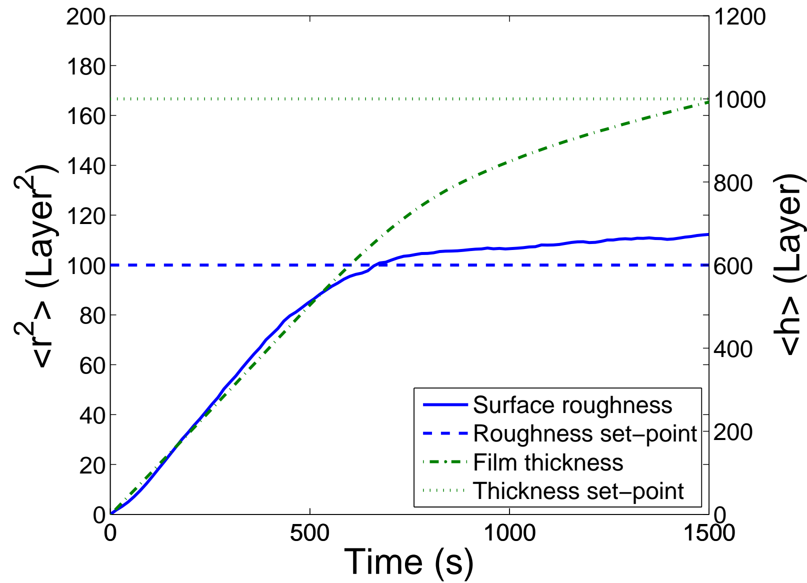

Figure 7.8: Profiles of the expected values of surface roughness square (solid line) and of the film thickness (dash-dotted line) under closed-loop operation; simultaneous regulation of film thickness, roughness and porosity.

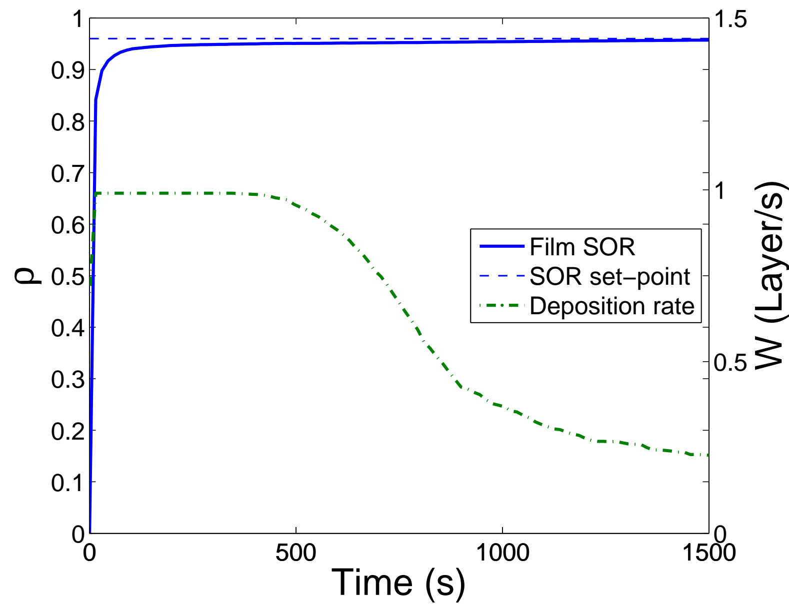

Figure 7.9: Profiles of the expected values of film SOR (solid line) and of the deposition rate (dash-dotted line) under closed-loop operation; simultaneous regulation of film thickness, roughness and porosity.

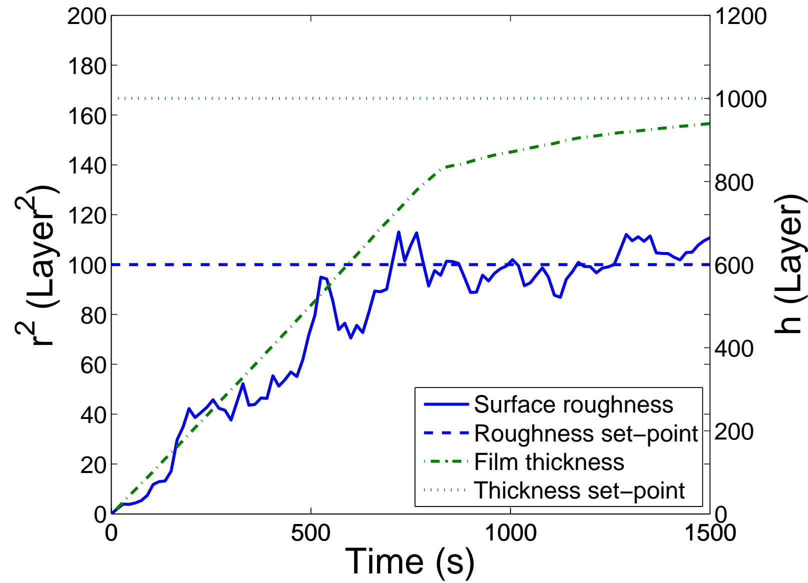

Figure 7.10: Profiles of the instantaneous values of surface roughness square (solid line) and of the film thickness (dash-dotted line) under closed-loop operation; simultaneous regulation of film thickness, roughness and porosity.

from a single simulation run, and thus, different runs may result in different profiles. The manipulated deposition rate is also shown in Figure 7.11. At the beginning, the controller saturates the deposition rate at the upper bound of 1 layer/s to achieve the minimal film thickness. Surface roughness square and film SOR also increase from 0 towards their respective set-points. At about 700 s, surface roughness square reaches its set-point, and soon after that, the optimal deposition rate drops fast close to the lower bound so as to keep the surface roughness square at the set-point and to increase the film thickness close to the minimal value.

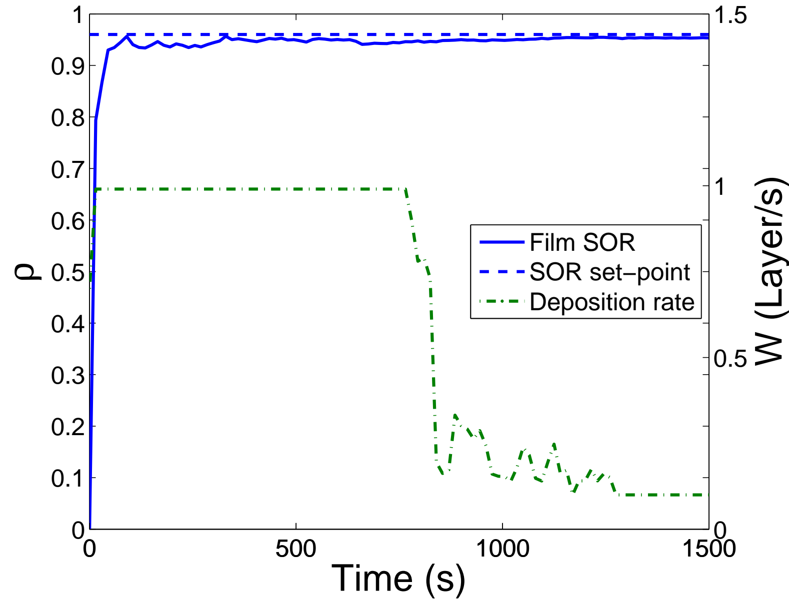

Figure 7.11: Profiles of the instantaneous values of film SOR (solid line) and of the deposition rate (dash-dotted line) under closed-loop operation; simultaneous regulation of film thickness, roughness and porosity.

7.6 Conclusions

Distributed control of film thickness, surface roughness, and porosity was developed for a porous thin film deposition process. The deposition process was modeled via kinetic Monte Carlo simulation on a triangular lattice. As a batch process, film thickness is an important target variable for the thin film growth process. The deposition rate was thus selected as the manipulated input due to its direct influence on the film thickness. To characterize the evolution of film surface roughness and account for the stochastic nature of the deposition process, a distributed parameter dynamic model was derived to describe the evolution of the surface height profile of the thin film accounting for the effect of deposition rate. The dynamics of film porosity, evaluated

as film SOR, were described by an ordinary differential equation. The developed dynamic models were then used as the basis for the design of a model predictive control algorithm that includes penalty on the deviation of film thickness, surface roughness and film porosity from their respective set-point values. A reduced-order model of the film surface height was included in the MPC formulation to calculate the prediction of expected surface roughness to meet the requirement of computational efficiency for real-time feedback control calculations. Simulation results demonstrated the applicability and effectiveness of the proposed modeling and control approach in the context of the deposition process under consideration. We found out that the film thickness requirement essentially places a lower bound on the deposition rate, and thus, it limits the range of achievable film porosity.

Chapter 8

Conclusions

Motivated by the increasing importance of thin film microstructure in semiconductor manufacturing, this dissertation developed a systematic methodology of modeling and control of thin film surface roughness, porosity, and film thickness within a unified framework. Kinetic Monte Carlo (kMC) methods and stochastic/deterministic differential equation models were constructed to account for the stochastic nature of the thin film growth/sputtering processes and were used as the basis for controller design.

Specifically, in Chapter 2, a dynamic output feedback covariance controller was initially introduced, which includes a state feedback controller and a Kalman-Bucy-type filter as the state estimator. The output feedback controller was designed to regulate the surface covariance (e.g., surface roughness) of a stochastic dissipative partial differential equation (PDE) subject to measurement sensor noise. Both theoretical

analysis and numerical simulations were performed to demonstrate the accuracy and effectiveness of the proposed output feedback covariance controller.

Subsequently, Chapter 3 presented a novel method of parameter estimation of a stochastic PDE model, the stochastic Kuramoto-Sivashinsky equation (KSE), for a sputtering process. The parameters of the stochastic KSE were estimated for the best prediction of the surface roughness profile of the kMC simulations in a least-square sense. Using the estimated parameters, a model-based output feedback controller was designed on the basis of the stochastic KSE to regulate surface roughness and was successfully applied to the kMC model of the sputtering process.

Chapter 4 focused on the development of model predictive control (MPC) algorithms for surface roughness regulation. Specifically, in Chapter 4, an MPC formulation was developed to regulate the state variance of nonlinear stochastic PDEs. A linear structure in the closed-loop was introduced in the MPC formulation by applying a nonlinear state feedback controller to the finite-dimensional approximation of the stochastic PDE. The optimization algorithm in the MPC formulation then solved for the optimal pole placement structure that leads to the closest prediction to the roughness reference trajectory.

The modeling and control of film porosity, another important film property that cannot be captured by the surface height profile, was addressed in Chapters 5, 6, and 7 of the dissertation. Film porosity was obtained from a thin film deposition process modeled on a triangular lattice. In Chapter 5, deterministic/stochastic ODE models

were derived to describe the time evolution of film SOR and its fluctuation. The developed dynamic models for the film SOR were used as the basis for the design of MPC algorithms to regulate the film porosity at a desired level and reduce run-to-run fluctuations by manipulating the substrate temperature.

Finally, Chapters 6 and 7 further extended the methods of stochastic modeling and MPC algorithm design presented in Chapter 5 to simultaneous regulation of film thickness, surface roughness, and film porosity. In Chapter 6, the MPC algorithm simultaneously regulated the surface roughness and film porosity with appropriate penalty weighting schemes. While in Chapter 7, we chose the deposition rate as the manipulated input to include the film thickness as the controlled variable in the simultaneous control problem of Chapter 6. As an essential thin film property that determines the electrical and mechanical properties, film thickness usually has a desired minimum value instead of a set-point. Thus, a one-sided penalty was imposed on the deviation of the thin film in the cost function in the MPC formulation. Simulation results successfully demonstrated the applicability and effectiveness of our approach of simultaneously regulating thin film porosity, surface roughness, and thickness.

Bibliography

[1] K. J. Åström. *Introduction to Stochastic Control Theory.* Academic Press, New York, 1970.

[2] Y. Akiyama, N. Imaishi, Y. S. Shin, and S. C. Jung. Macro- and micro-scale simulation of growth rate and composition in MOCVD of yttria-stabilized zirconia. *Journal of Crystal Growth*, 241:352–362, 2002.

[3] H. Aling, S. Benerjee, A. K. Bangia, V. Cole, J. Ebert, A. Emani-Naeini, K. F. Jensen, I. G. Kevrekidis, and S. Shvartsman. Nonlinear model reduction for simulation and control of rapid thermal processing. In *Proceedings of American Control Conference*, pages 2233–2238, Albuquerque, NM, 1997.

[4] F. Allgower and H. Chen. Nonlinear model predictive control schemes with guaranteed stability. In *NATO ASI on Nonlinear Model Based Process Control*, pages 465–494, Berber, R., Kravaris, C., Eds.; Kluwer: Dordrecht, the Netherlands, 1998.

[5] A. Armaou and P. D. Christofides. Plasma-enhanced chemical vapor deposition: Modeling and control. *Chemical Engineering Science*, 54:3305–3314, 1999.

[6] A. Armaou and P. D. Christofides. Dynamic optimization of dissipative PDE systems using nonlinear order reduction. *Chemical Engineering Science*, 57:5083–5114, 2002.

[7] A. Armaou and I. G. Kevrekidis. Equation-free optimal switching policies for bistable reacting systems. *International Journal of Robust and Nonlinear Control*, 15:713–726, 2005.

[8] A. Armaou, C. I. Siettos, and I. G. Kevrekidis. Time-steppers and 'coarse' control of distributed microscopic processes. *International Journal of Robust and Nonlinear Control*, 14:89–111, 2004.

[9] P. Astrid. *Reduction of Process Simulation Models: A Proper Orthogonal Decomposition Approach*. Technische Universiteit, Eindhoven, The Netherland, 2004.

[10] J. Baker and P. D. Christofides. Output feedback control of parabolic PDE systems with nonlinear spatial differential operators. *Industrial & Engineering Chemistry Research*, 38:4372–4380, 1999.

[11] A. Ballestad, B. J. Ruck, J. H. Schmid, M. Adamcyk, E. Nodwell, C. Nicoll, and T. Tiedje. Surface morphology of GaAs during molecular beam epitaxy growth: Comparison of experimental data with simulations based on continuum growth equations. *Physical Review B*, 65:205302, 2002.

[12] D. S. Bernstein and W. M. Haddad. Robust stability and performance analysis for linear dynamic systems. *IEEE Transactions on Automatic Control*, 34:751–758, 1989.

[13] A. Bindal, M. G. Ierapetritou, S. Balakrishnan, A. Armaou, A. G. Makeev, and I. G. Kevrekidis. Equation-free, coarse-grained computational optimization using timesteppers. *Chemical Engineering Science*, 61:779–793, 2006.

[14] T. Bohlin and S. F Graebe. Issues in nonlinear stochastic grey-box identification. *International Journal of Adaptive Control and Signal Processing*, 9:465–490, 1995.

[15] M. Bohm, M. A. Demetriou, S. Reich, and I. G. Rosen. Model reference adaptive control of distributed parameter systems. *SIAM Journal on Control and Optimization*, 36:33–81, 1998.

[16] R. P. Brent. *Algorithms for Minimization without Derivatives*. Prentice-Hall, Englewood Cliffs, New Jersey, 1973.

[17] C. Buzea and K. Robbie. State of the art in thin film thickness and deposition rate monitoring sensors. *Reports on Progress in Physics*, 68:385–409, 2005.

[18] J. O. Choo, R. A. Adomaitis, L. Henn-Lecordier, Y Cai, and G. W. Rubloff. Development of a spatially controllable chemical vapor deposition reactor with combinatorial processing capabilities. *Review of Scientific Instruments*, 76:062217, 2005.

[19] P. D. Christofides. *Nonlinear and Robust Control of PDE Systems: Methods and Applications to Transport-Reaction Processes*. Birkhäuser, Boston, 2001.

[20] P. D. Christofides and A. Armaou. Control and optimization of multiscale process systems. *Computers & Chemical Engineering*, 30:1670–1686, 2006.

[21] P. D. Christofides, A. Armaou, Y. Lou, and A. Varshney. *Control and Optimization of Multiscale Process Systems*. Birkhäuser, Boston, 2008.

[22] P. D. Christofides and J. Baker. Robust output feedback control of quasi-linear parabolic PDE systems. *Systems & Control Letters*, 36:307–316, 1999.

[23] P. D. Christofides and P. Daoutidis. Finite-dimensional control of parabolic PDE systems using approximate inertial manifolds. *Journal of Mathematical Analysis and Applications*, 216:398–420, 1997.

[24] P. D. Christofides and N. H. El-Farra. *Control of Nonlinear and Hybrid Process Systems: Designs for Uncertainty, Constraints and Time-Delays*. Springer-Verlag, Berlin, German, 2005.

[25] A. L. S. Chua, C. A. Haselwandter, C. Baggio, and D. D. Vvedensky. Langevin equations for fluctuating surfaces. *Physical Review E*, 72:051103, 2005.

[26] R. Cuerno, H. A. Makse, S. Tomassone, S. T. Harrington, and H. E. Stanley. Stochastic model for surface erosion via ion sputtering: Dynamical evolution

from ripple morphology to rough morphology. *Physical Review Letters*, 75:4464–4467, 1995.

[27] T. O. Drew, E. G. Webb, D. L. Ma, J. Alameda, R. D. Braatz, and R. C. Alkire. Coupled mesoscale - continuum simulations of copper electrodeposition in a trench. *AIChE Journal*, 50:226–240, 2004.

[28] S. Dubljevic and P. D. Christofides. Predictive control of parabolic PDEs with boundary control actuation. *Chemical Engineering Science*, 61:6239–6248, 2006.

[29] S. Dubljevic, P. Mhaskar, N. H. El-Farra, and P. D. Christofides. Predictive control of transport-reaction processes. *Computers & Chemical Engineering*, 29:2335–2345, 2005.

[30] S. Dubljevic, P. Mhaskar, N. H. El-Farra, and P. D. Christofides. Predictive control of parabolic PDEs with state and control constraints. *International Journal of Robust and Nonlinear Control*, 16:749–772, 2006.

[31] S. F. Edwards and D. R. Wilkinson. The surface statistics of a granular aggregate. *Proceedings of the Royal Society of London Series A - Mathematical Physical and Engineering Sciences*, 381:17–31, 1982.

[32] K. A. Fichthorn and W. H. Weinberg. Theoretical foundations of dynamical Monte Carlo simulations. *Journal of Chemical Physics*, 95:1090–1096, 1991.

[33] M. A. Gallivan and R. M. Murray. Reduction and identification methods for Markovian control systems, with application to thin film deposition. *International Journal of Robust and Nonlinear Control*, 14:113–132, 2004.

[34] C. E. Garcia, D. M. Prett, and M. Morari. Model predictive control: Theory and practices - a survey. *Automatica*, 25:335–348, 1989.

[35] D. T. Gillespie. A general method for numerically simulating the stochastic time evolution of coupled chemical reactions. *Journal of Computational Physics*, 22:403–434, 1976.

[36] C. Haselwandter and D. D. Vvedensky. Fluctuations in the lattice gas for Burgers' equation. *Journal of Physics A: Mathematical and General*, 35:L579–L584, 2002.

[37] A. Hotz and R. E. Skelton. Covariance control theory. *International Journal of Control*, 46:13–32, 1987.

[38] G. Hu, Y. Lou, and P. D. Christofides. Dynamic output feedback covariance control of stochastic dissipative partial differential equations. *Chemical Engineering Science*, 63:4531–4542, 2008.

[39] G. Hu, Y. Lou, and P. D. Christofides. Model parameter estimation and feedback control of surface roughness in a sputtering process. *Chemical Engineering Science*, 63:1810–1816, 2008.

[40] G. Hu, G. Orkoulas, and P. D. Christofides. Modeling and control of film porosity in thin film deposition. *Chemical Engineering Science*, 64:3668–3682, 2009.

[41] G. Hu, G. Orkoulas, and P. D. Christofides. Stochastic modeling and simultaneous regulation of surface roughness and porosity in thin film deposition. *Industrial & Engineering Chemistry Research*, 48:6690–6700, 2009.

[42] Z. Insepov, I. Yamada, and M. Sosnowski. Surface smoothing with energetic cluster beams. *Journal of Vacuum Science & Technology A - Vacuum Surfaces and Films*, 15:981–984, 1997.

[43] T. Iwasaki and R. E. Skelton. On the observer-based structure of covariance controllers. *Systems & Control Letters*, 22:17–25, 1994.

[44] H. C. Kan, S. Shah, T. Tadyyon-Eslami, and R. J. Phaneuf. Transient evolution of surface roughness on patterned GaAs(001) during homoepitaxial growth. *Physical Review Letters*, 92:146101, 2004.

[45] M. Kardar, G. Parisi, and Y. C. Zhang. Dynamic scaling of growing interfaces. *Physical Review Letters*, 56:889–892, 1986.

[46] S. Keršulis and V. Mitin. Monte Carlo simulation of growth and recovery of silicon. *Material Science & Engineering B*, 29:34–37, 1995.

[47] P. E. Kloeden and E. Platen. *Numerical Solutions of Stochastic Differential Equations*. Springer-Verlag, Heidelberg, 1995.

[48] G. Kloster, T. Scherban, G. Xu, J. Blaine, B. Sun, and Y. Zhou. Porosity effects on low-k dielectric film strength and interfacial adhesion. In *Proceedings of the IEEE 2002 International Interconnect Technology Conference*, pages 242–244, 2002.

[49] P. V. Kokotovic, H. K. Khalil, and J. O'Reilly. *Singular Perturbations in Control: Analysis and Design*. Academic Press, London, 1986.

[50] N. R. Kristensen, H. Madsen, and S. B. Jorgensen. Parameter estimation in stochastic grey-box models. *Automatica*, 40:225–237, 2004.

[51] M. Krstic and A. Smyshlyaev. Adaptive control of PDEs. *Annual Reviews in Control*, 32:149–160, 2008.

[52] J. C. Lagarias, J. A. Reeds, M. H. Wright, and P. E. Wright. Convergence properties of the Nelder-Mead simplex method in low dimensions. *SIAM Journal of Optimization*, 9:112–147, 1998.

[53] K. B. Lauritsen, R. Cuerno, and H. A. Makse. Noisy Kuramoto-Sivashinsky equation for an erosion model. *Physical Review E*, 54:3577–3580, 1996.

[54] Y. H. Lee, Y. S. Kim, B. K. Ju, and M. H. Oh. Roughness of ZnS:Pr,Ce/Ta_2O_5 interface and its effects on electrical performance of alternating current thin-film electroluminescent devices. *IEEE Transactions on Electron Devices*, 46:892–896, 1999.

[55] S. W. Levine and P. Clancy. A simple model for the growth of polycrystalline Si using the kinetic Monte Carlo simulation. *Modelling and Simulation in Materials Science and Engineering*, 8:751–762, 2000.

[56] S. W. Levine, J. R. Engstrom, and P. Clancy. A kinetic Monte Carlo study of the growth of Si on Si(100) at varying angles of incident deposition. *Surface Science*, 401:112–123, 1998.

[57] Y. Lou and P. D. Christofides. Estimation and control of surface roughness in thin film growth using kinetic Monte-Carlo methods. *Chemical Engineering Science*, 58:3115–3129, 2003.

[58] Y. Lou and P. D. Christofides. Feedback control of growth rate and surface roughness in thin film growth. *AIChE Journal*, 49:2099–2113, 2003.

[59] Y. Lou and P. D. Christofides. Feedback control of surface roughness of GaAs (001) thin films using kinetic Monte Carlo models. *Computers & Chemical Engineering*, 29:225–241, 2004.

[60] Y. Lou and P. D. Christofides. Feedback control of surface roughness in sputtering processes using the stochastic Kuramoto-Sivashinsky equation. *Computers & Chemical Engineering*, 29:741–759, 2005.

[61] Y. Lou and P. D. Christofides. Feedback control of surface roughness using stochastic PDEs. *AIChE Journal*, 51:345–352, 2005.

[62] Y. Lou and P. D. Christofides. Nonlinear feedback control of surface roughness using a stochastic PDE: Design and application to a sputtering process. *Industrial & Engineering Chemistry Research*, 45:7177–7189, 2006.

[63] Y. Lou, G. Hu, and P. D. Christofides. Model predictive control of nonlinear stochastic partial differential equations with application to a sputtering process. *AIChE Journal*, 54:2065–2081, 2008.

[64] A. Lucia, P. A. DiMaggio, and P. Depa. Funneling algorithms for multiscale optimization on rugged terrains. *Industrial* & *Engineering Chemistry Research*, 43:3770–3781, 2004.

[65] A. Lucia, P. A. DiMaggio, and P. Depa. A geometric terrain methodology for global optimization. *Journal of Global Optimization*, 29:297–314, 2004.

[66] M. A. Makeev, R. Cuerno, and A. L. Barabasi. Morphology of ion-sputtered surfaces. *Nuclear Instruments and Methods in Physics Research B*, 197:185–227, 2002.

[67] G. Makov and M. C. Payne. Periodic boundary conditions in ab initio calculations. *Physical Review B*, 51:4014–4022, 1995.

[68] P. B. Maksym. Fast Monte Carlo simulation of MBE growth. *Semiconductor Science and Technology*, 3:594–596, 1988.

[69] D. Q. Mayne, J. B. Rawlings, C. V. Rao, and P. O. M. Scokaert. Constrained model predictive control: Stability and optimality. *Automatica*, 36:789–814, 2000.

[70] D. Ni and P. D. Christofides. Dynamics and control of thin film surface microstructure in a complex deposition process. *Chemical Engineering Science*, 60:1603–1617, 2005.

[71] D. Ni and P. D. Christofides. Multivariable predictive control of thin film deposition using a stochastic PDE model. *Industrial & Engineering Chemistry Research*, 44:2416–2427, 2005.

[72] D. Ni, Y. Lou, P. D. Christofides, L. Sha, S. Lao, and J. P. Chang. Real-time carbon content control for PECVD ZrO_2 thin-film growth. *IEEE Transactions on Semiconductor Manufacturing*, 17:221–230, 2004.

[73] H. J. Qi, L. H. Huang, Z. S. Tang, C. F. Cheng, J. D. Shao, and Z. X. Fan. Roughness evolution of ZrO_2 thin films grown by reactive ion beam sputtering. *Thin Solid Films*, 444:146–152, 2003.

[74] J. B. Rawlings. Tutotial: Model predictive control technology. In *Proceedings of the American Control Conference*, pages 662–676, San Diego, CA, 1999.

[75] J. S. Reese, S. Raimondeau, and D. G. Vlachos. Monte Carlo algorithms for complex surface reaction mechanisms: Efficiency and accuracy. *Journal of Computational Physics*, 173:302–321, 2001.

[76] G. Renaud, R. Lazzari, C. Revenant, A. Barbier, M. Noblet, O. Ulrich, F. Leroy, J. Jupille, Y. Borensztein, C. R. Henry, J. P. Deville, F. Scheurer, J. Mane-Mane, and O. Fruchart. Real-time monitoring of growing nanoparticles. *Science*, 300:1416–1419, 2003.

[77] E. Rusli, T. O. Drews, D. L. Ma, R. C. Alkire, and R. D. Braatz. Robust nonlinear feedback-feedforward control of a coupled kinetic Monte-Carlo-finite difference simulation. In *Proceedings of the American Control Conference*, pages 2548–2553, Portland, OR, 2005.

[78] P. O. Scokaert, D. Q. Mayne, and J. B. Rawlings. Suboptimal model predictive control (feasibility implies stability). *IEEE Transactions on Automatic Control*, 44:648–654, 1999.

[79] T. Shitara, D. D. Vvedensky, M. R. Wilby, J. Zhang, J. H. Neave, and B. A. Joyce. Step-density variations and reflection high-energy electron-diffraction intensity oscillations during epitaxial growth on vicinal GaAs(001). *Physical Review B*, 46:6815–6824, 1992.

[80] M. Siegert and M. Plischke. Solid-on-solid models of molecular-beam epitaxy. *Physical Review E*, 50:917–931, 1994.

[81] C. I. Siettos, A. Armaou, A. G. Makeev, and I. G. Kevrekidis. Microscopic/stochastic timesteppers and coarse control: a kinetic Monte Carlo example. *AIChE Journal*, 49:1922–1926, 2003.

[82] R. E. Skelton, J. H. Xu, and K. Yasuda. Minimal energy covariance control. *International Journal of Control*, 59:1567–1578, 1994.

[83] A. Theodoropoulou, R. A. Adomaitis, and E. Zafiriou. Model reduction for optimization of rapid thermal chemical vapor deposition systems. *IEEE Transactions on Semiconductor Manufacturing*, 11:85–98, 1998.

[84] A. Theodoropoulou, R. A. Adomaitis, and E. Zafiriou. Inverse model based real-time control for temperature uniformity of RTCVD. *IEEE Transactions on Semiconductor Manufacturing*, 12:87–101, 1999.

[85] A. Varshney and A. Armaou. Multiscale optimization using hybrid PDE/kMC process systems with application to thin film growth. *Chemical Engineering Science*, 60:6780–6794, 2005.

[86] J. Villain. Continuum models of crystal growth from atomic beams with and without desorption. *Journal De Physique I*, 1:19–42, 1991.

[87] D. G. Vlachos. Multiscale integration hybrid algorithms for homogeneous-heterogeneous reactors. *AIChE Journal*, 43:3031–3041, 1997.

[88] D. G. Vlachos, L. D. Schmidt, and R. Aris. Kinetics of faceting of crystals in growth, etching, and equilibrium. *Physical Review B*, 47:4896–4909, 1993.

[89] B. Voigtländer. Fundamental processes in Si/Si and Ge/Si studied by scanning tunneling microscopy during growth. *Surface Science Reports*, 43:127–254, 2001.

[90] D. D. Vvedensky. Edwards-Wilkinson equation from lattice transition rules. *Physical Review E*, 67:025102(R), 2003.

[91] D. D. Vvedensky, A. Zangwill, C. N. Luse, and M. R. Wilby. Stochastic equations of motion for epitaxial growth. *Physical Review E*, 48:852–862, 1993.

[92] L. Wang and P. Clancy. Kinetic Monte Carlo simulation of the growth of polycrystalline Cu films. *Surface Science*, 473:25–38, 2001.

[93] P. Wolfrum, A. Vargas, M. Gallivan, and F. Allgower. Complexity reduction of a thin film deposition model using a trajectory based nonlinear model reduction technique. In *Proceedings of the American Control Conference*, pages 2566–2571, Portland, OR, 2005.

[94] Y. G. Yang, D. D. Hass, and H. N. Wadley. Porosity control in zig-zag vapor-deposited films. *Thin Solid Film*, 471:1–11, 2005.

[95] Y. G. Yang, R. A. Johnson, and H. N. Wadley. A Monte Carlo simulation of the physical vapor deposition of nickel. *Acta Materialia*, 45:1455–1468, 1997.

[96] J. A. Zapien, R. Messier, and R. W. Collin. Ultraviolet-extended real-time spectroscopic ellipsometry for characterization of phase evolution in BN thin films. *Applied Physics Letters*, 78:1982–1984, 2001.

[97] P. Zhang, X. Zheng, S. Wu, J. Liu, and D. He. Kinetic Monte Carlo simulation of Cu thin film growth. *Vacuum*, 72:405–410, 2004.

[98] R. M. Ziff, E. Gulari, and Y. Barshad. Kinetic phase transitions in an irreversible surface-reaction model. *Physical Review Letters*, 56:2553–2556, 1986.